Advances in the design and operation of atom chips

Isabel Llorente García

Thesis submitted in partial fulfilment of the requirements for the degree of Doctor of Philosophy of the University of London and the Diploma of Membership of Imperial College.

Imperial College London

University of London

October 2008

Abstract

Advances in the design and operation of atom chips

Isabel Llorente García

This thesis reports on the experimental research carried out in the field of atom optics by confining ultracold rubidium atoms with temperatures of the order of 10^{-7}–10^{-4} Kelvin in microscopic, magnetic traps created using a piece of periodically-magnetised videotape mounted on an atom chip.

The work presented in this thesis focuses on three different topics. Experimental and simulated results are presented for the resonant motional excitation of cold atoms confined in videotape magnetic micro-traps. These results are used to determine the transverse oscillation frequencies of the atoms in the traps and illuminate the dynamics of cold atoms in anharmonic traps during a resonant excitation.

Fragmentation is studied in ultra-cold atomic clouds with temperatures of a few microKelvin, at distances between 30μm and 80μm from the videotape-chip surface. This is used to characterise the inhomogeneities in the magnetic field created by the periodically magnetised videotape.

Finally, a novel transport mechanism is described for the displacement of cold atoms confined in arrays of videotape magnetic micro-traps. Results are presented on the transport of cold atoms over distances as large as $\sim$ 1cm, parallel to the chip surface, and along the transverse direction of the videotape traps.

Acknowledgements

I would like to thank my supervisor, Ed Hinds, for his continuous guidance and trust during the years of my PhD, for his encouragement, his enthusiasm and for his undying passion for physics.

I would also like to thanks Chris Sinclair and Anne Curtis for their infinite patience and for helping me so much at the beginning of my PhD. Thanks to Chris Sinclair for providing continuous advice and help with the experiment at all times and for always being willing to share his vast knowledge of the experiment. Thanks to Anne Curtis for being such a pleasant presence in the group and for her continuous optimism and happiness.

Infinite and most special thanks go to Benoît Darquié, for absolutely everything. Thanks for being such a great post-doc. Thanks for always working so hard and for helping so much with every aspect of the experiment, for making it fun to work in the lab for long hours, for teaching me so much and for knowing nearly everything about anything. I would like to thank him for being always so supportive and for caring about my well-being, for his everyday enthusiasm and optimism and very specially for taking the time and effort to read and correct this manuscript while working in Paris.

I would like to thank Rob Nyman for reading and correcting this thesis and for his continuous support, encouragement and positive comments during my writing-up period.

Many thanks to Michael Trupke for many useful discussions about different aspects of the work in this thesis and for his valuable help and support during the latter stages.

Thanks to Jonathan Ashmore for so much hard work and so many long hours of patience gluing fibres in the lab, and for being so much fun to work with.

Thanks to Manuel Succo for helping with lab work and calculations and for teaching me about sealing flanges and other vacuum stuff.

Thanks to Jony Hudson, Stefan Eriksson, Ben Sauer and Jos Dingjan for providing advice so many times on many different matters and for always being willing to help. Thanks also to Daniel Sahagún Sánchez, Fernando Ramírez Martínez, Rob Sewell and Sean Tokunaga for their friendship and for making a nice atmosphere at work.

Thanks to Jon Dyne and David Williams for their great work in the mechanical workshop and for always being so efficient despite our last-minute, short notices.

Thanks to Maki Tachikawa for developing the collision theory and the initial stages of the simulation presented in chapter 5. Thanks also to all the people that so kindly allowed me to make use of their computers for the same simulation: Rob Nyman, Manuel Succo, Benoît Darquié, Jon Goldwin, Michael Trupke and Athanasios Laliotis.

Thanks to professor Horst Dötsch, from Osnabrück University in Germany for kindly providing us with a garnet sensor for magneto-optical imaging and for being so helpful by

email.

I would also like to thank Oliva Garcia Cantu-Ros and Hamid Tisselli for making such a nice atmosphere at home and for so many unforgettable fun moments. Very special thanks to Oliva for her listening and comforting during some hard moments, and for her friendship. Many thanks to Dimitris Skipis also for his friendship and support during these years.

Finally, thanks to my family for being there throughout the entire way, for their warmth and love was most appreciated.

Contents

List of Figures

List of Tables

Chapter 1

Introduction

The field of experimental research in cold atoms has seen enormous progress in the last two decades, developing with particular intensity since the award of the Nobel prize for Physics to S. Chu, C. Cohen-Tannoudji and W. D. Phillips for laser cooling and trapping [1–3] in 1997, and to E. A. Cornell, C. E. Weiman and W. Ketterle for the achievement of Bose-Einstein condensation (BEC) in dilute gases of alkali atoms [4, 5] in 2001.

Neutral atoms can now be trapped and cooled down to temperatures of the order of 10^{-7}–10^{-4} Kelvin, opening a wide range of possibilities for fundamental studies and applications requiring a high degree of control of an atomic system. Initially atoms were captured and cooled using macroscopic, free-standing structures, such as coils and wires. Proposals for building miniaturised structures to combine all the elements needed for magnetically trapping, cooling and manipulating neutral atoms were made around 1995. These proposals explored the possibility of using either planar current-carrying-wire geometries [6–9] or permanent magnets [10, 11] for constructing microscopic magnetic traps. These miniaturised structures soon started to be built and are now known as "atom chips". They are centimetre-scale devices that integrate wires or permanent magnets (or both) in a flat geometry to generate the magnetic fields required to confine neutral atoms at distances of the order of a few to a few hundred micrometres from the surface of the atom chip. Microfabricated, magnetic, neutral-atom traps were first experimentally realised by J. Reichel et al. [12] in 1999, and by R. Folman et al. [13] in 2000, using surface-mounted wires on an atom chip. Bose-Einstein condensation of rubidium atoms on an atom chip was achieved in 2001 by the groups of T. W. Hänsch and J. Reichel [14, 15], and of C. Zimmermann [16].

References [10, 15, 17, 18] offer an overview of the progress in the field of magnetic microchip traps up to 2001-2002, and reference [19] offers a more complete review of the work on atom chips up to 2007.

The use of atom chips greatly simplifies the apparatus needed to produce ultracold atoms or Bose-Einstein condensates, compared to the first atom-optical experiments based on macroscopic traps. Atom chips only require modest currents (1-10A in most atom chip experiments based on current-carrying wires) or no currents at all (in the case of permanent-magnet atom chips), in order to generate large magnetic-field gradients and tight magnetic confinement in the proximity of their surface. These tight traps lead to high elastic collision

rates of the atoms in the trap and hence to fast thermalisation times during evaporative cooling, enabling the production of ultracold atoms in fast sequences of ten seconds or less. Such fast sequences decrease the importance of collisions of the trapped atoms with the background gas, which lead to the loss of atoms from the magnetic micro-traps. Hence, the vacuum requirements can be relaxed to a background pressure of 10^{-9}–10^{-10} Torr [14], less stringent than for previous experiments based on macroscopic structures.

Other advantages of atom chips are the flexibility of trap configurations that they can create, from single traps to arrays of multiple traps, and the possibility of integrating all elements necessary for the controlled manipulation of ultracold atoms, such as trapping and transport elements, and on-chip detection devices, into a single compact geometry.

Several atom-chip experiments throughout the world have been carrying out fundamental studies of the physics of ultracold atoms. The achievement of Bose-Einstein condensation on atom chips has enabled the possibility of studying the behaviour of Bose-condensed atoms as coherent matter waves in experiments such as atomic beam splitters and atomic interferometers [20–25]. A review of atom interferometers can be found in reference [26].

Atom chips offer the possibility of confining ultracold atoms in very elongated traps with very tight transverse confinement and large aspect ratios, enabling the study of one-dimensional quantum gases. The reduction of dimensionality has dramatic effects on a trapped Bose gas, modifying its properties with respect to a three-dimensional gas and leading to the appearance of new quantum degenerate regimes [27–33], such as the phase-fluctuating quasi-condensate (in one or two dimensions), and the so-called Tonks-Girardeau gas (in one dimension). While most of these low-dimensional regimes have been studied experimentally using optical lattices and optical dipole traps (see for example references [34–42]), relevant studies on one-dimensional quantum gases have also been conducted on atom chips (see references [24, 25, 43–46], for instance).

The confinement of ultracold atoms in very close proximity (a few micrometres) to surfaces has also enabled measurements of the Casimir-Polder force that describes the interaction between a bulk object and a gas-phase atom when the two are in close proximity (see references [47–49], for example).

An atom chip project is currently in progress [50] to realise a freely falling Bose-Einstein condensate in a drop tower for tests of inertial and gravitational forces, and to investigate the behaviour of ultracold quantum matter in micro-gravity conditions.

Research carried out with atom chips has also led to progress in several applied fields. One of these fields is quantum information processing and quantum computation. Atom chips offer a promising experimental approach towards the implementation of quantum information processing with neutral atoms, since they combine the realisation of accurate control of an atomic quantum system with the possibility of coherent manipulation of the atoms and of integrated detection tools, in a miniaturised device which also holds good expectations for scalability. References [51, 52] offer reviews of quantum computation and information processing. Proposals for quantum information processing with neutral atoms

on atom chips can be found in references [53–55], for instance.

Other applications of atom chips include the use of ultracold atoms as magnetic field sensors [56–60] or electric field sensors [58, 61] with high field sensitivity and high spatial resolution to probe the small fields created by a sample surface in the proximity of the trapped atoms. The experimental realisation of miniaturised atomic clocks [62–64] which can be incorporated into Global Positioning Systems (GPS) and navigation systems is yet another practical application of the use of ultracold atoms.

1.1 Outline of this thesis

This thesis presents experimental research carried out with ultracold rubidium atoms in a permanent-magnet atom chip based on videotape [65, 66], at the Centre for Cold Matter, at Imperial College in London, U.K., under the supervision of professor E. A. Hinds.

Magnetic data-storage media such as floppy disks, audiotape and videotape had been previously investigated in our group and used successfully to manipulate ultracold atoms [10, 11, 67–70]. Several cold-atom experiments around the world are working on atom chips based on different types of permanent magnets such as multilayer magnetic films [71], planar structures of hard magnetic material [72–76], hard disk platters [77] or ferrimagnetic transparent films [78, 79].

The work described in this thesis focuses on the characterisation and full understanding of the elongated, anharmonic, magnetic micro-traps created with our videotape atom chip for confining neutral atoms; on the study of atom-surface effects, such as fragmentation and potential roughness, experienced by atoms trapped in very close proximity to the surface of the atom chip; and on the implementation of a novel technique for the transport of cold atoms in videotape magnetic traps over large distances of the order of several millimetres, as an effective tool to expand the capabilities of our atom chip and increase the degree of control over the trapped atoms.

Chapter 2 begins by describing the videotape atom chip and all its components, and explains how it can create a variety of magnetic traps for neutral atoms.

Chapter 3 follows by describing the experimental apparatus used for the work presented throughout this thesis, including the ultra-high vacuum system, the coils for generating magnetic fields, the laser system, computer control of the experiment and the imaging-acquisition set-up.

Chapter 4 details the experimental sequence followed to confine ultracold atoms in videotape magnetic micro-traps, describing each step in the process and presenting relevant experimental data for the different stages of atom trapping and cooling in our experiment.

Chapter 5 presents experimental and simulated results for the resonant excitation of the motion of atoms in videotape traps. This leads to the characterisation of the transverse oscillation frequencies of the atoms in the anharmonic traps and to a good understanding of the cold-atom dynamics during the excitation.

Chapter 6 is dedicated to the study of roughness in the confining potential measured with ultra-cold atoms confined in videotape magnetic traps at different distances from the videotape chip surface. A full review of the subject of fragmentation of cold-atom clouds in the proximity of atom-chip surfaces is given at the beginning of this chapter.

Chapter 7 begins by reviewing the progress in the field of cold-atom transport and continues by explaining the effective transport mechanism implemented in the videotape atom chip, presenting results that show how rubidium atoms with temperatures between a few and a few hundred microKelvin were transported in arrays of videotape magnetic traps over distances of up to 7mm.

Finally, chapter 8 summarises the results of this thesis and presents an outlook into the future of the field of ultracold atoms on chips.

Chapter 2

The videotape atom chip

2.1 Introduction

The research presented in this thesis was carried out making use of a permanent-magnet atom chip based on commercial videotape. The chip was constructed by Jocelyn A. Retter at the University of Sussex around 2001, who characterised it in detail and carried out preliminary cold-atom experiments with it [80]. The whole experimental set up was moved from Sussex to London in 2003 and re-built at Imperial College London, where Chris D. J. Sinclair improved the set up and carried out further experiments with the same videotape atom chip [65, 81], which culminated in the achievement of Bose-Einstein condensation of rubidium atoms in videotape magnetic micro-traps in 2005 [66, 81].

The use of videotape to build an atom chip offers the advantage of miniaturised magnetic patterns that can generate strong magnetic fields and strong field gradients, up to ∼110G at the chip surface and a few G/μm, respectively, on our videotape atom chip. These features make videotape perfectly suitable for the manipulation of ultra cold atoms in miniaturised, tightly-confining, magnetic micro-traps. There is flexibility in the choice of the shape and length-scale of the magnetisation patterns recorded onto the videotape, which are determined by the recording process. The pattern of permanent magnetisation recorded onto the videotape piece that formed the chip used for the experiments described in this thesis, was sinusoidal with a wavelength of $\sim 106\mu$m, allowing the confinement of cold rubidium atoms, with temperatures between a few hundred μK and a few hundred nK, in arrays of elongated magnetic micro-traps.

Another advantage of the videotape is the fact that it is made of insulating material. This results in long trapping lifetimes, due to the reduced rate of thermally-induced spin flips for atoms trapped in the proximity of the insulating videotape, compared to the shorter lifetimes measured near bulk metallic materials [66].

This chapter begins by describing the videotape atom chip components, which consist of a piece of videotape and several wires, and continues by explaining how two different types of magnetic traps for ultra cold atoms can be created using the chip: a wire magnetic trap and videotape magnetic micro-traps.

2.2 Chip components

Figure 2.1 shows two photographs of the videotape atom chip with which the experiments described in this thesis were carried out. The base of the atom chip, shown on the right-hand-side image, consisted of a one-inch-square block of stainless steel, machined with channels to hold five wires used to create the magnetic fields needed for loading and trapping cold atoms in videotape magnetic micro-traps. The key element of the videotape atom chip was a piece of videotape recorded with a pattern of permanent magnetisation, glued onto a 150μm-thick, 22 $\times$ 22mm glass coverslip and coated with a reflective layer of gold, with an approximate thickness of 400nm. The glass coverslip was then glued onto the block of steel resulting in the final atom chip shown on the left-hand side of figure 2.1. A two-component, UHV-compatible epoxy, Bylapox 7285, was used as glue. Details of the fabrication process can be found in reference [80].

Four pieces of Macor ceramic with screws attached to them surrounded the steel block. The chip was mounted onto an aluminium post fixed to one of the flanges of the vacuum chamber. The electrical connections between the chip wires and the outside of the chamber were made by means of either ceramic-coated copper wires or bare-copper wires insulated with ceramic beads, which were connected on one end to the screws inserted into the Macor pieces, and on the other end, to the pins of the electrical feedthroughs located on the chip flange.

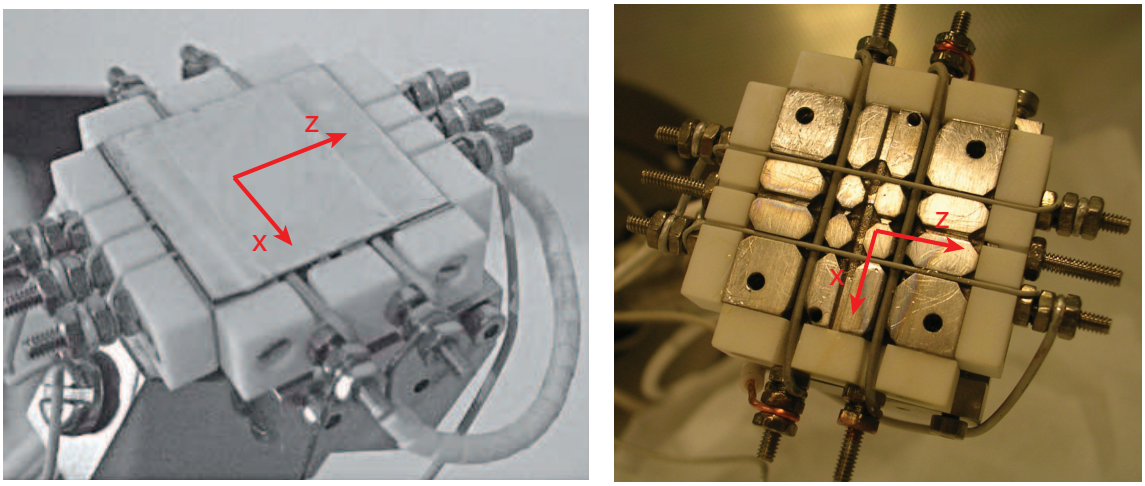

Figure 2.1: Photographs of the videotape atom chip. **Left**: final chip with all its elements and connections. **Right**: chip base showing the channels in which the chip wires were mounted. All wires are present except for the centre wire (see figure 2.2).

Figure 2.2 shows a schematic view of the chip wires located inside the channels of the steel block, below the glass coverslip and videotape. The arrows indicate the direction of the currents through the wires. The chip wires were ceramic-coated copper conductors and, throughout this thesis, we will refer to them with the following names: the centre wire, which ran along the z direction passing though the centre of the chip, with a total diameter of 0.5mm; the two end wires, 1mm in diameter, which ran perpendicular to the centre wire,

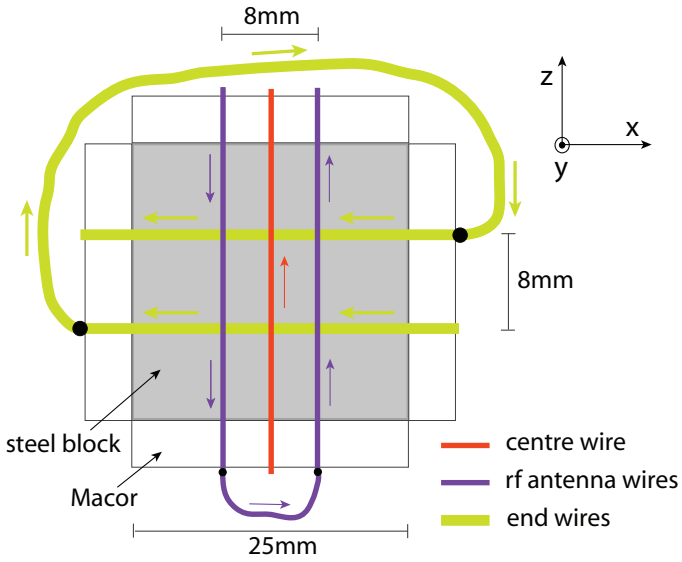

Figure 2.2: Schematic view of the chip wires. The total diameter of the centre wire and rf-antenna wires was 0.5mm, while the diameter of the end wires was 1mm. The arrows indicate the direction of the current inside the wires.

parallel to each other and with currents in the same direction, and which were connected in series through a short piece of wire inside the chamber, as shown in figure 2.2; and the radio-frequency-antenna wires, parallel to the centre wire and with their ends connected on one side to make a loop. These wires were able to sustain currents of up to 15-20A during times of up to 15-20 seconds. The function of each of these wires will be described in detail in section 2.3.

The chip was mounted upside down inside the chamber, with its gold-coated face pointing downwards. The x, y and z directions shown in figure 2.2 will be the ones used throughout this thesis. We establish here that y points down along the vertical direction, with $y = 0$ corresponding to the chip surface. Cold atoms were confined below the chip in elongated, tube-like traps, in such a way that z corresponded to the axial direction of the traps and x and y, to the transverse directions.

The plane containing the chip surface was not perfectly horizontal, but at a small angle of $\sim 2.6°$ to the horizontal [81].

Commercially available videotape of the type Ampex 398 Betacam SP was used to fabricate the atom chip. A 22×12.5mm piece with a total thickness of 14.5μm was used, consisting of an 11μm-thick support and a 3.5μm-thick magnetic layer. The magnetic layer was made of iron-composite needles with an average length of 100nm and an average diameter of 10nm, embedded in glue and aligned parallel to each other, along the x direction. The magnetic remanence of the videotape was $B_r = 2.3$kG and the coercive field was $B_c = 1.5$kG. The remanent magnetisation, B_r/μ_0, is the value of the magnetisation that remains in the sample when the applied magnetic field strength is reduced to zero. The coercive field is the value of the field that needs to be applied, opposite to the field that originally magnetised

the sample, to reduce the magnetisation to zero. It gives an estimate of the magnetic field strength to which a recorded sample can be exposed before becoming demagnetised. The large values of magnetic remanence and coercivity made the videotape ideal for generating large magnetic fields ($\sim$ 110G at the surface of the chip), without the risk of demagnetising, since the largest magnetic fields under which the videotape chip operated were below 100G. The recorded videotape can therefore be effectively treated as a permanent magnet. The videotape was recorded with a sinusoidal pattern of magnetisation along the x direction using a custom-built record head and a standard tape drive. The period of recorded magnetisation was $\sim 106\mu$m (see appendix A). More details about the videotape properties and recording process can be found in reference [80] and references therein.

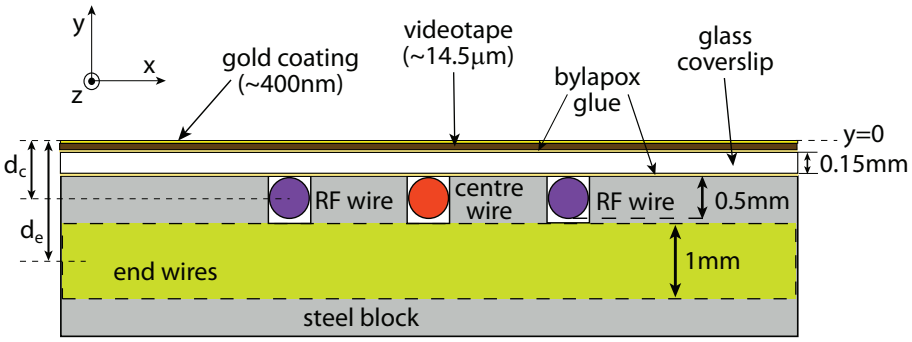

Figure 2.3: Cross-section of the videotape atom chip (not to scale).

Figure 2.3 shows a schematic view of the videotape atom chip cross-section. The total distances from the axis of the centre wire to the chip surface and from the axis of the end wires to the surface, named d_c and d_e, respectively throughout this work, were equal to $d_c \sim 440\mu$m (see section 4.4.1) and $d_e \sim 1.4$mm [80].

All elements that formed the chip were chosen to be compatible with ultra-high-vacuum (UHV) conditions, with the typical experimental pressures being of the order of 10^{-11}Torr. The videotape itself was UHV compatible after being cleaned with ethanol and baked at temperatures of up to 120°C for 200 hours. Remarkably low outgassing rates were reported in references [80, 82], showing how videotape was suitable for experiments with ultra-cold atoms in ultra-high-vacuum conditions.

2.3 Magnetic traps created by the chip: wire trap and videotape micro-traps

2.3.1 Principles of magnetic trapping

Paramagnetic neutral atoms can be magnetically trapped making use of the interaction of the intrinsic atomic magnetic moment with a spatially varying, external magnetic field. Alkali atoms are paramagnetic and have large intrinsic permanent magnetic moments due to their electronic structure with one unpaired electron.

In the work presented in this thesis we trap ^{87}Rb atoms. The atomic energy-level diagram of ^{87}Rb [83] is shown in figure 2.4. The coupling between the orbital angular momentum, $\vec{L}$, and the spin angular momentum, $\vec{S}$, of the atomic electronic shells gives rise to the atomic fine structure, with the term symbols $5^2S_{1/2}$, $5^2P_{1/2}$ and $5^2P_{3/2}$ corresponding to the ground state and first two excited states, respectively. For the ground state, the electronic configuration of the unpaired electron is $5s^1$, so that $L = 0$ and $S = 1/2$, and $\vec{J} = \vec{L} + \vec{S}$ gives $J = 1/2$. The first excited states correspond to an electronic configuration $5s^0\ 5p^1$, with $L = 1$ and $S = 1/2$ resulting in total electronic angular momenta $J = 1/2, 3/2$.

The hyperfine atomic structure arises from the coupling between the total electronic angular momentum, $\vec{J}$, and the total nuclear angular momentum, $\vec{I}$, with the total atomic angular momentum being $\vec{F} = \vec{J} + \vec{I}$. The value of I is 3/2 for ^{87}Rb. The ground state splits into two hyperfine levels with $F = 1, 2$, and the first and second excited states split in two and four levels with $F = 1, 2$ and $F = 0, 1, 2, 3$, respectively, as shown in figure 2.4.

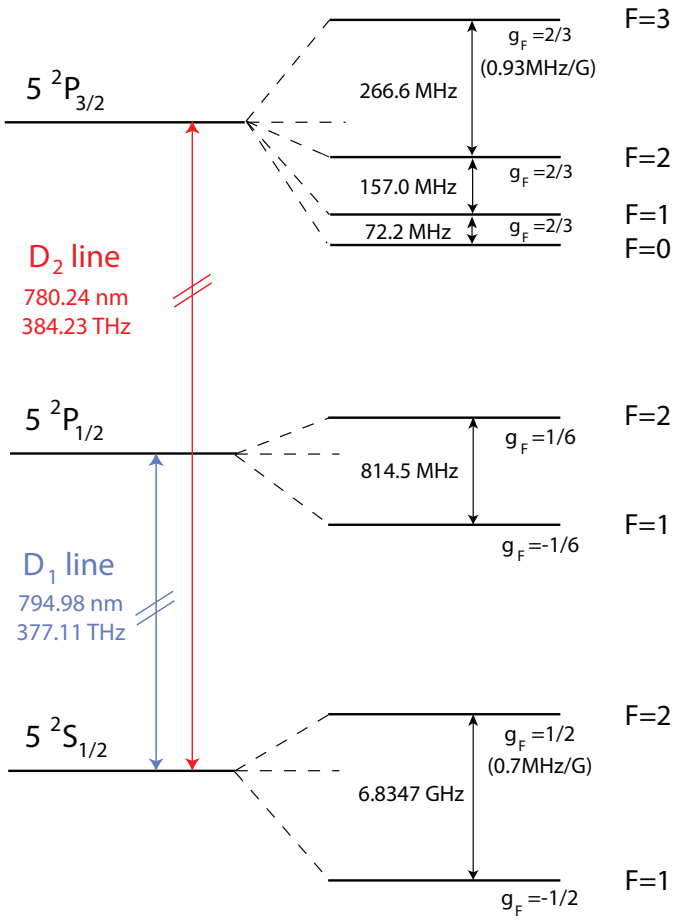

Figure 2.4: Energy-level diagram for ^{87}Rb. See reference [83].

The interaction of the intrinsic atomic magnetic moment, $\vec{\mu}$, with an applied magnetic field, $\vec{B}$, results in the splitting of each hyperfine level into $2F + 1$ Zeeman magnetic hyperfine sublevels, with $m_F = -F, ..., F$, where $m_F\hbar$ is the projection of the atomic angular

momentum onto the field direction. The interaction energy can be expressed as

$$U = -\vec{\mu} \cdot \vec{B}. \tag{2.1}$$

In the limit of weak magnetic fields (small Zeeman shifts compared to the hyperfine splittings), which always applies to the work in this thesis, the energy of each magnetic sublevel is shifted with respect to its hyperfine level by an amount that depends linearly on the magnetic field modulus, so that we can write

$$U = \mu_B g_F m_F |\vec{B}|, \tag{2.2}$$

where μ_B is the Bohr magneton and g_F is the g-factor of the hyperfine state F. In the presence of a spatially varying magnetic field the atom feels a force known as the Stern-Gerlach force:

$$\vec{F}_{\mathrm{S-G}} = -\nabla U = -\mu_B g_F m_F \nabla |\vec{B}|. \tag{2.3}$$

The magnetic sublevels with positive $g_F m_F$ are referred to as weak-field-seeking states, since their energy increases with increasing applied field strength and the Stern-Gerlach force pushes them towards the minimum of the magnetic field, in which they can be magnetically confined. On the other hand, the magnetic sublevels with negative $g_F m_F$ are known as strong-field seekers, since their energy decreases with increasing magnetic fields. These states cannot be trapped with static magnetic fields, due to the impossibility of a local magnetic field maximum in free space, intrinsic to Maxwell's equations.

In our experiments we magnetically trap the weak-field-seeking magnetic sublevel $|F = 2, m_F = +2\rangle$ of the ground state $5^2S_{1/2}$ of ^{87}Rb, for which $g_F = 1/2$. For the atoms to remain trapped, the changes in magnetic field direction must be slower than the Larmor frequency, i.e., the frequency of precession of the atomic moment $\vec{F}$ around the field direction, $\omega_L = \mu_B |g_F m_F \vec{B}|/\hbar$. For the atomic spins to be able to follow the field direction adiabatically, the adiabatic criterion needs to be satisfied [84]:

$$\frac{d\theta}{dt} < \omega_L \,, \tag{2.4}$$

where $\frac{d\theta}{dt}$ is the rate of change of the field direction.

If this criterion is not fulfilled, the total atomic spin can flip its orientation with respect to the field and transform the atomic state into a strong-field-seeking state which will be repelled by the minimum field at the trap centre, resulting in the loss of the atom from the trap. These changes of atomic-spin direction are known as Majorana spin flips [85] and their occurrence leads to reduced trap lifetimes. The presence of zero or very low magnetic-field values at the bottom of the trap can cause the atomic spins to flip due to the absence of a well defined quantisation axis. This effect is usually avoided by raising the minimum magnetic field at the bottom of the trap to a finite, non-zero value.

The usual procedure used to generate magnetic traps for weak-field-seeking states of ^{87}Rb with our videotape atom chip was based on creating a line of zero magnetic field by cancelling the magnetic field generated by either the centre wire or the magnetised videotape,

with a uniform bias field. This line of zero magnetic field formed a tube-like magnetic guide with its axis along the z direction and provided transverse confinement for the atoms on the x-y plane. Axial confinement was provided by the field generated by the two end wires. This field along the z direction also removed the zero of the total magnetic field modulus avoiding Majorana spin flips at the bottom of the trap, as discussed more fully in section 2.3.3.

Therefore, the videotape atom chip was capable of creating two different types of magnetic traps: the wire magnetic trap and the videotape magnetic micro-traps. Sections 2.3.2 to 2.3.6 show how to calculate all the relevant properties and parameters of these traps, such as the trap centre position, field gradient and trap frequencies. Sections 2.3.2 and 2.3.4 describe the wire magnetic trap, section 2.3.6 describes the videotape magnetic traps, and section 2.3.3 describes the axial confining potential.

2.3.2 The two-dimensional wire magnetic guide

Transverse confinement in a two-dimensional, wire magnetic guide is generated by superimposing a uniform bias field perpendicular to the direction of the wire axis to the magnetic field generated by the wire. The magnetic field generated by running a current I_c through a long, thin, straight wire is easily obtained from Ampere's Law as:

$$B_{cw}(r) = \frac{\mu_0 I_c}{2\pi r}, \tag{2.5}$$

where μ_0 is the free-space magnetic permeability and r is the distance to the axis of the wire. In our videotape atom chip, the centre wire (see section 2.2) is used to create a wire magnetic guide. Figure 2.5(left) shows the magnetic field lines of the centre wire, together with a uniform bias field, $\overrightarrow{B}_b$, along the x direction. The applied bias field cancels the centre-wire field at a distance from the wire equal to:

$$r_0 = \frac{\mu_0 I_c}{2\pi B_b}. \tag{2.6}$$

Figure 2.5(right) shows the contours of constant magnetic field strength in the magnetic guide formed by the centre-wire field and bias field. Atoms are attracted towards the line of minimum field along z, at the centre of the closed contours. When the bias field points horizontally along the x direction, the magnetic guide forms vertically above the wire and parallel to it, and we can write the distance from the guide axis to the chip surface, as:

$$y_w = \frac{\mu_0 I_c}{2\pi B_b} - d_c, \tag{2.7}$$

where d_c was previously defined in figure 2.3 as the distance from the centre-wire axis to the chip surface.

Without the addition of any axial fields (along z), the atoms are transversely confined but free to move along the axial direction. Close to the axis of the guide the transverse field has a quadrupole form: $|\vec{B}| = |\vec{B}_{cw} + \vec{B}_b| = \alpha_w r$, so that it is zero at the guide's axis and

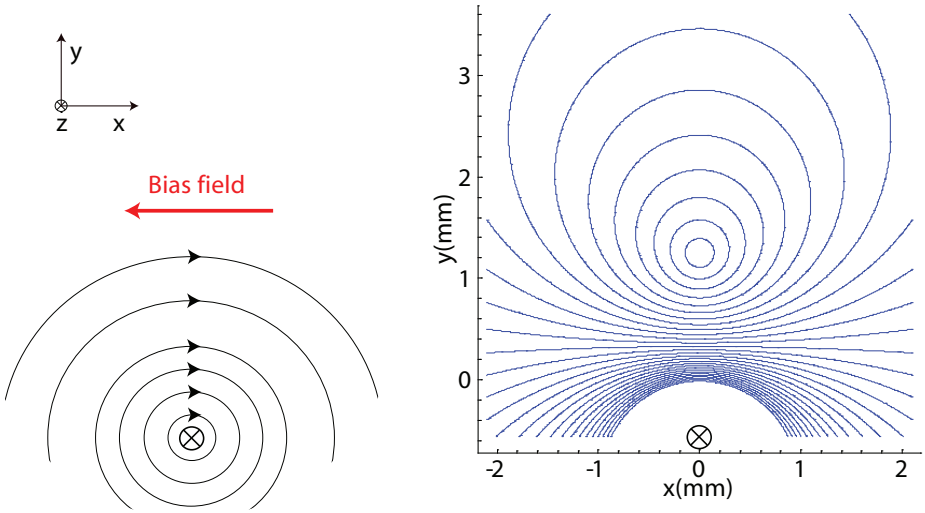

Figure 2.5: **Left**: Magnetic field lines created by the centre wire, and uniform bias field along the x direction. **Right**: contours of constant magnetic field strength in a wire magnetic guide, formed by the addition of the centre wire field with the bias field. The plots correspond to a current of 15A through the centre wire and a bias field of 17G. The distance from the trap to the chip surface is ~ 1.24mm. Contours between 0 and 40G are shown in the graph.

depends linearly on r, where α_w is the transverse gradient at the centre of the guide:

$$\alpha_w = \frac{\partial|\vec{B}|}{\partial r}\Big|_{r=r_0} = \frac{2\pi B_b^2}{\mu_0 I_c}. \tag{2.8}$$

2.3.3 Axial confinement provided by the end wires

Adding the magnetic field generated by the end wires to the two-dimensional guide created by the centre wire and bias field has two effects: it creates a trapping potential along the axis of the guide, i.e., along z, so that the atoms are confined in all three directions of space; and it lifts the zero of the magnetic field at the bottom of the trap, transforming the transverse linear potential into a harmonic potential, close to the trap centre.

The end wires ran parallel to the x direction, with currents in the same sense, as shown in figure 2.2. The typical currents in the end wires were 15A and 10A. The field generated by the end wires was of the form $\overrightarrow{B}_{\mathbf{ew}} = B_{y-ew}\hat{\mathbf{y}} + B_{z-ew}\hat{\mathbf{z}}$, with its components on the z-y plane given by the following expressions:

$$B_{y-ew} = \frac{\mu_0 I_{end}(z+\frac{s}{2})}{2\pi[(y+d_e)^2+(z+\frac{s}{2})^2]} + \frac{\mu_0 I_{end}(z-\frac{s}{2})}{2\pi[(y+d_e)^2+(z-\frac{s}{2})^2]} \tag{2.9}$$

$$B_{z-ew} = \frac{\mu_0 I_{end}(y+d_e)}{2\pi[(y+d_e)^2+(z+\frac{s}{2})^2]} + \frac{\mu_0 I_{end}(y+d_e)}{2\pi[(y+d_e)^2+(z-\frac{s}{2})^2]}, \tag{2.10}$$

where I_{end} is the end-wire current, s is the separation between the end wires along z and d_e is the distance from the axis of the end wires to the chip surface.

The two end-wire-field components, B_{z-ew} and B_{y-ew}, evaluated at a height $y = 0.5$mm, are plotted as a function of the axial coordinate of the trap, z, in figure 2.6(left), as an example. Figure 2.6(right) shows a plot of the z-component of the end-wire field at the

centre of the axial confinement ($z = 0$) versus the distance to the chip surface, y, for two different end-wire currents, $I_{end} = 15$A and $I_{end} = 10$A. This field corresponds to the offset axial field created by the end wires at the bottom of the trap.

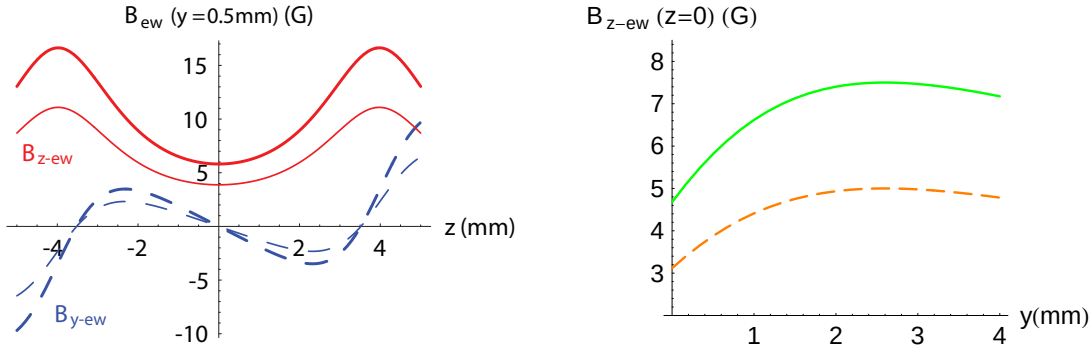

Figure 2.6: Magnetic field generated by the end wires for axial confinement, for $s = 8$mm and $d_e = 1.4$mm. The wires are located at $z = -4$mm and $z = 4$mm. **Left**: z-component (solid lines) and y-component (dashed lines) of the end-wire field at a height $y = 0.5$mm, as a function of z. Thick lines correspond to $I_{end} = 15$A, and thin lines to $I_{end} = 10$A. **Right**: calculated axial magnetic field offset: z-component of the end-wire field at $z = 0$, versus distance to the chip surface, y, for $I_{end} = 15$A (solid line) and $I_{end} = 10$A (dashed line).

The central region of the axial trapping potential generated by B_{z-ew} can be considered approximately harmonic, allowing us to define an axial trap frequency as follows:

$$f_z = \frac{1}{2\pi}\sqrt{\frac{\mu_B g_F m_F}{m}\frac{\partial^2 B_{z-ew}}{\partial z^2}\Big|_{z=0}}, \tag{2.11}$$

with

$$\frac{\partial^2 B_{z-ew}}{\partial z^2}\Big|_{z=0} = \frac{2\mu_0 I_{end}(d_e+y)}{\pi}\left[\frac{s^2}{\left(\frac{s^2}{4}+(d_e+y)^2\right)^3} - \frac{1}{\left(\frac{s^2}{4}+(d_e+y)^2\right)^2}\right]. \tag{2.12}$$

Figure 2.7(left) shows a plot of the axial trap frequency as a function of y, the distance to the chip surface, for the two end-wire currents used in our experiments: $Iend = 15$A and $I_{end} = 10$A. We can see that the typical axial frequencies lie between 10 and 15Hz.

The axial trap depth is given by the difference between the maximum and minimum magnetic field strengths, which are at positions $z = \pm\frac{s}{2} = \pm 4$mm and $z = 0$, respectively. The depth of the axial confinement as a function of y is plotted in figure 2.7(right) for $I_{end} = 15$A and $I_{end} = 10$A. The range of axial depths covered by the lines shown on the graph is equivalent to a temperature range of $200 - 1200\mu$K.

The B_z field

An additional uniform axial field, opposite to B_{z-ew} and created by a pair of Helmholtz coils with their axis along the z direction (see section 3.2.2), was available for the purpose of controlling the magnitude of the net-axial field at the bottom of the trap. The field from

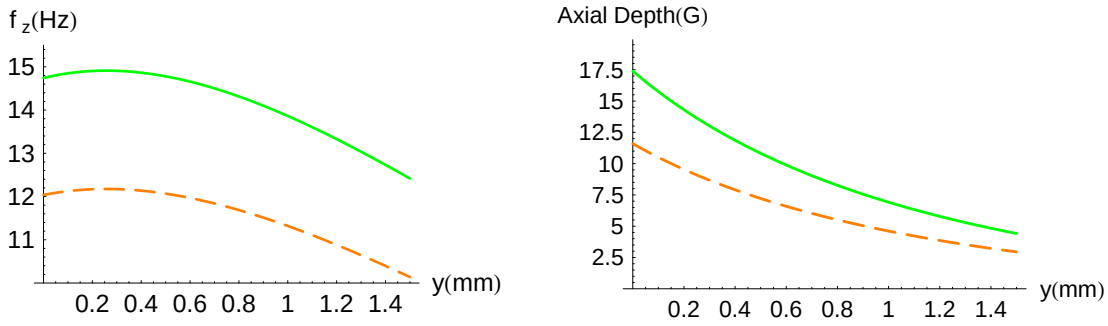

Figure 2.7: **Left**: calculated frequency of the axial confinement generated by the end wires as a function of the distance to the chip surface, y, for two different end-wire currents: 15A (solid line) and 10A (dashed line). **Right**: calculated depth of the axial confinement versus y for end-wire currents of 15A (solid line) and 10A (dashed line).

these external z-coils is referred to as B_z throughout this thesis and must not be confused with the net axial field at the bottom of the trap, which is equal to:

$$B_{z-net} = B_{z-ew} - B_z. \tag{2.13}$$

2.3.4 The wire magnetic trap

The wire magnetic trap is formed by the transverse confining potential of the wire magnetic guide, explained in section 2.3.2, added to the axial confinement provided by the end wires (section 2.3.3). Hence, atoms are confined in all three directions of space in this trap.

The coordinates of the trap centre, where the total magnetic field strength is minimum, are $(x, y, z) = (0, y_w, 0)$, with y_w given by equation 2.7.

In the central region of the trap, the addition of the axial field transforms the transverse linear potential into a near-harmonic potential, so that the total magnetic field strength at the trap centre can be approximated as follows:

$$|\vec{B}| = \sqrt{(\alpha_w r)^2 + B_{z-net}^2} \approx B_{z-net} + \frac{\alpha_w^2}{2B_{z-net}} r^2 \,, \tag{2.14}$$

where α_w is the radial trap gradient, defined in equation 2.8, and B_{z-net} is the net, axial, offset-magnetic field of equation 2.13. The transverse trap frequency can be defined in the central region of the trap as:

$$f_{r-wire} = \frac{1}{2\pi} \sqrt{\frac{\mu_B g_F m_F}{m} \frac{\partial^2 |\vec{B}|}{\partial r^2}} \,. \tag{2.15}$$

Using the approximate expression in equation 2.14 for $|B|$ and substituting for α_w (equation 2.8), we obtain:

$$f_{r-wire} = \frac{\alpha_w}{2\pi} \sqrt{\frac{\mu_B g_F m_F}{m B_{z-net}}} = \frac{B_b^2}{\mu_0 I_c} \sqrt{\frac{\mu_B g_F m_F}{m B_{z-net}}} \,. \tag{2.16}$$

Figure 2.8 shows the variation of the radial frequency in the wire magnetic trap, for a fixed centre-wire current of $I_c = 15A$, with the bias field strength, for two different values of the

net axial field.

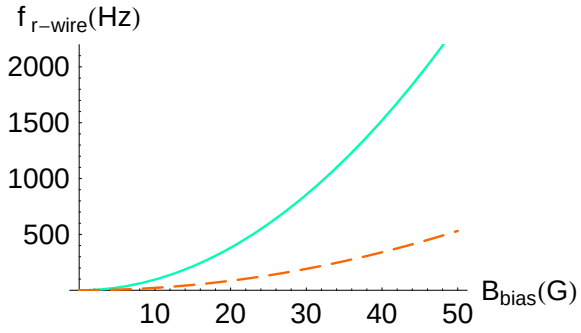

Figure 2.8: Radial frequency in the wire magnetic trap as a function of the bias field strength, for two different net axial fields: $B_{z-net} = 0.2$G (solid line) and $B_{z-net} = 4$G (dashed line). The centre-wire current is 15A.

The axial trap frequency is given by equation 2.11, as explained in section 2.3.3.

Figure 2.9 shows plots of the calculated total modulus of the magnetic field in a wire magnetic trap, as a function of each spatial coordinate. In this particular example the trap parameters are $I_c = 15$A, $I_{end} = 15$A, $B_b = 32$G and $B_z = 3.7$G, resulting in a trap height of $y_w \sim 400\mu$m, a net axial field $B_{z-net} \sim 2.4$G and radial and axial trap frequencies of ~ 270Hz and ~ 15Hz, respectively. Figure 2.9 shows how the transverse confinement along the x direction is harmonic in a very small region close to the trap centre, and then approximately linear up to distances of the order of 1mm from the trap centre. Along the y direction and away from the trap centre, the field modulus increases faster close to the chip surface than it does further from it, due to the decay of the centre-wire field with distance to its axis. Within a few hundred micrometres from the trap centre, the shape of the transverse confinement along y is very similar to that along x. Confinement along the z direction is less tight, and approximately harmonic within a few millimetres from the trap centre.

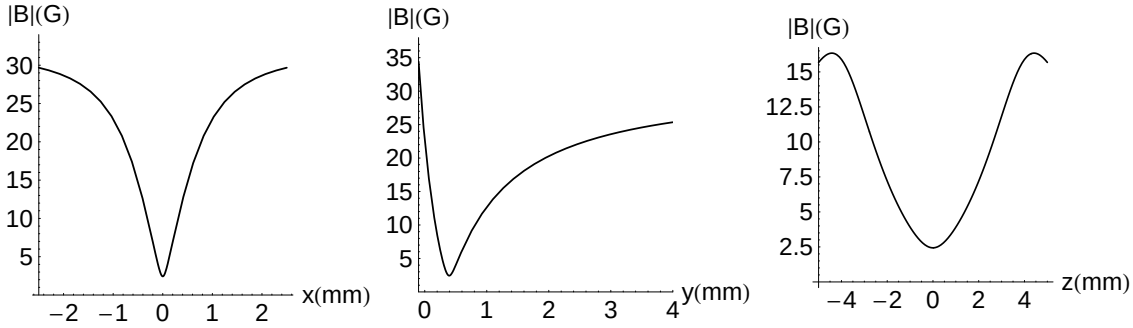

Figure 2.9: Total magnetic field strength in the wire magnetic trap as a function of the trap coordinates, for $I_c = 15$A, $I_{end} = 15$A, $B_b = 32$G and $B_z = 3.7$G. From left to right, the graphs show: $|B(x, y = y_w, z = 0)|$ as a function of x, $|B(x = 0, y, z = 0)|$ as a function of y and $|B(x = 0, y = y_w, z)|$ as a function of z.

2.3.5 Magnetic field generated by a periodically magnetised thin layer

We can consider a thin layer of thickness b, lying on the x-z plane with its upper surface at $y = 0$, and recorded with a periodic pattern of in-plane magnetisation along the x direction, with a magnitude that varies along x with a spatial period λ, as shown in figure 2.10.

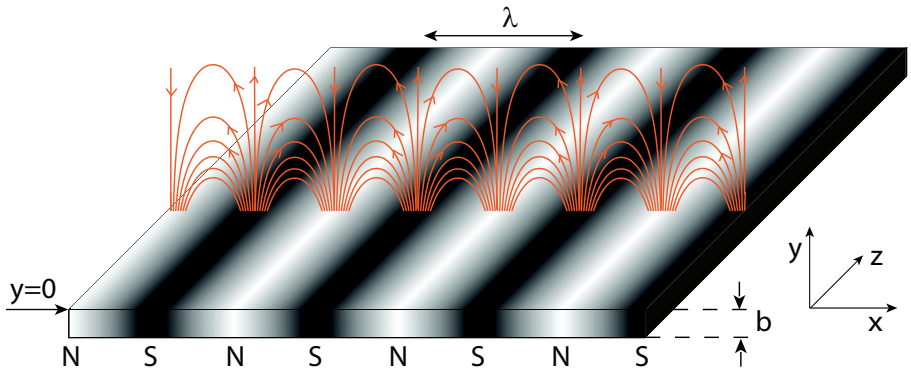

Figure 2.10: Magnetised videotape layer of thickness b. The magnetisation is in-plane along x and the colour gradient shows the periodic variation of its magnitude along x. The lines of the magnetic field generated by the periodically magnetised videotape are also shown.

The magnetic layer of the videotape used in our experiments had dimensions of $22\text{mm} \times 12.5\text{mm}$ on the x-z plane, a thickness of $b \sim 3.5\mu\text{m}$, and a spatial period of recorded magnetisation of $\lambda \sim 106\mu\text{m}$. Edge effects can be neglected in the central region of the chip, since the value of λ is much smaller than the length of the videotape piece along x.

The detailed calculation of the magnetic field generated by the periodically magnetised videotape can be found in references [10, 11, 86], and only a brief summary is outlined here.

The videotape magnetisation can be expressed as $\vec{M} = M\hat{\mathbf{x}}$, where M varies periodically with wavevector $k = \frac{2\pi}{\lambda}$, and can be expanded in a Fourier series as:

$$M = \frac{1}{2}\sum_{n=0}^{\infty} M_n e^{inkx} + c.c.\,, \tag{2.17}$$

with $c.c.$ indicating complex conjugate. The magnetic field above the magnetised film can be obtained as

$$\vec{B}_{video} = -\nabla\phi, \tag{2.18}$$

where ϕ is the scalar potential related to the magnetisation, $\vec{M}(\vec{r})$, by the following expression [87]:

$$\phi(\vec{r}) = -\frac{\mu_0}{4\pi}\int_V \frac{\nabla'\cdot\vec{M}(\vec{r}\,')}{|\vec{r}-\vec{r}\,'|}\mathrm{d}^3\vec{r}\,' + \frac{\mu_0}{4\pi}\oint_S \frac{\vec{n}\,'\cdot\vec{M}(\vec{r}\,')}{|\vec{r}-\vec{r}\,'|}\mathrm{d}^2\vec{r}\,'\,, \tag{2.19}$$

where V and S are the volume and surface area of the material, and $\vec{n}\,'$ is the normal to the surface. Considering the geometry of our problem, with the videotape magnetisation along $\hat{\mathbf{x}}$, and $\vec{n}\,'$ along $\hat{\mathbf{y}}$, equation 2.19 reduces to:

$$\phi(\vec{r}) = -\frac{\mu_0}{4\pi}\int_V \frac{\partial M/\partial x'}{|\vec{r}-\vec{r}\,'|}\mathrm{d}^3\vec{r}\,'\,, \tag{2.20}$$

and using equation 2.17 to substitute for M, assuming the magnetisation is uniform through the thickness of the sample, we can write:

$$\phi(\vec{r}) = -\frac{\mu_0}{8\pi}\sum_{n=0}^{\infty} inkM_n \int_V \frac{e^{inkx'}}{|\vec{r}-\vec{r}'|}\mathrm{d}^3\vec{r}' + c.c.\,. \tag{2.21}$$

This integral can be evaluated (see appendix A of reference [86]), so that the resulting videotape field, obtained from equation 2.18, has the form:

$$\vec{B}_{video} = \sum_{n=0}^{\infty} B_n e^{-nky}\left(-\cos(nkx+\delta_n)\hat{\mathbf{x}} + \sin(nkx+\delta_n)\hat{\mathbf{y}}\right)\,, \tag{2.22}$$

where δ_n is the magnetisation phase, and B_n is the magnetic field amplitude of the nth-order harmonic at the surface of the magnetised layer, given by:

$$B_n = \frac{\mu_0 M_n}{2}(1-e^{-nkb})\,. \tag{2.23}$$

Equation 2.22 shows how the videotape field decreases exponentially with the distance to its surface, and how this decay is faster the higher the order of the harmonics. At distances from the videotape surface $y \gg \frac{\lambda}{2\pi}$ only the contribution of the fundamental harmonic ($n = 1$) to the videotape field is relevant. The factor $(1 - e^{-nkb})$ corresponds to the effect of the finite videotape thickness, b, and becomes significantly lower than 1 when $\lambda \gg 2\pi b$ [86].

If we consider the videotape magnetisation to be sinusoidal, taking into account only the fundamental frequency component:

$$\vec{M} = M_1\cos(kx)\hat{\mathbf{x}}, \tag{2.24}$$

the resulting videotape magnetic field is given by:

$$\vec{B}_{video} = B_1 e^{-ky}\left(-\cos(kx)\,\hat{\mathbf{x}} + \sin(kx)\,\hat{\mathbf{y}}\right)\,, \tag{2.25}$$

with

$$B_1 = \frac{\mu_0 M_1}{2}(1-e^{-kb})\,. \tag{2.26}$$

The value of the surface field, B_1, was determined by C. D. J. Sinclair to be $B_1 = (110\pm10)$G [81]. This value was obtained from the measurement of the videotape-trap height as a function of the bias magnetic field (see future equation 2.27). The field lines corresponding to the magnetic field of equation 2.25 are shown in figure 2.10. Moving along the x coordinate, the videotape field direction changes periodically while its modulus remains constant.

Appendix A describes the analysis of the videotape magnetisation using polarisation microscopy, and shows that we can consider the videotape magnetic-field components to be close enough to pure sine and cosine functions. This assumption is made throughout the rest of this thesis, i.e., the effect of higher harmonics in the expression of the videotape magnetisation has always been neglected, and the videotape magnetic field has always been

considered to be that of equation 2.25.

2.3.6 The videotape magnetic micro-traps

The principle of the videotape magnetic traps is the same as that of the wire magnetic trap: a two-dimensional, magnetic quadrupole guide with zero field along its axis is formed by cancelling the magnetic field generated by the magnetised videotape with a uniform bias field, providing transverse confinement for the atoms. Due to the periodic nature of the videotape magnetic field, not only one guide, but an array of magnetic micro-guides, with their axes along z, and spaced along x by a distance $\lambda \sim 106\mu$m, can be created at a distance y_0 from the videotape chip surface.

When the uniform bias field is along the x direction $\vec{B}_b = B_b\hat{\mathbf{x}}$, videotape magnetic guides form at positions $x_0 = \pm n\lambda$, with n natural, and at a height, y_0, given by the position at which the bias field cancels the videotape magnetic field of equation 2.25, so that:

$$B_1 e^{-ky_0} = B_b \qquad \Longrightarrow \qquad y_0 = -\frac{1}{k}\ln(\frac{B_b}{B_1})\,, \tag{2.27}$$

where $k = 2\pi/\lambda$ and B_1 is the videotape field strength at the chip surface. The typical experimental values of y_0 were between 30μm and 120μm for the work presented in this thesis.

For each quadrupole, magnetic micro-guide, the dependence of the magnetic field strength on the distance to the guide axis is linear: $|B| = \alpha r$, where α is the transverse gradient at the centre of the micro-guide, found from the first order term in the Taylor expansion of the total field around its minimum:

$$\alpha = kB_b\,. \tag{2.28}$$

The videotape field lines (for the field in equation 2.25) are shown in figure 2.11(top) together with the bias field used to create the array of two-dimensional micro-guides. Figure 2.11(bottom) shows the contours of constant magnetic field strength that result from combining the videotape field and bias field. Ultra-cold atoms can be confined in a line along z, at the centre of each closed contour.

Axial confinement is provided by the end wires in exactly the same way as described for the wire magnetic trap in section 2.3.3. The axial frequency is given by equation 2.11 evaluated at the videotape trap height, y_0, of equation 2.27.

Note that the addition of the end-wire field causes the height of the videotape traps to differ slightly ($< 1\mu$m) from the expression in equation 2.27. With the field of the end wires present, the position at which the modulus of the total magnetic field:

$$|\vec{B}| = \sqrt{(B_{video-x}(x,y) + B_b)^2 + (B_{video-y}(x,y) + B_{y-ew}(y,z))^2 + (B_{z-ew}(y,z) + B_z)^2} \tag{2.29}$$

is minimum, is shifted by the fact that the z-component of the end-wire field, $B_{z-ew}(y,z)$, (see equation 2.10 and figure 2.6(right)) depends on y. Since the end-wire field components

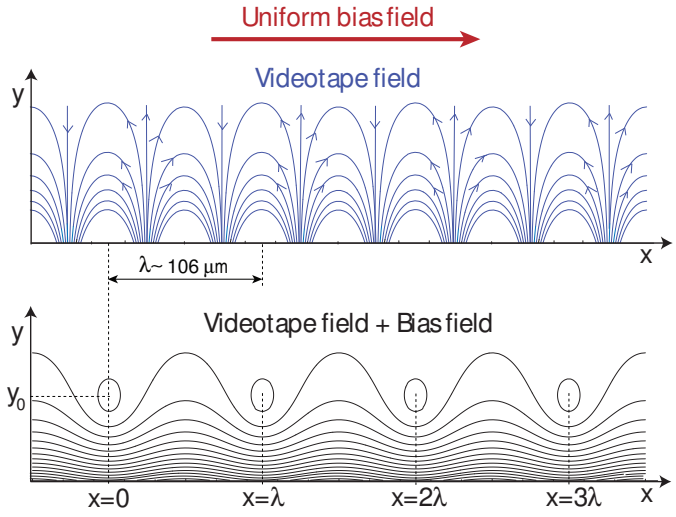

Figure 2.11: Magnetic fields used to create an array of videotape magnetic micro-traps. **Top**: field lines generated by the sinusoidally magnetised videotape, and uniform bias field. **Bottom**: contours of constant magnetic field modulus showing an array of magnetic guides separated by a distance λ along x.

are independent of x, the trap centre position remains at $x_0 = \pm n\lambda$. Due to the symmetry around $z = 0$ of the terms that depend on z inside the square root of equation 2.29, the position of the minimum $|\vec{B}|$ in the videotape trap remains at $z = 0$. Note that the same arguments are also true for the wire magnetic trap, so that the real wire-trap height differs slightly from y_w of equation 2.7.

The net axial field, B_{z-net}, given by the sum of the z-component of the end-wire field and the uniform field B_z, rounds off the bottom of the linear potential of the transverse guide, creating near-harmonic, radial confinement close to the trap centre. At the same time, the presence of this net axial field ensures that the total field at the bottom of the videotape traps differs from zero, to avoid atom loss due to Majorana spin flips.

At $z = 0$, the total field modulus can be approximated as follows in the central region (small r) of the videotape magnetic traps:

$$|\vec{B}(z=0)| = \sqrt{(\alpha r)^2 + B_{z-net}^2} \approx B_{z-net} + \frac{\alpha^2}{2B_{z-net}} r^2 , \tag{2.30}$$

where α is the transverse gradient, defined in equation 2.28. In this region, the transverse trap frequency can be defined as:

$$f_r = \frac{1}{2\pi}\sqrt{\frac{\mu_B g_F m_F}{m}\frac{\partial^2|\vec{B}|}{\partial r^2}} \approx \frac{\alpha}{2\pi}\sqrt{\frac{\mu_B g_F m_F}{m B_{z-net}}} = \frac{kB_b}{2\pi}\sqrt{\frac{\mu_B g_F m_F}{m B_{z-net}}} , \tag{2.31}$$

where the approximate expression of equation 2.30 has been used for $|B|$ and equation 2.28 has been used for α. The typical radial trap frequencies in the videotape traps range from ~ 500Hz to ~ 15kHz, for bias fields up to ~ 40G.

Figure 2.12 shows plots of the modulus of the total magnetic field in the videotape magnetic traps, as a function of each coordinate. The top plots show $|\vec{B}|$ as a function of x, at $y = y_0$ and $z = 0$: the plot on the left-hand side shows how the periodic potential forms an array of micro-traps separated by $\lambda \sim 106\mu$m along x, while the plot on the right-hand side zooms into a single micro-trap. The bottom plots show the dependence of the confining field strength on y, evaluating $|\vec{B}|$ at $x = 0$ and $z = 0$, and on z, evaluating $|\vec{B}|$ at $x = 0$ and $y = y_0$. Note how the length scale along z is around two orders of magnitude larger than that along x or y. The videotape magnetic micro-traps are very elongated, with their axis along z, and can have aspect ratios (ratio of the length of the cloud to its transverse width) of up to 1000.

The plots also show how the confinement is harmonic only in a limited region close to the centre of the videotape traps. Chapter 5 characterises the anharmonicity of the videotape trapping potential in detail and provides a full study of how the frequencies of the transverse oscillations of cold atoms in these traps depend on the distance to the trap centre.

Examples of the contours of constant magnetic field strength of an array of videotape traps, plotted on the cross-sections of the trap through the x-y, x-z and z-y planes, passing through the trap centre, are presented in figure 2.13. The plots correspond to an end-wire current of 15A, a bias field of 10.6G and a B_z of 2.6G, resulting in a trap height of $y_0 \sim 40\mu$m, a net axial field of $B_{z-net} \sim 2.6$G, a linear transverse gradient $\alpha \sim 6.3 \times 10^3$G/cm, a transverse trap frequency of ~ 5kHz and an axial trap frequency of ~ 16Hz.

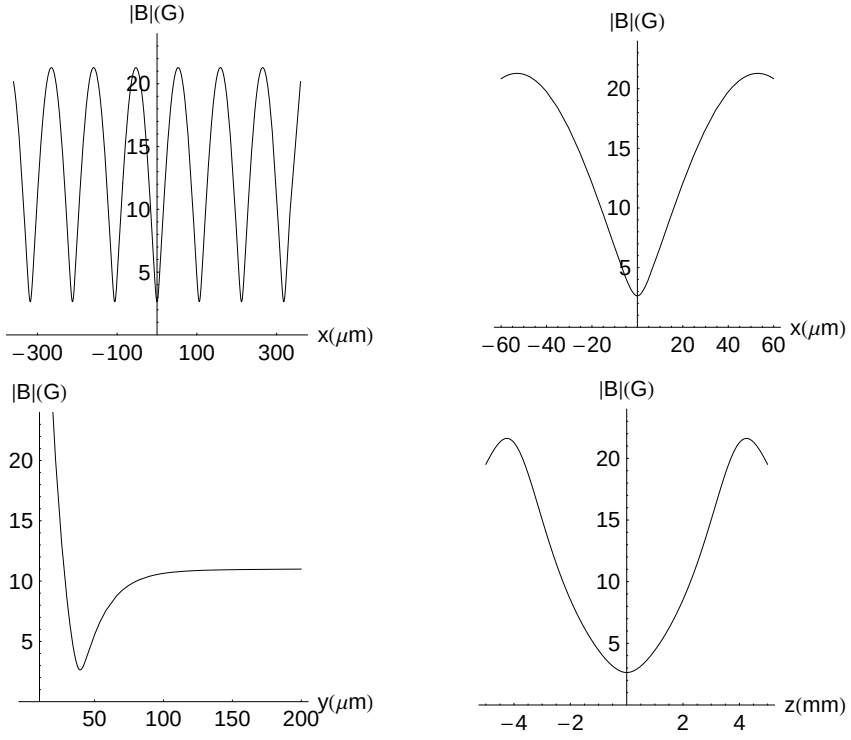

Figure 2.12: Total magnetic field strength in the videotape magnetic traps as a function of the trap coordinates, for $I_{end} = 15$A, $B_b = 10.6$G and $B_z = 2.6$G. The trap height is $y_0 \sim 40\mu$m.

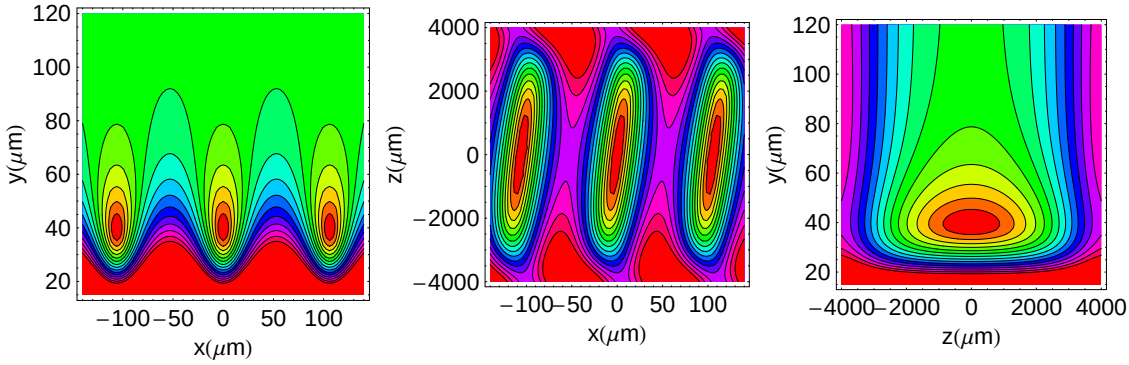

Figure 2.13: Contours of constant magnetic field strength of an array of three videotape magnetic traps, for $I_{end} = 15$A, $B_b = 10.6$G and $B_z = 2.6$G. The trap height is $y_0 \sim 40\mu$m. The contours shown, from left to right, correspond to cross-sections through the $z = 0$, $y = y_0$ and $x = 0$ planes, that pass through the centre of the trap. The contours correspond to a range of magnetic-field strengths of 2.6-26G.

The real trap axis

Due to the contribution of the end-wire field, the line of minimum magnetic field strength of the videotape traps, i.e., the real trap axis, is not the straight line $x = 0$, $y \simeq y_0$, but is instead curved in three dimensions.

The axes of the videotape magnetic micro-traps are tilted on the x-z plane by a small angle of the order of $\sim 0.7^\circ$ to the z direction, as we can see on the centre graph of figure 2.13.

This tilt is produced by the y-component of the end-wire field, which, as shown in section 2.3.3 (see figure 2.6), changes sign around $z = 0$. For $0 < z < 3.5$mm, B_{y-ew} is negative and adds up to the uniform bias field, $\vec{B}_b = B_b\hat{\mathbf{x}}$, so that the videotape trap is formed at the position at which the videotape magnetic field is cancelled by the total field applied on the x-y plane: $B_b\hat{\mathbf{x}} + B_{y-ew}\hat{\mathbf{y}}$. This position is not $x = 0$ anymore, but $x > 0$, resulting in a small tilt of the trap towards positive x values, for $0 < z < 3.5$mm. On the other side of $z = 0$, for $-3.5\text{mm} < z < 0$, B_{y-ew} is positive and the total bias field cancels the videotape field at positions with $x < 0$. This effect explains the small tilt of the axis of minimum magnetic field strength of the videotape traps on the x-z plane. Due to this tilt, the plot on the right-hand side of figure 2.13 does not really follow the line of minimum magnetic field of the trap, since the field is evaluated at $x = 0$ for all values of z.

In addition to this, the y-component of the end-wire field increases the total magnitude of the bias field at the edges of the trap, far from $z = 0$. For this reason, the edges of the trap are slightly closer to the chip surface than the centre of the trap, and the real axis of the trap is slightly curved. This means that the centre graph of figure 2.13 does not follow exactly the line of minimum field of the trap, since the field is evaluated at $y = y_0$ for all values of z, even if the height of the trap edges far from $z = 0$ is really lower than y_0.

Note that similar effects occur in the wire magnetic trap, since the symmetry of the

problem is the same and the field from the end wires is also present.

A rigourous determination of the trap properties therefore requires a numerical calculation in order to find the coordinates of the real bottom of the trap, the real line of minimum magnetic field strength, and the characteristic directions of the oscillations of the atoms in the trap. These concepts will be revisited in chapters 5 and 7.

Chapter 3

Experimental apparatus

The details of the experimental set up used for the experiments presented in this thesis were extensively described in reference [81]. This chapter offers only a brief summary of the apparatus used to achieve confinement of ultra-cold rubidium atoms in videotape magnetic micro-traps.

Section 3.1 describes the vacuum system, section 3.2 describes the external coils used to generate magnetic fields, section 3.3 describes the lasers used to drive the appropriate optical atomic transitions, section 3.4 refers to the computer control of the experiment and section 3.5 explains the set up used for fluorescence and absorption imaging of atoms.

The entire set up was mounted on top of a Melles-Griot floating optical table with dimensions of $3\text{m} \times 1.5\text{m}$. The table was surrounded by curtains to prevent the accumulation of dust on the optics and a clean-air outlet was located right above the table to create a positive pressure to push dust particles away from the table.

3.1 The vacuum system

The ultra-high vacuum system consisted mainly of two vacuum chambers: the LVIS (Low Velocity Intense Source) chamber and the main chamber or science chamber, both made of stainless steel. The pressure in the LVIS vacuum chamber was around 10^{-7}Torr, while the pressure in the main chamber was of the order of 10^{-11}Torr. Figure 3.1 shows a photograph of both vacuum chambers.

The LVIS chamber is a six-way cross with ports ending in $2\frac{3}{4}$-inch conflat flanges. Four of these ports were sealed with windows to bring laser light into the chamber in order to create an LVIS magneto-optical trap. One of the two remaining ports was connected to the main vacuum chamber through a large all-metal gate valve that enabled independent operation of the two chambers if necessary. The opposite port was connected to a T-piece that held on one of its ports the SAES Getters rubidium dispenser mounted on two pins of a vacuum feedthrough and, on the other port, a 6-way cross with a 20l/s ion pump, two small all-metal gate valves and a window to introduce laser light along the direction that connected the two chambers together (see page 58 of reference [81] for a detailed schematic

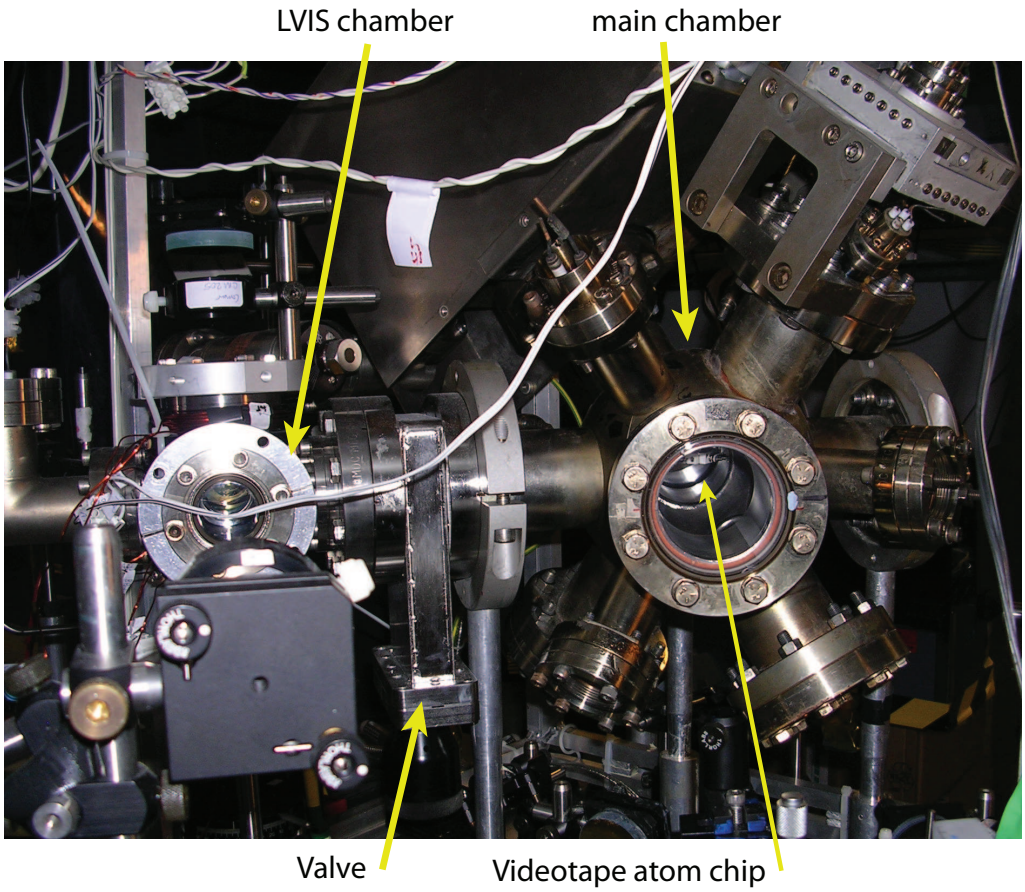

Figure 3.1: Photograph of the LVIS chamber and main chamber.

diagram of this set up).

Atoms collected on a magneto-optical trap (MOT) formed inside the LVIS chamber were transferred to the main chamber through a 1mm-diameter hole drilled through a 6mm-thick, 32mm-diameter $\frac{\lambda}{4}$ waveplate which was glued onto a stainless steel mount inside the tube that connected both chambers. The back face of this waveplate was coated with aluminium to make a mirror for retro-reflecting one of the LVIS MOT laser beams. A slow atomic beam travelled from the MOT in the LVIS chamber to the MOT in the main chamber over a distance of ∼30cm.

The main chamber consisted of a 6inch-diameter sphere which had fourteen ports and was raised on aluminium posts. Six of these ports had a length of $2\frac{3}{4}$inches and a diameter of $1\frac{1}{2}$ inches and ended in $2\frac{3}{4}$inch conflat flanges. The remaining eight ports had a length of $2\frac{1}{2}$inches and a diameter of $2\frac{3}{4}$inches and ended in $4\frac{1}{2}$inch flanges. The videotape atom chip was at the centre of the chamber, mounted on the closing flange of one of the large ports, with its gold-coated surface facing down and horizontal. Eight of the fourteen ports were sealed with quartz windows for optical access into the main chamber. The four windows used to bring laser light inside the science chamber for the formation of the main MOT had anti-reflection coatings to prevent laser-power losses.

A T-piece was connected to one of the large ports of the main chamber. This T-piece held a Varian StarCell, 60l/s ion pump on one of its ports and an all-metal valve on the other port, used to connect a roughing pump system to the main vacuum chamber when needing to open it or bake it. The usual procedure used to reach ultra-high vacuum in the main chamber is described in detail in appendix B. The ion pump was surrounded by a shield in order to try to prevent the magnetic fields generated by the strong magnet inside it from reaching the inside of the main vacuum chamber.

A Varian UHV-24 ionisation gauge was connected to one of the small ports of the main chamber and operated with a Varian L8350301 Multi-Gauge controller, in order to continuously monitor the pressure in the main chamber.

A non-evaporative getter pump, model SAES Sorb-AC MK5, was installed on one of the small ports of the main chamber and proved to be vital for achieving pressures below 10^{-10}Torr (see appendix B for more details).

All ports in both vacuum chambers were tightly sealed using copper gaskets on the knife edges of the conflat flanges.

3.2 Coils for generating magnetic fields

Apart from the wires that formed part of the videotape atom chip, located inside the main vacuum chamber, and described in section 2.2 of the previous chapter, several other coils placed outside both vacuum chambers assisted us in generating the appropriate magnetic fields needed to trap and cool atoms.

3.2.1 Coils around the LVIS chamber

Two 8.6cm-diameter coils, separated by $\sim$ 5.6cm, and wired in anti-Helmholtz configuration with their common axis along the vertical direction were used to generate the quadrupole magnetic field needed to create a magneto-optical trap inside the LVIS chamber. Each coil had 55 turns and a current of 2.2A was typically used to produce a magnetic field gradient of $\sim$7G/cm along the vertical direction.

Additionally, two more pairs of coils wired in Helmholtz configuration, one vertical pair and one horizontal pair, were placed perpendicular to the direction of the slow atomic beam and used to create small uniform magnetic fields (LVIS shim fields) for the adjustment of the position of the centre of the quadrupole field of the LVIS MOT, and for the optimisation of the flux and loading rate of atoms from the LVIS into the main chamber.

3.2.2 Coils around the main chamber

Figure 3.2 shows a schematic view of some of the coils that were placed around the main vacuum chamber and the magnetic fields they generated.

Two pairs of Helmholtz coils with their axes perpendicular to each other on the vertical x-y plane were used to generate the uniform magnetic field used as bias field to create the magnetic traps referred to in section 2.3 of the previous chapter. One pair of coils had its

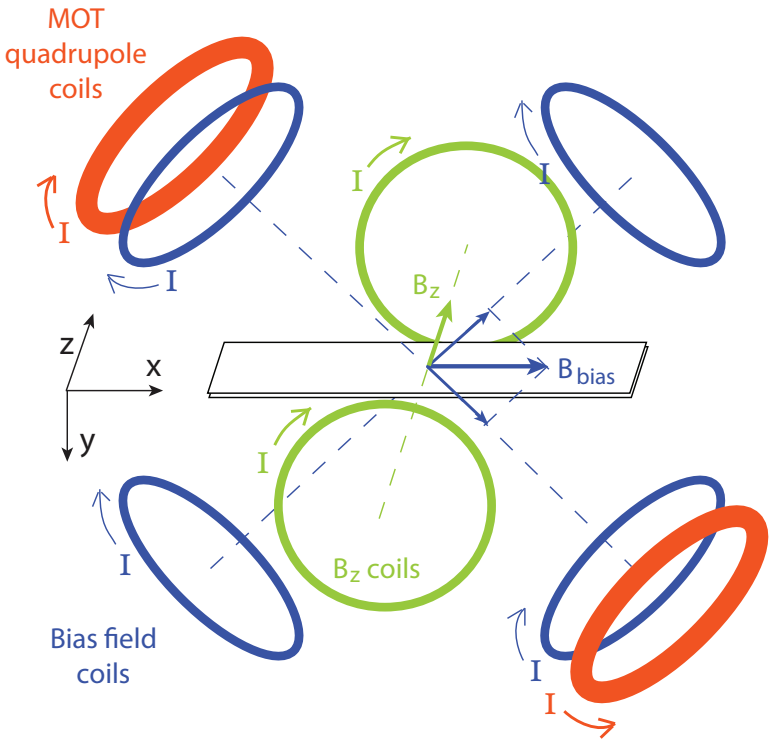

Figure 3.2: Schematic of the coils outside the main vacuum chamber.

axis along the $\hat{\mathbf{x}}+\hat{\mathbf{y}}$ direction while the other one had it along the $\hat{\mathbf{x}}-\hat{\mathbf{y}}$ direction, as shown in figure 3.2. The coils were mounted around the chamber ports, as close as possible to the central sphere of the main vacuum chamber. They consisted of 100 turns each, with a diameter of $\sim$ 10cm, and were separated by $\sim$ 17cm along their common axis. Each pair of coils produced a magnetic field of $\sim$ 3G/A at the centre of the chamber. When the fields from both pairs of coils were combined, the resulting field at the centre of the chamber was along the x direction, with a magnitude of $\sim$ 4.4G/A. The bias coil pairs were operated with bipolar power supplies, Kepco BOP 36-12M, capable of delivering maximum currents of 12A.

Two large coils with 528 turns each and inner and outer diameters of 7cm and 11cm, respectively, wired in anti-Helmholtz configuration and separated along their common axis by $\sim$ 21cm, were used to generate the quadrupole magnetic field for the main MOT in the science chamber. This pair of coils had its axis along the $\hat{\mathbf{x}}+\hat{\mathbf{y}}$ direction, as shown in figure 3.2. The typical operating current through these coils was 4.8A and the magnetic field gradient along their axis, at the position of the MOT in the centre of the chamber was $\sim$ 11G/cm. Since this current was on during times of a few tens of seconds, these coils needed to be water cooled in order to dissipate the Joule heat they generated. The laboratory was equipped with a closed circuit of chilled water for this purpose.

Two Helmholtz coils with their axes along the z direction were used to generate the field referred to as B_z throughout this thesis (see section 2.3.3). These coils were $\sim$ 10cm in diameter, with 100 turns each and separated by $\sim$ 16cm. They were capable of generating

a uniform magnetic field of ~ 3.7G/A along z, at the centre of the chamber.

Two more coils (not shown in figure 3.2) wired in Helmholtz configuration directly onto the chamber ports, with their axes horizontal along the $\hat{\mathbf{x}}+\hat{\mathbf{z}}$ direction, were able to generate a small uniform field of up to 1G, used as quantisation field for absorption imaging of atoms in magnetic traps. These coils had 30 turns with a diameter of ~ 6.4cm and were separated by ~ 20cm, generating a magnetic field of 0.33G/A at the centre of the main chamber.

Finally, six pairs of large rectangular coils with 15 turns each and dimensions of 60×60cm and 60×43cm were mounted in a box-like configuration around the main chamber providing small magnetic fields (MOT shim fields) of up to ~ 1G, used to adjust the position of the main MOT and to cancel the Earth's magnetic field (~ 0.5G), or any other stray magnetic fields.

3.2.3 Current control

The currents running through the wires in the chip (centre wire and end wires), through the coils described in the previous section (LVIS quadrupole coils, MOT quadrupole coils, bias coils, B_z coils, and LVIS and MOT shim coils), and through the rubidium dispenser, were controlled and stabilised by means of FET-driver circuits described in appendix C.

The response time of the current in the chip wires was of the order of 10-50μs, while the response time of the bias coils and B_z coils was of at least 1ms, due to the high inductance caused by the large number of turns of these coils.

3.3 Lasers

The laser system and optical equipment used to trap, cool and manipulate rubidium atoms in our experiment was described in detail and with full diagrams in reference [81], and only an overview is presented in this section. The wavelength of the optical transitions of ^{87}Rb involved in our experiments was in the infra-red range, with a value of ~ 780nm. The main trapping transition was the closed transition from the $5^2S_{1/2}\,F=2$ ground state to the $5^2P_{3/2}\,F=3$ excited state of ^{87}Rb. The energy-level diagram of rubidium was already presented in figure 2.4.

Four semiconductor diode lasers provided laser light tuned to the appropriate wavelengths during the different experimental stages, such as laser cooling and trapping of atoms in magneto-optical traps, optical pumping of the atomic states into the correct Zeeman magnetic hyperfine sub-levels before magnetic trapping, and absorption imaging of the atoms in magnetic traps.

3.3.1 The reference laser

The reference laser was a home-built, extended-cavity diode laser (ECDL) tuned to the main trapping transition: $5^2S_{1/2}\,F=2 \longrightarrow 5^2P_{3/2}\,F=3$ (see figure 2.4). The laser was operated

at a current of ~ 47mA and a temperature of $\sim 18.4°$C, with the diode's maximum output power being $\sim$ 70mW. The added grating that formed the external cavity of the ECDL resulted in a linewidth of $\sim$ 1MHz [80, 88], compared to the much larger linewidths, of the order of tens of MHz, typical for free-standing laser diodes. The narrow linewidths achieved with the ECDL set up were necessary to address the ^{87}Rb atomic transitions, which had natural linewidths of $\sim$ 6MHz [83].

The frequency of the reference laser was locked through polarisation spectroscopy [89] of the $5^2S_{1/2}\,F = 2 \longrightarrow 5^2P_{3/2}\,F = F'$ transitions. Polarisation spectroscopy is based on the birefringence induced by a circularly-polarised pump beam on a rubidium vapour cell. When a linearly-polarised probe beam propagates through the cell, the direction of its polarisation is slightly rotated and, after going through a polarising beam splitter, different absorption signals are obtained for the two polarisation components in each arm of the beam splitter. The difference of these two signals yields a dispersive signal with a steep slope that can be used for stabilising the laser frequency. Figure 3.3 shows the oscilloscope trace of the polarisation-spectroscopy-lock signal used to lock the reference laser.

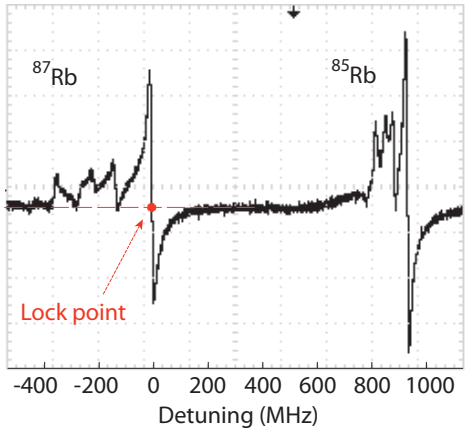

Figure 3.3: Oscilloscope trace of the signal used to lock the reference laser. Polarisation spectroscopy of the $5^2S_{1/2}\,F = 2 \longrightarrow 5^2P_{3/2}\,F = F'$ transition in ^{87}Rb was used to lock the reference laser. Vertical axis: 30mV/div. Horizontal axis: detuning with respect to the $F = 2 \longrightarrow F' = 3$ transition in ^{87}Rb. The signal for ^{85}Rb also appears on the right-hand side of the image.

The output of the reference laser was divided in three parts: one was used for polarisation spectroscopy, another one to provide a reference frequency when locking the TA100 laser (see section 3.3.2), and the remaining part served as optical pumping beam after a double pass through an acousto-optic modulator (AOM) (see section 3.3.4).

3.3.2 The TA100 laser system

The Toptica TA100 laser was a commercial, tapered-amplifier laser system that provided the high power needed for the LVIS-MOT and main MOT beams. Its frequency was tuned to the main trapping transition: $5^2S_{1/2}\,F = 2 \longrightarrow 5^2P_{3/2}\,F = 3$. This laser system consisted of an extended-cavity diode laser (master oscillator) and a tapered amplifier for power amplification. Its total output power was $\sim$ 500mW, its linewidth $\sim$ 1MHz, and its tuning range, 10-15nm, as specified by the manufacturer. The master oscillator was

commonly operated at currents of 75-110mA and temperatures of 18-25°C, and the tapered amplifier was usually kept constant at a current of 2A and a temperature of 19.9°C.

A small realignment of the output of the master oscillator into the amplifier was needed daily to maximise the total output power. This was done by tweaking the screws of two alignment mirrors located inside the laser box.

A part (20mW) of the output of the master oscillator was picked up and divided into two parts: one for saturated absorption spectroscopy, and the other one for offset-locking the laser (see figure 3.4). The final output of the tapered amplifier ($\sim$ 500mW) was divided in two parts: one part made the LVIS beams ($\sim$ 400mW), used for the magneto-optical trap inside the LVIS chamber, and the other part made the MOT beams ($\sim$ 100mW), used for the MOT in the main chamber.

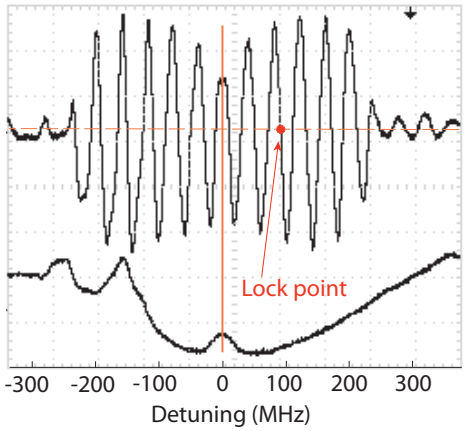

Figure 3.4: Oscilloscope traces of the signals used to lock the TA100 laser. Upper trace: offset lock signal showing the locking point. Lower trace: saturated-absorption spectrum of the $5^2S_{1/2}\,F = 2 \longrightarrow 5^2P_{3/2}\,F = F'$ transition in ^{87}Rb. The vertical line corresponds to $F' = 3$. Vertical scale: 308mV/div (upper trace) and 424mV/div (lower trace). Horizontal scale: detuning with respect to the $F = 2 \longrightarrow F' = 3$ transition.

An offset-lock mechanism was used to stabilise the frequency of the TA100 master oscillator. The mechanism was based in combining light from the master oscillator with light from the reference laser, and comparing the beat frequency of the combined signal with that of a tunable, local oscillator. The frequency of the TA100 laser with respect to the reference laser depended on the frequency of the local oscillator, which could be modified via a control voltage provided by a computer. This locking mechanism allowed us to shift the TA100-laser frequency away from the resonant trapping transition by up to -54MHz and +32MHz. The TA100 laser frequency needed to be ramped no faster than $\sim$ 6MHz/ms for the laser to remain locked during the frequency ramp.

The locking signal was the set of fringes shown in figure 3.4, with the distance between fringes corresponding to 36MHz. A displacement of the fringes occurred when the frequency of the voltage-controlled, local oscillator was modified. The laser was always locked to the point shown in the figure which, at resonance, was +92MHz away from the frequency of the reference laser. Both LVIS and MOT beams were passed through -92MHz AOMs in

order to bring their frequencies back to resonance with the main trapping transition. For the magneto-optical trapping stages the locking point was $\sim +80$MHz away from resonance, corresponding to a red detuning of ~ -12MHz from resonance, after passing through the AOMs.

3.3.3 The repump lasers

A separate laser system was needed for the repump transition: $5^2S_{1/2}\,F = 1 \longrightarrow 5^2P_{3/2}\,F = 2$ (see figure 2.4). The trapping lasers, tuned to the closed transition $5^2S_{1/2}\,F = 2 \longrightarrow 5^2P_{3/2}\,F = 3$, have a linewidth of $\sim$ 1MHz and can therefore also produce non-resonant excitations to the levels $5^2P_{3/2}\,F = 1, 2$, which can subsequently decay to the $5^2S_{1/2}\,F = 1$ ground state, given the selection rule $\Delta F = 0, \pm 1$. Atoms in the $F = 1$ ground state cannot absorb the trapping light and are therefore lost from the cooling and trapping cycle. A repump beam is needed to continuously excite these atoms out from the $F = 1$ ground state and repopulate the $F = 2$ ground state.

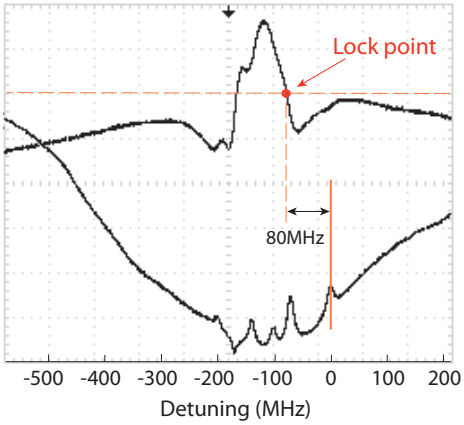

Figure 3.5: Oscilloscope traces of the signals used to lock the repump laser. Polarisation-spectroscopy-lock signal of the master-repump laser (upper trace) and saturated-absorption spectrum of the slave-repump laser (lower trace), for the $5^2S_{1/2}\,F = 1 \longrightarrow 5^2P_{3/2}\,F = F'$ transitions in ^{87}Rb. The solid vertical line marks the repump transition, corresponding to $F' = 2$. Vertical scale: 500mV/div (upper trace) and 100mV/div (lower trace). Horizontal scale: detuning with respect to the $F = 1 \longrightarrow F' = 2$ transition.

Two lasers in master-slave configuration were used for this purpose. The master-repump laser was a home-built extended-cavity diode laser with an output power of $\sim$ 16mW, locked using polarisation spectroscopy to a dispersive feature situated -80MHz away from the repump transition, as shown in figure 3.5. An AOM was used to shift the frequency of the light by +80MHz, bringing it back to the repump transition. The slave-repump laser was a free-standing diode laser seeded by the master laser and forced to lase at the master-laser frequency. Its maximum output was of $\sim$ 22mW. Saturated-absorption spectroscopy of the slave-repump laser is also shown on figure 3.5 for comparison.

The master-repump laser was usually operated at a current of $\sim$ 68mA and a temperature of $\sim$ 16°C, while the current and temperature settings of the slave-repump laser were $\sim$ 70mA and $\sim$ 27°C, respectively.

The output of the slave-repump laser after the AOM ($\sim$ 12mW) was coupled into a single-mode optical fibre resulting in $\sim$ 8mW of repump light out of the fibre. This power was then divided into three parts that were overlapped with the MOT-beam light, LVIS-beam light and optical pumping light, respectively, as described in the next section.

3.3.4 Final output laser beams

A black box consisting of a large frame with six lids contained all the lasers and optics needed to produce the appropriate output laser beams used to trap and cool atoms. Four final output laser beams came out of small holes in this box, described as follows.

The LVIS beam had a total power of $\sim$ 100mW and corresponded to part of the output of the TA100 laser (400mW), which passed through a -92MHz AOM, was coupled into a single-mode, polarisation-maintaining, optical fibre and overlapped with $\sim$ 2.6mW of repump light.

The MOT beam had a total power of $\sim$ 35mW and corresponded to part of the output of the TA100 laser (100mW), after passing through a second -92MHz AOM, being fibre-coupled and combined with $\sim$ 1.3mW of repump light.

The optical pumping beam was tuned to the $5^2S_{1/2}\,F = 2 \longrightarrow 5^2P_{3/2}\,F = 2$ transition (see figure 2.4). It was derived from the reference laser by double passing a part of its output through an AOM to reduce its frequency by 246MHz, so that the optical pumping beam was blue-detuned by $\sim$ 20MHz from the optical pumping transition. The optical pumping light ($\sim$ 0.8mW) was overlapped with part of the repump beam ($\sim$ 0.2mW), resulting in a total power of $\sim$ 1mW.

The imaging beam was resonant with the main trapping transition, $5^2S_{1/2}\,F = 2 \longrightarrow 5^2P_{3/2}\,F = 3$ and was picked up from the LVIS beam. Its power was of $\sim$ 10mW.

Mechanical shutters operated by computer-controlled TTLs were used to block or unblock these beams. Faster switching was also available for most beams via their AOMs, which also enabled attenuation of the beam intensities.

The reference laser and repump laser usually stayed locked for up to a few hours during experimental data taking, while the TA100 was more sensitive to temperature variations in the laboratory and more difficult to stabilise, and needed re-locking approximately every half an hour. The temperature in the laboratory usually remained constant to within 1°C, maintained by the college estates department. It was necessary to maximise the power of every output beam every day, by tweaking the alignment mirrors in the TA100 laser, as mentioned before, and by adjusting the alignment into the optical fibres to which the beams were coupled.

3.4 Computer control

Computer control of the different settings that needed to be varied during experimental data taking was possible through 32 digital-channel (TTL) outputs and 8 analog-channel outputs generated by two National Instruments PCI boards inserted in the PCI slots of a personal computer (see reference [81] for details).

Most of the experimental parameters could be chosen and controlled simply by entering the required values in a graphical-user interface as the one shown in figure 3.6. The user interface was written by C. D. J. Sinclair in Java programming language and ran using an Eclipse platform [81].

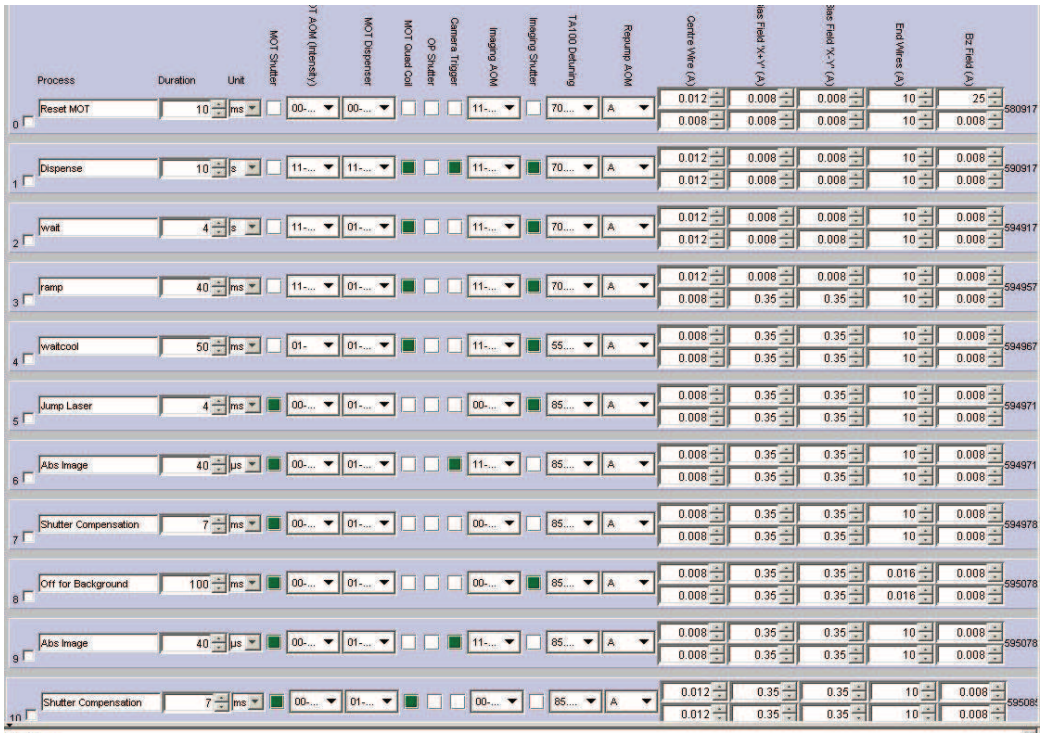

Figure 3.6: Image of the user interface for computer control of the experimental equipment. The time duration of each line in an experimental sequence could be set in the second column. The TTL controls are shown on the left-hand side of the image: square boxes that could be ticked on and off, and level setters formed by the combination of two TTL outputs. The analog channels can be seen on the right-hand side of the image.

This computer-control system allowed the following tasks:

- control of the timing for each step in an experimental sequence;
- use of TTL outputs to switch on and off certain currents, fields and AOM's, to set laser detunings, to open and close mechanical shutters or to externally trigger equipment;
- use of analog outputs to generate voltage ramps for changing magnetic fields and laser frequencies over chosen times;
- pre-configuration of the time resolution of the entire sequence and pre-setting of the delay of the signal generated by each TTL or analog channel, enabling pre-triggering of slow-response shutters, for instance;
- triggering of the camera and image-acquisition software, Roper Scientific Winview, for the acquisition of fluorescence and absorption images during a run of an experimental sequence.

3.5 Image acquisition

A Princeton Instruments PentaMax camera with a Kodak KAF-1400 CCD chip, with dimensions of 1317×1035 pixels, pixel size of $6.8 \times 6.8 \mu\text{m}^2$ and detection efficiency of 0.03 counts per photon, was used for the acquisition of fluorescence and absorption images for all the work presented in this thesis, except for that in chapter 5, which was carried out with another camera, of the same type but with a different CCD chip: Kodak KAF-0400, with dimensions of 768×512 pixels, pixel size of $9 \times 9 \mu\text{m}^2$ and detection efficiency of 0.019 counts per photon [80].

The camera was connected to a temperature controller in order to cool and maintain the temperature of the CCD chip at around $-30°\text{C}$. The camera was externally triggered by a TTL signal generated by the computer. The camera's shutter needed approximately 7ms to fully open or close.

3.5.1 Fluorescence imaging

Atoms captured in a magneto-optical trap are continuously scattering photons from the MOT beams directed to them. These photons are emitted randomly in all directions and can be detected by a camera as a way to image the MOT and estimate the number of atoms in it.

Each atom in the MOT scatters photons at a rate:

$$R = \frac{\Gamma}{2} \frac{I/I_{sat}}{1 + \frac{I}{I_{sat}} + 4\left(\frac{\Delta}{\Gamma}\right)^2}\,, \tag{3.1}$$

where I is the total intensity of the laser trapping beams, Δ is the detuning of the light with respect to the frequency of the main atomic trapping transition ($5^2S_{1/2}\,F = 2 \longrightarrow 5^2P_{3/2}\,F = 3$ of ^{87}Rb in our experiment), I_{sat} is the saturation intensity of this transition and $\Gamma = 2\pi \times 6.07\text{MHz}$ is the natural linewidth of the same transition [83].

The atoms in a MOT are in a mixture of Zeeman hyperfine sublevels (m_F) and absorb light with multiple polarisations. For three-dimensional optical molasses we can use a value of I_{sat} of 3.58mW/cm^2, for the D_2 line of ^{87}Rb, if we ignore the magnetic field and assume that the atoms move and are on average illuminated by all light polarisations [83]. This value is an overestimate of the effective saturation intensity. Typical experimental values for our main MOT were $\Delta \simeq -2\pi \times 12\text{MHz}$ and $I \simeq 14\text{mW/cm}^2$, resulting in scattering rates of $R \simeq 4 \times 10^6$ photons/s.

Only a fraction of all the photons scattered by each atom was collected by the lens, which was situated at a distance d from the atoms, and focused onto the CCD chip of the camera. This fraction, f_γ, can be approximated by the ratio of the area of the lens to the surface of a sphere of radius d, centred on the atom, since the area of the lens was small compared to the total area of the sphere:

$$f_\gamma = \frac{\pi r_{lens}^2}{4\pi d^2}\,, \tag{3.2}$$

where r_{lens} is the radius of the lens. Considering the values of $r_{lens} = 1.27$cm and $d = 20$cm for our imaging set up, we obtain a value of f_γ of $\sim 10^{-3}$.

The detection efficiency of the camera was measured to be of $\eta \sim 0.03$ counts/photon (for the KAF-1400 CCD chip) by calibrating the image of a beam of known power and wavelength, for a beam size approximately equal to the size of the CCD chip, and for a given exposure time.

The usual experimental procedure consisted of recording a fluorescence image of the atoms in the MOT and a background image in the same conditions but with no atoms. The background image was subtracted from the fluorescence image of the atoms and the counts in all the pixels of the resulting image were added to obtain the total number of fluorescence counts, N_{flu}. The number of atoms, N, in the MOT was estimated from this number of counts using the following expression:

$$N = N_{flu} \frac{1}{R\, t_{exp}\, \eta\, f_\gamma} \tag{3.3}$$

where t_{exp} is the exposure time, typically equal to 7ms. The calibration for our fluorescence images, given by the factor $1/(R\, t_{exp}\, \eta\, f_\gamma)$, was of ~ 1 atom per count in the fluorescence image.

3.5.2 Absorption imaging

When atoms are confined in a magnetic trap they can be imaged by passing a beam of light, resonant with a given atomic transition, through the trap, and measuring the absorption of light by the atoms. This process is destructive, and the atomic cloud is lost from the magnetic trap after being imaged. A collimated imaging beam, resonant with the $5^2S_{1/2}\, F = 2 \longrightarrow 5^2P_{3/2}\, F = 3$ transition and with circular polarisation (σ^+ with respect to the imaging quantisation field), was sent through the magnetically trapped atoms during typical pulsed durations of $100 - 150\mu$s, and then collected and focused by a lens into the CCD chip of the camera, in order to acquire an absorption image of the trapped cloud.

Given a beam of light propagating through an atomic cloud along the z direction, the Beer-Lambert law describes the light absorbed by the atoms as:

$$I(x,y) = I_0(x,y) \exp\left[-\sigma_L \int n(x,y,z)dz\right], \tag{3.4}$$

where $n(x,y,z)$ is the three-dimensional atom-number density, $I(x,y)$ and $I_0(x,y)$ are the final and initial light-intensity profiles corresponding to the images recorded with and without atoms, respectively, and σ_L is the photon absorption cross-section, given by:

$$\sigma_L = \frac{hc}{\lambda}\frac{\Gamma}{2}\frac{1/I_{sat}}{1 + \frac{I}{I_{sat}} + 4\left(\frac{\Delta}{\Gamma}\right)^2}, \tag{3.5}$$

where h is Planck's constant, λ is the wavelength of the imaging light and the rest of the symbols are the same as those of equation 3.1. Equation 3.4 is valid when σ_L can be assumed to be independent of I, and therefore independent of position, i.e., when the

condition $I \ll I_{sat}$ is fulfilled in equation 3.5. The quantity $\sigma_L \int n(x,y,z)dz$ is often referred to as the optical depth of the cloud. At a given position (x,y) on the image plane, the two-dimensional atom number density, $n_{2D}(x,y)$, is given by:

$$n_{2D}(x,y) = \int n(x,y,z)dz = \frac{-1}{\sigma_L} \ln \left[\frac{I(x,y)}{I_0(x,y)} \right] , \tag{3.6}$$

and the total number of atoms, N, can be obtained by summing over all the pixels in the image and taking into account the area represented by one pixel, S_{pixel}:

$$N = \frac{-1}{\sigma_L} S_{pixel} \sum_{x,y} \ln \left[\frac{I(x,y)}{I_0(x,y)} \right] , \tag{3.7}$$

where $\sum_{x,y} \ln [I(x,y)/I_0(x,y)]$ corresponds to the total number of counts measured in the processed absorption image. The processed absorption image was calculated by dividing the image acquired with atoms by the image acquired without atoms, and taking the natural logarithm of the result.

For resonant absorption imaging in our experiments, using imaging "set-up I" (see section 3.5.3), for instance, the typical parameters were: $\lambda \sim 780$nm, $\Delta = 0$MHz, $I \simeq 0.2 I_{sat}$ and $S_{pixel} \simeq 1.2 \times 6.8 \times 6.8 \mu\text{m}^2$, resulting in a calibration factor, S_{pixel}/σ_L, of ~ 230 atoms per count in the processed absorption image.

When the atomic cloud was imaged after being released from the magnetic trap, a small magnetic field of up to 1G, referred to as imaging field, and generated by a pair of coils with their common axis along the direction of the imaging beam (see section 3.2.2), was applied during the image acquisition time. The purpose of this field was to provide a quantisation axis for the magnetic state of the atoms. The imaging beam had σ^+ circular polarisation with respect to this imaging field, so that the released atoms were quickly pumped to the $m_F = +2$ magnetic sublevel of the $5^2S_{1/2}\, F = 2$ ground state, from which they could absorb imaging light in transitions to the $5^2P_{3/2}\, F = 3, m_F = +3$ excited state, for which the Clebsch-Gordan coefficient is maximum.

When the atoms were imaged while they remained confined in a magnetic trap, the variation of the axial magnetic field along the trap axis resulted in a more complex picture, with the Zeeman shifts of the atomic levels varying along the length of the cloud and leading to position-dependent detunings with respect to the imaging transition. For this reason, the simple formulas presented in this section did not provide a good estimate of the number of atoms in the trap when in-trap absorption images were recorded.

3.5.3 Imaging set up

The same imaging set up was used to acquire both fluorescence and absorption images. Two geometrical configurations were used, explained as follows, and referred to as "imaging set-up I" and "imaging set-up II" throughout this thesis.

Imaging set-up I

In this imaging configuration, a collimated laser beam reflected off the gold-coated surface of the videotape-atom chip at a small angle to the horizontal, $\theta = (14 \pm 2)^\circ$, and was then focussed by a doublet lens onto the CCD chip of the camera, as shown in figure 3.7. The imaging beam propagated at an angle of $\alpha = (35 \pm 2)^\circ$ to the x direction.

The imaging beam diameter was $D \sim 2.2$cm, limited by the diameter of the linear polariser and $\lambda/4$ waveplate which were placed in the path of the beam to make circularly polarised light. The diameter of the doublet lens was 2.54cm, and its focal length was $f = 10$cm. The doublet was placed at a distance of $2f$ from both the atomic cloud and the CCD chip of the camera in order to achieve unit magnification.

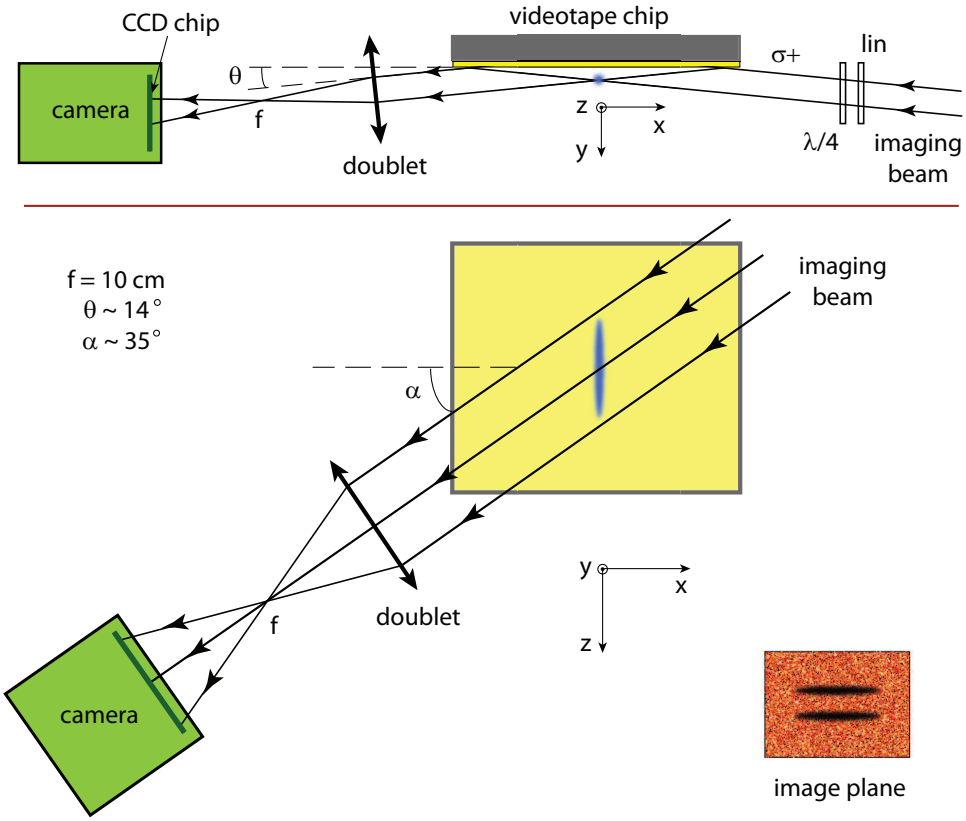

Figure 3.7: Schematic diagram of imaging set-up I. Projections on the x-y plane (top) and x-z plane (bottom).

A double absorption image appeared on the image plane, with two clouds corresponding to the images of the atomic cloud and its reflection on the chip surface, as shown on figure 3.7. The distance between these two images along the vertical direction on the image plane was equal to twice the distance from the cloud to the chip surface and was often measured in order to determine the atom-surface separation.

Due to the angle α along which the cloud was imaged, distances along the z direction appeared to be shorter by a factor of ~ 1.2 along the horizontal direction on the image

plane. Vertical distances along the y direction remained unmodified on the image plane.

Imaging set-up II

In this set up, atomic clouds were imaged along their axial direction (z), with the imaging beam reflecting off the chip surface at an angle of $\beta \sim 45°$, as shown in figure 3.8.

The imaging beam diameter was also $D \sim 2.2$cm. A different lens was used, with a focal length of $f = 12.5$cm, placed also in a $2f$–$2f$ configuration for unit magnification.

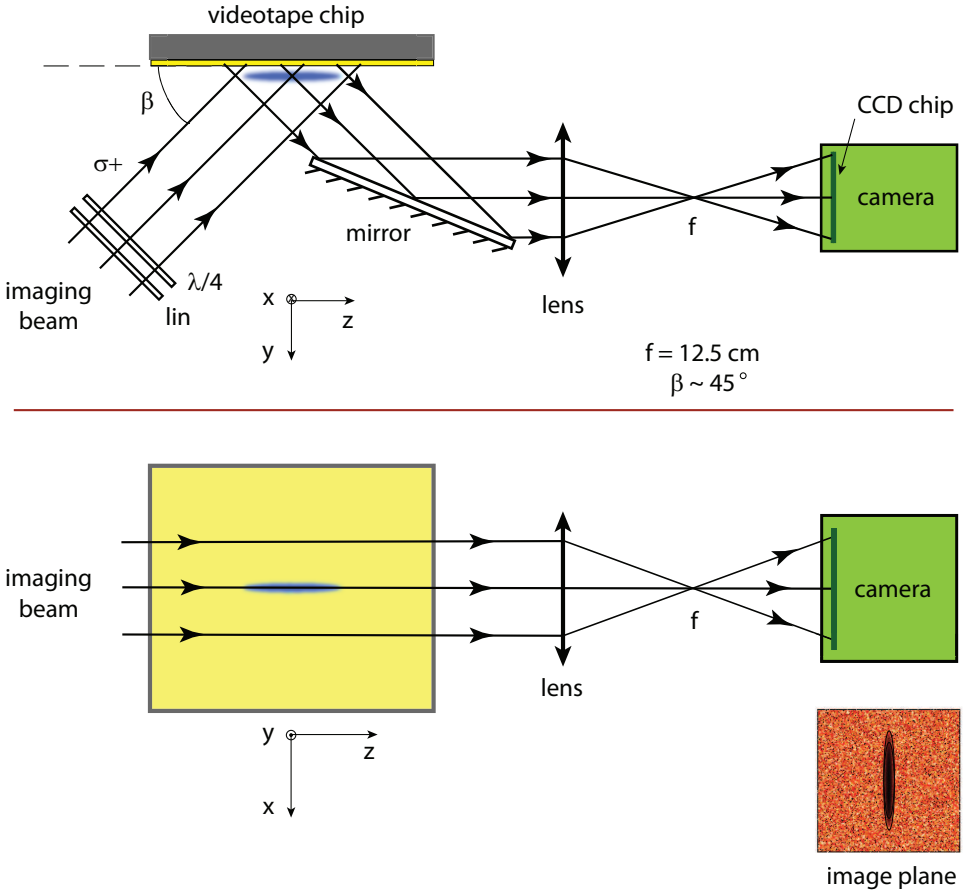

Figure 3.8: Schematic diagram of imaging set-up II. Projections on the y-z plane (top) and x-z plane (bottom).

The resulting image consisted of two nearly-overlapped, elongated clouds with their axes along the vertical direction on the image plane, as shown in figure 3.8. The two clouds corresponded to the images of the cloud and its reflection, which had their centres separated along the vertical direction of the image by a distance equal to $\sqrt{2}$ times the atom-surface separation. Features along the x direction, perpendicular to the direction of propagation of the imaging beam, appeared unmodified along the horizontal direction on the image plane, while features along the z direction, i.e., along the axis of the cloud, vertical on the image plane, appeared to be re-scaled by a factor of $1/\sqrt{2}$, due to the angle β.

Spatial resolution

The spatial resolution of our imaging system was limited on one hand by the pixel size of the camera (9μm or 6.8μm, depending on the CCD chip), and on the other hand by the diffraction limit given by $1.22\frac{\lambda f}{D}$, according to the Rayleigh criterion, where D is the diameter of the limiting aperture of the imaging system, λ is the wavelength of the light and f is the focal length of the imaging lens. The value of D was 2.2cm for both imaging set ups, limited by the diameter of the linear polariser and $\lambda/4$ waveplate in the path of the imaging beam, and the values of f were 10cm and 12.5cm for imaging set ups I and II, respectively. These values yield spatial resolutions of 4.3μm and 5.4μm, respectively, leading to the conclusion that the resolution of our imaging system was effectively limited by the camera's pixel size, if we assume that optical aberrations were sufficiently small in our imaging set-ups. An achromatic doublet lens was used for "imaging set-up I" in order to minimise optical aberrations.

Chapter 4

Description of the experimental sequence

4.1 Introduction

The experimental sequence followed to confine cold atoms in videotape traps is briefly outlined as follows. The rubidium dispenser was turned on in order to load our LVIS MOT and main MOT. The main MOT was then moved closer to the surface of the videotape atom chip and further cooled in a sub-Doppler cooling stage. The trapping light and quadrupole field of the MOT were then switched off, the atoms were optically pumped into the $5S_{1/2}$, $F = 2$, $m_F = +2$ magnetic hyperfine sublevel, and then recaptured in a wire magnetic trap. The wire trap was then compressed and the atoms were cooled through RF evaporation, down to typical temperatures of $1 - 50\mu$K. After that, the atoms were transferred into one or several videotape magnetic micro-traps, in order to carry out experiments. Further RF evaporation was possible in the videotape traps if needed. An absorption image of the atoms was typically recorded at the end of this sequence, either in-trap or after release, as explained in section 3.5.2.

This chapter explains each step of the experimental sequence in detail, stating the typical experimental parameters and presenting relevant experimental data for each step.

4.2 Magneto-optical traps: LVIS and MOT stages

The theory of magneto-optical trapping is well understood and detailed explanations can be found in a large number of references, such as [1–3, 90–92], for instance.

Laser cooling and trapping of neutral alkali atoms is possible thanks to the presence of cycling transitions in their energy-level structure, and to the large hyperfine energy splittings that enable independent addressing of the different atomic transitions. In our experiment, we start by confining ^{87}Rb atoms in magneto-optical traps, using the closed atomic transition from the $5^2S_{1/2}\,F = 2$ ground state to the $5^2P_{3/2}\,F = 3$ excited state (see the ^{87}Rb full energy diagram in figure 2.4).

Laser cooling takes advantage of the detuning of laser light with respect to an atomic transition, caused by the Doppler shift of the light frequency in the moving frame of the

atom, to bias the absorption of photons by the atoms. Atoms in the presence of counter-propagating, red-detuned, laser beams preferentially absorb photons from the beams that oppose their motion, while they emit photons randomly in all directions of space. As a result, the average scattering force exerted by light on the atoms opposes the atomic motion and is able to damp the atomic velocities, slowing the atoms down and, therefore, cooling them.

A quadrupole magnetic field can additionally confine the atoms to a region of minimum magnetic field, overlapped with the laser-cooling region, in what is known as a magneto-optical trap (MOT). A combination of the spatially-varying Zeeman shifts of the atomic hyperfine sublevels, induced by the quadrupole magnetic field, with the correct beam polarisations ensures that atoms preferentially absorb light from the beams that oppose their displacement from the trap centre, experiencing a spatially-dependent, restoring force that pushes them towards the minimum of the magnetic field at the centre of the trap.

The Doppler limit is the temperature achieved in a magneto-optical trap when there is equilibrium between the cooling rate, due to the damping force of light, and the heating rate due to the spontaneous emission of photons by the atoms. The Doppler temperature for ^{87}Rb is $\sim 145\mu$K. Sub-Doppler cooling mechanisms (section 4.2.3) explain how it is possible to reach temperatures below the Doppler limit in a MOT. A further limit, known as the recoil limit, is set by the recoil of an atom after a scattering event with a photon. The recoil limit for ^{87}Rb is of 362nK [83]. More complicated optical cooling methods that use Raman transitions or transitions into dark states, have been successfully implemented to achieve temperatures below the recoil limit [90]. Temperatures below the recoil limit are usually achieved by transferring the atoms to magnetic traps, where they can be efficiently cooled through radio-frequency evaporative cooling (see section 4.4.2).

The steps taken to confine rubidium atoms in magneto-optical traps in our experiment are described in sections 4.2.1 to 4.2.4, and summarised here as follows. Atoms were released from a rubidium dispenser located in the LVIS chamber and captured in a MOT inside the LVIS chamber (section 4.2.1). A slow beam of atoms travelled from this LVIS MOT to the main chamber, and atoms were re-captured in a second MOT at the centre of the main chamber (section 4.2.2). This second MOT, referred to as main MOT, was moved from a distance of $\sim$ 6–7mm to a distance of $\sim$ 2mm from the videotape-chip surface and then cooled in a sub-Doppler cooling stage (section 4.2.3), after which the MOT temperature was of $\sim$ 30–60μK (section 4.2.4).

4.2.1 The LVIS

A low velocity intense source (LVIS) was used to provide a slow atomic beam that travelled over a distance of around 30cm, from the MOT in the LVIS chamber to the main MOT in the science chamber, passing through the 1mm-diameter hole drilled in the mirror located in between the two chambers (see section 3.1). Atoms were transferred from the LVIS MOT to the main MOT thanks to the hole in the retro-reflecting mirror of the LVIS-push beam, that created an intensity imbalance in the central column of this beam (see figure 4.1), pushing the atoms through the hole towards the main chamber.

Having two separate vacuum chambers enabled us to have a high pressure of $\sim 10^{-7}$Torr in the LVIS chamber, for achieving large capture rates in our LVIS MOT, while maintaining a much lower pressure of $\sim 10^{-11}$Torr in the main vacuum chamber. This led to higher atom numbers being loaded into the main MOT, and resulted in longer lifetimes for all the different stages of atom trapping and cooling, from the MOT to the magnetic traps.

Figure 4.1 shows the geometry of the MOT formed inside the LVIS chamber. A six-beam-MOT configuration was used, in which three pairs of counter-propagating laser beams (one vertical pair and two horizontal pairs, perpendicular to each other), intersected at the centre of the chamber. All beams were retro-reflected at their corresponding mirrors and the appropriate $\lambda/4$ waveplates were used to obtain the correct beam polarisations. The quadrupole magnetic field required for magneto-optical trapping was generated by two anti-Helmholtz coils (see section 3.2.1) aligned with their axes along the vertical direction, as shown in figure 4.1.

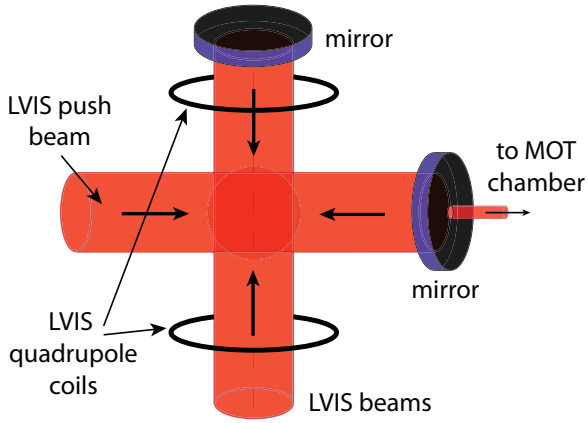

Figure 4.1: Schematic diagram of the LVIS magneto-optical trap configuration with three pairs of mutually orthogonal laser beams. One pair of beams is perpendicular to this page.

The total power of the LVIS MOT beams was $\sim$ 100mW, with the beam diameter being $\sim$ 3.5cm. The mean velocity of the atoms in the LVIS beam was $\leq$ 10m/s, determined by the fact that the atoms took at least 30ms to travel the distance of $\sim$ 30cm between the LVIS MOT and the main MOT.

The rubidium dispenser was located inside the LVIS chamber. A current of 7.5A was typically run through the dispenser during a time of 20-30 seconds in order to fill the LVIS MOT and load the main MOT.

4.2.2 The main MOT

Atoms were loaded in the main MOT by switching on the MOT-quadrupole magnetic field and MOT-light beams at the same time as the dispenser, LVIS-quadrupole field and LVIS-light were turned on to make a MOT in the LVIS chamber.

A mirror-MOT configuration was used, consisting of two counter-propagating, horizontal laser beams and two diagonal beams propagating in a vertical plane and reflecting off

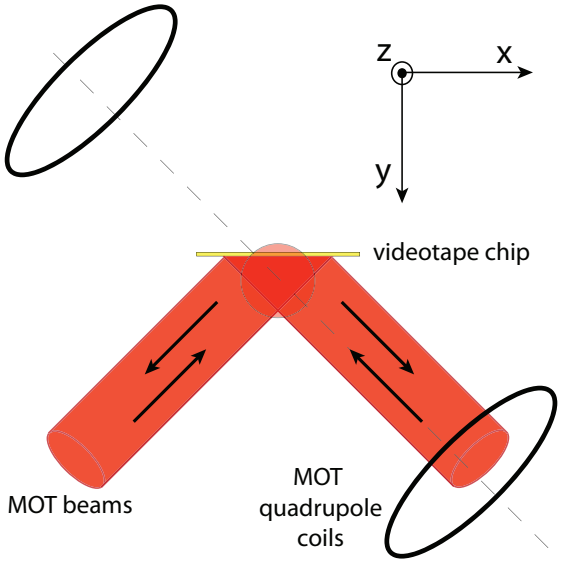

Figure 4.2: Schematic diagram of the MOT configuration. Two counter-propagating beams are perpendicular to this page.

the gold-coated surface of the chip at an angle of 45°, as shown in figure 4.2. Four separate MOT laser beams were used (not retro-reflected), and a $\lambda/4$ waveplate was placed in the path of each beam before the chamber in order to adjust the beam polarisations. The MOT-quadrupole coils (see section 3.2.2), wired in anti-Helmholtz configuration, were aligned with the $\hat{\mathbf{x}} + \hat{\mathbf{y}}$ direction, as shown in the figure.

The diameter of the MOT-beams was $\sim$ 2.5cm, with a total power of $\sim$ 35mW. The detuning of the MOT beams with respect to the main trapping transition was typically of -2Γ, where $\Gamma \simeq 2\pi \times 6$MHz is the natural linewidth of the transition. The MOT was positioned close to the centre of the main chamber, at a distance of 6–7mm below the surface of the videotape atom chip.

Small homogeneous magnetic fields (LVIS and MOT shim fields) generated by coils located around the LVIS and main chambers (see section 3.2), were used to adjust the position of the LVIS and main MOT in order to achieve optimum loading of atoms into the main MOT. The alignment of the LVIS-push beam could also be adjusted in order to change the direction of the slow atomic beam that carried atoms from the LVIS chamber into the main MOT.

Atoms were captured in the MOT during dispensing at a rate of $\sim 10^7$ atoms/s. Typical atom numbers in the MOT, at the end of the dispensing and loading process, were 10^8–10^9 atoms. The MOT radius was as large as 3–4 mm, resulting in densities of 10^9–10^{10} atoms/cm^3. The typical MOT temperature was $\sim 500\mu$K, leading to phase space densities (see future equation 4.5) of 10^{-10}–10^{-9}.

The lifetime of the atoms in the MOT was typically between 50s and 160s, limited by the background pressure in the main vacuum chamber. Figure 4.3(left) shows an example

of the lifetime of a small MOT measured by detecting the decay of the MOT fluorescence on a photodiode after switching off the LVIS light and LVIS-quadrupole field to stop the flux of atoms from the LVIS. The initial lifetime was $\sim$ 94s, increasing with time towards a value of $\sim$ 156s, as indicated by the linear fits shown in the figure. Figure 4.3(right) shows the dependence of the initial MOT lifetime on atom number. The initial decay in MOT atom number was measured by recording fluorescence images with the CCD camera during 50 seconds, for different initial atom numbers. The MOT was approximately 7mm away from the chip surface and its half size along the vertical direction ranged between 1mm and 2.5mm. We measured longer lifetimes for lower atom numbers. This could be due to a lower rate of interatomic collisions at the centre of the MOT or, possibly, to the lower background pressure in the main vacuum chamber when the atom number was lower (due to less dispensing).

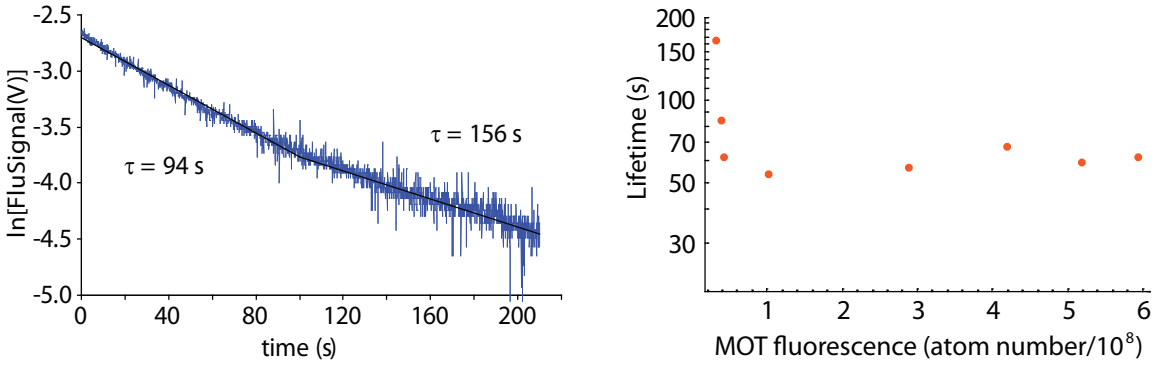

Figure 4.3: **Left**: MOT lifetime measured by detecting the decay of the MOT fluorescence on a photodiode. The LVIS-quadrupole field and LVIS light were off during this measurement. The natural logarithm of the fluorescence signal is plotted versus time. The solid lines are linear fits for the initial and final data points. **Right**: initial MOT lifetime versus atom number, measured by fluorescence imaging.

Moving the MOT closer to the chip surface

Right after dispensing, the main MOT was moved from a distance of $\sim 6-7$mm to a distance of $\sim$ 2mm from the videotape-chip surface. The atoms were moved using a magnetic field generated by the bias coils on the x-y plane, ramped up typically in 100ms, to displace the zero of the MOT-quadrupole magnetic field towards the chip surface. Due to the symmetry and orientation of the quadrupole-field lines, the total bias field required to move the MOT along a vertical direction was the combination of $\sim$ 1.9G generated by the bias-coil pair along the $\hat{\mathbf{x}}+\hat{\mathbf{y}}$ direction, with $\sim$ 3.1G from the bias-coil pair along the $\hat{\mathbf{x}}-\hat{\mathbf{y}}$ direction.

The lifetime of the atoms in the MOT decreased drastically as the atoms moved closer to the chip surface. Figure 4.4(left) shows how the MOT lifetime decreased with the ratio of atom-surface separation to total radius of the MOT. The reason for this was the interaction of the atoms with the surface of the chip, that led to a great loss of atoms when the total MOT radius along the vertical direction was of the same order or larger than the distance from the centre of the cloud to the chip surface. Figure 4.4(right) presents the MOT lifetime

corresponding to the same data set as a function of the MOT radius for different atom-surface separations. We can see how the lifetime seems to decrease as the MOT radius increases at a constant height.

The MOT was typically moved to a distance of $\sim$ 2mm from the chip surface for the purpose of loading atoms into a magnetic trap. At this distance, and given the typical size of our MOT, the lifetime was reduced to a few seconds.

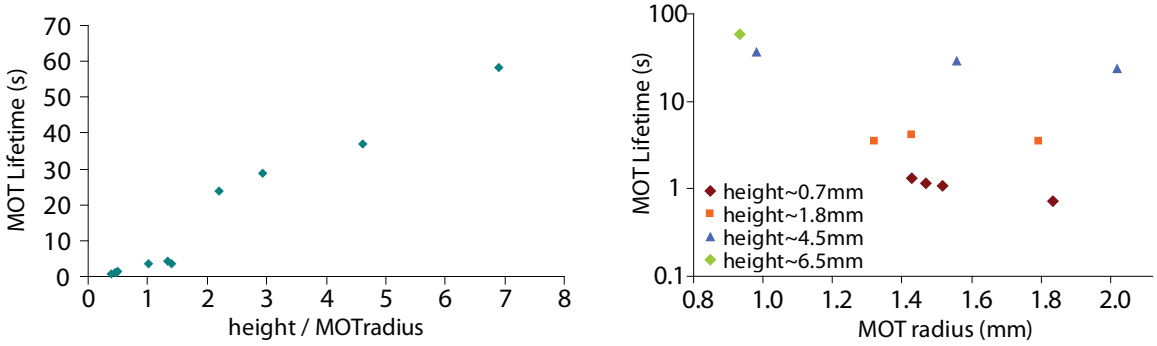

Figure 4.4: **Left**: MOT lifetime as a function of the ratio of atom-surface separation to total MOT radius. **Right**: MOT lifetime versus MOT radius for the same data set. The MOT lifetimes were obtained by recording 17 consecutive fluorescence images during a total time of 50s. The atom-surface separation (MOT height) was between 0.7mm and 6.5mm, and the MOT radius ranged between 1mm and 2mm along the vertical direction.

Maintaining a steady atom number

A fluorescence image of the MOT after it was moved closer to the chip surface was usually recorded and used to monitor the initial atom number in each repetition of the experimental sequence. Since rubidium atoms accumulated in both vacuum chambers after each realisation of the experimental sequence, it was necessary to wait for a time of 60-150s, depending on the amount of dispensing, between the end of one sequence and the start of the next one, for these atoms to be pumped away in order to maintain a steady and repeatable initial atom number during data taking.

Figure 4.5(left) shows how the initial atom number, measured from the number of counts in the fluorescence image of the MOT after 10s of dispensing, varied with the time waited between consecutive realisations of the experimental sequence. A steady state was reached for a waiting time of $\sim$ 60s in this particular example. Figure 4.5(right) shows two examples of how the atom number was maintained constant during 14 consecutive realisations of the experimental sequence. The standard deviation of the atom-number fluctuations was as low as 3% in these examples, representative of the typical noise in initial atom number during data taking.

Maintaining a constant initial atom number was very important when varying experimental parameters for the optimisation of the different stages of the sequence that led to the confinement of ultra-cold atoms in videotape magnetic traps. Large atom-number fluctuations would have resulted in noisy data, making it difficult to distinguish the effect that varying certain parameters had on the atomic properties.

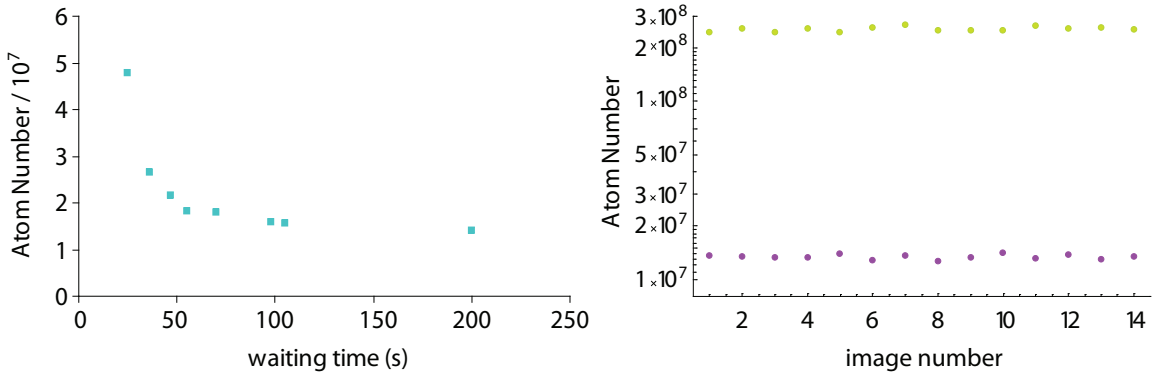

Figure 4.5: Maintaining a steady atom number in the MOT. **Left**: atom number measured from MOT-fluorescence images after 10s of dispensing, as a function of the time waited between two consecutive realisations of the experimental sequence. **Right**: steady atom number achieved by waiting a constant time between 14 consecutive experimental sequences, for two different data sets corresponding to atom numbers of $\sim 10^7$ and $\sim 10^8$. The waiting time was of $\sim$ 100s and $\sim$ 150s, respectively. The atom number fluctuations had standard deviations of $\sim 3\%$ for both data sets.

4.2.3 Sub-Doppler cooling stage

Sub-Doppler cooling, also referred to as polarisation-gradient cooling or Sisyphus cooling, relies on the Stark shifts of the different atomic magnetic sublevels trapped in a MOT. These Stark shifts depend on the spatially-dependent, total polarisation that the atoms see in the presence of the counter-propagating MOT beams, and therefore vary with position. As the atoms move through these polarisation gradients, they are forced to climb up hills of potential energy due to the spatially-varying light shifts. Once at the top of these hills, the atoms preferentially absorb MOT light in transitions to excited states, and then de-excite returning preferentially to the bottom of the potential-energy hills. In this way the atoms cool by emitting photons with an energy higher than that of the photons they absorb [92].

The temperature reached at the end of the sub-Doppler cooling stage is proportional to I/Δ in the limit of $|\Delta| \gg \Gamma$ (see equation 30, reference [91]), where I is the total intensity of the MOT beams, Δ is their detuning from resonance with the main atomic trapping transition, and $\Gamma \simeq 2\pi \times 6$MHz is the natural linewidth of the transition. Therefore lower temperatures can be achieved by increasing the detuning from resonance and reducing the intensity of the MOT beams. Increasing the detuning of MOT light minimises the scattering rate and allows the temperature of the atoms to decrease below the Doppler limit.

A sub-Doppler cooling stage was implemented in our main MOT by red-detuning the frequency of the MOT laser beams away from resonance. A reduction in MOT-beam intensity was found to have no obvious effect on the MOT temperature.

The MOT-quadrupole magnetic field remained constant while the detuning of the MOT beams was ramped from ~ -12MHz to ~ -45MHz in 5ms and subsequently held at ~ -45MHz for another 5ms. These detuning values and ramp and hold times were experimentally chosen for yielding the lowest MOT temperatures for the maximum acceptable atom loss. Figure 4.6 shows plots of the MOT size (proportional to the square root of the temperature if we ignore radiation pressure), the maximum optical density (see section 3.5.2) and the atom number inferred from absorption images of the MOT, as a function of

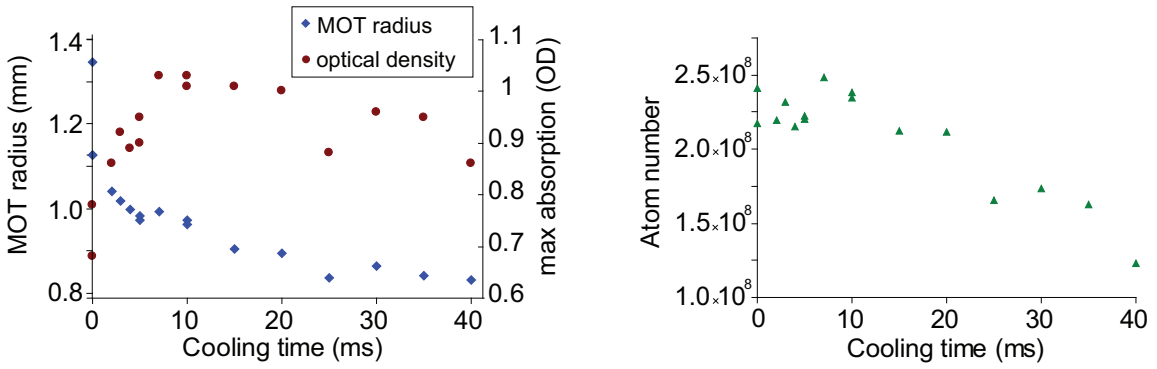

Figure 4.6: Optimisation of the sub-Dopper cooling stage by varying the time during which the MOT light is detuned by -45MHz from resonance. The graph on the left shows the MOT radius and maximum optical density (maximum absorption) of the MOT measured from absorption images. The graph on the right shows the approximate atom number.

the time during which the MOT beams were detuned by -45MHz from resonance.

The usual temperatures achieved after the sub-Doppler cooling stage were around $30 - 60\mu$K. These temperatures were determined by absorption imaging of the atoms in the MOT, during ballistic expansion in time-of-flight temperature measurements, as explained in the following section, 4.2.4. Typical atom numbers were between 10^8 and 10^9 atoms at this stage, for an approximate MOT radius of 1mm, leading to typical densities of $10^{11} - 10^{12}$ atoms/cm^3, and phase space densities of 10^{-7}–10^{-6}.

4.2.4 Time-of-flight measurement of the MOT temperature

The temperature of the MOT was measured using the standard time-of-flight technique consisting of releasing the atomic cloud from the trap and monitoring its expansion as it falls under gravity. Along a given direction of space, x, we can assume that the initial spatial probability distribution of the atoms in the MOT is given by the Gaussian function:

$$p_0(x) \propto \exp\left(\frac{-x^2}{2\sigma_{x0}^2}\right), \tag{4.1}$$

where σ_{x0} is the initial rms size of the cloud in the trap. We can assume the initial velocity distribution to be the Maxwell-Boltzmann distribution, given by:

$$p_0(v) \propto \exp\left(\frac{-mv^2}{2k_BT}\right). \tag{4.2}$$

As the cloud is released from the MOT, it expands, and the atoms move with the velocity they had in the trap, v. At a given instant t, an atom finds itself at a position x if its original position in the trap was $x - vt$, and its velocity in the trap was v. Therefore, the probability for an atom to be at position x at time t after release, is given by:

$$p(x,t) = \int_{-\infty}^{\infty} p_0(x - vt)p_0(v)dv \propto \int_{-\infty}^{\infty} \exp\left(\frac{-(x - vt)^2}{2\sigma_{x0}^2}\right) \exp\left(\frac{-mv^2}{2k_BT}\right) dv\,. \tag{4.3}$$

The result of the integration is another Gaussian with a variance equal to:

$$\sigma_x^2(t) = \sigma_{x0}^2 + \frac{k_B T}{m} t^2 \,. \tag{4.4}$$

This last formula can be used to measure the temperature of a cloud of atoms released from a trap, by measuring its rms size, $\sigma_i(t)$, along a given direction $i = x, y, z$, as a function of the expansion time, t.

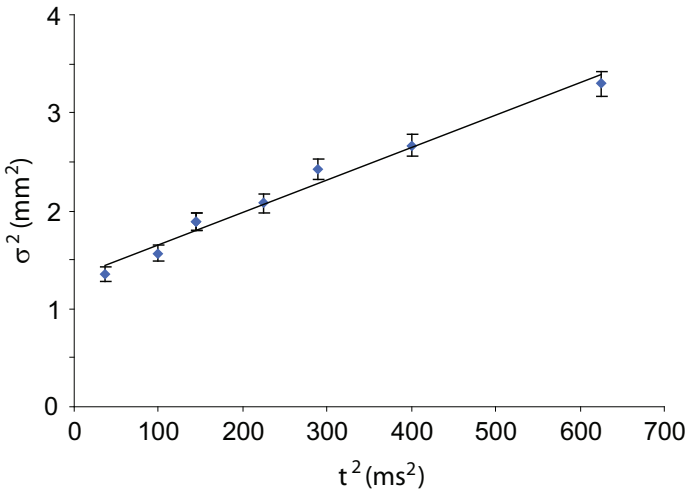

Figure 4.7: Time of flight measurement of the MOT temperature after the sub-Doppler cooling stage. The square of the rms-size of the MOT, σ^2, measured from absorption images, is fitted versus the square of the time, t^2, after release to obtain a temperature of $(33 \pm 2)\mu$K.

Figure 4.7 shows an example of this type of measurement, where a linear fit of $\sigma^2(t)$ versus t^2, for expansion times between 6ms and 25ms, served to determine a temperature of $(33 \pm 2)\mu$K for a MOT after the sub-Doppler cooling stage. The values of $\sigma(t)$ were obtained from Gaussian fits of the cloud's profiles, which were measured via absorption imaging. The initial rms size of the cloud in the MOT was of $\sim$ 1mm, inferred from the offset of the fit, and the atom number was around 10^8 for this particular set of data.

Figure 4.8(first image from the left) shows a fluorescence image of the atoms in a MOT just after the trap was moved close to the chip surface, and before the sub-Doppler cooling stage. The rest of the images in the figure are absorption images of a MOT released after the sub-Doppler cooling stage, for the data corresponding to the time-of-flight temperature measurement of figure 4.7.

Note that this time-of-flight technique based on releasing atoms from a trap and measuring their expansion with absorption imaging, was also used to determine the temperature of the atoms in the magnetic traps, both in the wire magnetic trap and in the videotape magnetic micro-traps.

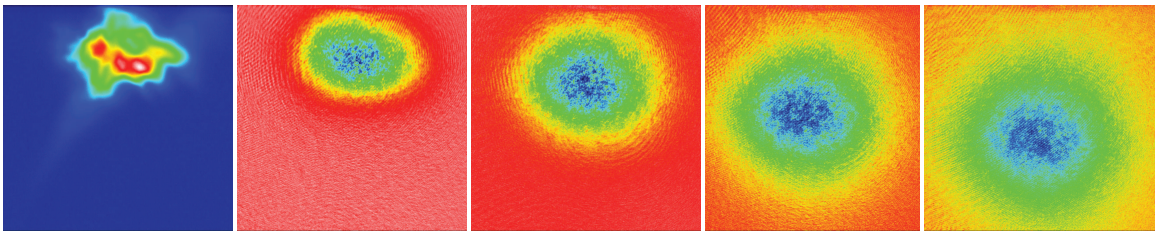

Figure 4.8: Fluorescence and absorption images of a MOT. The images correspond to the data shown in figure 4.7. The first image from the left shows the fluorescence of atoms in a MOT, just before sub-Doppler cooling. The rest show absorption images of atoms released from a MOT after sub-Doppler cooling, for release times of 6, 12, 17 and 20ms, from left to right.

4.3 Optical pumping stage

Since the atoms in the MOT populated all the different magnetic sublevels of the $5^2S_{1/2}\,F = 2$ ground-state hyperfine level, optical pumping was needed to transfer them to the correct magnetic sublevel, i.e., to the $5^2S_{1/2}\,F = 2, m_F = +2$ sublevel, in which they could be magnetically trapped, as detailed in section 2.3.1.

The optical-pumping beam was tuned to the $5^2S_{1/2}\,F = 2 \longrightarrow 5^2P_{3/2}\,F = 2$ transition (see full energy-level diagram in figure 2.4). This beam was derived from the reference laser, as explained in section 3.3.4, and propagated along the z direction, parallel to the chip surface. The optical-pumping beam diameter was ~ 2.5cm.

The polarisation of this beam was circular and σ^+ with respect to a quantisation axis set by a uniform magnetic field generated by the B_z coils. This polarisation resulted in optical pumping transitions with $\Delta m_F = +1$, as shown in figure 4.9 (thick black arrows). The figure also shows the possible de-excitations (thin blue and green lines) allowed by the selection rules $\Delta F = 0, \pm 1$, $\Delta m_F = 0, \pm 1$. After several cycles of excitation and de-excitation, atoms accumulated in the $5^2S_{1/2}\,F = 2, m_F = +2$ ground-state sublevel, in which they could be magnetically trapped, and from which they could no longer absorb optical-pumping light. The fact that atoms accumulated in this dark state at the end of the optical-pumping cycle prevented heating due to further scattering events. This is the reason why the $5^2S_{1/2}\,F = 2 \longrightarrow 5^2P_{3/2}\,F = 2$ transition was used for optical pumping as opposed to the $5^2S_{1/2}\,F = 2 \longrightarrow 5^2P_{3/2}\,F = 3$ transition.

Due to the possibility of decays into the $5^2S_{1/2}\,F = 1$ hyperfine ground state after absorption of optical pumping light (see figure 4.9), repump light (~ 0.2mW) had to be combined with optical pumping light (~ 0.8mW) in order to avoid the loss of atoms undergoing such de-excitations.

The optical-pumping sequence was optimised experimentally by maximising the number of atoms captured in the wire-magnetic trap at the end of the sequence. Various parameters such as the optical-pumping beam alignment and detuning with respect to the $5^2S_{1/2}\,F = 2 \longrightarrow 5^2P_{3/2}\,F = 2$ transition, the optical-pumping pulse duration and the strength of the B_z quantisation field, were varied in order to maximise the number of counts in the

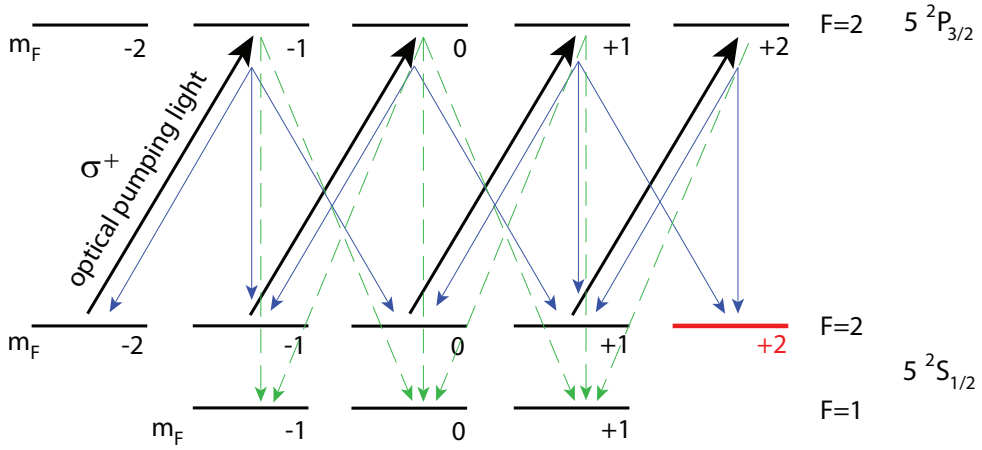

Figure 4.9: Atomic levels involved in the optical pumping transition. Thick (black) lines correspond to the excitations driven by optical pumping light, while thin (green and blue) lines correspond to the de-excitations allowed by the selection rules that apply. At the end of the optical-pumping cycle atoms accumulated in the $5^2S_{1/2}\,F = 2, m_F = +2$ ground-state magnetic sublevel, marked with a thicker (red) line in the figure.

absorption image of the atoms re-captured in the wire-magnetic trap. The optimum values were found to be a detuning of $\sim$ 20MHz (blue detuning) [80], a pulse duration of 400μs and a quantisation field of $\sim$ 3.7G. The number of atoms captured in the wire magnetic trap after the optical-pumping stage was up to three times higher than that without optical pumping.

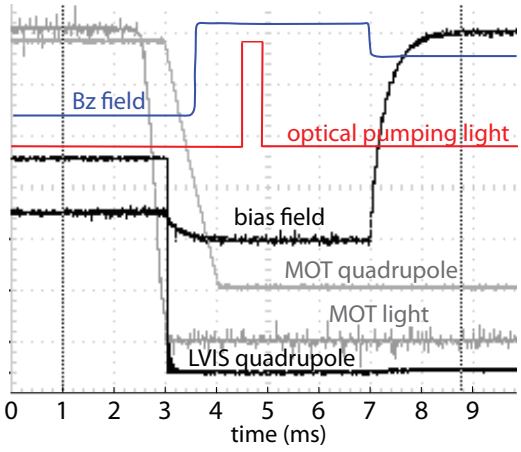

Figure 4.10: Timing of magnetic fields and light for the optical-pumping sequence. The B_z and optical-pumping light traces have been drawn, copying the actual measured traces. The rest are measured oscilloscope traces. At t = 7ms the bias field and B_z field were modified to capture the atoms in the wire magnetic trap (see section 4.4).

It was important to ensure that all laser beams, except for the optical-pumping beam, and all magnetic fields, except for the B_z field, were switched off during the optical pumping pulse. The MOT beams could be switched off as fast as $\sim$ 400ns by means of the MOT AOM, but $\sim$ 1ms had to be allowed for switching off the MOT-quadrupole magnetic field and the bias field. Figure 4.10 shows the oscilloscope traces resulting from monitoring the

currents through the MOT and LVIS quadrupole coils, bias coils and B_z coils (drawn), as well as the MOT light and optical-pumping light (drawn), during the optical-pumping sequence.

4.4 The wire magnetic trap

At the end of the optical pumping stage the atoms were re-captured in a wire magnetic trap by suddenly switching on a current of 15A through the centre wire, a current of 15A through the end wires, a bias field along the x direction of $\sim$ 17G, and a uniform B_z field of $\sim$ 3G along the z direction. Figure 4.11 shows the timing of the currents involved in the recaptured process.

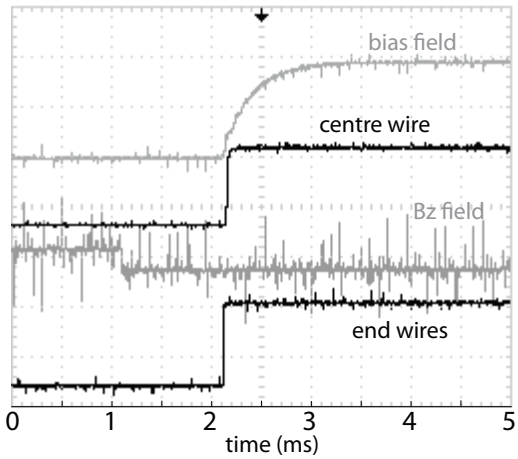

Figure 4.11: Timing for the recapture of atoms in the wire magnetic trap. Oscilloscope traces of the centre-wire, end-wire, Bz and bias currents monitored while switching on all the magnetic fields that made the wire trap.

The distance from this initial wire magnetic trap to the chip surface was (1.8 ± 0.3)mm. The calculated transverse and axial frequencies in this trap were $\sim$ 50Hz and $\sim$ 15Hz, respectively. The calculated limiting trap depth was $\sim$ 7G ($\sim 470\mu$K), with atoms escaping mainly along the axial direction of the trap, while the temperature of the recaptured atoms was $\sim 30 - 60\mu$K after the sub-Doppler cooling stage. For efficient loading to occur, the limiting trap depth should be of the order of 10 times larger than the thermal energy of the atoms [93], or else free evaporation will occur. For this reason, it was very important to obtain the lowest possible MOT temperatures at the end of the sub-Doppler cooling stage in order to maximise the number of atoms loaded into the wire trap.

The wire magnetic trap was optimised by varying the bias field, B_z field and MOT-shim fields in order to match the position, shape and size of the atomic cloud, just after the optical pumping stage, with those after recapture in the wire magnetic trap. When these properties were not ideally matched, an excitation of the atomic cloud would take place during the loading process, resulting in an axial oscillation of the position and width of the cloud in the wire trap. The initial amplitude of these oscillations was of the order of $\sim 800\mu$m, and it could be reduced to $\sim 300\mu$m by applying the appropriate shim fields when

moving the MOT closer to the chip surface. These initial oscillations were damped in a time of $\sim$ 300ms. The number of atoms and optical density of the cloud in the wire trap, obtained by absorption imaging, were maximised by varying the B_z field and MOT-shim fields.

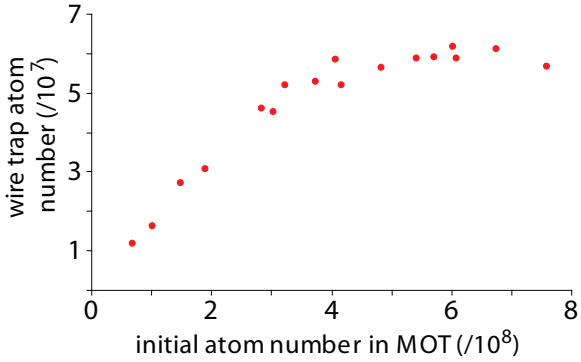

Figure 4.12: Number of atoms loaded in the wire magnetic trap versus initial atom number in the MOT.

The number of atoms recaptured in the wire magnetic trap was around 5×10^7, approximately ten times lower than that of the MOT stage. Increasing the number of atoms in the initial MOT by increasing the dispensing time helped only up to a certain extent. Figure 4.12 shows the number of atoms loaded into the wire trap, measured from absorption images of the cloud after 2ms of release, as a function of the MOT atom number, measured from fluorescence images of the MOT after it was moved close to the surface. We can see that having a MOT atom number larger than around $5 - 6 \times 10^8$ did not help load more atoms into the wire magnetic trap. This was probably due to the fact that large MOTs were not well matched to the shape and size of the wire trap, and had higher temperatures than smaller MOTs, resulting in a less efficient loading of the wire magnetic trap, given its limited depth.

4.4.1 Adiabatic compression of the wire magnetic trap

In order to reduce the temperature of the atoms in the wire magnetic trap through RF evaporation it was necessary to compress the trap for the purpose of achieving the high collision rates required for efficient evaporative cooling (see section 4.4.2). Compression was achieved through an increase in transverse confinement, with the optimum experimental realisation corresponding to ramping up the bias field to a value of 44G in a time of 400ms, while keeping the centre wire (15A), end wires (15A) and B_z coils (3G), the same. This had the effect of moving the trap closer the chip surface, to a distance of $\sim 200\mu$m, where the videotape magnetic field was still too weak to have an influence on the atoms. The calculated transverse frequency in this compressed wire magnetic trap was 460Hz, with the axial trap frequency being 16Hz. The calculated limiting trap depth was 16G (1.1mK) along the axial direction of the trap.

If the compression of the trap is adiabatic, the phase-space density of the atoms in the

trap remains constant. The phase-space density is given by:

$$PSD = n_0 \lambda_{dB}^3 \,, \tag{4.5}$$

where n_0 is the peak-number density and λ_{dB} is the de-Broglie wavelength, given by:

$$n_0 = \frac{N}{(2\pi)^{3/2}\sigma_x\sigma_y\sigma_z} \,, \qquad \lambda_{dB} = \frac{h}{\sqrt{2\pi m k_B T}} \,, \tag{4.6}$$

with $\sigma_{x,y,z}$ being the rms sizes of the cloud, m and T being the mass and temperature of the atoms, respectively, h being Planck's constant and k_B being Boltzmann's constant. Assuming a harmonic potential, we can express $\sigma_i = \sqrt{\frac{k_B T}{m}}\frac{1}{\omega_i}$, with $i = x, y, z$, and assuming that $\omega_x = \omega_y = \omega_r$, we have that the phase-space density varies as:

$$PSD \propto \frac{\omega_r^2 \omega_z}{T^3} \,. \tag{4.7}$$

An adiabatic compression that maintains a constant phase-space density therefore leads to the fact that the final temperature, T_f, after compression of the transverse confinement, scales with the initial temperature, T_i, before compression as:

$$T_f = \left(\frac{\omega_{r,f}}{\omega_{r,i}}\right)^{2/3} T_i \,. \tag{4.8}$$

The temperature of the atoms in the compressed wire magnetic trap, measured through time-of-flight absorption imaging as explained in section 4.2.4, was a few hundred micro-Kelvin. This is consistent with the value of T_f obtained using equation 4.8, for a value of $T_i \simeq 30{-}60\mu$K, corresponding to the temperature of the atoms after sub-Doppler cooling and recapture in the wire magnetic trap, and for a ratio of frequencies $\omega_{r,f}/\omega_{r,i} = 460/50 \simeq 10$, calculated for our experimental conditions.

The estimated number of atoms in the compressed wire magnetic trap was $2 - 4 \times 10^7$. The atom number was typically measured by absorption imaging of the cloud 2ms after release from the trap, using a polarised imaging beam and an imaging field of $\sim$ 1G, for imaging set-up I (see section 3.5.2).

The rms transverse and axial radii of the atomic cloud in this trap were $60 - 80\mu$m and $2 - 2.5$mm, respectively. The total axial length of the cloud could reach values of $6 - 7$mm in the trap, with an aspect ratio of ~ 30. The typical densities in this trap were $\sim 3 \times 10^{11}$atoms/cm^3, and the phase space density was up to 8×10^{-7} at this stage.

In-trap measurement of the temperature of the atoms in the wire-magnetic-trap

Apart from the time-of-flight technique explained in section 4.2.4, the temperature, T, of an atomic cloud confined in a magnetic trap can also be determined from the length of the cloud measured by in-trap absorption imaging. Assuming that the cloud has a Maxwell-

Boltzmann distribution along the z direction of the trap:

$$p(z) \propto \exp(-\frac{U(z)}{k_B T}) \,, \tag{4.9}$$

where $U(z)$ is the potential energy of the atoms in the trap, k_B is the Boltzmann constant and T is the temperature of the atoms, and assuming that the axial potential is harmonic:

$$U(z) \simeq \frac{1}{2} m \omega_z^2 z^2 \,, \tag{4.10}$$

where m is the mass of the atom and $\omega_z = 2\pi f_z$ is the axial trap frequency, we can substitute for $U(z)$ in equation 4.9, and compare the result to a Gaussian distribution of width σ_z:

$$p(z) \propto \exp\left(-\frac{\frac{1}{2} m \omega_z^2 z^2}{k_B T}\right) = \exp\left(-\frac{z^2}{2\sigma_z^2}\right) \,. \tag{4.11}$$

Therefore, we can extract the temperature of the cloud from its axial width using the expression:

$$\frac{1}{2} m (2\pi f_z)^2 \sigma_z^2 = \frac{1}{2} k_B T \,, \tag{4.12}$$

where σ_z is the width of the Gaussian fit of the axial profile of the cloud, obtained by absorption imaging.

Note that this type of measurement only provides an approximate temperature, since the magnetic fields present in the trap modify the absorption of light. In very elongated clouds the atoms can feel magnetic field strengths of the order of up to ~ 10G at the edges of the trap. These large fields lead to Zeeman shifts of the magnetic hyperfine sublevels involved in the imaging transition introducing an effective detuning (1.4MHz/G) of the imaging light with respect to the atomic transition and therefore reducing the absorption of light by the atoms (see section 3.5.2). In this way, the width of a cloud measured from an in-trap absorption image is an underestimate of the real width of the cloud, and therefore the temperature obtained using equation 4.12, is also an underestimate. However, if the atoms are cold enough, the effect of the axial field variation is small and this type of measurement gives a reasonably reliable temperature.

Measurement of the wire-magnetic-trap height

Figure 4.13 shows how the distance from the wire magnetic trap to the chip surface (trap height) decreased when increasing the magnitude of the applied bias field. The height of the trap relates to the bias field magnitude by the previously explained equation 2.7, so that a linear dependence is expected for the trap height as a function of the inverse bias field, as shown by the linear fit in figure 4.13. The trap height was determined by recording an absorption image of the cloud "in-situ" in the wire trap, and measuring the vertical separation between the cloud and its reflection on the absorption image. This separation was equal to twice the trap height (see section 3.5.3, imaging set-up I.), and the uncertainty associated with this measurement was of 1-3pixels, for a pixel size of 6.8μm. We observe different slopes for large and small heights. This is probably due to the effect of the finite

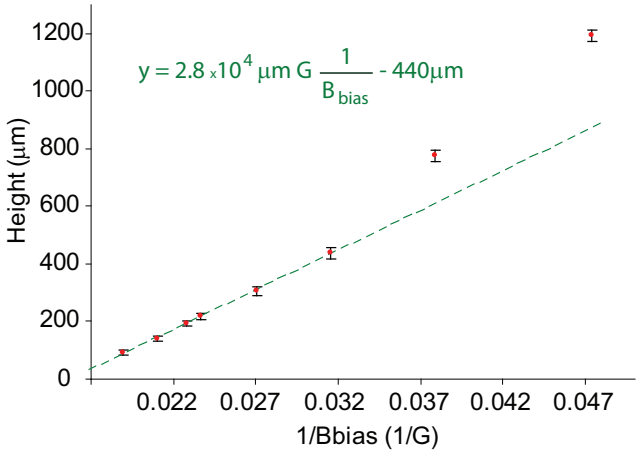

Figure 4.13: Distance from the wire magnetic trap to the chip surface as a function of the inverse of the bias field, measured from absorption images. The centre wire current was 15A and the bias field was varied between 21G and 53G. The dashed line shows a fit to equation 2.7, with the offset corresponding to $-d_c$ and the slope to $\mu_0 I_c/(2\pi)$.

length of the centre wire ($\sim$ 3cm). Another explanation could be the presence of stray fields, opposite to the bias field, and with magnitudes that vary with height (see section 4.6.2).

From the offset of the fit of the data points at low heights, we obtain a value of the distance from the axis of the centre wire to the chip surface equal to $d_c = (440 \pm 20)\mu$m. This value is consistent with the sum of the expected thicknesses of the gold coating, videotape, glass slide, the centre-wire radius, and some extra thickness due to the glue layers (see section 2.2). The slope agrees with the expected value of $\mu_0 I_c/(2\pi)$ within 8%.

Measurement of the axial frequency in the wire magnetic trap

The axial frequency of the oscillations of the atoms in the trap could be measured by inducing an excitation of the atomic motion along the axial direction. Given that the chip surface was not perfectly horizontal but at an angle of $\sim 2.6^\circ$ to the horizontal (see section 2.2), the small component of the force of gravity along the axial direction of the trap meant that it was possible to shift the position of the centre of mass of the cloud along its axis by modifying the frequency of the axial confinement.

A sudden displacement of the position of the cloud away from the centre of the axial potential was used as a way to induce an axial oscillation of the atoms in the trap in order to measure the axial trap frequency. Figure 4.14 shows an example of this type of measurement in which the axial confinement was suddenly tightened by increasing the end-wire current from 5A to 15A, and the oscillations of the centre-of-mass position and width of the cloud were measured via absorption imaging, as a function of the time the atoms where held in the trap. The dipole-mode oscillation of the axial position of the centre of mass of the cloud is expected to occur at a frequency close to the axial trap frequency, while the quadrupole-mode oscillation of the axial width of the cloud should happen at a frequency close to twice

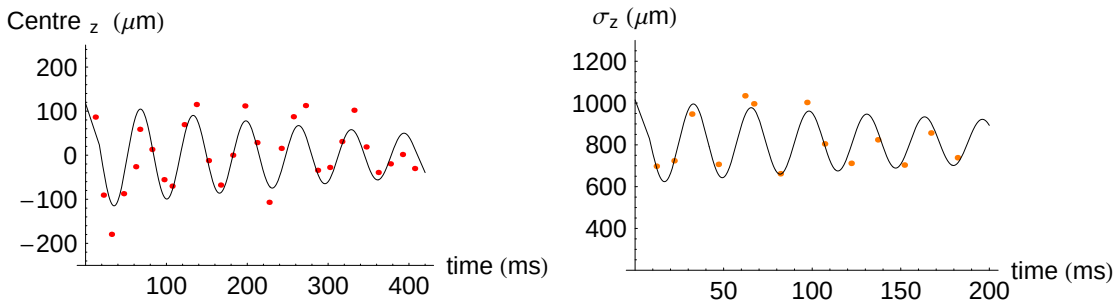

Figure 4.14: Measurement of the axial trap frequency in the wire magnetic trap by exciting the axial motion of the atoms in the trap. **Left**: oscillation of the axial position of the centre of mass of the cloud in the trap after the excitation. The solid line shows a fit to a damped sinusoidal function. The frequency obtained is (15.3 ± 0.3)Hz (see footnote), consistent with the calculated axial trap frequency. **Right**: oscillation of the axial width of the cloud in the trap after the excitation. The fit to a damped sinusoidal function gives a frequency of (30.6 ± 0.5)Hz, consistent with twice the calculated trap frequency.

the axial trap frequency. The obtained frequencies were (15.3 ± 0.3)Hz[1] and (30.6 ± 0.5)Hz[2], respectively, consistent with the expected values.

Removing fringes from the absorption images

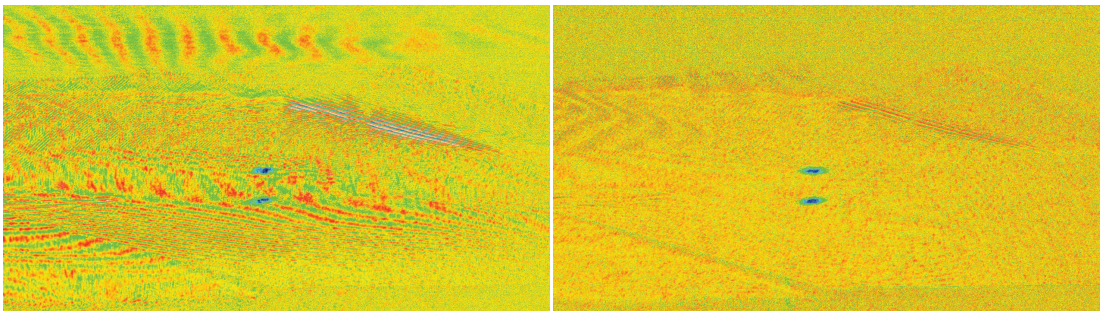

Figure 4.15: Removing fringes in the absorption images. Atoms after 2ms of expansion following release from the compressed wire magnetic trap after evaporation. **Left**: absorption image with many fringes. **Right**: absorption image with hardly any fringes.

As explained in section 3.5.2, each processed absorption image was the result of dividing an absorption image recorded when atoms were present, by a background absorption image recorded with no atoms, and taking the natural logarithm of the result. A time of typically 300ms had to be allowed in the experimental sequence for the software to read out each of these two images after their acquisition. During the time that the centre wire and end wires were on to confine the atoms, heating probably caused either motion or dilation of certain chip components, resulting in changes of the reflectivity of the gold-coated surface of the chip. The first absorption image (with atoms) was usually acquired either with these wires

[1] The data points were fitted to different periodic functions: a damped sinusoidal function, a fourth-order polynomial multiplied by a sinusoidal function and a fourth-order polynomial added to a sinusoidal function. The different functions fitted yielded very similar values for the frequency, with small errors of the order of $\sim 1\%$. The combination of these values and their errors resulted in the frequency values quoted in the text.

[2] Obtained from the fit to a damped sinusoidal function.

on, i.e., in-trap, or a very short time (a few ms) after the wires were turned off to release the atoms. After that, the chip had time to cool down, before the background absorption image was acquired. Therefore, the temperature of the chip was different at the time of the acquisition of each of the two absorption images (with and without atoms). Clear fringes appeared in the processed absorption image, as shown in the example of figure 4.15(left). A current of 15A was run through both the centre wire and the end wires during the 300ms read-out time between the two images in order to heat the chip before the second absorption image to a similar temperature to that during the first absorption image. This was found to solve the problem of fringes in the processed images, in a reproducible way, as shown in the image on the right-hand side of figure 4.15.

4.4.2 RF evaporation

The theory of radio-frequency (RF) evaporative cooling can be found for instance in references [93–96]. Evaporative cooling reduces the temperature of the atoms confined in a trap by forcing the escape of the most energetic atoms (with energies greater than the average energy) from the trap and by making use of re-thermalisation of the remaining atoms through interatomic collisions to redistribute the energies and reach a new equilibrium at a temperature lower than the initial one, with an increased phase-space density.

The mean elastic collision rate of the atoms in the trap, γ_{el}, is given by the following expression:

$$\gamma_{el} = \langle n \rangle \sigma_{el} \langle v_{rel} \rangle \,, \tag{4.13}$$

where $\langle n \rangle$ is the average atom number density, equal to $\langle n \rangle = \frac{n_0}{2\sqrt{2}}$ if we assume a harmonic potential, with the peak density, n_0, given by equation 4.6, and σ_{el} is the elastic scattering cross-section, given by:

$$\sigma_{el} = \frac{8\pi a^2}{1 + k_{dB}^2 a^2} \,, \tag{4.14}$$

where $a = 5.53 \times 10^{-9}$m is the s-wave scattering length of ^{87}Rb [97], $k_{dB} = \frac{2\pi}{\lambda_{dB}}$ and λ_{dB} is the de-Broglie wavelength given in equation 4.6. Finally, $\langle v_{rel} \rangle$ is the average relative velocity between particles, equal to [98]:

$$\langle v_{rel} \rangle = \sqrt{\frac{16 k_B T}{\pi m}} \,, \tag{4.15}$$

where m is the mass of the ^{87}Rb atom, k_B is the Botzmann constant and T is the temperature of the cloud.

Experimentally, evaporation was achieved by applying an RF signal to the RF-antenna wires located underneath the videotape in our atom chip (see section 2.2). The RF field could drive transitions with $\Delta m_F = \pm 1$ between the magnetic sublevels of the $F = 2$ ground state (see figure 4.16), resulting in the loss of atoms from the magnetically trapped sublevel, $5^2S_{1/2}\, F = 2, m_F = +2$, through subsequent transitions to lower m_F states. The spatial variation of the magnetic field in the trap gave rise to position-dependent Zeeman shifts of

the m_F sublevels, as seen in figure 4.16. The RF field, of frequency ν_{rf}, became resonant with the atomic transitions when:

$$h\nu_{rf} = \mu_B g_F B\,, \tag{4.16}$$

where B is the magnetic field strength felt by the atoms at a given position in the trap. Atoms were forced to escape from the trap when their total energy, E, fulfilled the condition:

$$E \geq m_F h\nu_{rf} - E_{bottom}\,, \tag{4.17}$$

where $E_{bottom} = \mu_B g_F m_F B_{z-net}$, B_{z-net} is the net magnetic field strength at the bottom of the trap, and $g_F = 1/2$, $m_F = +2$ for the $F = 2$ hyperfine sublevel we trap (see section 2.3.1).

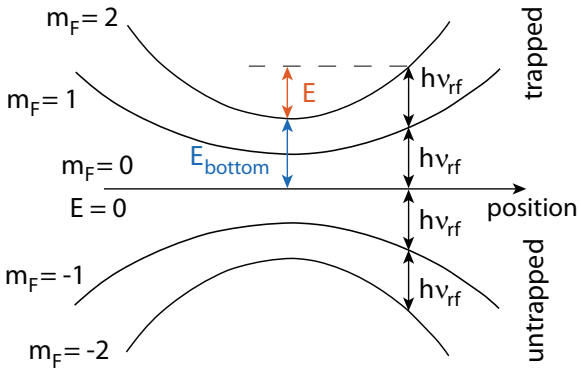

Figure 4.16: Schematic diagram for RF evaporation in our magnetic traps.

The frequency of the RF field was typically lowered in an exponential sweep in order to decrease the effective trap depth and force the hottest atoms to escape. The exponential sweep needed to be fast enough compared to the lifetime of the atoms in the trap but slow enough to allow interatomic collisions to re-thermalise the cloud. A versatile function generator[3] was used for this purpose, which allowed simultaneous control of the frequency and amplitude of the RF signal, for frequencies between DC and 150MHz. The exponential ramps were chosen to have the shape:

$$\nu_{rf}(t) = f_\infty + (f_{start} - f_\infty)\exp\left(-\frac{t}{\tau}\right)\,, \tag{4.18}$$

where τ is the time constant of the exponential sweep, f_{start} is initial frequency of the RF signal and f_∞ is the frequency at $t = \infty$, which was typically chosen close to the bottom of the trap.

Figure 4.17 shows an example of how the magnetic field at the bottom of the trap could be measured. A constant RF signal was applied to the atoms in the trap during a time of 500ms before recording an absorption image, 2ms after releasing the cloud from the trap. The number of atoms remaining in the trap after the RF field was applied was measured for different RF frequencies, as shown in the figure. For high enough frequencies the RF signal

[3]VFG-150, fabricated by the Quantum Optics Group at the University of Siegen, Germany

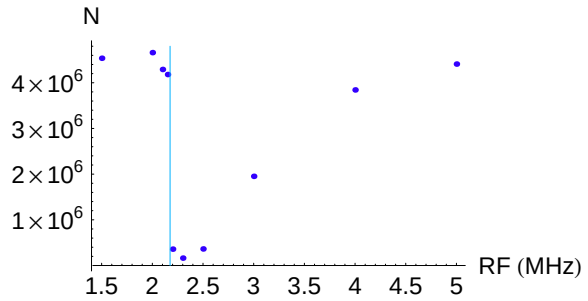

Figure 4.17: Measurement of the bottom field in the compressed wire magnetic trap via RF spectroscopy of the atomic distribution in the trap. The graph shows the atom number, N, as a function of the frequency of a constant RF signal. The vertical line indicates the bottom of the trap at $\nu_{rf-bottom} \sim 2.2$MHz, corresponding to ~ 3.2G.

was not resonant with the atomic transition, but as the RF frequency decreased, more atoms were lost from the trap, until the trap bottom was reached (vertical line in the figure). For frequencies below that, the RF had no effect on the atoms. From equation 4.16 we find that the magnetic field strength at the bottom of the trap is related to the appropriate RF as: $B_{bottom} = h\nu_{rf-bottom}/(g_F\mu_B)$.

A discrepancy of $1-1.5$G was commonly found between the bottom of the trap, measured in this way, and the calculated one. This discrepancy could be explained by the presence of stray magnetic fields that add to the axial fields of the trap (see section 4.6.2).

For efficient cooling and runaway evaporation to occur, the collision rate needs to be much larger than the loss rate of the atoms in the trap, given by the inverse of the lifetime, and this is the reason why the wire magnetic trap needed to be compressed. In this regime, an exponential decrease in atom number and temperature, and an exponential increase in phase space density and collision rate at the centre of the trap are expected.

In a harmonic trap, the rms size of the cloud, σ, is proportional to $\sqrt{T}$, and hence the elastic collision rate varies as $\gamma_{el} \propto N/T$. The phase space density, given by equation 4.5, is the relevant parameter to take into account during evaporative cooling, and it varies as $PSD \propto N/T^3$. As the temperature of the atoms decreases below a critical value of the order of a few hundred nK (for ^{87}Rb), and a phase space density of the order of 1 is reached, a transition into a degenerate Bose-Einstein condensate (BEC) can take place. No experiments with BECs are presented in this thesis. However, reaching temperatures as low as $\sim 1\mu$K was vital for the investigation presented in the following chapters of this thesis, and therefore efficient evaporation had to be implemented.

Figure 4.18 provides an example of a single RF evaporation sweep carried out in the optimised, compressed wire magnetic trap (see figure caption). The measured atom number, temperature, phase space density and elastic collision rate, are presented in a logarithmic scale as a function of time during the sweep. The atom number and temperature decrease close to exponentially, with a temperature of $\sim 1\mu$K reached after 18 seconds of evapora-

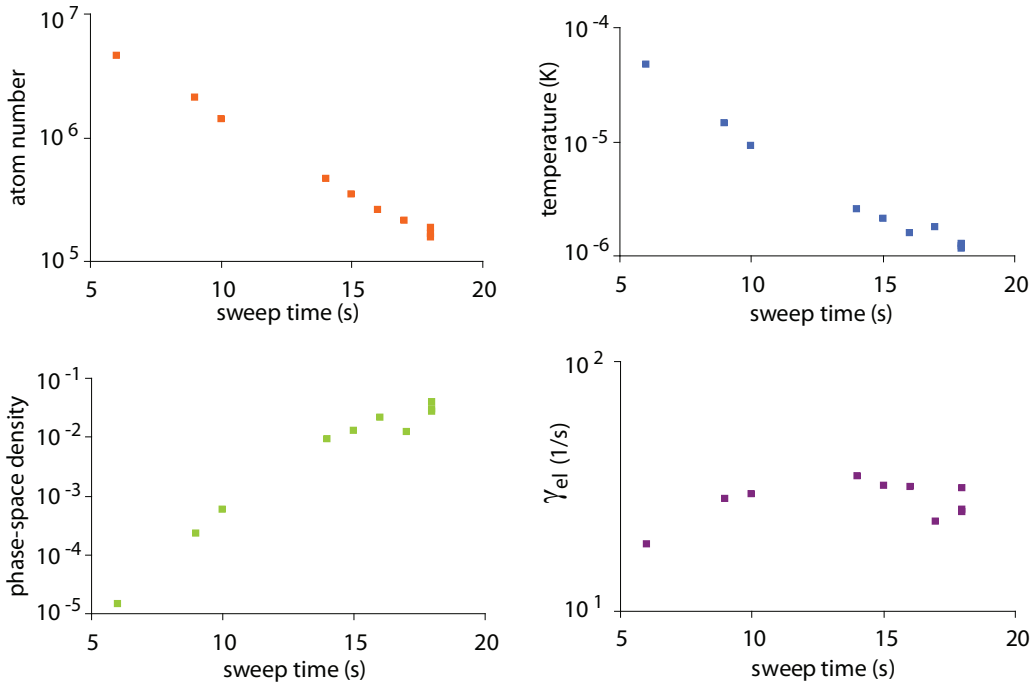

Figure 4.18: Example of RF evaporation measurements in the optimised, compressed wire magnetic trap ($I_c = 15$A, $I_{end} = 15$A, $B_b \simeq 44$G and $B_z \simeq 3$G). Clockwise the graphs show the atom number, temperature, phase space density and elastic collision rate, γ_{el}, as a function of the duration of an RF sweep with $\tau = 3s$, $f_{start} = 30$MHz and $f_\infty = 2.2$MHz. The final RF at the end of the sweep ranged between 5.96MHz for the first point and 2.27MHz for the last point.

tion. The phase space density increases exponentially at the beginning but the evaporation becomes less efficient towards the end of the sweep, where the increase is much slower. Equivalently, the elastic collision rate shows that more efficient cooling takes place at the beginning of the RF sweep than at the end.

The RF-evaporation stage in the compressed wire magnetic trap was experimentally optimised in order to achieve the best possible loading of atoms in the videotape magnetic micro-traps (see section 4.5), trying to maximise the phase-space density of the atomic cloud in each videotape trap while keeping a reasonably large, detectable atom number. This optimised realisation consisted of two RF exponential sweeps, one with $\tau = 3s$, $f_{start} = 30$MHz and $f_\infty = 2$MHz, during a time of 3.4s, for which the final RF was of ~ 11MHz, and a consecutive, second sweep with $\tau = 5s$, $f_{start} = 11$MHz and $f_\infty = 2$MHz, during a time of 5s, for which the final RF was of ~ 5.3MHz.

The ionisation gauge was turned off during data taking, since it generated noise at several radio-frequencies, limiting the lifetime of the atoms in the trap. One of the factors that limited the total duration of the RF sweeps in this trap was the fact that the end wires outgassed when being kept on at 15A during long times, increasing the pressure inside the main chamber substantially and, therefore, the atom-loss rate from the trap.

Figure 4.19 shows an example of three absorption images of atoms in the compressed wire magnetic trap before and after RF evaporation down to final temperatures of approximately

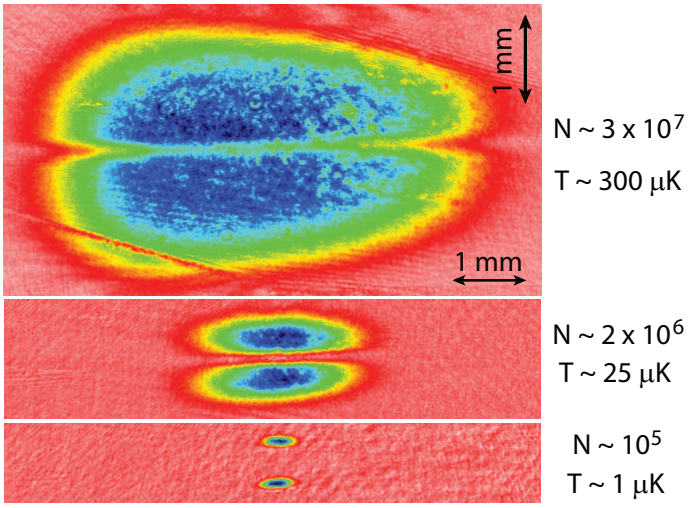

Figure 4.19: Absorption images of the atoms 2ms after release from the compressed wire magnetic trap. **Top**: before RF evaporation. **Middle and bottom**: after RF evaporation. The length scale is the same for all images.

$\sim 300\mu$K, $\sim 25\mu$K and $\sim 1\mu$K, from top to bottom. The images were recorded 2ms after the atoms were released from the trap.

Lifetime in the compressed wire magnetic trap

The lifetime of the atoms in the compressed wire trap was measured to be $\sim$ 7s. The reason for this relatively short lifetime was the escape of the hottest atoms from the trap, due to the fact that the atomic temperature was of the order of a few hundred microKelvin, while the limiting depth of the potential was only of $\sim$ 1.1mK along the z direction. The axial trap depth was limited by the current that could be run through the end wires. Higher currents than 15A resulted in substantial outgassing of the end wires, leading to an unacceptable increase in pressure inside the main vacuum chamber.

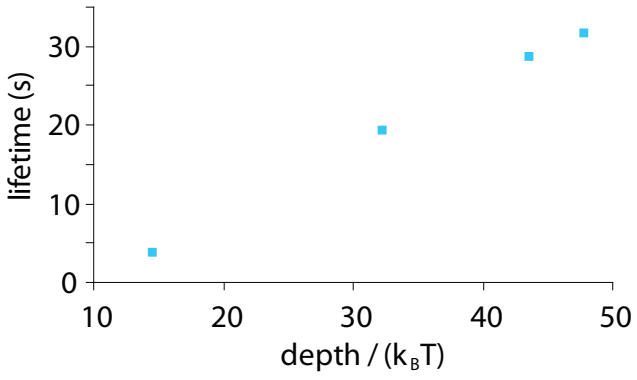

Figure 4.20: Measured lifetime of the atoms in the wire magnetic trap as a function of the ratio of axial trap depth to atomic thermal energy.

Figure 4.20 shows how the measured lifetime depended on the ratio of the axial depth of the wire magnetic trap to the thermal energy of the atoms (k_BT). We observe how the

lifetime in the trap increased with this ratio, reaching values of up to ~ 30s. The trap depth was modified by varying the value of the bias field in order to modify the position, y_w, of the trap centre, since the depth of the axial confinement provided by the end wires depended on this (see figure 2.7). The bias field values were between 32G and 49G, corresponding to values of y_w ranging between 140μm and 450μm. The trap depths were between 0.9mK and 1.2mK in units of temperature, and the minimum magnetic field strength at the bottom of the trap ranged between 1.1G and 6.3G. The temperature of the atoms was reduced via RF evaporation. The data corresponds to atomic temperatures of $25 - 64\mu$K.

4.5 Transfer from the wire trap to the videotape micro-traps

Following the ideas in reference [81], atoms were transferred from the compressed wire magnetic trap into one or several videotape magnetic micro-traps typically in two stages, as shown in figure 4.21, where the ramps for the centre-wire and end-wire currents and for the bias field and B_z field are presented.

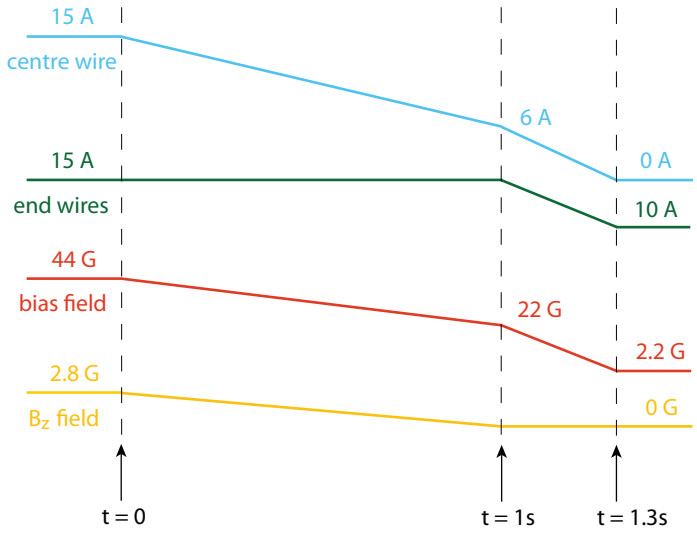

Figure 4.21: Typical currents and magnetic fields for the transfer of atoms from the compressed wire magnetic trap to the videotape magnetic micro-traps.

These stages were optimised experimentally in order to obtain the highest possible phase-space densities at large enough atom numbers in the videotape traps. For the loading of the videotape traps to be efficient the transfer stages had to be slow enough to be adiabatic, given that it was very difficult to maintain constant trap frequencies during the whole transfer process. The end-wire current was decreased from 15A to 10A in order to avoid overheating these wires, since high currents during long times had been seen to result in unwanted outgassing.

Figure 4.22 shows contour plots of the final steps of the transfer, from $t = 0.5$s to $t = 1.3$s of figure 4.21. We see how the magnetic field of the wire trap merges with that of the videotape traps as the wire trap is moved closer to the chip surface by decreasing the current through the centre wire. At the end, when the centre-wire current is zero, the atoms

are confined in magnetic micro-traps created solely by the combination of the videotape field with the bias field.

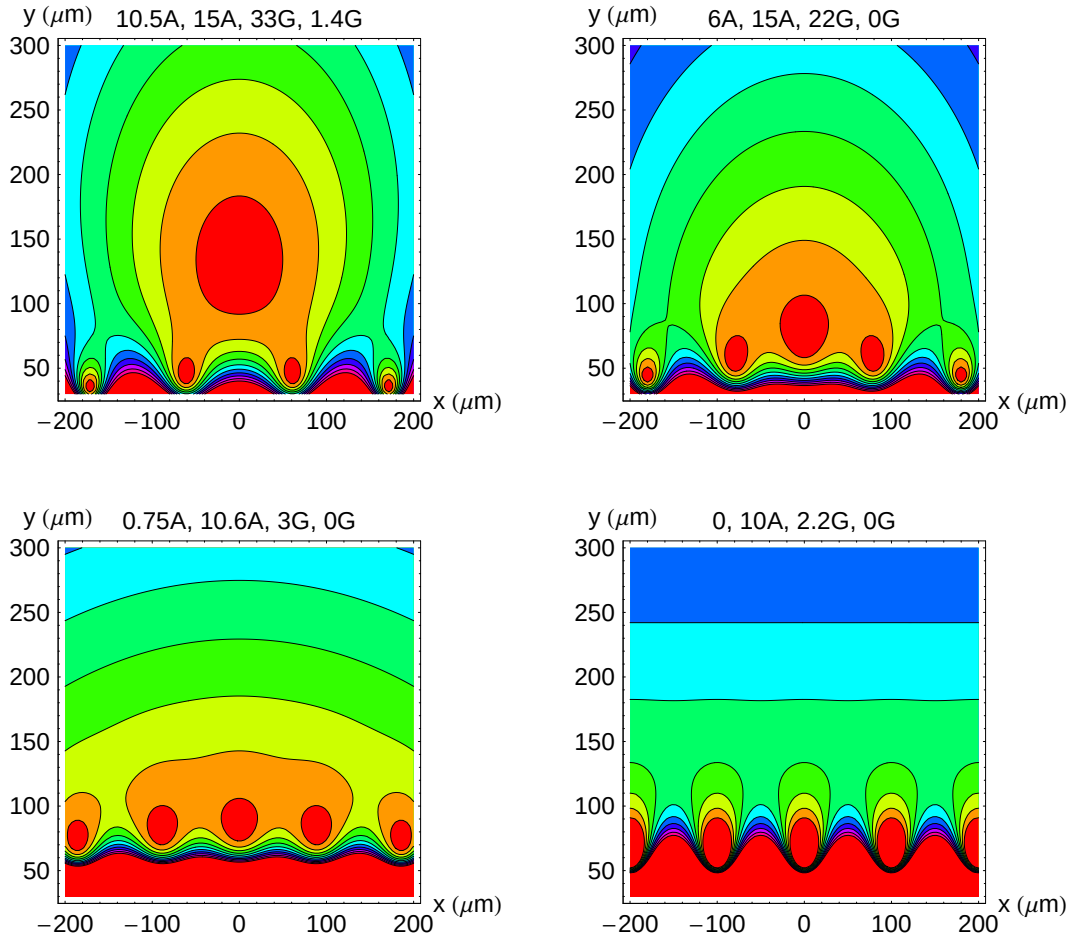

Figure 4.22: Contours of constant magnetic field strength during the final steps of the transfer from the wire magnetic trap to the videotape magnetic micro-traps. The label at the top of each plot indicates the centre-wire current, end-wire current, bias field and B_z field, in this order. Ten magnetic-field contours are shown in each plot, corresponding to magnetic-field ranges of 6-27G, 5-22G, 3-18G and 3-19G, from top to bottom and from left to right.

The measured change in minimum magnetic field strength at the bottom of the trap during the entire transfer process (for the values shown in figure 4.21) was from ~ 3.1G to ~ 1.4G. The calculated frequencies changed from ~ 460Hz to ~ 890Hz, and from ~ 16Hz to ~ 13Hz along the radial and axial directions of the trap, respectively. Calculations show that the limiting trap depth decreased from ~ 16G (~ 1mK) to $2-3$G ($\sim 170\mu$K). The calculated position of the compressed wire magnetic trap was $y_w \sim 200\mu$m, while that of the final videotape traps was $y_w \sim 70\mu$m.

The number of videotape micro-traps loaded depended on the size of the atomic cloud in the compressed wire magnetic trap, and therefore on the temperature of the atoms in that trap. Figure 4.23 shows a sequence of absorption images of atoms loaded in either one videotape trap or an array of 2 to 5 videotape traps, depending on how low the final RF frequency was in the compressed wire magnetic trap. These are in-trap absorption images,

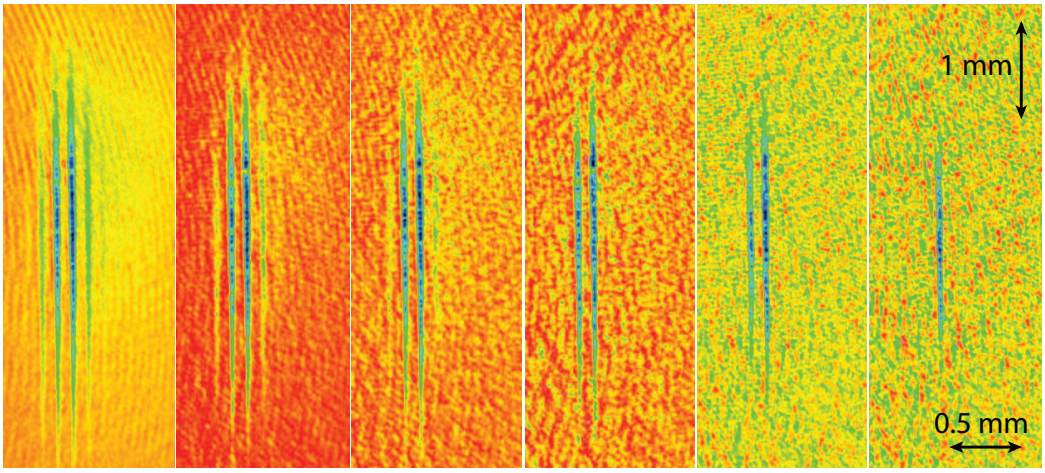

Figure 4.23: Absorption images of the loading of atoms into one or several videotape traps. The final RF of the evaporation in the compressed wire magnetic trap decreases from left to right. The length scale is the same for all images.

acquired using imaging set-up II, as described in section 3.5.3. From left to right, the final frequency of the RF-evaporation sweep in the compressed wire magnetic trap ranged from 8MHz to 2.5MHz, the temperature of the best-loaded videotape trap varied from $\sim 50\mu$K to $\sim 10\mu$K and the atom number in that trap changed from $\sim 8 \times 10^5$ to $\sim 2 \times 10^5$. Therefore, it was possible to control the number of microscopic videotape traps that we loaded by controlling the temperature of the atoms in the compressed wire magnetic trap before loading.

4.6 Videotape magnetic micro-traps

The experimental procedures described in the previous sections for the measurement of atomic properties in a trap were also valid for the videotape magnetic traps. The fluctuations in initial atom number were kept to a minimum following the ideas described in section 4.2.2. The atomic temperatures were measured either in-trap or by time-of-flight absorption imaging, as explained in section 4.2.4. The atom-surface separation was obtained from the distance between the cloud and its reflection in in-trap absorption images, as mentioned in section 3.5.2. The measurement of the axial trap frequency in the videotape traps was performed as described in section 4.4.1 for the wire magnetic trap, and the way in which the transverse oscillation frequencies of the atoms in the videotape traps were measured will be described in detail in chapter 5. Estimates of the minimum magnetic field at the bottom of the videotape traps were typically obtained using a constant RF signal, and RF studies were carried out in the videotape magnetic traps following the ideas presented in section 4.4.2.

The third image starting from the left of figure 4.23 corresponds to the typical loading employed for many of the experiments described in the following chapters of this thesis. The atom number per videotape trap was $7 - 8 \times 10^5$ atoms and the temperature of the atoms in these traps was $\sim 40\mu$K. The rms sizes of the atomic cloud in one videotape trap were $\sim 10\mu$m and $\sim 750\mu$m along the transverse and axial directions, respectively,

resulting in an aspect ratio of around 75. The atom number density in these traps was $\sim 6 \times 10^{11}$atoms/cm^3, and the phase space density was approximately 2×10^{-5}.

The videotape magnetic traps could be simultaneously compressed along their transverse direction and moved closer to the chip surface by increasing the applied uniform bias field. Transverse trap frequencies as high as 15kHz could be achieved using bias fields of up to 40G, reaching aspect ratios of up to 1000. The typical atom-surface separation during experiments with atoms in videotape magnetic traps ranged between 30μm and 110μm.

RF evaporation was also implemented in the videotape traps and temperatures down to $\sim$ 500nK could be reached, very close to the BEC transition.

The lifetime of the atoms in the videotape traps was measured after RF evaporation down to $\sim$ 15μK. The lifetime was estimated to be larger than 30s and possibly up to around 80s, with the large error of this estimate coming from the fact that the atoms could only be kept confined in the videotape traps with the end wires on at 10A for up to around 25s before the end wires started to heat up and outgas. This hold time was not enough to measure the exponential decay of the number of atoms in the trap, and therefore there was a large error in the estimate of the lifetime of the atoms in these traps, which was consistent with the loss due to collisions with the background gas inside the chamber at the typical pressure of 10^{-11}Torr.

4.6.1 Cancelling stray fields to release atoms from the videotape traps

An atomic cloud released from a videotape magnetic trap by switching off all non-permanent magnetic fields, was expected to fall under gravity and expand at a rate determined by the distribution of atomic velocities in the trap, enabling time-of-flight measurements (see section 4.2.4) and providing useful information about the properties of the cloud in the trap. In fact, in the case of our videotape chip, atoms should have not only fallen under gravity but also been pushed away by the field gradient of the videotape, since the permanent magnetisation of the videotape could not be switched off.

When trying to release very cold atoms from videotape traps, we found that, while a few atoms were released from the trap, most of them were re-trapped in a magnetic trap formed by the combination of the videotape field with a stray magnetic field present in the trapping region inside the chamber (see section 4.6.2). The presence of this stray field prevented the atoms from falling freely under gravity after release, making all time-of-flight measurements difficult.

Figure 4.24**(a)** shows a cold-atom cloud 7ms after release from a videotape trap by switching all fields off. We see a few released atoms falling in a more extended and diffuse cloud, and some atoms re-trapped in the central region of the image. Figure 4.24**(b)** shows an absorption image of atoms loaded directly into a videotape magnetic trap formed by the videotape field and the stray field that acted as bias field. All other magnetic fields were off: the bias field, the B_z field, the imaging field and the end-wire field. The absence of axial confinement resulted in the very elongated trap that we see in the image.

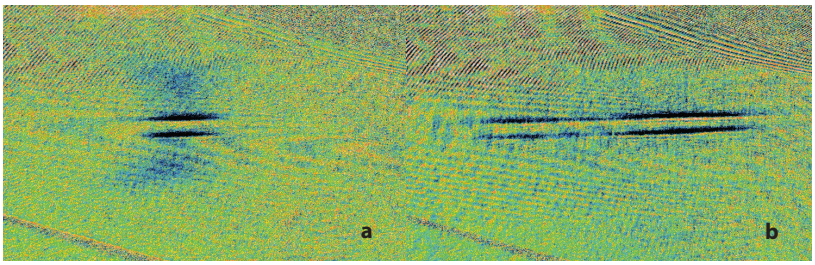

Figure 4.24: **(a)** Absorption image of a videotape trap 7ms after switching off all non-permanent magnetic fields. Atoms were re-trapped by the stray field plus videotape field. **(b)** Absorption image of a magnetic trap formed by the magnetic field of the videotape together with a stray magnetic field present inside the vacuum chamber. The absorption images were acquired using imaging set-up I (see section 3.5.3). No imaging quantisation field was applied during the acquisition (for both **(a)** and **(b)**).

In order to prevent the atoms from becoming re-trapped after release from the videotape trap, a small current ($\sim$ 0.5A) was run through the centre wire with the aim of pushing the atoms away from the re-trapping region. This helped release most of the atoms but distorted the shape of the released cloud, causing its length to oscillate in time. Most probably, the atomic cloud felt the influence of the re-trapping region as it was pushed away from the chip surface, and this induced an oscillation in the cloud's length. This effect would have provided false information in time-of-flight temperature measurements, and therefore needed to be avoided.

Another idea was to measure the magnitude of the x and y components of the stray field responsible for re-trapping the released atoms, in order to cancel them out using the field generated by the two pairs of bias coils. The distance from the videotape trap to the chip surface was studied as a function of the applied bias field for this purpose, first for bias fields applied in the x direction (B_{b-x}) and then for bias fields applied in the y direction (B_{b-y}).

We recall at this point that when a bias field, B_b, with components in the x-y plane, is applied, a videotape trap forms at a distance from the chip surface given by the following expression (see section 2.3.6):

$$y_0 \simeq \frac{\lambda}{2\pi} \ln\left(\frac{B_1}{|\vec{B}_b|}\right). \tag{4.19}$$

Following from this equation and assuming that the total field on the x-y plane was the sum of the applied bias field ($B_{b-x}\hat{\mathbf{x}}$ or $B_{b-y}\hat{\mathbf{y}}$) and the stray field ($Stray_x\hat{\mathbf{x}} + Stray_y\hat{\mathbf{y}}$) we can substitute $|\vec{B}_b|$ by the modulus of the total field and write:

$$y_0 \simeq \frac{\lambda}{2\pi} \ln\left(\frac{B_1}{\sqrt{(B_{b-x} + Stray_x)^2 + Stray_y^2}}\right), \tag{4.20}$$

$$y_0 \simeq \frac{\lambda}{2\pi} \ln\left(\frac{B_1}{\sqrt{Stray_x^2 + (B_{b-y} + Stray_y)^2}}\right), \tag{4.21}$$

for the cases in which the applied bias field was $B_{b-x}\hat{\mathbf{x}}$ and $B_{b-y}\hat{\mathbf{y}}$, respectively.

A videotape trap was loaded initially using a bias field, B_{b-x}, of 2.2G, a B_z of 1.1G and a current of 10A through the end wires. The B_z field and end-wire current were switched off in 5ms, while B_{b-x} was ramped to a given final value. All magnetic fields were held at these values for 2 more milliseconds and during the acquisition of absorption images. Repeating this sequence several times varying the final value of B_{b-x}, and measuring the atom-surface separation, y_0, for each value, yielded the graph in figure 4.25(a) (data points). A similar plot was obtained for final bias fields along the y direction, with the result shown in figure 4.25(b) (data points).

The experimental data points were fitted to the functions in equations 4.20 and 4.21 in order to measure the value of the stray fields, $Stray_x$ and $Stray_y$. Note that these equations turn into exact equalities when the field from the end wires is removed (see section 2.3.6). The fit parameters were λ, $Stray_x$ and $Stray_y$, and the fit results were rather sensitive to the value of λ. From the best fits, we obtained the following values for $Stray_x$ and $Stray_y$:

$$Stray_x \simeq (0.35 \pm 0.02)\text{G} \tag{4.22}$$

$$Stray_y \simeq (0.48 \pm 0.02)\text{G} \tag{4.23}$$

The fits shown in figure 4.25 (solid lines) correspond to $Stray_x = 0.35$G and $Stray_y = 0.48$G, and to $B_1 = 110$G and $\lambda = 122\mu$m. This value of λ was larger than the expected one of $\lambda \simeq 106\mu$m. This could be explained by an imaging magnification factor slightly larger than unity in imaging "set-up I".

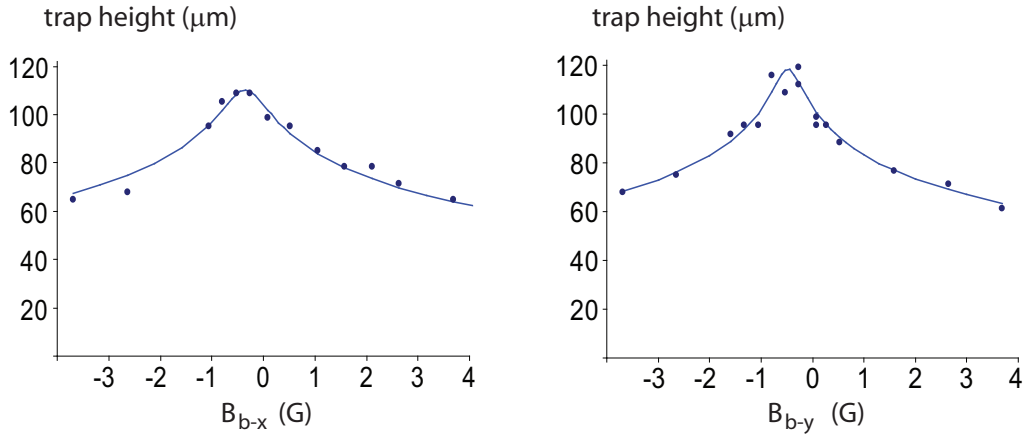

Figure 4.25: Distance from the videotape trap to the chip surface as a function of the applied bias field magnitude in Gauss. The dots correspond to experimental data and the solid lines to fits to equations 4.20 and 4.21. **Left**: for an applied bias field in the x direction. **Right**: for an applied bias field in the y direction.

Following these results, and in order to release the atoms from a videotape trap without re-trapping, a correcting bias field with x and y components equal to $B_{b-x} = -0.35$G and $B_{b-y} = -0.48$G, respectively, was turned on as soon as all other fields were switched off to release the atoms. A release sequence corrected in this way is shown in figure 4.26, for times of flight ranging from 4 to 8ms. We can see how the atoms are no longer re-trapped after

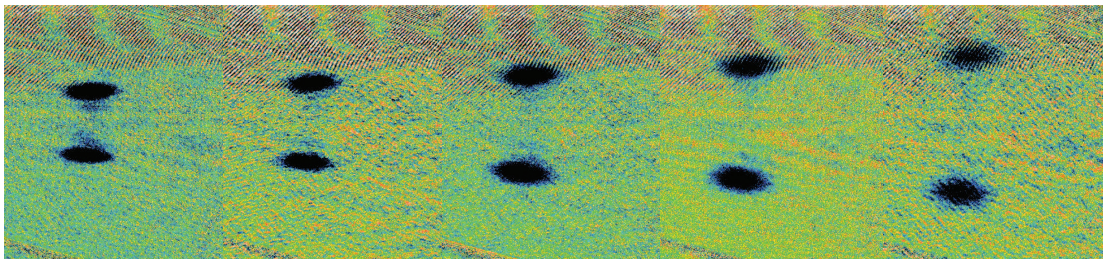

Figure 4.26: Time of flight sequence of atoms released from a videotape magnetic trap. The appropriate bias field is used to correct for the presence of stray magnetic fields and allow the atoms to be properly released. Release times from left to right are 4, 5, 6, 7 and 8ms. An imaging field of 1G was applied during the acquisition of these absorption images. The temperature obtained for the atoms from the time-of-flight measurement was $\sim 5\mu$K.

release and how the cloud expands and falls under gravity. The atoms in this videotape trap were previously cooled down to about 5μK during 1.5s of RF evaporation in the trap.

4.6.2 Origin of the stray magnetic fields present in the trapping region

Stray magnetic fields with components in all three directions of space were known to be present in the trapping region inside the chamber. We distinguish here between permanent stray magnetic fields, generated by magnetised material or equipment that needed to be always on during data taking, and stray magnetic fields present only when current was running through certain chip wires.

The x and y components of the permanent stray magnetic fields were determined in the previous section, 4.6.1. These fields could have been created by the equipment surrounding the main chamber, such as the ion pump, which might have been not properly shielded, or by the ion gauge. As for the materials inside the vacuum chamber, later on we discovered that the stainless-steel block that formed the base of the videotape-atom chip, which had holes on its surface, and groves with sharp corners to house the chip wires (see section 2.2), generated magnetic fields close to its surface. Fields of up to a few Gauss, along the y direction, were measured with a sensitive Hall probe at distances of $\sim$ 1mm from the surface of the steel block. These fields can be explained by the fact that non-magnetic, stainless steel can become magnetic through certain machining procedures, such as those employed to create the channels to house the chip wires on the steel base. Some of the stainless-steel screws and nuts used to make the electrical connections to the chip wires were also found to be magnetic, with fields of up to a few Gauss measured in their proximity with the Hall probe.

The Earth's magnetic field ($\sim$ 0.5G) should have components along both the y and z directions, possibly with a small component along x, given the orientation of the optical table in the laboratory and London's latitude (51° North). The presence of steel in the structure of the building can introduce variations in the magnitude and direction of the magnetic field present in the laboratory with respect to the expected Earth's magnetic field.

In addition to these permanent, stray magnetic fields, other stray fields of the same

order of magnitude where found to be present in the trapping area when current was running through the end wires. These are thought to be generated by the piece of wire that connected both end wires together inside the chamber (see section 2.2).

Stray fields directed along the z direction and depending on end-wire current and atom-surface separation, would explain the observed discrepancy between calculated and measured magnetic fields at the bottom of the magnetic traps (see section 4.4.2). They could also be a possible explanation for the large axial-potential inhomogeneities observed when transporting atoms to different locations across the chip surface, and described in chapter 7.

A stray magnetic field of ~ 1G along the x direction was also found from a calibration of the magnetic field generated by the bias coils, obtained using ultra-cold atoms in videotape traps, as detailed in chapter 5.

4.7 A disaster

On the 14^{th} of March of 2007, a disaster occurred in the experiment when we were in the middle of a period of very productive data taking, at a time when the videotape-atom-chip experiment was at the peak of its performance and starting to produce results after having gone through severe realignment and optimisation during more than two years.

A high current stayed on in the centre wire at the end of one realisation of the experimental sequence, instead of being switched off as usual by the computer control at the end of the sequence. The high current stayed on possibly for some minutes, causing the centre wire to break, the glass coverslip to crack and the videotape and gold coating to tear and break as shown in the photograph in figure 4.27. The most probable cause for the accident was a problem with the software that controlled the experimental sequence, which failed to switch the current off at the time it was programmed to do so.

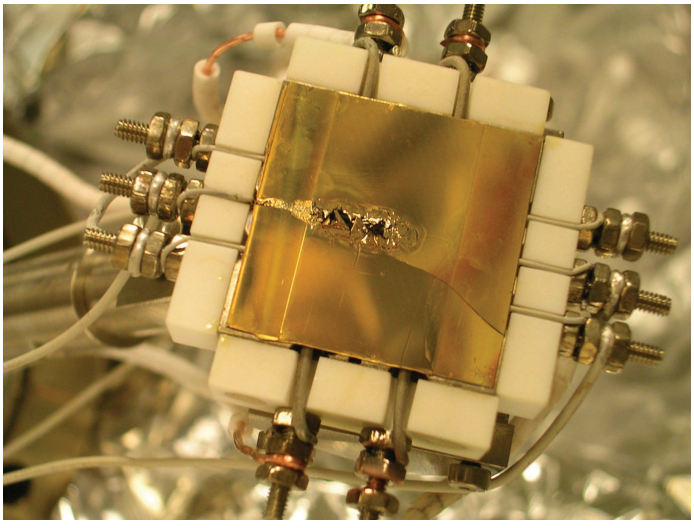

Figure 4.27: Destroyed videotape atom chip.

Building safety features to avoid high currents staying on at the end of an experimental

sequence or longer than a given time, would be a very recommendable step to take when building a future experiment.

The videotape chip was declared useless after some careful diagnosis, and a new, simpler chip was built with the idea of integrating optical fibres for on-chip detection of low atom numbers (refer to section 8.2).

The chapters that follow present several studies based on experiments carried out with cold atoms confined in videotape magnetic micro-traps. A more detailed knowledge of the properties of our videotape traps was gained through these studies. Chapter 5 describes the measurement of the frequency of the transverse oscillations of the atoms in the videotape traps by shaking the position of the trap centre to excite the transverse motion of the atoms in the trap. Interesting aspects of the atomic dynamics were revealed by these measurements. Chapter 6 is dedicated to fragmentation studies in the videotape traps, and chapter 7 describes the transport of cold atoms over distances of up to seven millimetres while confined in videotape magnetic traps.

Chapter 5

Shaking-induced dynamics of cold atoms in videotape traps

5.1 Introduction

This chapter describes an experiment in which a cold thermal cloud of rubidium atoms confined in a videotape trap was excited by shaking the position of the centre of the trapping potential, mainly along the direction perpendicular to the long axis of the cloud. The experimental procedure is described here and results for the measured temperature as a function of the excitation frequency are presented for seven different values of the bias field. The aim of these measurements was to determine the transverse oscillation frequencies of the atoms in these traps. A detailed characterisation of the properties of the confining potential, such as anharmonicity, that influenced the values of these frequencies is presented here. A simulation was carried out leading to results that closely reproduced our measurements, as well as allowing us to study the dynamics of the cold atoms in our videotape traps. This simulation helped us interpret our measurements and allowed us to obtain precise estimates of the transverse oscillation frequencies of the atoms in these traps.

5.2 The experiment

5.2.1 Principles of the experiment

It is possible to determine the oscillation frequencies of atoms in a magnetic trap by exciting their motion via some perturbation. If the centre of the confining potential is suddenly displaced to one side, a dipole-mode collective excitation takes place, resulting in an oscillation of the centre of mass of the cloud at the trap frequency. On the other hand, if the trapping potential is suddenly compressed or decompressed, a quadrupole-mode collective excitation takes place resulting in an oscillation of the width of the cloud at twice the final trap frequency (for independent particles). In this type of experiment, the centre of mass position and width of the atomic cloud can be measured as a function of time, over several oscillation cycles, in order to determine the trap frequencies (see section 4.4.1).

In the case of our elongated videotape traps, measurements of the position and width of the atomic cloud to determine the trapping frequencies were possible only for excitations

along the longitudinal direction of the trap (see [65, 66]). Accurate measurements became impossible along the transverse direction of the trap due to the high trapping frequencies (of the order of kHz): the transverse oscillation amplitude and size of the cloud lay below the resolution of our imaging system and were hence too low to be measured through the absorption imaging technique described in section 3.5.2. For this reason, the transverse trap frequency had to be determined by means of a different procedure.

Resonant heating can be induced when atoms are excited by shaking the centre of the trapping potential at a frequency close to the trap frequency. Measurements of the temperature of the atoms as a function of the excitation frequency can therefore be used to determine the transverse trap frequency [65]. A transverse excitation was induced in our videotape traps and the increase in temperature during the resonance was detected as an increase in the axial length of the trapped cloud, observed through absorption imaging. This was possible because the energy absorbed by the resonantly excited transverse degrees of freedom could be transferred to the axial degree of freedom through elastic collisions between the atoms in the cloud, during and after the excitation.

5.2.2 Experimental details

In our elongated videotape magnetic traps the transverse confining magnetic field came from the sum of the videotape field and the external bias field (see section 2.3.6), both in the x-y plane, with x and y being the horizontal and vertical directions respectively. The position of the centre of the trap in that plane depended on the magnitude and direction of the applied bias field and could therefore be modulated by modulating the bias field. In this way we were able to shake transversely the magnetic-trap centre in order to resonantly excite and heat our atoms. In the absence of shaking, the bias field was purely along the x direction and the trap centre position could be expressed as $(x_0, y_0, z_0) \simeq (0, \frac{1}{k}\ln(\frac{B_1}{B_b}), 0)$, neglecting the contribution of the end wires, where $k = \frac{2\pi}{\lambda}$, λ is the period of the videotape magnetisation, B_b is the bias field and B_1 is the strength of the videotape magnetic field at the chip surface (see section 2.3.6). When the shaking was introduced, the minimum of the magnetic field modulus was displaced, resulting in a time dependent trap centre position, $(x_0 + \Delta x(t), y_0 + \Delta y(t), z_0 + \Delta z(t))$, as detailed in the following section.

The bias field was made by two pairs of external coils wired in Helmholtz configuration, one pair along the $\hat{\mathbf{x}}+\hat{\mathbf{y}}$ direction and the other along $\hat{\mathbf{x}}-\hat{\mathbf{y}}$ (see figure 3.2 in section 3.2.2). A small sinusoidal amplitude modulation of frequency Ω was superimposed on the field created by one of these pairs of coils in order to transversely shake the trap. A $50\mathrm{mV}_{pp}$ modulation was provided by a DS345 Stanford function generator and added to the computer control voltage signal using a summing op-amp. The resulting voltage signal was fed into the FET control circuit of one of the two pairs of bias coils.

The results of the experiments detailed in this chapter actually led to a calibration for the bias field as a function of the computer control voltage, V_c: $B_b(G) \approx 1G + 4.95V_c$, with V_c in Volts. The way this was obtained will be explained later on. The bias field was proportional to V_c, as expected, but an offset was found due to the presence of stray magnetic

fields in the trapping region (see section 4.6.2). The 0.025V amplitude modulation of the voltage produced a modulation amplitude of ~ 0.125G on the bias field of one of the coil pairs. We define the relative amplitude of the bias field modulation as $depth = \frac{0.025\text{V}}{V_c(\text{V})}$.

The total bias field was modulated both in magnitude and direction, leading to an oscillating displacement of the trap centre in space. The effect of the transverse displacement was dominant compared to that of the axial displacement, as we will see in section 5.3.2.

A calculated example that reproduces some particular experimental conditions and gives an idea of the magnitude of the perturbation caused by the bias field modulation shows that, for a bias field of 3.48G modulated with $depth = 0.05$, the trap centre oscillates with a displacement amplitude of $\sim 0.42\mu$m in the x and y directions, and of $\sim 0.58\mu$m in the z direction. These displacements will be explained in detail in section 5.3.2. An 8.3μK cloud in such trap would have an initial spatial distribution with standard deviations of approximately 2.3μm, 3.6μm, and 231μm in the x, y and z directions of the trap, respectively (see table 5.1). This example shows that the displacements produced by the bias field modulation are at least 5 times smaller than the rms sizes of the cloud in the videotape trap.

A experimental sequence similar to that described in chapter 4 was used to produce cold atoms in videotape traps. Atoms were loaded into a videotape trap with a bias field of 3.5G, an end-wire current of 15A and no B_z field, and then evaporated to a temperature of around 10μK. The cold cloud was then adiabatically compressed during 3s in order to reach the final videotape trap parameters at which the shaking was performed. These corresponded to an end wire current of 15A, a final horizontal bias field between 3.5 and 31G and a B_z field of 2.2G.

The atoms were excited by shaking the final videotape trap during 5s by means of a superimposed bias field modulation, as mentioned before. After that, they were either held in the same videotape trap in which the excitation took place, or adiabatically moved back to the initial 3.5G bias field videotape trap, during 3s. An in-trap absorption image was finally recorded during an exposure time of 150μs, using the CCD camera with a pixel size of 9μm, in an imaging set-up very similar to "set-up I", described in section 3.5.3. The spatial resolution of the imaging system was determined by the pixel size.

The shaking experiment was performed for seven different values of the bias field. For the four lowest bias fields, the trapped atoms were far enough from the chip surface for the cloud and its reflection to be clearly resolved in the absorption images. However, this was not the case for the three highest bias fields, since the videotape traps were very close to the chip surface. For this reason, at the end of the shaking, the atoms were moved away from the chip surface and ramped back over 3s to a videotape trap with a lower bias field of 3.5G, where clearer images could be obtained.

The cloud temperature, T, was determined from the cloud length in the recorded in-trap absorption images using equation 4.12, as explained in section 4.4.1. The measured value, equal to 15Hz, of the axial trap frequency corresponding to an end-wire current of 15A was used.

The effect of gravity has been neglected throughout this chapter.

5.2.3 Experimental results

Figure 5.1 shows the measured temperature of the cloud after the excitation, as a function of the frequency of modulation of the bias field, Ω. Each data set corresponds to a different value of the bias field, onto which the modulation was superimposed, and shows a resonance taking place as the excitation frequency approaches the transverse trap frequency. The resonance is revealed as an increase in cloud temperature. Note that during the shaking, not only did the position of the trap centre oscillate, but there was also a small modulation of the transverse trapping frequency, known as parametric resonance (see future section 5.3.3). The effect of this is larger when the excitation frequency is close to twice the value of the trap frequency, and this is why, for $B_b = 3.48$G, we see a smaller, second resonant peak at a frequency close to twice the frequency of the first resonant peak. For higher values of the bias field only the first resonant peak was measured.

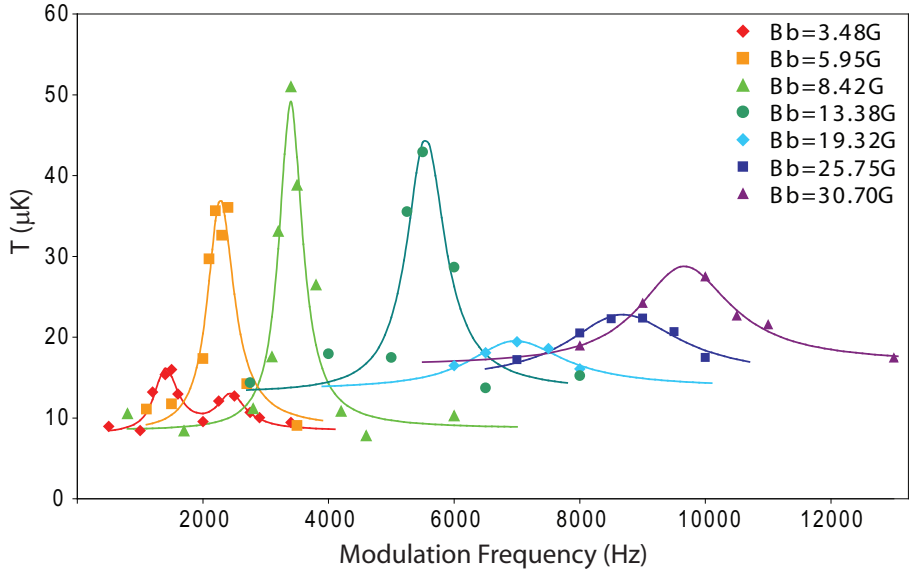

Figure 5.1: Measured atomic cloud temperature after excitation for seven different bias fields, B_b. The solid lines are Lorentzian fits to the experimental data points.

The solid lines in figure 5.1 show the fits of the experimental data points to a sum of two Lorentzians using the expression $T(f) = T_{offset} + \frac{A \cdot W}{W^2 + (f - \frac{f_0^2}{f})^2} + \frac{B \cdot W'}{W'^2 + (f - \frac{(2f_0)^2}{f})^2}$, where $f = \frac{\Omega}{2\pi}$ is the excitation frequency, f_0 corresponds to the central frequency of the first resonant peak, T_{offset} corresponds to the initial temperature before the shaking started, and W is the frequency width (FWHM) of the resonant peak. The reason why a Lorentzian was chosen to fit the data will be explained in section 5.3.1. The central frequencies of the peaks should correspond to the transverse trap frequencies and increase with increasing bias fields. However, this increase is not linear as we would expect if we consider the harmonic approximation of the trapping potential (see section 2.3.6, equation 2.31). Instead, the transverse trap frequencies, f_0, obtained from the resonant peaks for each bias field, lie below the calculated harmonic ones, as shown in figure 5.2 [65]. The harmonic frequencies

were calculated from the second order coefficients of the Taylor expansion of the full potential (including the end-wire field) around the centre of the trap, in terms of x and y. The plotted harmonic frequency is an average of the calculated harmonic frequencies of oscillation along the x and y directions.

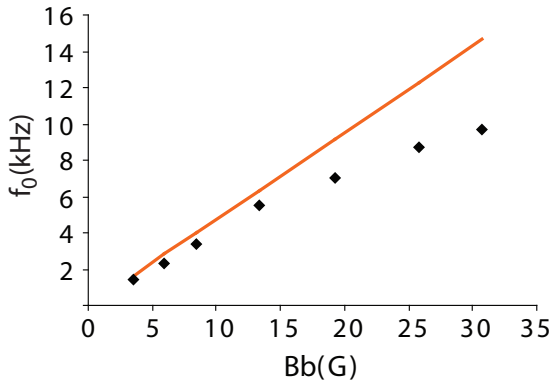

Figure 5.2: Data points: transverse videotape trap frequencies obtained from the centre of the measured resonant peaks, versus bias field. Solid line: transverse frequency versus bias field, calculated assuming a harmonic videotape trapping potential.

The transverse confining potential is harmonic only in a very limited region around the centre of the trap. Very cold atoms lie within the extent of the harmonic region of the potential and oscillate with frequencies close to the harmonic one. Hotter atoms oscillate with larger amplitudes, exploring regions further away from the centre of the potential. In these regions the curvature of the potential is lower than that of a harmonic potential and hence the atoms oscillate with frequencies below the harmonic ones. The radial frequency of oscillation of each atom depends on its oscillation amplitude, and therefore on its energy. For a given initial distribution of energies in the videotape trap there is a corresponding range of oscillation frequencies, as opposed to the case of a harmonic potential in which all atoms oscillate with the same frequency, regardless of their energy. The transverse frequencies also decrease as we move along the length of the cloud from $z = 0$ to $|z| > 0$, as we will see in section 5.3.2. This fact, together with the anharmonicity of the potential causes the centre of the resonance, f_0, to shift towards a frequency below the harmonic one. Additionally, the frequency width of the resonance increases due to the fact that the atoms oscillate with a range of different frequencies in the trap. The measured widths (FWHM) of the experimental resonant peaks, obtained from the Lorentzian fits to the data shown in figure 5.1, were: ∼455Hz, ∼505Hz, ∼449Hz, ∼740Hz, ∼1858Hz, ∼2183Hz and 1783Hz, in order of increasing bias field.

More detailed information about the consequences of the anharmonicity of the potential and the decrease in transverse oscillation frequency along the axis of the cloud, away from the trap centre, will be provided in the following section.

5.3 Description of the trapping potential and the effect of modulating the bias field

This section shows the effect that the bias field modulation has on the videotape trapping potential, which consists mainly of a periodic shaking of the trap centre position. The consequences of the anharmonicity of the trap and of the change in transverse trap frequency along the axis of the cloud are highlighted here, and the contribution of parametric resonance during the trap shaking is considered.

5.3.1 Simplified one-dimensional approach

For the moment, we will consider the simplified approach of a particle of mass m in a one-dimensional harmonic potential of natural frequency ω_0, where x is our only coordinate. If the equilibrium position of this potential, $x = 0$, is modulated in time with frequency Ω and amplitude A, the one-dimensional Lagrangian of the system is given by:

$$L = T - U = \frac{1}{2}m\dot{x}^2 - \frac{1}{2}m\omega_0^2(x - A\cos\Omega t)^2. \tag{5.1}$$

Using Lagrange's equations: $\frac{d}{dt}\left(\frac{\partial L}{\partial \dot{x}}\right) - \frac{\partial L}{\partial x} = -m\gamma\dot{x}$, including the non-conservative damping force, $-m\gamma\dot{x}$, on the right hand side, we obtain the following equation of motion, which is that of a driven and damped harmonic oscillator, with γ being the damping coefficient:

$$\ddot{x} + \gamma\dot{x} + \omega_0^2 x = A\omega_0^2\cos(\Omega t). \tag{5.2}$$

The analytical solution of this equation of motion consists of a transient state that decays in time as $e^{-\frac{\gamma}{2}t}$ and a steady state solution given by the oscillations after the transient has died away. The driving force provides the incoming power to maintain this steady state of oscillations that would otherwise die out due to the damping. The steady state solution is given by:

$$x(t) = \frac{A\omega_0^2}{\sqrt{(\gamma\Omega)^2 + (\Omega^2 - \omega_0^2)^2}}\sin(\Omega t - \varphi); \qquad \text{with} \quad \varphi = \arctan\left(\frac{\Omega - \frac{\omega_0^2}{\Omega}}{\gamma}\right). \tag{5.3}$$

From this solution, we can calculate the average power dissipated over a cycle, using the driving force, $F_{driving} = mA\omega_0^2\cos(\Omega t)$, or the damping force, $F_{damping} = -m\gamma\dot{x}$, as:

$$P_{av}(\Omega) = \frac{\oint(F_{driving}\dot{x})dt}{2\pi/\Omega} = \frac{\oint(F_{damping}\dot{x})dt}{2\pi/\Omega} = \frac{m\gamma(A\omega_0^2)^2}{2(\gamma^2 + (\Omega - \frac{\omega_0^2}{\Omega})^2)} \tag{5.4}$$

The average power dissipated by the system per cycle of modulation as a function of the driving frequency, Ω, has a shape very similar to that of a Lorentzian curve, with ω_0 corresponding to the central frequency and γ being the FWHM. The width of the peak in the simplified case of the harmonic oscillator depends only on the damping coefficient, γ, that would arise from interatomic collisions.

The experiment performed in the laboratory measured the increase in temperature as a function of the driving frequency. If the atomic cloud is thermalised, we can assume that its

temperature is proportional to its total energy, and therefore that the measured resonant peaks should also have a Lorentzian shape. This is the reason why Lorentzian curves were fitted to the experimental peaks shown in figure 5.1.

However, the model considered in this section is too simple, since it is one-dimensional, it is based on a purely harmonic potential and contains a damping term which is not entirely realistic. In the case of the more complicated potential of our videotape traps, the width of the resonant peaks comes from the anharmonicity of the transverse confinement and from the change of radial trap frequency along the cloud's axis, as well as from the inhomogeneous collisional broadening. All these contributions will be discussed in more detail in the following section.

5.3.2 The real videotape trap potential

The shaking experiment in our videotape atom traps cannot be properly described by such a simple approach as that of a one-dimensional driven and damped harmonic oscillator. The problem remains in essence that of a forced oscillator, but is instead a three-dimensional problem in which not all the coordinates are separable, and where the important roles of the anharmonicity of the trapping potential and the interatomic collisions cannot be neglected.

The choice of using classical mechanics, instead of quantum mechanics, to solve the problem is justified by the fact that the thermal energy of the atoms in our experiment is large compared to the separation between the quantum energy levels of our trap. The atomic thermal energy, $k_B T$, given our experimental conditions, is around two orders of magnitude larger than the spacing, $\hbar\omega_r$, of the quantum levels of radial oscillation of our videotape traps.

In order to understand the effect that the modulation of the bias field has on the trapping potential, we need to take into account all the magnetic fields that are used to create a videotape trap (see section 2.3.6).

As mentioned before, the bias field that, together with the videotape field, created a transverse potential minimum in which to trap the atoms, was produced by two pairs of Helmholtz coils. One pair generated a field along the $\hat{\mathbf{x}} + \hat{\mathbf{y}}$ direction and the other pair, along the $\hat{\mathbf{x}} - \hat{\mathbf{y}}$ direction (see figure 3.2). In the absence of a shaking excitation, the field from each pair of coils would be the same and equal to $\frac{B_b}{\sqrt{2}}$ in modulus, in order to produce a total bias field of modulus B_b along the x direction. However, while shaking the trap, the field from one pair is constant and equal to $\frac{B_b}{\sqrt{2}}$ along the $\hat{\mathbf{x}} - \hat{\mathbf{y}}$ direction, while the field from the other pair along $\hat{\mathbf{x}} + \hat{\mathbf{y}}$ is modulated and equal to $\frac{B_b}{\sqrt{2}}[1 + \mathit{depth}\sin(\Omega t)]$, where *depth* is the previously defined relative modulation amplitude and Ω is the frequency of the modulation. This means that the total bias field is given by:

$$\overrightarrow{B}_{\mathbf{bias}} = B_b[1 + \frac{\mathit{depth}}{2}\sin(\Omega t)]\hat{\mathbf{x}} + B_b\frac{\mathit{depth}}{2}\sin(\Omega t)\hat{\mathbf{y}}, \tag{5.5}$$

where $\hat{\mathbf{x}}$ and $\hat{\mathbf{y}}$ are the unit vectors in the x and y directions respectively. The field produced

by the videotape (see section 2.3.5) can be expressed as:

$$\overrightarrow{B}_{\mathbf{video}} = -B_1 e^{-ky}\cos(kx)\hat{\mathbf{x}} + B_1 e^{-ky}\sin(kx)\hat{\mathbf{y}}, \tag{5.6}$$

where B_1 is the videotape magnetic field strength at the surface of the chip, $k = \frac{2\pi}{\lambda}$ and λ is the period of the videotape magnetisation.

The remaining magnetic fields necessary to form the videotape traps are the uniform field in the z direction, $\overrightarrow{B}_{\mathbf{z}} = -B_z\hat{\mathbf{z}}$, and the contribution of the end wires, $\overrightarrow{B}_{\mathbf{ew}} = B_{y-ew}\hat{\mathbf{y}} + B_{z-ew}\hat{\mathbf{z}}$, where $B_{y-ew}(y,z)$ and $B_{z-ew}(y,z)$ are given by equations 2.9 and 2.10.

Adding all these fields together, we can write the total magnetic field of the videotape trap, in x, y and z coordinates, as:

$$\overrightarrow{B}_{\mathbf{total}} = \begin{pmatrix} -B_1 e^{-ky}\cos(kx) + B_b[1 + \frac{depth}{2}\sin(\Omega t)] \\ B_1 e^{-ky}\sin(kx) + B_b\frac{depth}{2}\sin(\Omega t) + B_{y-ew}(y,z) \\ -B_z + B_{z-ew}(y,z) \end{pmatrix} \tag{5.7}$$

The potential energy of the atoms in the videotape trap is proportional to the total magnetic field strength, i.e., $U = \mu_B g_F m_F |\overrightarrow{B}_{\mathbf{total}}|$, where $g_F m_F = 1$ for the $|F = 2, m_F = +2\rangle$ magnetic hyperfine sublevel of the ground state $5^2S_{1/2}$ of ^{87}Rb that we trap.

The addition of the bias field modulation along the $\hat{\mathbf{x}} + \hat{\mathbf{y}}$ direction causes the centre of the trap to oscillate radially, approximately along that same direction. There is also an oscillation of the trap centre along the longitudinal direction of the trap, but this is very small compared to the scale of the potential along the axial z direction. It is not obvious how a displacement of the trap centre along the axis of the cloud takes place when it is the transverse bias field that is modulated. This is due to the fact that the y-component of the field of the end wires changes sign around $z = 0$ when the bias field is purely along the x direction, and around $z < 0$ or $z > 0$ when we add to it a bias field with positive or negative y-components, respectively (see section 2.3.3).

Since the bias field modulation amplitude was kept constant at 0.125G for all bias fields, the relative modulation amplitude, *depth*, shown in table 5.1, decreased as the value of the bias field increased. The amplitude of the oscillation of the centre of the trap is proportional to the value of *depth*, as explained below, so that the magnitude of the perturbation of the trap centre position decreased as the bias field increased.

The maximum displacement of the trap centre took place at a time $t = \frac{\pi}{2\Omega}$, while the minimum occurred at a time $t = \frac{3\pi}{2\Omega}$, where $\frac{2\pi}{\Omega}$ is the period of modulation. Table 5.1 shows the calculated maximum and minimum trap centre displacements along the x, y and z directions for a given bias field (B_b) and *depth* of modulation. These were calculated by finding the coordinates at which the total magnetic field strength is minimum at a given time t. The numerical solution was easily found, but there are no analytical expressions for the trap displacements when taking into account all the magnetic fields present.

Analytical expressions for the transverse displacements were found by simplifying the

B_b(G)	*depth*	Max(Δx, Δy, Δz)(μm)	Min(Δx, Δy, Δz)(μm)	(σ_x, σ_y, σ_z)(μm)
3.48	0.050	(-0.42, -0.41, -0.55)	(0.44, 0.41, 0.61)	(3.6, 2.3, 231)
5.95	0.025	(-0.21, -0.21, -0.17)	(0.22, 0.21, 0.18)	(2.2, 1.4, 248)
8.42	0.017	(-0.14, -0.14, -0.080)	(0.14, 0.14, 0.082)	(1.5, 0.91, 236)
13.38	0.010	(-0.084, -0.084, -0.031)	(0.085, 0.084, 0.031)	(1.1, 0.68, 280)
19.32	0.0068	(-0.057, -0.057, -0.014)	(0.057, 0.057, 0.015)	(1.4, 0.92, 501)
25.75	0.0050	(-0.042, -0.042, -0.0081)	(0.042, 0.042, 0.0082)	(1.3, 0.84, 589)
30.70	0.0042	(-0.035, -0.035, -0.0057)	(0.035, 0.035, 0.0057)	(1.2, 0.79, 644)

Table 5.1: Numerically calculated maximum and minimum displacements of the videotape trap centre when a modulation of relative amplitude *depth* is applied to one of the bias field coil pairs. The total bias field modulus is shown in the first column. The calculated standard deviations of the x, y and z atomic position distributions for our initial experimental conditions are shown in the last column for comparison.

problem assuming that we are at the centre of the axial confinement, i.e., at $z = 0$, where the contribution of the end wires to the y-component of the total magnetic field is zero (see section 2.3.3). Taylor expansions of these analytical expressions can be calculated in terms of *depth*, which is $\ll 1$, finding that the displacements are of the order of $\pm\frac{depth}{2k} + \mathrm{O}(depth)^2$.

The right hand side column of table 5.1 shows the calculated x, y and z initial rms sizes of the cloud in the videotape trap, at the experimental temperature at which the shaking started for each bias field (between 8 and 70μK). This shows that the magnitude of the trap displacement caused by the bias field modulation was small compared to the initial size of the cloud, especially along the z direction.

The bias field values in table 5.1 were obtained by calibrating the computer control voltage sent to the bias coils in order to match the measured transverse resonant frequencies shown on figure 5.2 with the ones obtained from the simulation described in the next section. The calibration obtained for the bias field was $B_b(G) \approx 1G + 4.95V_c$, where V_c is the computer control voltage in Volts. The offset of 1G was not unexpected as stray fields were known to be present in the trapping area inside the chamber, as mentioned in section 4.6.2.

Figure 5.3 shows the magnetic field strength as a function of each trap coordinate, for a videotape trap with $B_b = 3.48$G. The black lines correspond to the field modulus of the trap at rest, when no modulation of the bias field is applied. The blue and red lines correspond to the maximum and minimum displacements of the potential respectively, when a modulation with $depth = 0.05$ is applied. These plots were produced using the following parameters: $s = 8$mm, $d_e = 1.4$mm, $\lambda = 106\mu$m, $B_1 = 110$G, $B_z = 2.22$G and $I_{end} = 15$A. We can clearly appreciate from the plots how the centre of the trap is displaced in each direction, how the bottom of the trap changes and how the trap depth, U_0:

$$U_0 = \max(|\overrightarrow{B}_{\mathbf{total}}|) - \min(|\overrightarrow{B}_{\mathbf{total}}|), \tag{5.8}$$

not to be confused with *depth*, which is the strength of the modulation, changes as well, mostly for the confinement along the x direction. The oscillation amplitude of the bottom of the trap in units of temperature is very small compared to the temperature of the atoms: $\sim 0.07\mu K$ for the lowest bias field, and $\sim 0.006\mu K$ for the highest one. The curvature of

the potential is also slightly modified. For all directions, the frequency of the trap increases when the displacement of the centre of the potential is maximum, and decreases when it is minimum. This implies that there is a small oscillation of the trap frequency as the trap is shaken, which gives rise to parametric resonance and therefore to additional resonant heating of the atoms in the oscillating trap. This contribution will be explained in more detail in section 5.3.3.

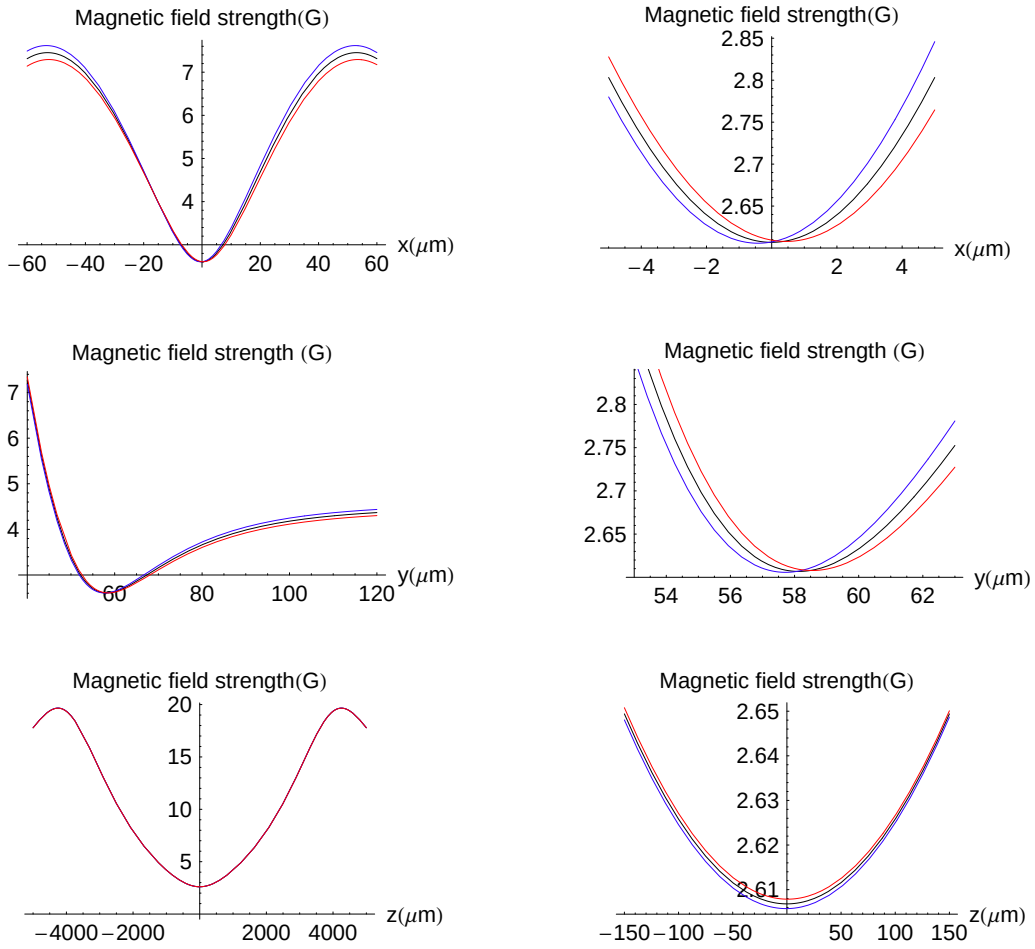

Figure 5.3: Plots of the total magnetic field strength of a videotape trap with bias field $B_b = 3.48$G versus each coordinate. The black lines show the un-displaced, unmodulated trap. The blue and red lines show the modulated trap at its maximum and minimum displacements, respectively, for $depth = 0.05$. The graphs on the left show the potential on a larger scale, while the ones on the right zoom into the central region.

The anharmonicity of the videotape trap potential

Close to the trap centre, the videotape potential is approximately harmonic. However, as we move away from the minimum of the potential, its curvature decreases below that of a quadratic potential and the frequency of the oscillations is lower than the harmonic frequency. Therefore, the transverse frequencies decrease as the distance from the centre of the trap increases. For an atomic cloud confined in a videotape trap, the atoms lie within certain ranges of positions given by their temperature, and therefore oscillate with varied amplitudes that in turn determine their varied oscillation frequencies. This subsection cal-

culates the dependence of the transverse trap frequencies on the amplitude of the oscillations and shows the range of radial frequencies that are possible in the trap taking into account the experimental parameters.

As a way to estimate the degree of anharmonicity of the videotape trap potential, we can define the extent of the harmonic region in the following way. Considering only the confinement in the x-y plane, the modulus of the total magnetic field can be written as $|\overrightarrow{B}_{\mathbf{total}}| = \sqrt{(\alpha r)^2 + B_z^2} = B_z\sqrt{1 + \frac{k^2 B_b^2}{B_z^2} r^2}$, where $\alpha r = kB_b r$ and B_z are the transverse and axial field components respectively (see section 2.3.6). The Taylor expansion that yields the harmonic approximation of the radial potential, $\overrightarrow{B}_{\mathbf{total}} \approx B_z + \frac{k^2 B_b^2}{2B_z} r^2$, is only valid for $|\frac{kB_b}{B_z} r| \ll 1$. Therefore, we can define $r_h = \frac{B_z}{kB_b}$ and the limit of the harmonic region as $r \ll r_h$. Since B_z was left constant for all bias fields, the size of the harmonic region decreased as the bias field increased. The values of r_h corresponding to $B_z = 2.22$G and the bias fields in table 5.1, in ascending order of bias field, were: 10.8μm, 6.3μm, 4.4μm, 2.8μm, 1.9μm, 1.4μm and 1.2μm (see figure 5.4).

As shown in the previous section, the magnitude of the displacement of the trap centre due to the bias field modulation is approximately $\Delta x, \Delta y \approx \frac{depth}{2k}$, with $depth \approx \frac{\Delta B_b}{B_b}$. This displacement is small compared to the extent of the harmonic region if $|\Delta x|, |\Delta y| \ll r_h$ i.e., if $\frac{\Delta B_b}{2B_z} \ll 1$. This condition was fulfilled for all bias fields, as the value of the left hand side of the inequality lay between 0.03 and 0.04. Therefore, the perturbation did not take the atoms outside the harmonic region straight away, but did so after a number of cycles, as energy was brought into the system by the modulation of the bias field.

Given an ensemble of atoms with a Gaussian distribution of x positions, with centre $x = x_0$ and width σ_x, 99.73% of the atoms will be found between $x_0 - 3\sigma_x$ and $x_0 + 3\sigma_x$. The values of σ_x and σ_y can be estimated from the experimental temperatures prior to the shaking perturbation (see experimental data in figure 5.1). We can consider $3\sigma_{x,y}$ approximately as the maximum radius of the atom cloud and compare it to the value of r_h. At the temperatures at which the shaking experiment took place, the values of the ratios $\frac{3\sigma_x}{r_h}$ and $\frac{3\sigma_y}{r_h}$ increase from ~ 1 to ~ 3 and from ~ 0.6 to ~ 2, respectively, as we go from the smallest to the largest bias field. Since the harmonic region corresponds to $r \ll r_h$, a value of $\frac{3\sigma_{x,y}}{r_h}$ equal to 1 already means that some atoms reach the anharmonic regions of the potential. The obtained values show that, for our experimental conditions, the degree of anharmonicity explored by the atoms was larger for the traps with larger bias fields. As more atoms explore the anharmonic regions of the trap, more atoms oscillate with frequencies below the harmonic one, shifting the centre of the resonant peaks towards lower frequencies. This is one of the reasons that explains why the deviation from the harmonic frequency in figure 5.2 is larger for larger bias fields. The other main reason is the decrease of the transverse trap frequencies away from the centre of the potential, along the axis of the cloud, detailed in a following section.

Anharmonic correction for small oscillations close to the trap centre.

According to reference [99], starting from the equation of motion of an anharmonic oscillator

in one dimension, $\ddot{x} + \omega_0^2 x + \alpha x^2 + \beta x^3 = 0$, we can approximate the frequency of the anharmonic oscillations analytically as $\omega = \omega_0 + \omega^{(2)}$, where ω_0 is the frequency of the solution to the harmonic equation, $\ddot{x} + \omega_0^2 x = 0$, and $\omega^{(2)}$ is its correction, given by:

$$\omega^{(2)} = (\frac{3\beta}{8\omega_0} - \frac{5\alpha^2}{12\omega_0^3})A_x^2, \tag{5.9}$$

where A_x is the oscillation amplitude. This expression is valid for $\alpha A_x, \beta A_x^2 \ll \omega_0^2$, i.e., when the deviation from a harmonic potential is small.

It is possible to calculate a one-dimensional Taylor expansion of the videotape trap potential around the centre of the trap, in order to find the anharmonic coefficients, α and β, in each transverse direction. Therefore, we can obtain the correction to the harmonic frequency, $\omega^{(2)}$, which we find to be negative for all values of the bias field. Following this, we predict a decrease in radial frequency that is proportional to the square of the amplitude of the oscillations, as shown in figure 5.4. Note that the expression in equation 5.9 is only valid for small oscillations close to the bottom of the potential, where also our Taylor expansion of the potential is valid. As the atoms move away from the centre of the trap, the shape of the potential becomes nearly linear and this is no longer a reliable way to predict the radial frequency.

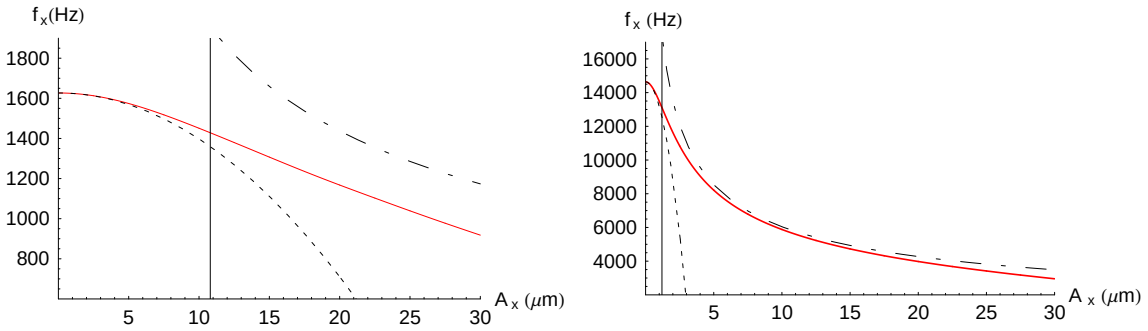

Figure 5.4: **Left**: $B_b = 3.48$G. **Right**: $B_b = 30.70$G. Transverse trap frequency, f_x, versus amplitude of oscillation, A_x. **Solid red line**: calculated frequency from the fit to the numerical solution of the equation of motion (see text). **Dashed line**: analytical prediction of the frequency from classical theory of small oscillations in an anharmonic trap using the correction given by equation 5.9, valid only for small A_x. **Dot-dashed line**: frequency of the linear part of the potential, calculated using equation 5.10. **Solid vertical line**: value of r_h, with the harmonic region corresponding to $r \ll r_h$.

Oscillations far from the trap centre: linear approximation.

We can estimate a frequency for the oscillation of particles in the linear part of the trap by assuming a linear quadrupole potential with gradient $\mu_B k B_b$ in the transverse direction of the trap, as it is before B_z is added (see section 2.28). The solution of the equation of motion of a particle with initial position A in a one-dimensional linear potential is easily calculated, and the frequency can be estimated as the inverse of the time taken to go from A to $-A$ and back. Hence, we can write:

$$f_{r-linear} \sim \frac{1}{4}\sqrt{\frac{\mu_B k B_b}{2mA}}. \tag{5.10}$$

The frequency of motion in the linear part of the potential drops with increasing amplitude of the oscillations, as shown in figure 5.4.

Complete numerical calculation of the transverse frequencies in the full videotape potential.

It is possible to calculate the numerical solution of the one-dimensional equation of motion of the atoms in the videotape trap, for a given amplitude of oscillation and zero initial velocity, and fit it to a sinusoidal function to find the radial frequency as a function of the radial amplitude. The one-dimensional equations of motion (one for x and one for y) were derived from the cross-sections of the complete three-dimensional videotape trap potential through the position of the minimum magnetic field strength. Figure 5.5 shows the transverse trap frequencies, f_x and f_y, calculated in this way, as a function of the radial amplitude of oscillation, A_r. Each figure indicates its bias field value, B_b, and is plotted over a range of initial amplitudes equivalent to approximately three times the standard deviation of the positions, corresponding to the initial experimental conditions of the measurements shown in figure 5.1. The plots therefore give an idea of the range of transverse oscillation frequencies that are possible for the atoms confined in these anharmonic videotape traps, at the temperatures at which the experiment took place.

Comparison between the full frequency calculation and the estimations for small oscillations and oscillations in the linear part of the potential.

Figure 5.4 shows the comparison between the numerical calculation of the decrease in radial frequency as a function of oscillation amplitude (shown in figure 5.5), the analytical prediction from classical theory of small oscillations in an anharmonic potential (calculated using equation 5.9), and the analytical expression for the frequency of the oscillations in the linear part of the trapping potential (calculated using equation 5.10). Only the two extreme bias fields are shown, as an example for comparison.

As expected, The prediction for small oscillations close to the bottom of the trap matches the numerical calculation for small oscillation amplitudes but gives an underestimate of the frequency when the atoms go far enough from the centre of the trap.

The graph corresponding to $B_b = 3.48$G in this figure shows a shallow trap, in which the frequency never reaches the frequency of the linear potential. The graph for $B_b = 30.70$G shows a much tighter and deeper trap in which, as the amplitude of oscillation increases, the frequency goes from its harmonic to its linear value and then decreases again under the linear value as the curvature of the potential decreases when we approach the position of the next videotape trap in the array of traps formed along the x direction (recall section 2.3.6).

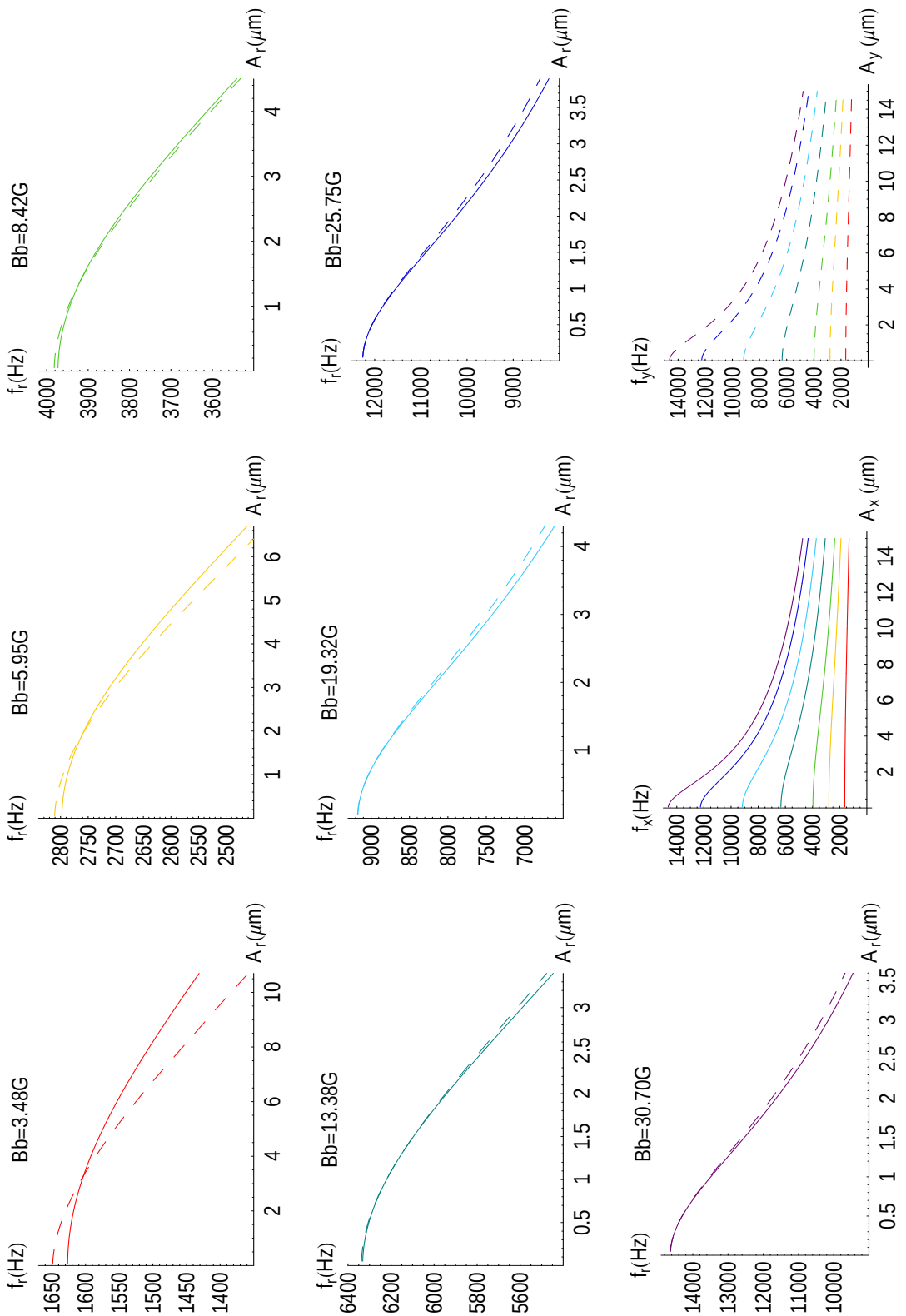

Figure 5.5: Transverse trapping frequencies, f_x (solid lines) and f_y (dashed lines), versus initial amplitude, A_r, of oscillation at $t = 0$, over a range $\sim 3\sigma_x$, for each bias field, B_b. The last two figures combine the plots for all bias fields on a wider range of initial amplitudes, from 0 to 15μm.

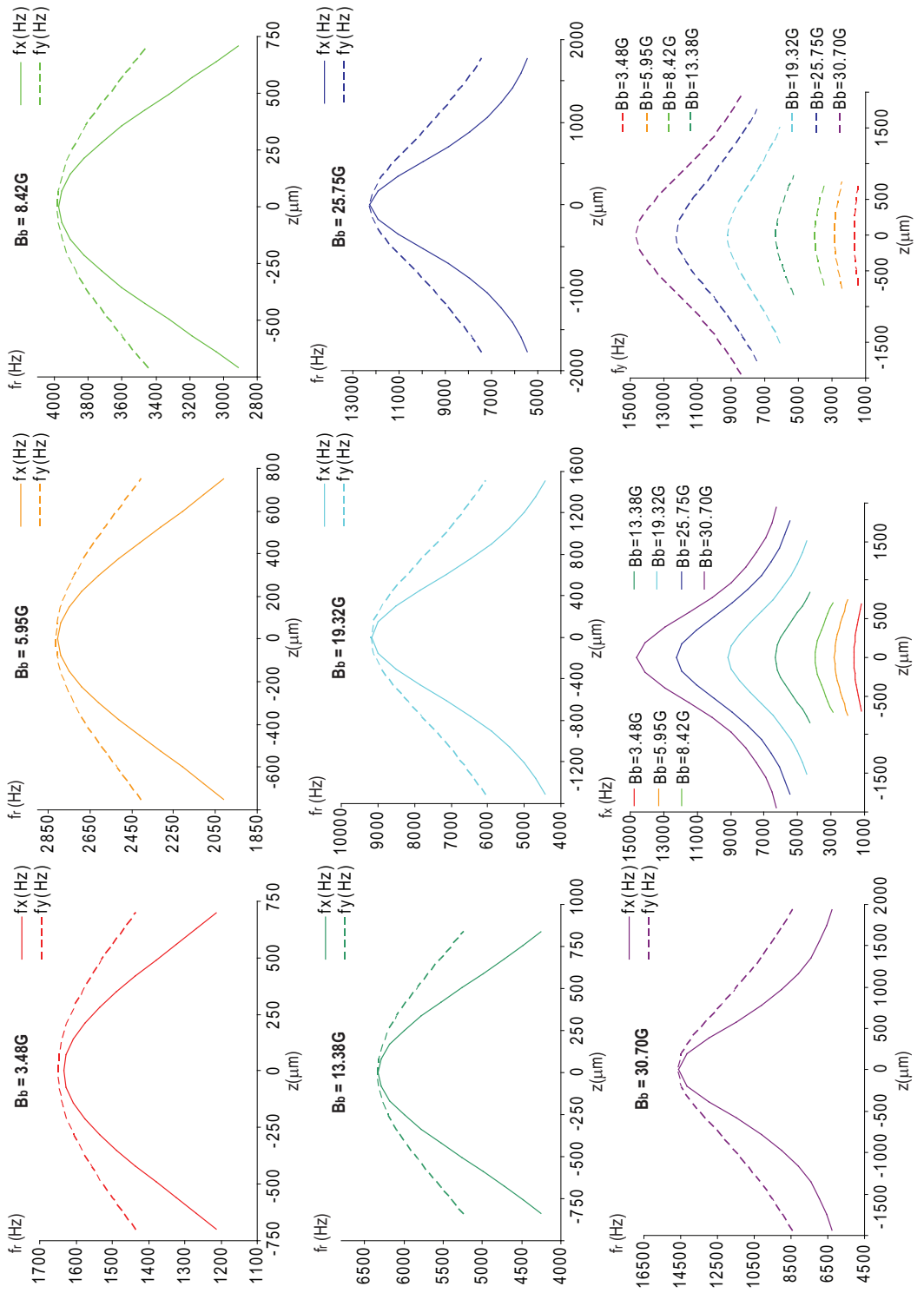

Figure 5.6: Transverse videotape trap frequencies, f_x and f_y, as a function of the axial coordinate of the trap, z, over a range of $\sim 3\sigma_z$, calculated from the experimental conditions. Each graph is labelled with the bias field value, B_b. The last two graphs show the plots for all bias field together, to give an idea of the frequency ranges that correspond to each B_b.

Variation of the transverse frequencies along the axial direction of the trap

The transverse oscillation frequencies varied along the axial direction of the elongated cloud as a result of the change in the net z-component of the total magnetic field, which affects the calculated transverse frequencies, since the harmonic approximation of the radial frequency is $f_{r-harm} \approx \frac{kB_b}{2\pi}\sqrt{\frac{\mu_B}{mB_{z-net}}}$ (see equation 2.31).

At the centre of the axial confinement, $z = 0$, the net z-component of the field is minimum and therefore the radial frequencies find their maximum. As we move to $|z| > 0$, the net z-component of the field increases and hence the transverse frequencies decrease, as shown in figure 5.6, where we can see the transverse frequencies as a function of z for each bias field, plotted over a range of z values equal to $\sim 3\sigma_z$, in accordance with the experimental parameters.

These frequencies were calculated by choosing first a z value, finding the minimum of the potential in the x-y plane, then calculating the best harmonic fit to the two-dimensional x-y potential in a very small region around the obtained minimum, and repeating the process for different values of z. They provide a harmonic approximation of the transverse frequencies as we move along z.

The last two subsections have shown how the transverse frequencies vary as the atoms move away from the centre of the trap, along the transverse directions, due to anharmonicity, and along the axial direction, due to the effect of the change in net B_z. The ranges of frequencies shown in figures 5.5 and 5.6 give an idea of the possible frequencies with which the atoms can oscillate in these videotape traps, given their initial temperature, found from the experimental data. These arguments show how the initial conditions contribute to explain the fact that the widths of the experimental resonant peaks, measured to be between 450Hz and 2200Hz (see section 5.2.3), were much larger than those expected for a simple harmonic potential, and give a correct idea of the order of magnitude of these widths.

The remaining contribution to the width of the resonant peaks is that from collisional broadening, not taken into account up to now. Section 5.4 describes a simulation of the evolution of atoms in a shaking videotape trap, accounting for inter-atomic collisions and explaining their importance.

5.3.3 Parametric resonance

It has been shown how, for a trap of frequency ω_0, the major effect of the bias field modulation is to shake the centre of the trap in time. Resonant heating occurs when we shake the trap centre at a frequency $\Omega \approx \omega_0$. There is also the much weaker effect of an oscillation of the trap frequencies in time, as the bias field is modulated, known as parametric resonance.

Parametric resonance for particles confined in a harmonic potential takes place when the spring constant oscillates in time. The one-dimensional classical equation of motion in the presence of parametric excitation at frequency Ω is:

$$\ddot{x} + \omega_0^2(1 + h\cos(\Omega t))x = 0, \tag{5.11}$$

where $0 \leq h \leq 1$ is the strength of the excitation. When the frequency of the excitation is tuned to a value $\Omega \approx \frac{2\omega_0}{n}$, for n natural, the system becomes unstable and the oscillation amplitude of a particle in the excited trap increases exponentially with time as $\exp(st)$ [99]. The strongest resonance is for $n = 1$. As n increases, the amplitude and width of the resonance decrease quickly, the latter as h^n. In this section we will only consider the first ($n = 1$) and second order ($n = 2$) parametric resonances. Their frequency widths are respectively $\Delta f_1 \simeq \frac{h_1\omega_0}{2\pi}$ and $\Delta f_2 \simeq \frac{h_2^2\omega_0}{8\pi}$, where the subscripts indicate the order n of the resonance. The exponents of the amplitude growth in time are $s_1 \simeq \frac{h_1\omega_0}{4}$ and $s_2 \simeq \frac{\sqrt{5}}{24}h_2^2\omega_0$, for $n = 1$ and $n = 2$, respectively [99].

Considering the excitation that takes place in the videotape traps when the bias field is modulated at a frequency Ω, we can write an equation of motion for each of the radial coordinates of our videotape trap in a way that resembles equation 5.11 as follows:

$$\ddot{x} + \omega_0^2[1 + \frac{depth}{2}\sin(\Omega t) + \frac{B_b^2 depth^2}{4B_z^2}\cos(2\Omega t) + ...]x = 0 \tag{5.12}$$

$$\ddot{y} + \omega_0^2[1 + \frac{depth}{2}\sin(\Omega t) + \frac{B_b^2 depth^2}{4B_z^2}\cos(2\Omega t) + ...]y = 0, \tag{5.13}$$

with $B_z = 2.2$G, and B_b and *depth* given by the values in table 5.1. This can be done by obtaining the equations of motion using the modulus of the full expression of the videotape magnetic field (equation 5.7), that includes the excitation, and calculating its Taylor expansion in terms of *depth*, the relative amplitude of the bias field modulation, since $depth \ll 1$.

We can first consider the case when the modulation frequency is $\Omega \simeq 2\omega_0$. In this case, the coefficients of $\sin(\Omega t)$ can be identified as the strengths of the first order parametric resonance, h_1. The terms in $\cos(2\Omega t)$ do not contribute to any of the sub-harmonics of the parametric resonance (higher order resonances with $n > 1$). Since *depth* and ω_0 are known, we can calculate the exponent s_1 and the width of this resonance for each of the experimental bias fields. At the centre of the resonance the energy increases as $(\exp s_1 t)^2$, with a value of s_1 that we calculate to decrease from 60s^{-1} to 43s^{-1} from the lowest to the highest bias field. For the width of the resonance, Δf_1, we obtain ~ 40Hz for the lowest bias field and ~ 30Hz for the largest one. This resonance was only measured experimentally for the lowest bias field (smallest peak around 2500Hz in figure 5.1), and its width was of the order of 500Hz, much larger than the one calculated here. Note that this calculation assumes a harmonic trap, and that the multiple frequencies possible in our anharmonic traps (section 5.3.2) would make the resonance wider.

We can also consider the effect of the parametric resonances that take place when the bias field is modulated at a frequency $\Omega' \simeq \omega_0$, and their contribution to our measured resonant peaks. In this case, we can identify the coefficients of the terms in $\sin(\Omega' t)$ in equations 5.12 and 5.13, as the strengths of the second order ($n = 2$) parametric resonance, h_2', and the coefficients of $\cos(2\Omega' t)$ as the strengths of the first order parametric resonance, h_1'. The calculated exponents, from lower to higher bias field, are $s_2' \simeq 0.5 - 0.03s^{-1}$ for

$n = 2$ and $s_1' \simeq 2 - 10s^{-1}$ for $n = 1$; and the calculated widths of these resonances are $\Delta f_2' \sim 0.2 - 0.01$Hz and $\Delta f_1'$ ∼1-7Hz, respectively. We can compare these widths to the previously calculated width, Δf_1, of the stronger parametric resonance at $\Omega \simeq 2\omega_0$: for $n = 2$ we have $\Delta f_1/\Delta f_2' \simeq 160 - 1920$, and for $n = 1$ we have $\Delta f_1/\Delta f_1' \simeq 27 - 4$.

When the excitation frequency is $\Omega' \simeq \omega_0$, we can calculate the amplitudes of the resonances in energy at the end of the bias field modulation as $(\exp s_2' t)^2$ and $(\exp s_1' t)^2$, using the experimental value, t=5seconds, and the previous values of s_1' and s_2'. When $\Omega \simeq 2\omega_0$, we can use $(\exp s_1 t)^2$ and the calculated s_1. The amplitudes of the parametric resonances at $\Omega' \simeq \omega_0$ are $\sim 10^{100}$ times smaller than that of the resonance at $\Omega \simeq 2\omega_0$.

We can conclude that the calculated contribution of parametric resonance to our resonant peaks at $\Omega' \simeq \omega_0$ is negligible, since both the calculated widths and amplitudes of these resonances are much lower than those calculated for the parametric resonance at $\Omega \simeq 2\omega_0$, for which experimental data were available for reference.

It is not possible to find a simple analytical solution to the complicated problem of the excitation via bias-field modulation in our videotape traps and separate the contribution of parametric resonance from that of the modulation of the trap centre position, but we can perform a simulation in order to solve the full equation of motion numerically, as detailed in the following section.

In the last section of this chapter I refer to work published by other groups reporting studies of parametric resonance of confined particles.

5.4 The simulation

A Monte Carlo simulation was carried out in order to combine all the effects mentioned in the previous section and to introduce collisions, that have not been taken into account up to now. Additional insight into the dynamics of the trapped atoms was gained from looking at the evolution of the cloud properties in time. The resonant peaks obtained from the simulation held a close resemblance to the experimentally measured ones.

In order to reproduce the behaviour of the confined cloud of atoms during the shaking experiment, an ensemble of atoms with given three-dimensional initial distributions of positions and velocities was generated and allowed to evolve in the shaken videotape trap potential including collisions through a model detailed in section 5.4.1. The individual motion of the atoms in this complicated potential was numerically solved and average ensemble properties were obtained.

Lagrangian formulation was used to write the equations of motion for each atom in three-dimensions. The kinetic energy is given by $E_k = \frac{1}{2}m(\dot{x}^2+\dot{y}^2+\dot{z}^2)$, while the potential energy is expressed as $U = \mu_B g_F m_F |\overrightarrow{B}_{\mathbf{total}}(\mathbf{x},\mathbf{y},\mathbf{z})|$, where $\overrightarrow{B}_{\mathbf{total}}(\mathbf{x},\mathbf{y},\mathbf{z})$ is the total field given by equation 5.7, which includes the bias field modulation. The Lagrangian of the system is

$L = E_k - U$ and the equations of motion were obtained from Lagrange's equations:

$$\begin{aligned}
\frac{d}{dt}\left(\frac{\partial L}{\partial \dot{x}}\right) - \frac{\partial L}{\partial x} &= 0 \\
\frac{d}{dt}\left(\frac{\partial L}{\partial \dot{y}}\right) - \frac{\partial L}{\partial y} &= 0 \\
\frac{d}{dt}\left(\frac{\partial L}{\partial \dot{z}}\right) - \frac{\partial L}{\partial z} &= 0
\end{aligned} \tag{5.14}$$

and solved for each atom of the ensemble, for certain initial positions, x_0, y_0, z_0, and velocities, v_{x0}, v_{y0}, v_{z0}, chosen randomly from some initial distributions of positions and velocities. Since a classical description was used to solve the problem, we assumed a Maxwell-Botzmann distribution of energies, so that we can write

$$N = \int g(E) e^{-E/(k_B T)} dE \tag{5.15}$$

where N is the total atom number, T is the initial temperature of the atoms and $g(E)$ is the density of states:

$$\int g(E) dE = \int\int\int\int\int\int \frac{dx dy dz dp_x dp_y dp_z}{h^3} \tag{5.16}$$

with $g(E)dE$ being the number of states with energy between E and $E + dE$, and where it was assumed that, if $dxdydzdp_xdp_ydp_z$ is the volume element of the phase space, each energy state occupies a phase space volume h^3. Therefore, we can write:

$$N = \frac{1}{h^3} \int_{-\infty}^{+\infty} e^{-U(x,y,z)/(k_B T)} dx dy dz \int_{-\infty}^{+\infty} e^{-(p_x^2+p_y^2+p_z^2)/(2mk_B T)} dp_x dp_y dp_z \tag{5.17}$$

and separate the position and momentum distributions. For each atom, the simulation randomly picked the values of each velocity component, v_x, v_y, v_z, from a normalised Gaussian distribution centred around 0, with $\sigma_v = \sqrt{\frac{k_B T}{m}}$. As for the position distribution, in order to match the shape of the actual trapping potential, the position coordinates for each atom, (x, y, z), were chosen at random from an initial three-dimensional distribution of positions, obtained directly from the full videotape potential and the initial temperature as $e^{-U(x,y,z)/(k_B T)}$, and normalised.

The initial temperature at which the shaking started in the simulation was obtained for each bias field from the baseline temperature of the Lorentzian fit to the experimental data shown in figure 5.1. For the three highest bias fields the atoms were shaken in a trap with $B_b = 19.32$, 25.75 or 30.7G, and then ramped to a trap with $B_b = 3.48$G before the image of the cloud was recorded. The temperature for the simulation was found assuming an adiabatic decompression (done in 3s) in a harmonic trap, from the high field to $B_b = 3.48$G, so that $T_f = \left(\frac{\omega_{rf}}{\omega_{ri}}\right)^{2/3} T_i$ (see section 4.4.1), where i and f denote the high and low bias field traps respectively. T_f was the offset of the Lorentzian fit to the data, used to calculate T_i for the simulation. Table 5.2 in page 109 shows the values of the initial temperatures used in the simulation.

5.4.1 Collisions in the simulation

The role of collisions

Collisions transfer part of the energy absorbed by the excited radial degrees of freedom to the axial degree of freedom. The axial length of the cloud was the property measured in order to calculate the temperature of the atoms after the excitation.

As a test, we initialised an ensemble of atoms at $z = 0$ and $v_z = 0$, with Gaussian distributions of positions and velocities in the x and y directions, and let it evolve without collisions in the unperturbed potential. We expected a small energy transfer from the oscillations along the x direction to the z direction, due to the small tilt of the trap in the x-z plane (see section 2.3.6). We found this energy transfer was negligible and took place in a time scale of the order of one or two radial oscillations. The only mechanism that can guarantee that the temperature is similar in all the directions of the trap is the redistribution of energy by collisions.

As the trapping potential is perturbed at a given excitation frequency, the atoms that oscillate with frequencies close to that absorb energy from the excitation and increase their oscillation amplitudes. Their oscillation frequency is reduced as they explore regions of decreased curvature of the potential when they move away from the centre of the trap. Eventually, as they absorb more and more energy, they fall out of resonance and cannot absorb any more energy from the excitation. The second role of collisions is to redistribute the velocities of the atoms and repopulate the transverse velocity states that are resonant with the excitation. In this way, energy can continue to be absorbed from the excitation, leading to an energy increase higher than that expected without collisions. Collisions therefore effectively cause an increase in both the height and the width of the simulated resonant peaks by redistributing the atomic velocity components. The next section (5.4.3) that describes the evolution of the ensemble properties in time shows a comparison of the results obtained with and without collisions.

The collision model

Interatomic elastic collisions were implemented through a "fixed-ball" collision model. In this model the atoms were taken as balls of radius a and it was assumed that, for each atomic collision, the atom elastically collides with an infinitely massive, imaginary atom which is pinned in space and does not move. When an atom collides in three dimensions with one of these imaginary pinned atoms, the component of its velocity that lies along the line that joins the centres of the two balls, is inverted, while the other components that lie perpendicular to that line are not modified. If $\hat{\mathbf{e}}$ is the unit vector along the line of centres of the balls and $\vec{v}_i$ is the initial velocity of the atom, then we can write its final velocity as:

$$\vec{v}_f = \vec{v}_i - 2\,(\vec{v}_i \cdot \hat{\mathbf{e}})\,\hat{\mathbf{e}} \tag{5.18}$$

With the help of figure 5.7(left), we can write $\hat{\mathbf{e}}$ as:

$$\hat{\mathbf{e}} = -\frac{1}{2a}\left(\sqrt{4a^2 - b^2}\,\hat{\mathbf{e}}_\mathbf{1} + b\,\hat{\mathbf{e}}_\mathbf{2}\right) \tag{5.19}$$

where b is the impact parameter and $\hat{\mathbf{e}}_\mathbf{1}$ and $\hat{\mathbf{e}}_\mathbf{2}$ are the unit vectors parallel and perpendicular to the initial velocity of the atom respectively. Substituting equation 5.19 into equation 5.18 we find:

$$\vec{v}_f = \frac{b^2 - 2a^2}{2a^2}\,\vec{v}_i - \frac{b\sqrt{4a^2 - b^2}}{2a^2}|\vec{v}_i|\,\hat{\mathbf{e}}_\mathbf{2}. \tag{5.20}$$

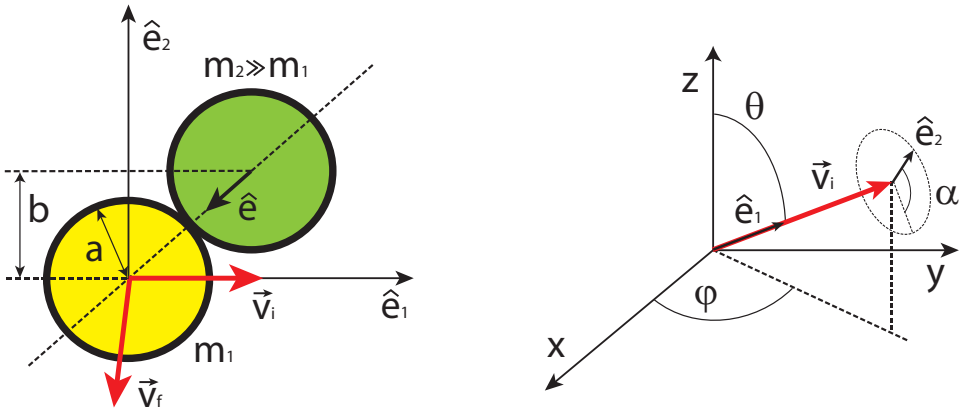

Figure 5.7: Geometry of the collision model. The green ball is an atom pinned in space.

In Cartesian coordinates, the initial velocity is $\vec{v}_i = v_{ix}\hat{\mathbf{x}} + v_{iy}\hat{\mathbf{y}} + v_{iz}\hat{\mathbf{z}}$. In order to consider the three-dimensional character of the problem we need to take into account the extra degree of freedom given by the fact that vector $\hat{\mathbf{e}}_\mathbf{2}$ can be rotated in the plane perpendicular to $\hat{\mathbf{e}}_\mathbf{1}$ by a random angle α, as shown in figure 5.7(right). In terms of the angles in this figure, $\hat{\mathbf{e}}_\mathbf{2}$ can be expressed as:

$$\hat{\mathbf{e}}_\mathbf{2} = (\cos\varphi\cos\theta\cos\alpha - \sin\varphi\sin\alpha)\hat{\mathbf{x}} + (\sin\varphi\cos\theta\cos\alpha + \cos\varphi\sin\alpha)\hat{\mathbf{y}} - (\sin\theta\cos\alpha)\hat{\mathbf{z}}. \tag{5.21}$$

Expressing the functions of φ and θ as $\cos\varphi = \frac{v_{ix}}{\sqrt{v_{ix}^2+v_{iy}^2}}$, $\sin\varphi = \frac{v_{iy}}{\sqrt{v_{ix}^2+v_{iy}^2}}$, $\cos\theta = \frac{v_{iz}}{|\vec{v}_i|}$, $\sin\theta = \frac{\sqrt{v_{ix}^2+v_{iy}^2}}{|\vec{v}_i|}$, and substituting for $\vec{v}_i$ and $\hat{\mathbf{e}}_\mathbf{2}$ in equation 5.20, we reach the following expressions for the final velocity components:

$$\begin{aligned}
v_{fx} &= \frac{(c^2-2)\,v_{ix}}{2} - \frac{c}{2}\sqrt{4-c^2}\left(\frac{v_{ix}v_{iz}\cos\alpha}{\sqrt{v_{ix}^2+v_{iy}^2}} - \frac{v_{iy}|\vec{v}_i|\sin\alpha}{\sqrt{v_{ix}^2+v_{iy}^2}}\right)\\
v_{fy} &= \frac{(c^2-2)\,v_{iy}}{2} - \frac{c}{2}\sqrt{4-c^2}\left(\frac{v_{iy}v_{iz}\cos\alpha}{\sqrt{v_{ix}^2+v_{iy}^2}} + \frac{v_{ix}|\vec{v}_i|\sin\alpha}{\sqrt{v_{ix}^2+v_{iy}^2}}\right)\\
v_{fz} &= \frac{(c^2-2)\,v_{iz}}{2} + \frac{c}{2}\sqrt{4-c^2}\sqrt{v_{ix}^2+v_{iy}^2}\cos\alpha
\end{aligned} \tag{5.22}$$

where $c = \frac{b}{a}$ and $|\vec{v}_i| = \sqrt{v_{ix}^2 + v_{iy}^2 + v_{iz}^2}$. The final velocity depends on the initial velocity, on the dimensionless impact parameter, c, which is chosen at random between -2 and 2, and on the angle α, also chosen at random between 0 and 2π.

After the collision, the total energy and momentum of the atom are conserved, but its velocity components have changed.

The elastic collision rate, γ_{el}, was calculated using equation 4.13 as detailed in section 4.4.2, using the rms sizes of the cloud in the anharmonic potential, calculated as the standard deviations of the x, y and z position distributions, respectively. The number of atoms used in the calculation was $N = 10^5$, since the experimental atom number ranged between 10^4 and 10^5atoms.

As the atoms get excited by the perturbation and oscillate with increasing amplitudes, the volume occupied by the ensemble increases, leading to a decrease in density and an increase in temperature. This causes a drop in collision rate that can be as large as a factor of 4 after 30ms of bias field modulation, compared to the experimental total modulation time, equal to 5s. For this reason we need to take into account the evolution of the collision rate as the atoms are excited in the shaken trap. This was done by calculating the solution of the equation of motion of the ensemble of particles after a given time, Δt, then re-calculating the ensemble properties like the average density, collision rate, temperature and average energy, then solving again the equation of motion after shaking for another Δt, and repeating the process until the total shaking time was 5s. These 5s were broken into several blocks with different time steps: 100ms with step of $\Delta t_1 = 1$ms, 300ms with step of $\Delta t_2 = 3$ms, 1100ms with step of $\Delta t_3 = 10$ms and 3500ms with step of $\Delta t_4 = 20$ms. Prior to the excitation, the atoms were left to evolve for 100ms in the unperturbed potential until a few collisions redistributed their energies to match the trapping potential and to re-thermalise the cloud in its different directions.

The time interval between collisions obeys an exponential distribution [100]. The probability that an atom survives a time t without suffering a collision is independent of the history of the atom and can be expressed as $P(t) = \gamma_{el} e^{-\gamma_{el} t}$, where γ_{el} is the previously defined elastic collision rate. In the simulation an atom evolved in the shaking potential during certain time Δt. Then the collective properties of the ensemble and the new collision rate were re-calculated. Following that, a random number, R, between 0 and 1 was generated and the probability of surviving without collisions for a time Δt was calculated using the new collision rate. If this probability was larger than R the atom survived, otherwise, it collided, in which case, the ensemble properties were updated again. This process of deciding whether an atom collided or not was repeated after every step of the calculation. For this to be reasonable the step of the calculation needed to be small compared to the time interval between collisions. The average time between collisions ($1/\gamma_{el}$) was between 10 and 50ms before the shaking started, compared to the initial calculation time step of 1ms, and went up to between 130 and 320ms at the end of the excitation, compared to the final time step of 20ms at the end of the simulation.

Discussion of the collision model

We verified that the broadening of the resonance caused by the collisions in our model resulted in a frequency width proportional to $\frac{\gamma_{el}}{2\pi}$ [101]. A test simulation was run using a three-dimensional purely-harmonic potential, $\frac{1}{2}m\left(\omega_x^2x^2+\omega_y^2y^2+\omega_z^2z^2\right)$, with frequencies close to the calculated harmonic frequencies of the experiment, and perturbed by a displacement of its centre of the same order as the one corresponding to the experimental parameters. Collisions were included as explained in the previous paragraphs and the ratio of final total energy, after a given perturbation time, to initial energy was plotted versus the excitation frequency Ω (see figure 5.8(left)). Several resonant peaks were obtained for several initial temperatures of the atoms in the cloud, from 5 to 30μK. Since the trap was harmonic in all directions the only contribution to the width of the resonant peaks was that of collisions. At constant atom number and trap frequencies, the elastic collision rate is inversely proportional to the temperature, and the width of the resonant peaks should decrease as the initial temperature increases. The width, W, was obtained from a fit to a Lorentzian function, $offset+\frac{AW}{W^2+(f-f_0)^2}$, where W corresponded to the half width at half maximum. As expected, we found that the width of the simulated resonant peaks depended linearly on the elastic collision rate. However, the slope we found was 0.73 ± 0.01 instead of 1 (see figure 5.8(right)). This is due to the nature of the collisions in our model. These collisions are not entirely realistic, since one atom does not collide and exchange energy with another atom from the ensemble, but with an imaginary particle of infinite mass that appears at the time of the collision and is pinned in space. The individual speed and energy of each atom is conserved after the collision and only the direction of its velocity is modified.

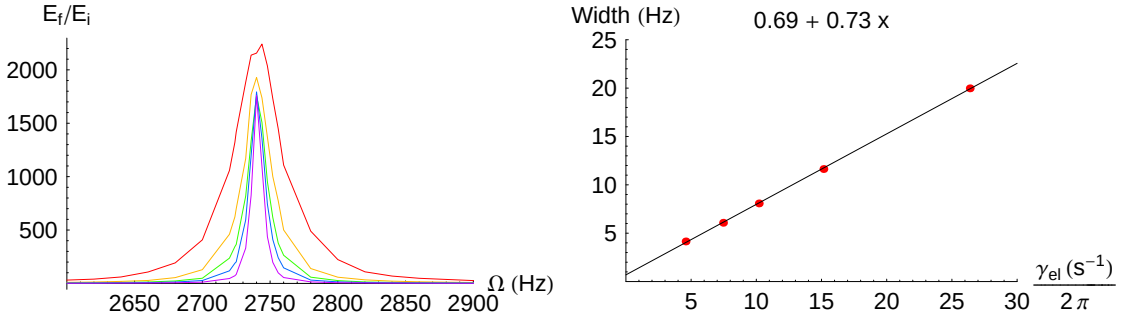

Figure 5.8: **Left**: simulated resonance when shaking the centre of a three dimensional harmonic potential with collisions. Increasing widths correspond to increasing collision rates and decreasing temperatures. **Right**: width obtained from the simulation as a function of the elastic collision rate.

The estimated contribution of collisions to the width of the experimental resonant peaks is of the order of 3 to 15Hz, as calculated from the initial collision rates. This collisional broadening is negligible compared to the experimental half-widths, which are between 250Hz and 1000Hz, and come mostly from the anharmonicity of the potential and the change in radial frequency along the axis of the trap.

5.4.2 Dependence on initial temperature

From preliminary test simulations using the full videotape-trap potential, we found that interatomic collisions lead to an increase in both the height and width of the resonant peaks, and that the anharmonicity effects cause the centre of the resonant peaks to shift to lower frequencies, the width of the peaks to increase substantially and the height to decrease, due to the fact that the atoms are distributed over a large range of frequencies.

The increase in height and width due to collisions is larger for lower cloud temperatures, since the collision rate is inversely proportional to the temperature. On the other hand, the frequency shift, width increase and height decrease of the resonant peaks due to the anharmonicity of the trap, are more pronounced for higher initial temperatures, due to the wider range of frequencies of the atoms in the trap.

5.4.3 Evolution of the ensemble properties in time

It is possible to look at the properties of the simulated ensemble as the atoms evolve in the excited potential in order to learn more about the dynamics of the atoms during the resonance. As the trap is shaken we can see how the mean and spread of the energy distribution of the ensemble increase in time, how the density of the ensemble and the elastic collision rate decrease, how the atoms are lost from the trap as they heat up and oscillate with increasing amplitudes, and how the partition of the total energy into kinetic and potential anergy evolves in time. Furthermore, we can compare the results of the evolution with and without collisions.

As the bias field is modulated, the resonantly excited atoms increase their oscillation amplitudes and can eventually escape from the trap. Atom loss was taken into account in the simulation by rejecting atoms that lay outside the confining region of the potential of one videotape trap. This means that after each calculation step, only atoms at positions $|x| < 53\mu$m, $|z| < 4250\mu$m (see figure 5.3), and $y < 2600\mu$m (see figure 2.6(right)) were kept.

Figure 5.9 shows an example for $B_b = 19.32$G in which the potential is shaken at a frequency $\frac{\Omega}{2\pi} = 6800$Hz, approximately at the peak of the corresponding resonance shown in figure 5.1. From top to bottom and from left to right the first plot shows how the mean energy increases with time during the excitation, and the second plot shows how the absolute energy spread also increases with time. When we compare the simulated results with collisions (blue lines) and without collisions (green lines), we see that the mean and the spread of the distribution of energies of the ensemble increase much further with collisions than without them, since more energy is absorbed by the atoms from the excitation when collisions are included in the simulation. This phenomenon was already explained in the previous section.

The third plot in figure 5.9 shows how the calculated collision rate decreases much further when collisions are included due to a larger decrease in density as the excited atoms get hotter and move away from the centre of the trap, and due to the higher rate of temperature increase.

The fourth plot in figure 5.9 shows that the atom loss is slightly larger when collisions

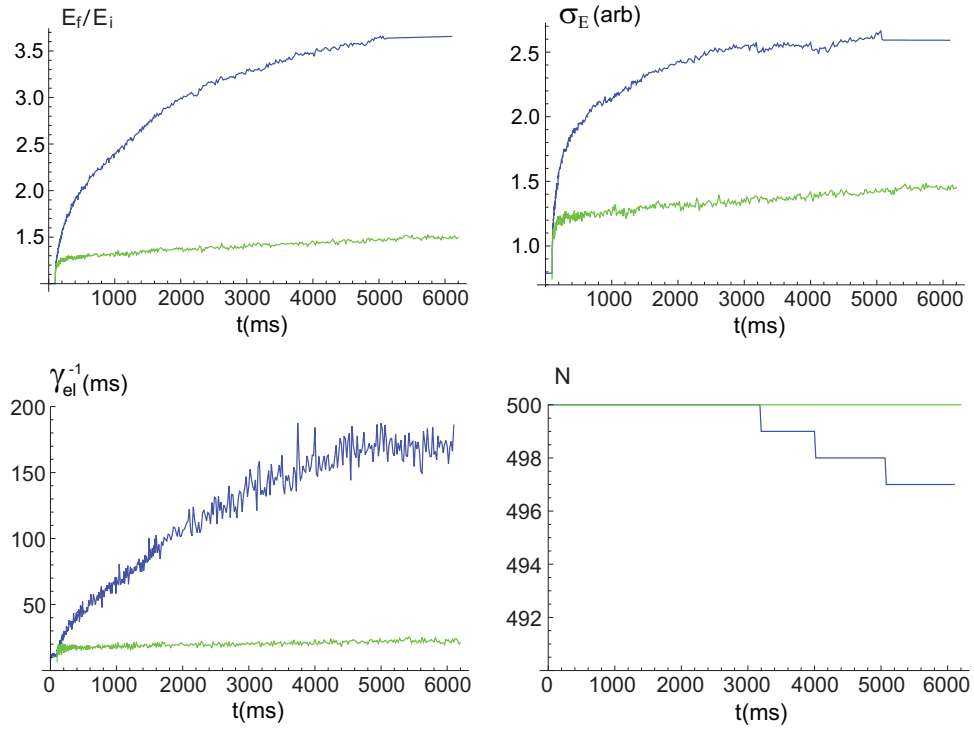

Figure 5.9: Evolution of the properties of an ensemble of atoms as their confining potential is shaken at the resonance frequency $\frac{\Omega}{2\pi} = 6800$Hz. The bias field is $B_b = 19.32$G. Clockwise, the graphs show: the ratio of final to initial average total energy per atom, the spread of the distribution of energies of the ensemble, the average time between collisions, γ_{el}^{-1}, and the atom number. The **blue** lines correspond to the results of the simulation including collisions while the **green** ones correspond to those without collisions.

are present in the simulation due to the larger growth of energy. The value of the parameter η, i.e., the ratio of the limiting depth of the trapping potential, U_0 (equation 5.8 and future table 5.3), to the temperature of the atoms: $\eta = \frac{U_0}{k_B T}$, commonly used to describe evaporative cooling of trapped atoms, evolves from ~ 28 to ~ 8 with collisions and from ~ 28 to ~ 19 without them. It is accepted that significant atom loss takes place when $\eta < 8$ [93].

Figure 5.10 shows the plots of the energy distributions of the ensemble with and without collisions, for the same parameters as in figure 5.9. Both the total energy and the kinetic energy distributions are shown and different colours indicate different evolution times from the beginning to the end of the perturbation, as indicated by the arrow of time. We can see that the energy increase is larger when the simulation includes collisions.

We observe a hole in the total energy distribution around a value of E/U_0 equal to 0.15. This is due to the continuous excitation into higher energy states of the atoms that are resonant with the shaking frequency of 6800Hz. The number of excitation cycles per collision is around 60, so that the redistribution of velocities that takes place due to collisions is too slow compared to the excitation rate that depletes the energy region of the atoms that are resonant with the perturbation. The resonant atoms are those that oscillate transversely in the trap with frequencies around 6800Hz, and going back to figure 5.5, we find that this radial frequency corresponds to a radial oscillation amplitude of $\sim 4\mu$m. In the one-dimensional

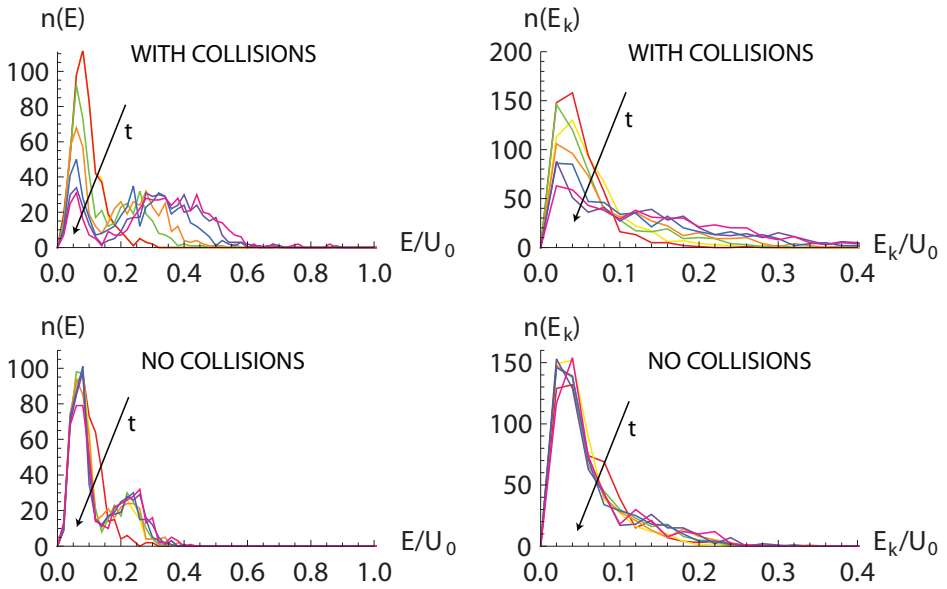

Figure 5.10: Evolution of the distributions of total energy, E, and kinetic energy, E_k, in a videotape trap with $B_b = 19.32$G, excited at a frequency $\frac{\Omega}{2\pi} = 6800$Hz. Results simulated with collisions are shown on the top graphs while those without collisions can be seen on the bottom ones. The size of the bins was $0.02U_0$ and the atom number was 500. The arrows indicate the evolution of time, t.

problem, when either x or y are equal to this amplitude, we can assume that all the energy of the atom is potential energy. From similar plots to those in figure 5.3, but for $B_b = 19.32$G, we obtain that for $x \sim 4\mu$m, the value of $\mu_B(|B(x = 4\mu\text{m})| - |B(x = 0\mu\text{m})|)/U_0$ is ~ 0.15, and similarly for the y-coordinate. This is consistent with the value of E/U_0 at which we see the dip in the energy distribution in figure 5.10. As the excitation continues, atoms keep moving from the energy states resonant with the perturbation to the higher energy anharmonic parts of the potential until fewer atoms remain around $E/U_0 \sim 0.15$ and the growth of energy saturates.

There is a complicated interplay between the energy increase due to the excitation and the decrease in energy due to the loss of the most energetic atoms from the finite-depth trap. The heating rate depends on the strength of the perturbation (*depth*), on the collision rate which in turn depends on the temperature, and on how close the excitation frequency is to resonance. The heating rate decreases as the excitation progresses because the atoms move further from the centre of the potential, causing a decrease in collision rate through a decrease in density and an increase in temperature, and falling out of resonance. The cooling rate due to the escape of the most energetic atoms from the trap depends on the initial temperature of the atoms compared to the limiting depth of the trapping potential, U_0, and on the rate of energy brought into the system. The heating effect dominates at the start of the excitation until the energy of the atoms becomes high enough compared to the trap depth, at which point, the onset of the cooling effect takes place.

It is possible to control whether an overall heating or cooling results from the excitation. Changing the strength of the perturbation, i.e., the value of the parameter *depth*, is one

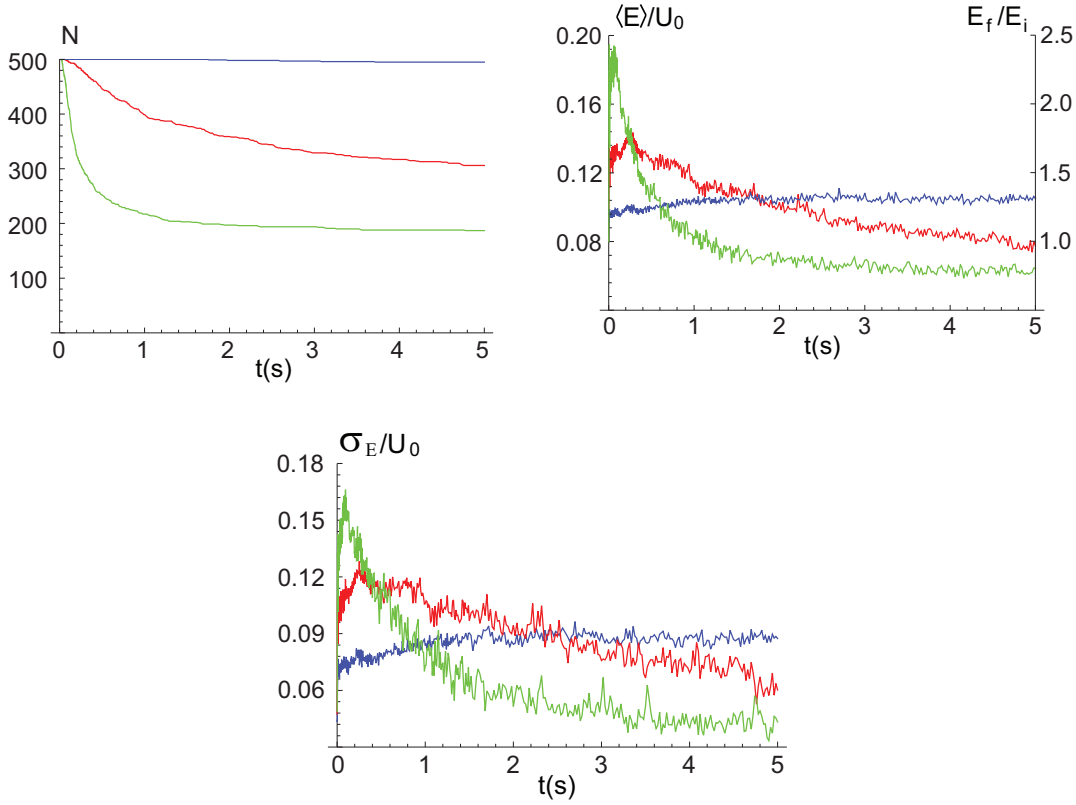

Figure 5.11: Simulated evolution of the atom number and the mean and standard deviation of the energy distribution of an ensemble of atoms in a perturbed videotape trap. The bias field was $B_b = 3.48$G, the initial temperature was $T = 8.3\mu K$, the initial atom number was $N_i = 500$ and no collisions were included in the simulation. The green, red and blue curves correspond to modulation amplitudes of $depth = 0.07$, 0.05 and 0.03 respectively.

way to do this, as shown on the example in figure 5.11. This figure shows the evolution of the mean and spread of the energy distribution, and of the atom number for a videotape trap with $B_b = 3.48$G, the shallowest of all measured. No collisions were included in this example in order to save calculation time, but the concept of modifying the balance between the heating rate due to resonant excitation and the cooling rate due to the loss of atoms from the trap remains valid. When the amplitude of the perturbation is large, i.e., $depth = 0.07$ or $depth = 0.05$, the heating rate is initially very fast and decays as the atoms fall out of resonance with the perturbation, so that the energy increases until the loss of the most energetic atoms becomes the dominant effect, leading to an subsequent decrease in energy. For the highest modulation amplitude, $depth = 0.07$, the rate of energy absorption from the excitation is high enough to result in large atom loss, leading to a final energy below the initial one, i.e., to produce some cooling. When the amplitude of the perturbation is lower i.e., $depth = 0.03$, the heating rate is initially slower but there is hardly any atom loss from the finite-depth trap, so that the final energy reached is higher than for the other cases.

Note that the conditions plotted in figure 5.11 do not correspond to the experimental ones, since no collisions were included in this particular simulation. No overall cooling was observed in our experiment. The heating effect was dominant in all cases since the strength of the perturbation remained small enough and the depths of our videotape traps were large

enough compared to the initial temperatures of the atoms at the start of the excitation.

Another way to control whether a hotter or colder cloud is obtained at the end of the perturbation is to modify the ratio of initial temperature to trap depth, for instance by applying an RF knife to limit the depth of the trapping potential. References [102], [103] and [104] report on experimental observations of cooling by exciting trapped atoms through parametric resonance. Further details on these references can be found in the last section of this chapter.

5.4.4 Simulation results

The simulation results are presented and discussed in this section, and they are compared with the experimental measurements. The simulation was carried out using Mathematica for the parameters given in table 5.2.

B_b(G)	$T(\mu$K)	*depth*	B_z(G)	N	$U_0(\mu$K)	t_c(days)
3.48	8.31	5.0×10^{-2}	2.22	5000	249	13.5
5.95	8.62	2.5×10^{-2}	2.22	500	360	3.8
8.42	8.61	1.7×10^{-2}	2.22	500	494	6.0
13.38	13.25	1.0×10^{-2}	2.22	500	793	5.4
19.32	42.04	6.8×10^{-3}	2.22	500	1172	7.0
25.75	57.17	5.0×10^{-3}	2.22	500	1179	8.8
30.70	69.64	4.2×10^{-3}	2.22	500	1182	5.0

Table 5.2: Parameters used to carry out the full simulation of the evolution of atoms in a videotape trap with modulated bias field. T is the initial temperature of the ensemble of atoms, *depth* is the relative strength of the modulation, N is the number of atoms in the ensemble, U_0 is the limiting depth of the trapping potential and t_c is the computation time.

Figure 5.12 shows the comparison between experimental and simulated results. The experimental results are presented normalised to the offset temperature from the Lorentzian fit. The simulated ones show the ratio of final to initial total energy of the ensemble of atoms after 5s of bias field modulation. If we assume that the cloud is in thermal equilibrium, we can say that the total energy of the simulated ensemble is proportional to the temperature and therefore it is fair to compare both graphs. The simulated results are in good agreement with the experimental measurements.

The resonant peaks corresponding to $B_b = 19.32$G, $B_b = 25.75$G and $B_b = 30.70$G are clearly broader and smaller in height, both in the simulation and in the experiment. For these three bias fields, the experimental absorption images at the end of the excitation were taken after moving the cloud away from the chip surface, to a less confining videotape trap (see section 5.2.2). This movement caused the cloud to expand adiabatically, reducing its temperature. This means that, for these bias fields, the temperature measurements shown in figure 5.1 correspond to lower temperatures than those in the trap in which the atoms were shaken.

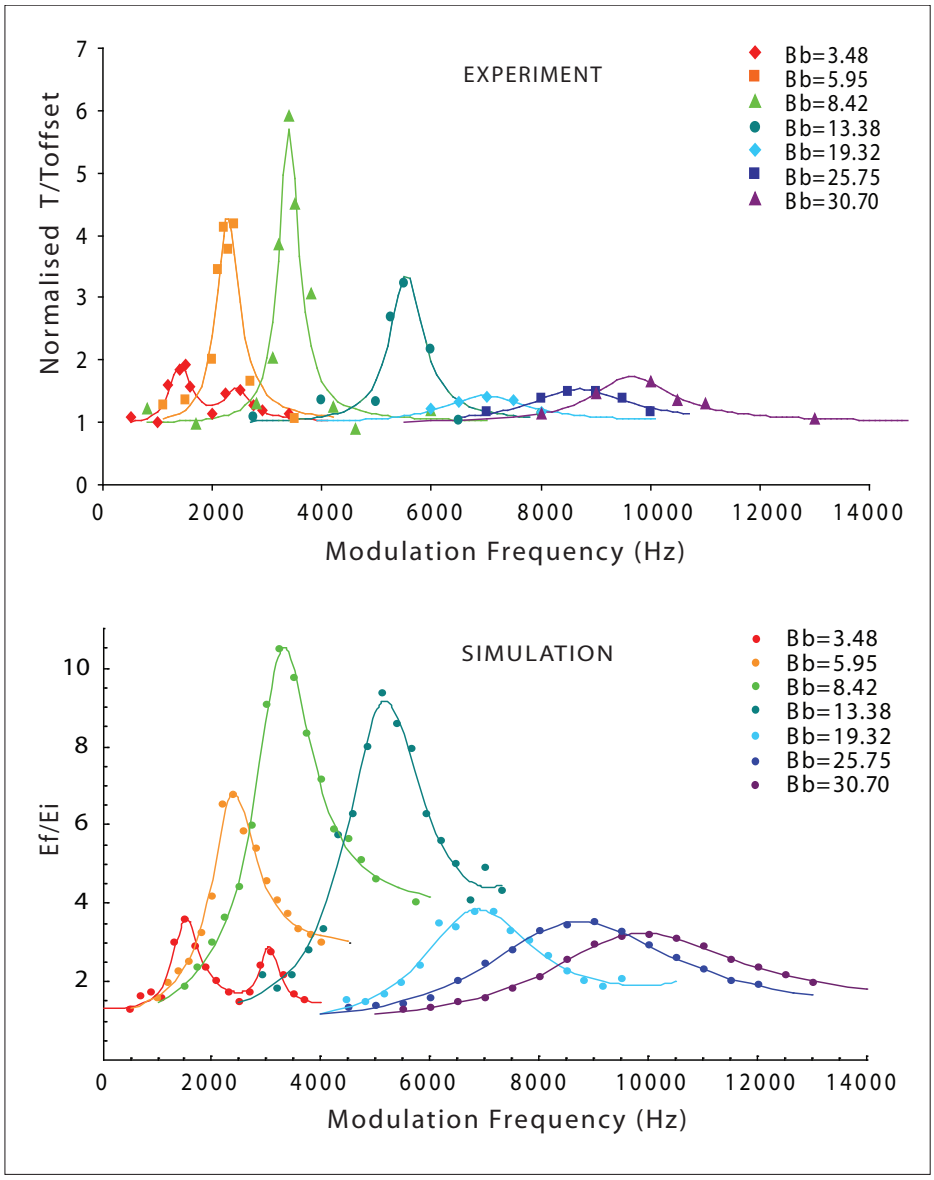

Figure 5.12: **Top**: measured atomic cloud temperature, normalised to the offset temperature, versus modulation frequency, for the seven different bias fields B_b, in Gauss. **Bottom**: simulation results for the ratio of final to initial average total energy per atom as a function of the excitation frequency, for the same values of the bias field. The markers correspond to the experimental or simulated data, while the solid lines correspond to the Lorentzian fits to the data.

The temperatures used in the simulation for these bias fields are shown in table 5.2: they are considerably higher than those for lower bias fields. Due to these larger temperatures, and as mentioned in section 5.3.2, the departure from harmonic confinement was considerably larger for the three highest bias fields, leading to smaller and broader resonant peaks compared to the higher and narrower resonances that correspond to the lowest four bias fields. For the three highest bias fields, the temperatures in table 5.2 were obtained assuming an adiabatic decompression from the shaking trap to the trap in which the clouds were imaged (see the beginning of section 5.4).

Using the temperatures shown in table 5.2, we calculate that the number of radial oscillation cycles per collision was between 50 and 70 for the four lowest bias fields, and

between 170 and 200 for the three highest bias fields. The lower collision rates also explain the lower height of the resonant peaks observed for the three highest bias fields. The number of axial oscillation cycles per collision went from ~ 0.75 to ~ 0.3 when going from lower to higher bias fields.

Figure 5.13 shows the fit of the simulated frequencies versus the experimental ones. Note that the calibration of the bias field as a function of the computer control voltage (see section 5.2.2) was adjusted so that the central frequencies of the simulated resonant peaks would be as close as possible to the experimental ones. After using the same bias field calibration ($B_b(G) \approx 1G + 4.95V_c(Volts)$) for all bias field values, we found a slope of 1.00 ± 0.03 for the fit of the simulated frequencies versus the experimental ones. An offset of $(-0.4 \pm 2) \times 10^2$Hz was found, consistent with zero and very small given the scale of transverse trap frequencies that lie between 1500Hz and 10000Hz.

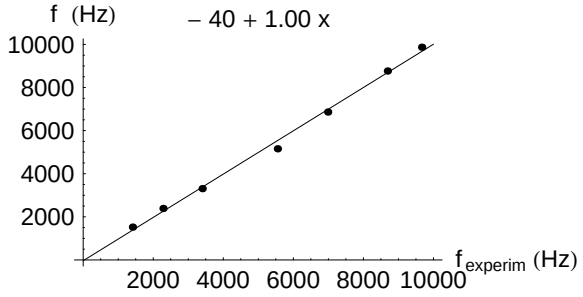

Figure 5.13: Fit of the simulated versus experimental radial videotape trap frequencies. The frequencies are obtained from the centres of the Lorentzian fits to the simulated or measured resonant peaks.

Both the height and the width of the simulated resonant peaks are overestimates compared to the experimental ones. The widths of the simulated resonant peaks strongly depend on the initial temperature of the atoms (see section 5.4.2) and therefore on the range of transverse oscillation frequencies possible in the trap before the excitation. These in turn depend on the anharmonicity of the potential along its radial directions and on the variation of the transverse frequencies along z. The uncertainty in the determination of the initial temperatures is explained in the following subsection about discussion of errors.

The height of the peaks depends strongly on the collision rate: the higher it is, the more energy that can be absorbed by the system. The collision rate was calculated for an atom number equal to 10^5 in the simulation, while the measured atom number in the experiment was between 10^4 and 10^5. Since the upper bound of the atom number range was used, the calculated collision rate could have been up to a factor of 10 higher than in experiments, causing a noticeable difference and resulting in higher simulated peaks.

Figure 5.14(left) shows the simulated resonance in atom loss together with the simulated resonance in energy ratio, the latter re-scaled for clarity. Note how the resonance in atom loss takes place at frequencies below those of the resonance in energy. This is due to the fact that the most energetic atoms that are likely to escape from the trap are those that

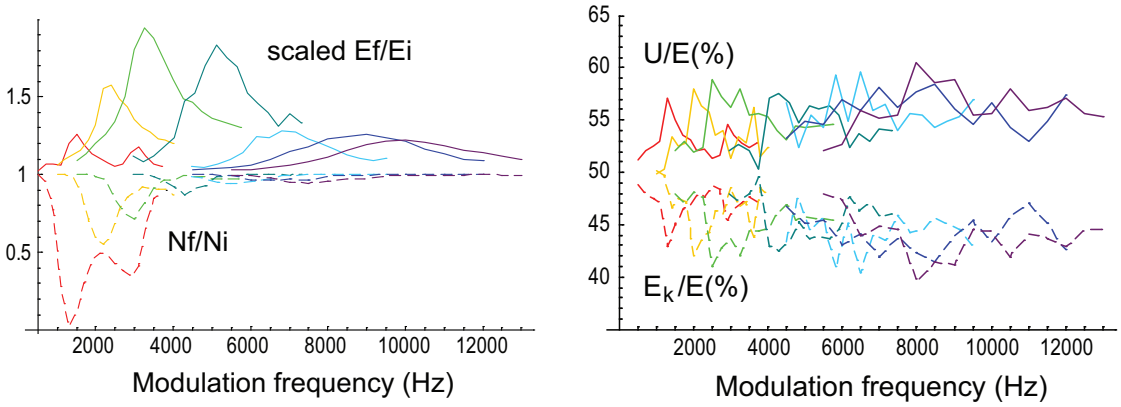

Figure 5.14: Results from the simulation. **Left:** the solid lines show the total final average energy per atom divided by the initial one and re-scaled for clarity, as a function of the excitation frequency. The dashed lines show the resonance in atom loss, with the ratio of final to initial atom number plotted versus the modulation frequency. **Right**: partition of energy versus modulation frequency. The solid lines show the average potential energy (U) as a percentage of the average total energy, while the dashed ones do the same for the average kinetic energy (E_k). The colour code indicates the same bias field values as in figure 5.12.

explore its anharmonic regions and hence oscillate with the lowest frequencies.

Experimental observations of this fact have been reported by several groups, as summarised in section 5.5. Unfortunately, the atom number obtained from our measured absorption images was too noisy (see the following subsection about discussion of errors) and did not reveal a resonance in atom loss, so no data can be offered here for comparison.

The simulated atom loss is bigger for low bias field values. For the lowest bias field, the trap depth is similar and low along both the x and y directions, with much larger depth along z (see table 5.3). For all other bias fields, the depth of the trap along x is about twice that along y. This explains why the trap loss is higher for the lowest bias field, as the radially excited atoms can escape along both the x and y directions. For the first four bias fields the limiting depth is the one along y, while for the last three, it is the one along z, which means that collisions are needed to transfer energy to the axial degree of freedom before the atoms can escape[1]. This explains the lower atom loss obtained for the highest three bias fields.

Figure 5.14(right) shows how the total energy of the ensemble is distributed into kinetic (E_k) and potential (U) energy. From the Virial theorem we know that, for a potential of the form $U(r) = \alpha r^n$, we can write $\langle E_k \rangle = \frac{n}{2}\langle U \rangle$. Therefore, in a spherical harmonic potential, the average kinetic and potential energies correspond to 50% of the total energy each. In a linear trap with equal confinement in the three directions, the average kinetic energy would correspond to $\sim 33\%$ of the total energy while the potential would account for the remaining $\sim 67\%$. Since our trap is nearly harmonic along its axial direction and close to linear for large oscillations along its transverse directions, the potential energy should correspond to $\sim 61\%$ of the total energy. In the figure we see how, as the resonance is approached,

[1]The collision rate is low. We calculate $\sim 50 - 200$ radial oscillation cycles per collision.

B_b(G)	$T(\mu$K)	Trap Depth-$x(\mu$K)	Trap Depth-$y(\mu$K)	Trap Depth-$z(\mu$K)	$U_0(\mu$K)
3.48	8.31	323	249	1142	249
5.95	8.62	643	360	1152	360
8.42	8.61	970	494	1158	494
13.38	13.25	1630	793	1167	793
19.32	42.04	2424	1172	1174	1172
25.75	57.17	3286	1592	1179	1179
30.70	69.64	3949	1919	1182	1182

Table 5.3: Trap depths along the x, y and z directions, in units of temperature, compared to the initial temperatures used in the simulation for each bias field value. The limiting depth of all of them, U_0, is shown in the last column.

the partition of the energy departs from close to the harmonic values of $50-50\%$ towards the more linear values around $61-39\%$. The initial conditions for higher bias fields are less harmonic than those for lower bias fields, in agreement with the previously calculated estimations of the anharmonicity, obtained from $\frac{3\sigma_{x,y}}{r_h}$ (see section 5.3.2).

Figure 5.15 shows the resonance in the mean and the standard deviation of the total energy and of the kinetic energy of the simulated ensemble of atoms as a function of the excitation frequency. Note how the resonance in the spread of the energy distributions takes place at frequencies below those of the resonance in mean value. This is due to the fact that the excitation of high-energy atoms that oscillate with frequencies below the harmonic ones can lead to a large increase in the spread of the energy distribution.

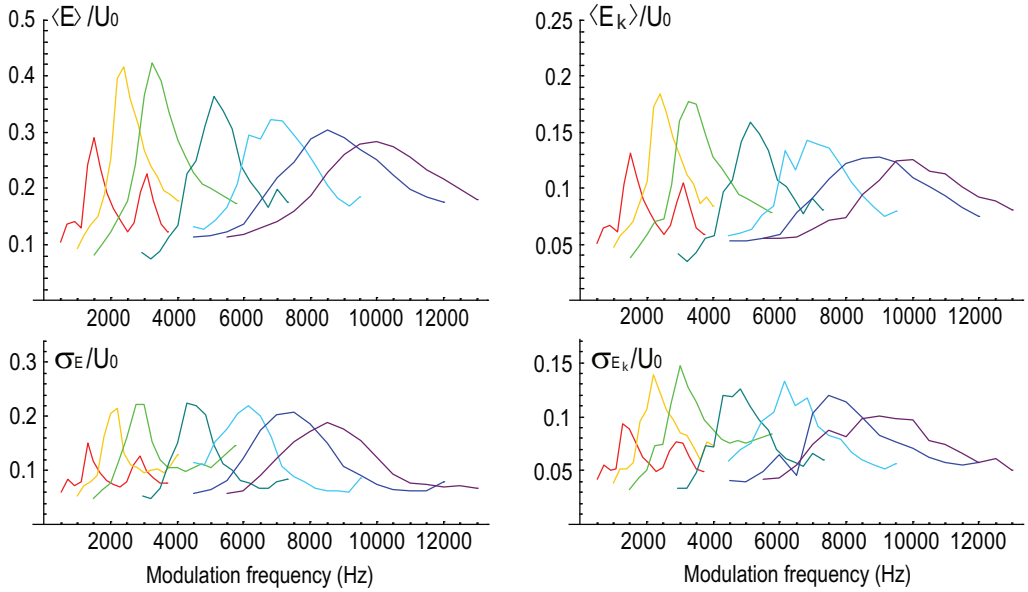

Figure 5.15: Mean and standard deviation of the distribution of total energy (**left**) and kinetic energy (**right**) of the atoms in the ensemble, normalised to the limiting trap depth, U_0. The colour code indicates the same bias field values as in figure 5.12.

Discussion of errors

It was mentioned already how the atom number, $N = 10^5$, chosen to calculate the collision rate possibly contributed to produce simulated resonant peaks higher than the experimental ones. The fact that the expressions used for $\langle n \rangle$ and $\langle v_{rel} \rangle$ in the calculation of the elastic collision rate (see equation 4.13) assume a harmonic potential also introduces an error in the simulation.

The temperature of the atoms at the end of the excitation was obtained by fitting the integrated axial density profile obtained from the in-trap absorption image of the cloud. The confining magnetic field varies along the axial direction of the trap inducing a different Zeeman shift of the hyperfine sub-levels relevant for the imaging transition as we move along the axis of the cloud. The Zeeman shift of the energy of the imaging transition from $5\ ^2S_{1/2}$, $F = 2$, $m_F = +2$ to $5\ ^2P_{3/2}$, $F = 3$, $m_F = +3$ is 1.4MHz/G. This reduces the absorption cross-section further for large $|z|$ than for $z = 0$. Hence, the measured width of the recorded axial density profile was underestimated. This means that the temperature values used for the simulation were underestimated by a factor that we calculate to be $\sim 1.2-1.3$. Since the height of the resonant peaks increases as the initial atomic temperature in the simulation decreases, this could also explain why the simulated peaks are higher than the measured ones.

The precision in the determination of the initial temperatures for the simulation from the offset of the Lorentzian fits to the data was low due to the fact that only a few points were measured for each resonant peak. The error given by the fit for the initial temperatures ranged between 21% and 36%, for all bias fields, except for $B_b = 19.32$G, for which the error was much larger, of 88%, due to the lack of data points in the wings of the Lorentzian.

The initial atom number was not perfectly reproducible from point to point within the same resonant peak during data taking. The experimental technique explained in section 4.2.2 to maintain a steady initial atom number during data acquisition had not yet been implemented when these data were taken. Fluctuations in the initial atom number led to changes in the initial collision rate before the excitation resulting in noise in the measured temperature data points. This noise was estimated to be between 4% and 8% in atom number for $B_b = 30.70$G, 19.32G and 13.38G, and between 19% and 27% for the remaining bias fields.

5.5 Published work related to the subject

While a good number of papers have reported studies of parametric excitation of particles in a trap, we were able to find very few reports of the excitation of trapped particles by shaking the trap centre. However, these two phenomena share many common features, and we found the studies of parametric resonance reported here very relevant and useful for a better understanding of the dynamics involved in the experiments detailed on this chapter.

Theoretical studies of parametric resonance can be found, both from a classical and quantum point of view. Reference [99] shows how to solve the classical equation of motion of a harmonic oscillator under parametric excitation and how to predict the amplitude and width of each resonance. References [105, 106] and [107, 108] solve a classical Mathieu equation of motion to explain the parametric resonances they measured with electrons in a Penning trap and with neutral atoms in a magneto-optical trap, respectively. As for the quantum point of view, references [109–113] present a non-perturbative treatment of the problem, valid only for harmonic traps, that yields the same results as the classical treatment. This approach includes no collisions, takes into account atom trap loss and is mostly applied to far-detuned optical traps.

References [109–111] describe laser-noise-induced heating in far-off resonance optical traps. Noise in the trapping laser intensity causes fluctuations of the trap's spring constant, through which atoms can be parametrically excited when the frequency of this noise is close to twice the trap frequency. At resonance, the average energy of the atoms increases exponentially, with a time constant that is directly proportional to the amplitude of the power spectrum of the laser intensity noise at the given excitation frequency. In a similar way, beam-pointing noise causes fluctuations in the centre of the trap and leads to linear heating. Faster heating is observed when the frequency of this noise matches the trap frequency. The evolution of the energy distribution, $n(E, t)$ and of the trapped population is calculated in references [110, 111]. The mean of the energy distribution can increase or decrease depending on the ratio of atomic temperature to trap depth. A satisfactory comparison between the calculated and measured lifetimes of atoms trapped in an optical trap with laser-induced noise is reported in reference [111].

References [112,113] provide a quantum perturbative treatment of the problem, extending the model to include the anharmonicity and broadening due to the band structure of the energy levels in a one-dimensional sinusoidal optical lattice. Their calculations are in good agreement with the experimentally measured spectrum of the atom loss associated to the parametric excitation of ^{40}K fermionic atoms in a 1D optical lattice [112]. Broadening due to the lattice band structure was also reported in reference [114], where the main radial and axial parametric resonances, along with their first sub-harmonics were measured in a 1D optical lattice and compared to the narrower resonances in an optical dipole trap.

In the experiments reported in reference [112] the laser intensity was modulated intentionally in order to measure the lattice vibrational frequency and trap depth. The resonances in atom loss were observed at 0.9, 1.85 and 3.5 times the axial frequency of the trap. High energy atoms that explored the edges of the trap, where the curvature of the sinusoidal lattice potential was decreased, oscillated with lower frequencies than low-energy atoms that were close to the near-harmonic trap centre. Therefore, the loss of atoms was stronger when the excitation frequency was tuned to the red of the temperature resonance. This has been observed in several experiments for both parametric shaking [102,103,112,115,116], and for shaking of the trap centre [104], and agrees with the results of our simulations.

Parametric excitation can be used as a way of energy-selective removal of the hottest atoms from the trap, resulting in cooling when the depth of the trap is small compared to

the temperature of the atoms. Cooling was reported in reference [102], where the atomic temperature of ^{40}K atoms in a 1D optical trap was around 80μK, with a trap depth of around 700μK. Data for radial and axial parametric resonances in atom loss and temperature was presented. Heating took place when the excitation was tuned to a narrow range of frequencies around $2\omega_0/n$, while cooling occurred for a broad range of excitation frequencies on the red of $2\omega_0/n$, showing an exponential decrease in atom number and temperature.

Reference [103] reports on the observation of parametric excitation of rubidium atoms in a magnetic quadrupole Ioffe configuration (QUIC) trap. The resonance in atom loss and temperature was measured as well as their time evolution for the excitation at twice the axial trap frequency and also slightly to the red of that. Two values of the ratio of temperature to trap depth were used: 0.57 and 0.07, highlighting the importance of this ratio in producing either resonant cooling or heating. They acknowledged the fact that interatomic collisions can play an important role but did not take them into account.

Parametric resonance has also been used to experimentally confirm the double structure of a magneto-optical trap (MOT) by selectively exciting its Doppler part to separate it from the sub-Doppler part, allowing further studies of the sub-Doppler component [107]. Parametric excitation induced in a MOT by modulating the intensity of one pair of laser beams can also be used to measure the natural trap frequency for different magnetic field gradients, as reported in reference [108].

The characteristic oscillation frequencies of trapped ions or charged particles can be measured by resonantly exciting their motion in the trap (see for example [105, 106, 117, 118]). Measurements of the motional excitation spectrum of electrons in a Penning trap are reported in references [105,106]. They observed resonances at the fundamental trap frequencies and at linear combinations of them due to the non-separability of the trapping potential. They also observed parametric sub-harmonics at frequencies $2\omega_0/n$ up to $n = 10$. The anharmonicity and non-linearity of the trapping potential was used to explain the observed asymmetric line-shape of the first-order parametric resonance. Measurements of parametric axial resonances for Ar^+ ions in a Paul trap are presented in reference [119], along with a numerical calculation. The phase difference between the driving excitation and the ion motion (φ in equation 5.3) was measured as a function of the excitation frequency in reference [117]. The aim was to obtain the damping rate of the ion motion (γ) in order to determine the laser cooling rates of the different motions of beryllium ions in a Penning trap.

Fewer references study in detail the excitation of trapped particles by shaking the centre of the trap [104, 109, 110, 113, 117]. As mentioned before, references [109, 110, 113] describe the theory of the problem from a non-perturbative quantum approach yielding results that can also be obtained classically. This theory is applied to truncated harmonic traps to include the loss of atoms from the trap, and does not account for inter-atomic collisions or for the anharmonicity of the trap.

M. Kumakura et al. [104] investigated the excitation of neutral atoms (rubidium) in a cloverleaf configuration magnetic trap. The centre of the confining potential was shaken along its transverse direction during two seconds by varying a bias magnetic field sinusoidally. The atomic cloud was then left to thermalise for 3s and its absorption image was recorded

after a time of flight of 5ms. Radial resonances were observed in atom loss and temperature as a function of the excitation frequency, around ω_0 and $2\omega_0$. An RF knife was applied in order to truncate the trap depth. When the initial temperature of the atoms was around 0.36mK, with a ratio of this temperature to the effective depth of 0.075, some atoms were lost during the shaking and the remaining ones at the end of the excitation appeared to be hotter for most of the excitation frequencies. However, when the ratio of atom temperature to effective trap depth was increased to 0.18, the loss of atoms during the excitation was higher and a dispersive resonance was observed in the temperature as a function of the frequency of the excitation, with cooling or heating taking place at the low-frequency or high-frequency side of the resonance respectively. They measured an increase in phase-space density by a factor of 2 and proposed this as a method to produce controlled evaporative cooling in a magnetic trap. They also presented a numerical simulation based on the classical solution of a one-dimensional equation of motion. Their model is much simpler than the one presented in this thesis, since it is one-dimensional, does not include atomic collisions and does not account for the loss of atoms from the finite-depth trap.

5.6 Conclusion

Experimental measurements of the excitation of the transverse motion of cold thermal atoms confined in videotape traps were presented here and successfully compared to the simulated results. The excitation was induced by modulating the position of the trap centre in time. The transverse trap frequencies were obtained from the measured resonant peaks for various values of the bias field and a good understanding of the dynamics of the trapped atoms during the perturbation was gained through the simulation.

We learnt through both the simulation and the experiment that, at temperatures around $10 - 70\mu$K, the atoms oscillate with a wide range of transverse frequencies in the videotape traps and that the central frequencies of the observed resonances lie below the calculated harmonic frequencies, which are only valid for very small oscillations close to the bottom of the trap.

As compared to other models and simulations mentioned in the bibliography, our simulation provides one of the most detailed and complete attempts to reproduce the observed resonances, since there seems to be no other models in the literature that include collisions between particles together with anharmonicity effects. Our experiment provides one of very few measurements of resonant heating of trapped particles through shaking of the centre of the confining potential, as opposed to through parametric excitation.

Chapter 6

Fragmentation studies

6.1 Introduction

Ultra-cold neutral atoms can be trapped in confining potentials generated by current-carrying structures, permanent magnets or tightly-focused light. When an atom chip is used to produce the confining potential, the ultra-cold atoms can be trapped in very close proximity (a few μm) to the surface of the chip. Most atom-chip experiments have observed surface effects such as lifetime reduction due to thermally-induced spin-flip loss and fragmentation of the trapped cloud due to corrugations in the confining potential. These effects have been an obstacle in the progress towards the experimental realisation of one-dimensional (1D) quantum gases on atom chips, as the high transverse frequencies needed to reach this regime can usually only be achieved very close to the surface of the chip. Corrugation of the trapping potential has also constituted an added difficulty for the guided transport of ultra-cold atoms close to the surface of atom chips.

This chapter focuses on the study of the roughness of the magnetic potential produced with our permanently magnetised videotape atom chip. Section 6.2 begins by mentioning the first experimental observations of corrugated trapping potentials in current-carrying wire atom chips, and follows by giving an overview of the subsequent studies on the subject with permanent-magnet atom chips and optical traps up to 2008. Section 6.3 describes and analyses the observed axial fragmentation of elongated clouds of ultra-cold ^{87}Rb atoms in our videotape atom-chip experiment.

6.2 Disorder in the trapping potential

A thermal cloud of atoms confined in a corrugated magnetic potential will begin to break up in fragments when the thermal energy of the atoms is comparable to the depth of the corrugations in the potential, which can typically reach up to a few microKelvin for atom-surface separations below 100μm, in most atom-chip experiments. The relevant energy scale for a thermal cloud is therefore the temperature of the atoms, while for a Bose-Einstein condensate (BEC), it is the chemical potential.

For the past ten years, several experimental groups around the world have been able to routinely prepare ultra-cold thermal or condensed atomic clouds, allowing the study of

surface effects such as fragmentation using atom chips.

6.2.1 Fragmentation on atom chips based on current-carrying wires

Observations of axial fragmentation of cold thermal clouds or Bose-Einstein condensates trapped in the proximity of atom chips based on current-carrying wires were first reported in 2002-2003 by the research groups of C. Zimmermann in Tübingen, Germany [120–122], of W. Ketterle and D. E. Pritchard in Cambridge, Massachusetts, U.S.A [123, 124], and of E. A. Hinds in London, U.K [125].

J. Fortágh et al. [120] and A. E. Leanhardt et al. [123] observed periodic fragmentation of condensates and thermal clouds at distances between 50μm and 150μm from the micro-structured conductors in their chips. Axial expansion in the waveguide revealed pinning of the condensed fraction in the fragmented potential while the thermal component of the cloud propagated in the waveguide [120]. The reflection and transmission of a sodium condensate through the perturbations of the potential was studied as a function of its incident velocity in reference [123]. M. P. A. Jones et al. [125] observed how a thermal cloud of ^{87}Rb atoms at a temperature of around 5μK started to fragment at distances below 100μm from the surface of a 500μm-diameter wire.

These experimental observations of fragmentation of atomic clouds when approaching the surface of metal conductors revealed the presence of an unexpected surface potential of unexplained origin. The magnetic origin of fragmentation was first confirmed by S. Kraft et al. [121] who managed to invert the maxima and minima of the fragmented atomic density profile by inverting either the offset axial field or the current through the trapping wire together with the bias field. They were able to show that the corrugations in the axial trapping potential were due to an anomalous longitudinal component of the magnetic field along the wire.

A. E. Leanhardt et al. [124] also demonstrated the magnetic origin of the observed disorder potential by showing how condensates confined in micro-fabricated magnetic traps were fragmented, while they remained intact under optical confinement at the same location. They concluded that the corrugation of the potential arose from deviations of the current flow from a straight line inside the micro-conductors, possibly due to imperfect micro-fabrication or bulk defects.

An ideal infinitely-long and infinitely-thin wire along the z direction generates a magnetic field with components only in the plane perpendicular to the wire. However, a real, finite-cross-section wire can generate a small longitudinal field component along z, several orders of magnitude smaller than the main transverse circular field component, due to the deviations of the current flow from a straight line parallel to the direction along the wire (see figure 6.1).

The way in which a magnetic trap for atoms can be created by combining the magnetic field of a straight wire with a uniform bias field was explained in section 2.3. Only the small anomalous magnetic field components, ΔB_z, directed along the wire axis and generated by current flow deviations inside the wire can give rise to a corrugated axial potential. Fluc-

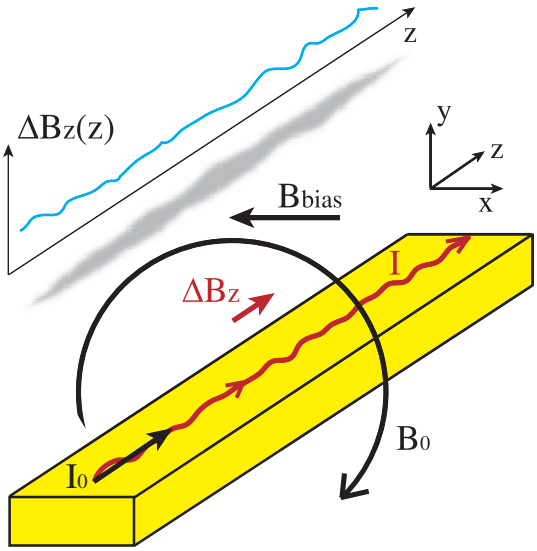

Figure 6.1: Example of fluctuations in the current flow direction inside a non-ideal wire. Deviations of the current from a straight line generate an anomalous axial magnetic field component, ΔB_z, that gives rise to axial fragmentation of an atomic cloud in a trap formed by the field of the wire, B_0 and a bias field B_{bias} (no axial confinement of the cloud shown).

tuations of the transverse magnetic field components created by the conductor in the x-y plane can only lead to small displacements of the trap centre in the transverse plane. The fluctuations in the transverse magnetic field components are usually very small compared to the bias field used to create the magnetic trap, and therefore the small displacements of the trap-centre position usually lie below the typical imaging resolution.

It is possible to obtain the disorder potential and the anomalous component of the magnetic field, ΔB_z, in these atom traps by measuring the density profile of ultra-cold thermal clouds via absorption imaging (see section 3.5.2). The integrated axial density profile, $n(z)$, is proportional to the axial probability distribution of the atoms in the trap, which, for a cold cloud of atoms in thermal equilibrium at temperature T, is given by the Maxwell-Boltzmann probability distribution: $n(z) \propto \exp(-\frac{U(z)}{k_B T})$. In this way, the absorption images reveal the axial potential, $U(z)$, that the atoms feel in the trap, which consists of the disorder potential, $U_{dis}(z)$, superimposed on the intended axial-confinement potential. For the case of the expansion of atoms in a waveguide with no axial confinement, $U(z)$ directly yields the disorder potential. Along the axis of the trap, where the transverse magnetic field is zero, the disorder potential is related to the anomalous longitudinal magnetic field, $\Delta B_z(z)$, as follows: $U_{dis}(z) = \mu_B g_F m_F \Delta B_z(z)$.

In the work presented by M. P. A. Jones et al. [126], density profiles of fragmented thermal clouds were measured for several distances to the wire surface, and a map of the anomalous magnetic-field component, $\Delta B_z(y, z)$, was obtained as a function of the position,

z, along the wire and the distance, y, to its surface, as explained in the previous paragraph. Both references [126] and [121] showed how the depth of the disorder potential increased monotonically with the current in the wire and decreased with the distance from the wire, d. A power law dependence of $d^{-2.2}$ for the strength of the disorder potential was measured in reference [121] by splitting a BEC in the disorder potential at different distances to the chip surface between 80 and 109μm. Measuring over a wider range of distances, between 7 and 97μm, M. P. A. Jones et al. [126] measured a decay of the amplitude of the anomalous field ΔB_z well described by the modified Bessel function, $K_1(k_0 d) \sim \frac{\exp(-k_0 d)}{\sqrt{k_0 d}}$, consistent with an oscillating current flow inside the wire with a sinusoidal transverse component of wave-vector k_0. In the cases in which the transverse deviations of the current flow inside the wire have more than a single spatial Fourier component, the above expression stops being a good approximation.

Initially, it was thought that fragmentation phenomena might be limited to copper conductors, as fragmented clouds had been observed near copper wires [120–123, 125, 126], but similar corrugations in the potential were soon observed also for cold atom clouds trapped in the proximity of wires made of other metallic elements such as silver [127] or gold [124, 128, 129].

Possible physical causes of the fluctuations in the current-flow direction had been thought to be edge or surface roughness of the current-currying wire, or the microscopic structure within the wire (grains and defects). In a theoretical paper, D.-W. Wang et al. [130] proposed small deviations of the positions of the edges of a flat wire as the cause for a fluctuating current density, and showed how these were enough to explain the observed fragmentation of atomic clouds at distances much larger than the height of the wire. For a white noise spectrum, the strength of the disorder potential was found to have a dependence of $d^{-2.5}$ at distances d much larger than the width of the wire. Note, however, that this mechanism was considered in reference [126] and shown not to be the cause of the potential roughness observed in that experiment.

Following the ideas in reference [130], J. Estève et al. [128] were able to conclude that the potential roughness produced by their gold-electroplated micro-wire was indeed due to the geometric fluctuations of the edges of the wire. They measured the disorder potential using ultra-cold thermal clouds of ^{87}Rb atoms trapped at distances between 33 and 170μm from a rectangular cross-section wire of height equal to 4.5μm and width equal to 50μm. They found good agreement between the disorder potential measured with cold atoms and the potential computed following the theory in reference [130], for which they used the geometric roughness of the wire edges measured with a scanning electron microscope. In a later, more detailed paper [129], the same group included the effect of geometrical roughness in the top surface of the wire showing theoretically how it becomes increasingly important as the distance to the wire decreases. In contrast, the effect of wire edge roughness saturates as the wire is approached. Considering either edge-roughness or surface-roughness effects, they calculated the same dependence of $d^{-2.5}$ for the rms potential roughness as reference [130], valid for distances much larger than the width of the wire.

P. Krüger et al. [131] later measured the roughness potential at distances below 50μm from the surface of two flat wires 3.1μm in height, and 10 and 100μm in width respectively. The amplitude and frequency spectrum of the roughness potential scaled similarly with the distance to the wire, d, for both wires, and the scaling with d was stronger than expected from the edge roughness model provided by [130]. Measuring 10μm away from the 100μm-wide wire, the spectral amplitude of the roughness at several spatial frequencies was found to be nearly constant over the whole wire width. These observations, together with reference [126], indicated that wire-edge fluctuations were not the dominant cause for fragmentation at distances small compared to the width of the wire, suggesting other effects such as local current-path deviations due to inhomogeneous conductivity or top surface roughness.

Given that macroscopic or electroplated micro-wires were being used by most experimental groups at the time, and that their geometrical roughness had been shown in some cases to be the cause of fragmentation, different fabrication techniques started to be used around 2004-2005, such as electron-beam or optical lithography followed by gold evaporation [57, 129, 131], leading to substantially smoother wires. P. Krüger et al. [131] reported that no fragmentation had been observed for thermal clouds with temperatures $\sim 1\mu$K trapped at distances down to 5μm from the surface of the micro-fabricated wires in their chip while the more sensitive 1D quasi-condensates started to fragment at distances below 30μm from the chip surface.

The edges of lithographically patterned wires were found to usually exhibit self-affine fractal roughness [132]. Edge roughness is the main cause of potential roughness when the distance from the magnetic trap to the wire surface is comparable to the width of the wire. Z. Moktadir et al. [132] studied the effect of self-affine fractal roughness on the magnetic noise of atom traps, as opposed to previous studies [126, 129, 130] which had considered edges with a white noise spectrum or other specific spectra.

The group of J. Schmiedmayer [56–58] demonstrated the possibility of using fragmentation effects in a one-dimensional quasi-condensate with very small chemical potential as a tool for microscopic magnetic field imaging. They showed how high field sensitivity and high spatial resolution could be achieved simultaneously, as opposed to conventionally used magnetic field sensors such as magnetic force microscopes, Hall probes, SQUIDs (superconducting quantum interference devices) or thermal atom magnetometers, which can only provide either one or the other. With accurate position control of the quasi-condensate they were able to image the magnetic field of both the trapping wire and an independent sample wire with a sensitivity of 4nT and a spatial resolution of 3μm at a distance of 3μm from the surface of the wires.

The same group [59] used ultra-cold atoms as a sensitive probe for solid-state science and studied the microscopic deviations of the current flow in poly-crystalline gold films. Edge roughness effects were negligible due to the smooth fabrication, the planar shape of the metallic films (0.3-2.1μm high by 200μm wide), and the fact that the atoms were trapped at a distance from the film of 3.5μm, very small compared to the wire width. Defects present in

the bulk of the metal were expected to produce current deviations with short wavelengths of the order of nanometres. Surprisingly, long-range fluctuations were observed in the current flow pattern, with regions of maximal current inclined by $\sim \pm 45^\circ$ to the main current flow parallel to the wire. The observed pattern could not be explained from wire thickness variations or changes in grain size, but it was instead found to be consistent with the scattering of the current flow at defects inside the wire.

Following the success of the improved fabrication techniques that had led to a reduction of the potential roughness in wire magnetic traps by up to two orders of magnitude, a new method to reduce fragmentation was successfully implemented by J.-B. Trebbia, I. Bouchoule et al. [133,134] that consisted of rapid current modulation to smooth and average out the fragmentation potential. This method had been first proposed by S. Kraft et al. [121] who showed that the maxima and minima of the fragmented atomic density profile could be inverted by inverting the direction of the current in the trapping wire and the bias field. In the experiment of reference [133], both the current in the trapping wires and the bias field were modulated simultaneously at frequencies around 30kHz, higher than the trapping frequencies but lower than the Larmor frequency associated with the axial magnetic field at the bottom of the trap. In the modulated (AC) trap, the atoms saw a time-averaged potential, and the roughness was reduced by at least a factor of 5 with no observed heating or atom loss. The radial frequency decreased by a factor of $\sqrt{2}$ as compared to the frequency in the un-modulated (DC) trap. A dramatic reduction of the damping of the centre-of-mass oscillations of a cold thermal cloud was observed for the AC trap, with 10 times longer damping time than for the DC trap[1].

P. Krüger et al. [131] proposed a similar technique to reduce the potential roughness based on replacing the static offset axial field by an RF field orbiting in a plane transverse to the axis of the trap. Calculations for the typical parameters of their traps showed that this method could reduce the corrugations in the potential by several orders of magnitude at the same time as relaxing the longitudinal confinement, providing an ideal situation for the study of the 1D Tonks-Girardeau regime in magnetic traps.

Other interesting references are the reviews of magnetic micro-traps for ultra-cold atoms written by J. Fortágh and C. Zimmermann [135,136].

6.2.2 Fragmentation on atom chips based on permanent magnets

Clouds trapped next to atom chips based on permanently-magnetised materials were expected not to suffer from fragmentation effects, since no electrical currents are used to produce the confining magnetic fields. However, potential roughness was also observed in permanent-magnet atom chips. It was first measured in the videotape atom chip experiment detailed in this thesis and reported by C. D. J. Sinclair et al. [65]. Cold thermal clouds at temperatures around 1μK were seen to fragment at distances below 100μm from the chip surface and used to probe the magnetic smoothness of the videotape. The observed

[1] Damping had also been observed in the oscillations of a BEC in our videotape experiment and its cause had been thought to be the potential roughness [66].

fragmentation was thought to result from height variations in the videotape topography, as measured with an atomic force microscope. Section 6.3.1 in this thesis provides a more detailed study of the axial disorder potential that affected our videotape atom traps.

Another two experimental groups have reported observations of potential roughness close to permanent-magnet atom chips: the group of B. V. Hall, P. Hannaford and A. I. Sidorov in Melbourne, Australia [71, 137–141], and the group of W. Ketterle and D. E. Pritchard in Cambridge, Massachusetts, U.S.A. [77].

In the experiment of the Melbourne group cold atoms were trapped next to the edge of a TbGdFeCo magneto-optical film with magnetisation perpendicular to the film surface. They characterised the corrugations in the potential using radio-frequency spectroscopy of the cold atoms combined with high-spatial-resolution absorption imaging. They exploited the disorder features of the potential to produce a string of eleven independent condensates along 3mm of the corrugated magnetic potential [137, 139], and to study the splitting of a BEC in an asymmetric double well potential present in the central region of the fragmented potential [140], as a basis for an atom interferometer with controlled barrier height and asymmetry.

In a more detailed study of the disorder potential [138] they found that the corrugations at distances between 50 and 115μm from the film surface were significantly stronger than those observed at the same distances from evaporated micro-wires. They found that the principal cause of the potential roughness was not the imperfections along the film edge, but the inhomogeneity of the magnetic material itself, which they attributed to deterioration during the bake-out process. A spectral analysis revealed that long-range magnetisation fluctuations were the main cause for the observed potential roughness. A magnetic force microscope study of the film showed characteristics close to white noise. A calculation that included in-plane, two-dimensional, white-noise spatial variations in the magnetisation component perpendicular to the film led to a power-law dependence of the potential roughness with the distance d to the magnetic film of d^{-2}, similar to the exponent measured with cold atoms: $d^{-1.85}$.

The same group developed a method for measuring magnetic fields with a field sensitivity of $\sim 0.1\mu$T and a spatial resolution of $\sim 2.5\mu$m. They used a home-built scanning magnetoresistance microscope [138, 141] based on magnetic tunneling junction sensors to measure the magnetic-field noise next to their chip, and found good agreement with the results obtained with ultra-cold atoms. Additionally, they fabricated a thin current-carrying wire with periodic geometrical fluctuations along one edge and compared the field measured with their magnetoresistance probe with the calculated one, finding excellent agreement. Their magnetoresistance microscope was shown to be a reliable method, faster and easier than the use of ultra-cold atoms, and very useful for characterising atom chips prior to their installation in the vacuum chamber.

M. Boyd et al. [77] explained how fragmentation was observed in cold-atom clouds confined at distances $\leq 40\mu$m from an atom chip made of a hard-disk platter written with a

sinusoidal magnetisation pattern. This chip is very similar to our videotape chip, the only difference being that the magnetisation is normal to the chip surface, whereas the videotape magnetisation was in-plane. They attributed the measured potential roughness to imperfections caused by the sputtering process used to create the magnetic film and possibly to the recording process.

6.2.3 Studies of disorder effects using optical traps

Despite some of its negative consequences, the existence of disorder in trapping potentials has also led to interesting studies of quantum effects in which the combined role of disorder and interatomic interactions determines different dynamic regimes for quantum degenerate gases. I review this briefly below. The subject is not really central to my thesis and could be easily skipped over by the reader, but I include it because I found it interesting.

Optical lattices have been used to confine atoms and study some of these interesting quantum regimes, since they allow precise control of interatomic interactions. In the absence of disorder, ultra-cold bosons trapped in an optical-lattice potential undergo a transition from a superfluid to a Mott-insulator [142] as the on-site repulsive interactions, U, increase with respect to the tunnel-coupling between adjacent sites, J.

It is possible to create disorder deliberately in an optical-lattice potential using, for instance, an incommensurate lattice or a laser speckle potential. As the ratio U/J increases, the system is expected to enter an insulating Bose-glass phase when the disorder in the system is large enough compared to the interaction energy. This Bose-glass phase is characterised by vanishing long-range coherence, vanishing superfluid fraction, a gapless excitation spectrum and finite compressibility. The first experimental evidence suggesting the formation of a Bose-glass was provided by L. Fallani et al. [143], where controlled disorder was introduced by means of an incommensurate bichromatic optical lattice.

The increase of disorder in the presence of interactions therefore leads to the formation of a Bose glass. A lattice is not needed for this transition to occur, and a Bose glass can also be achieved by increasing disorder in a weakly-interacting BEC.

In the absence of interactions, arbitrarily weak disorder leads to the phenomenon of Anderson localisation, first proposed in 1958 to explain the metal-insulator transition in electron transport in disordered solids. This phenomenon applies to ultra-cold atoms if we consider them as matter waves propagating in a disordered potential and leads to the suppression of transport and to an exponential decay in atomic density moving away from the localisation centre. It is due to the destructive interference of the de-Broglie waves due to multiple scatters from the modulations of the disordered potential.

In the case of strong disorder, the localisation results from a disorder-induced trapping and is not related to Anderson localisation [144].

In the presence of weak interactions localisation effects only persist to a certain extent [145]. The increase of disorder leads to a transition from an extended superfluid to a localised state. Strong suppression of the centre-of-mass motion and of the expansion of a

Bose-Einstein condensate was experimentally observed by D. Clément et al. [146, 147] and C. Fort et al. [148] in a one-dimensional waveguide in which strong disorder was induced by laser speckle. Similarly, J. E. Lye et al. [149] reported on the blockage of the centre-of-mass motion of a Bose-Einstein condensate in a disordered, 1D, incommensurate, bichromatic lattice for low atom number (low interactions) and a return to motion when the atom number was increased. For weak-enough disorder, the expansion of an interacting 1D Bose-Einstein condensate in a random potential should exhibit Anderson localisation, as calculated by L. Sanchez-Palencia et al. [144, 150].

P. Lugan et al. presented theoretical studies of the quantum states of a system of ultra-cold bosons in the presence of 1D disorder as a function of the strength of the interactions and amplitude and correlation length of the random potential [151]. The same group has recently reported experimental observations of disorder-induced large density modulations in time-of-flight images of elongated Bose-Einstein condensates initially confined in a harmonic trap with weak disorder created by a speckle potential [152].

The experimental observation of the Anderson transition with atomic matter waves was reported by J. Chabé et al. [153], who used an atomic kicked rotor consisting of cold cesium atoms in a modulated optical potential onto which they applied a sequence of kicks. This system offered a mapping onto momentum space of the Anderson localisation phenomenon. Anderson localisation in real space of a Bose-Einstein condensate with negligible interatomic interactions in a one-dimensional optical potential with weak disorder was reported in the same issue of Nature by two different experimental groups: that of A. Aspect [154] and that of M. Inguscio [155].

6.3 Fragmentation in our videotape atom chip

6.3.1 Fragmentation in the videotape magnetic traps

There were no currents flowing inside the magnetised videotape to create the magnetic traps that confined the ultra-cold atoms. The periodic, in-plane magnetisation recorded in the videotape along the x direction should have generated a magnetic field with components only in the x-y plane. However, fragmentation was observed, revealing a fluctuating anomalous magnetic field component along the z direction, $\Delta B_z(z)$, responsible for the corrugations in the axial potential felt by the atoms in the videotape traps.

This section is dedicated to the study of the observed axial fragmentation of ultra-cold thermal clouds of rubidium atoms confined in videotape traps at distances between 30 and 80μm from the chip surface. The experimental procedure is described here and absorption images of fragmented clouds are shown and analysed in order to obtain the axial disorder potential for several values of the distance between the atomic cloud and the chip surface. The dependence of the rms potential roughness on atom-surface separation is studied and the strength of this roughness is compared to that observed by other experimental groups. The frequency spectrum of the disorder potential is analysed and the possible origins of fragmentation on our atom chip are discussed. Finally, a method for reducing fragmentation is outlined and applied to the parameters of our videotape atom traps.

Experimental data

A thermal cloud of atoms confined in a trap with potential roughness will break into localised fragments when the thermal energy of the cloud is of the same order or less than the depth of the disorder potential. The depth of the axial disorder potential felt by the atoms in the videotape traps increases from $\sim$ 200nK to $\sim 4\mu$K as the atoms move from a distance of $\sim 80\mu$m to $\sim 30\mu$m from the permanently-magnetised surface of the videotape. For this reason, very cold atom clouds need to be produced in order to observe the phenomenon of fragmentation.

The experimental sequence used to produce ultra-cold atoms in videotape traps was that described in chapter 4. The dispensing time was of 30s. Cold atoms were loaded into videotape traps with bias-field values between 0.5G and 15.8G. The atoms were then cooled in the final videotape traps in which fragmentation was studied, by using an exponential RF sweep from $f_{start} = 5.3$MHz to a final RF value between 4 and 1.5MHz, with a time constant of 0.5s, in order to reach temperatures of a few μK. An in-trap absorption image of the atoms was recorded using a CCD camera with a pixel size of 6.8μm, placed as detailed in section 3.5.3 for imaging "set-up I". The distance from the videotape traps to the chip surface was obtained from the recorded absorption images as explained in section 3.5.3. The uncertainty of this measurement was of 0.5-1 pixels. The temperatures were determined from the in-trap absorption images as explained in section 4.4.1.

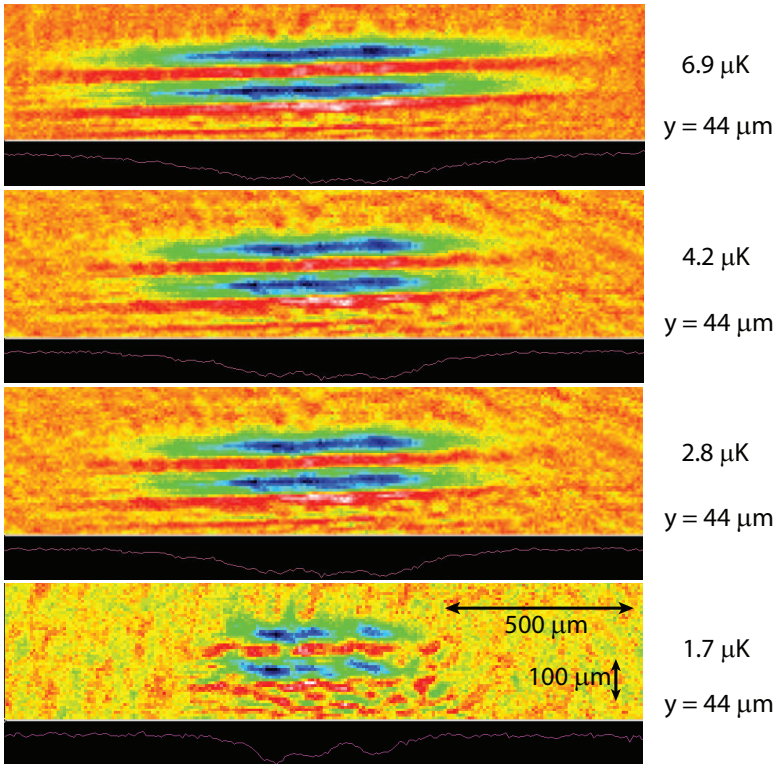

Figure 6.2: Fragmentation in a videotape atom trap $\sim 44\mu$m away from the chip surface. False-colour absorption images are shown in each plot, together with axial line density profiles. The fragments become more apparent as the temperature decreases from top to bottom as indicated by the labels. The scale is the same for all images.

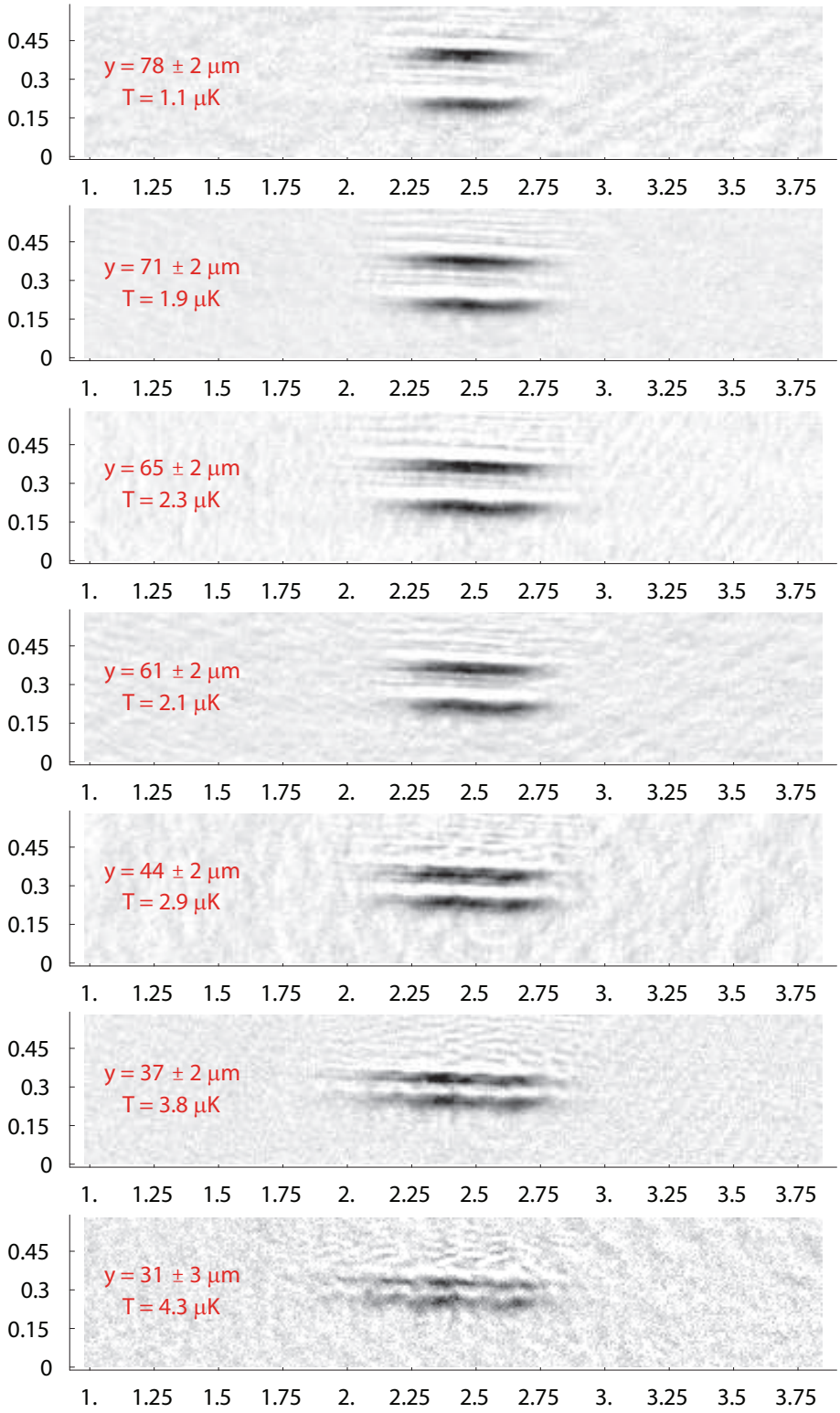

Figure 6.3: Absorption images of fragmented atomic clouds with similar temperatures in videotape atom traps at different distances from the chip surface. The atom surface separation decreases from top to bottom as indicated by the labels on each image. The vertical and horizontal axes show the y and z coordinates in mm, respectively. The contrast was scaled in the same way for all images.

Several realisations of the above experimental sequence were carried out for seven different bias field values, corresponding to seven different distances from the videotape trap to the surface of the chip.

For each of these distances, various in-situ absorption images of atomic clouds with different temperatures were obtained by modifying the final frequency of the RF sweep that cooled the atoms in the videotape trap. At a given distance d, as the temperature decreased during evaporative cooling, the cloud began to fragment due to the potential roughness. As the temperature of the atoms became low enough compared to the depth of the disorder potential the fragments became more apparent in the absorption image. Figure 6.2 shows an example of the absorption images of an atom cloud confined $\sim 44\mu$m away from the surface of the chip, for four different temperatures: $\sim 6.9\mu$K, $\sim 4.2\mu$K, $\sim 2.8\mu$K and $\sim 1.7\mu$K. The fragments become more obvious as the temperature of the cloud decreases.

On the other hand, if we compare clouds with similar temperatures but confined at different distances from the chip surface, we can see how the corrugations in the axial potential become stronger as the atoms move closer to the videotape surface. Figure 6.3 shows absorption images of atomic clouds with temperatures around 1-4μK, trapped at distances, d, from the chip surface, that range from 78μm to 31μm, from top to bottom in the figure. The corresponding uniform horizontal bias fields used to create the videotape trap were: 0.5G, 1.1G, 1.6G, 2.2G, 5.3G, 10.6G and 15.8G, respectively. The temperatures of the clouds shown, from top to bottom, were of the same order of magnitude: $\sim 1.1\mu$K, $\sim 1.9\mu$K, $\sim 2.3\mu$K, $\sim 2.1\mu$K, $\sim 2.9\mu$K, $\sim 3.8\mu$K and $\sim 4.3\mu$K.

Data analysis: fragmented density profiles and disorder potentials

A quantitative analysis of the recorded absorption images of fragmented clouds can be carried out in order to obtain the potential roughness for the different atom-surface separations, and therefore the anomalous axial magnetic field component, $\Delta B_z(z)$, responsible for the corrugations in the axial potential felt by the atoms.

The integrated axial absorption profile of the cloud, $p(z)$, was obtained by summing over ten rows of pixels in the absorption image of the cloud. This profile is proportional to the axial probability distribution, which, as explained before, can be assumed to be given by the Maxwell-Boltzmann factor, $\exp(-\frac{U(z)}{k_B T})$, where $U(z)$ is the axial potential felt by the atoms in the trap, k_B is the Boltzmann constant and T is the temperature of the atoms. We can write $U(z) = U_0(z) + U_{dis}(z)$, where $U_0(z)$ is the axial trapping potential and $U_{dis}(z)$ is the disorder potential. The potential without disorder can be expressed as $U_0(z) = \frac{1}{2}m\omega_z^2(z - z_0)^2 + mg(z - z_0)\sin\alpha$, where the first term is the axial confinement created by the end wires, that is approximately harmonic in the regions explored by the atoms in these experiments, and the second term is a very small correction to account for the gravitational potential due to the tilt of the chip surface with respect to the horizontal (see section 2.2). m is the mass of ^{87}Rb, ω_z is the measured axial oscillation frequency of the atoms in the trap, equal to $2\pi \times 12.8$Hz, g is the acceleration of gravity, z_0 is the central

position of the cloud, and $\alpha \simeq 3°$ is the small angle by which the chip was tilted with respect to the horizontal.

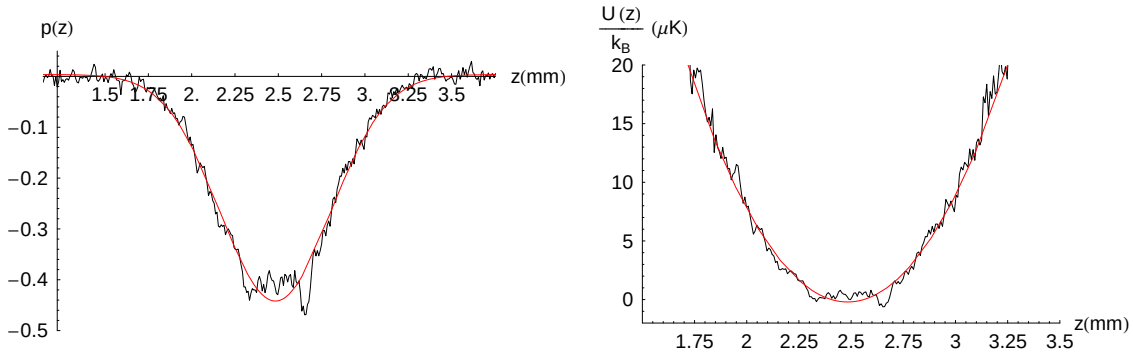

Figure 6.4: Example of the analysis of a fragmented image. **Left:** Gaussian fit of the integrated axial absorption profile. **Right:** plot of the measured and fitted harmonic potentials. The subtraction of the fitted potential from the measured one yields the axial disorder potential, $\frac{\mu_B}{k_B}\Delta B_z(z)$. The height of the trap was $d \simeq 44\mu$m and the obtained temperature was $T \simeq 6.9\mu$K.

The analysis procedure followed to obtain the disorder potential consisted of first finding out the ordered component of the potential, $U_0(z)$, by fitting the absorption profile of the cloud, and then subtracting it from the total potential in order to obtain the disordered component, $U_{dis}(z)$. Therefore, the first step was to fit the integrated axial absorption profile, $p(z)$, to the Gaussian function:

$$p(z) \simeq a + b \exp\left(-\frac{\frac{1}{2}m\omega_z^2(z-z_0)^2 + mg(z-z_0)\sin\alpha}{k_B T}\right) = a + b\, n(z), \tag{6.1}$$

where a is a residual background and $n(z)$ is the axial density profile of the cloud. The fit parameters were z_0, T, a and b. Figure 6.4(left) shows an example of this type of fit.

Figure 6.5 shows the integrated axial density profiles of atom clouds confined in videotape traps at different distances from the chip surface, between 78μm and 31μm. These profiles were obtained as $n(z) = -\frac{p(z)-a}{b}$, using the parameters obtained from the fits. The temperature of the cloud was similar for all images, ranging between 1.3μK and 4.3μK. It is possible to see how the profile became more fragmented as the trapped atoms were brought closer to the surface of the videotape atom chip.

The obtained fit parameters gave us the axial confining potential without disorder, $U_0(z) = \frac{1}{2}m\omega_z^2(z-z_0)^2 + mg(z-z_0)\sin\alpha$. The next step was to include the disorder potential, $U_{dis}(z)$, in the expression of the axial profile of the cloud, $p(z)$, as follows:

$$p(z) = a + b \exp\left(-\frac{U_0(z) + U_{dis}(z)}{k_B T}\right). \tag{6.2}$$

The full axial potential felt by the atoms, including the disorder, was therefore obtained as $-k_B T \ln\left(\frac{p(z)-a}{b}\right)$, using the fit parameters and the absorption profile, $p(z)$, obtained from the absorption image. Figure 6.4(right) shows this full axial potential with disorder, measured with cold atoms (black line), together with the fitted, smooth, axial confining potential, $U_0(z)$, (red line). Subtracting the fitted potential from the full one measured with atoms yielded the axial disorder potential, $U_{dis}(z)$. Along the axis of the trap, this

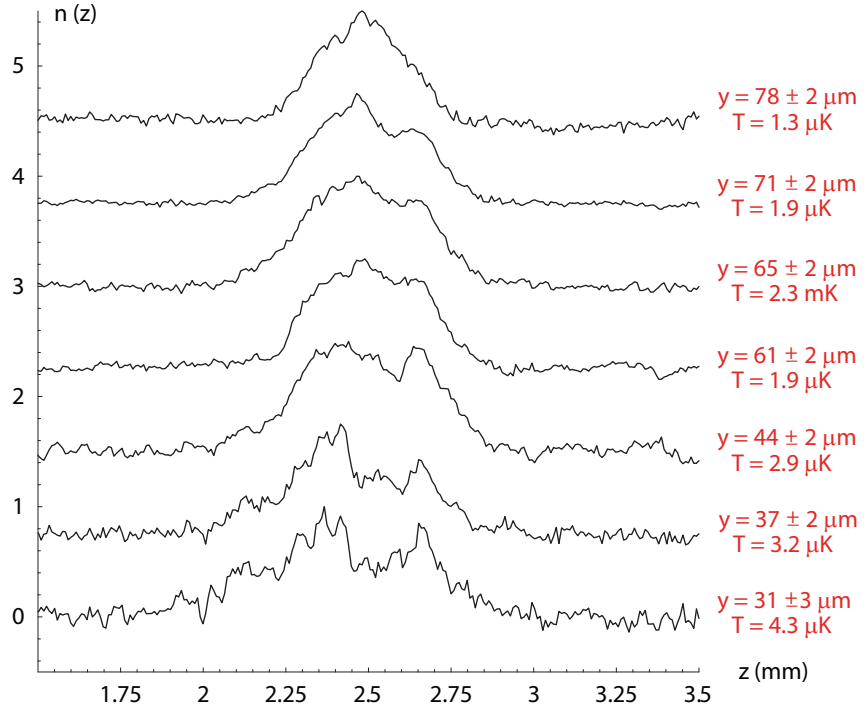

Figure 6.5: Integrated axial density profiles of atomic clouds with temperatures of the same order in videotape atom traps at different distances from the chip surface. The atom-surface separation decreases from top to bottom, as indicated by the labels. All profiles were scaled to lie between 0 and 1 and a vertical offset was added to each of them for clarity.

disorder potential can be related to the anomalous magnetic field, $\Delta B_z(z)$, responsible for the potential roughness, as follows:

$$U_{dis}(z) = \mu_B g_F m_F \Delta B_z(z)\,, \tag{6.3}$$

where $g_F m_F = 1$ for the magnetic hyperfine sub-level of ^{87}Rb that we trap.

Figure 6.6 shows the axial disorder potential measured from in-trap absorption images of cold clouds confined at different distances from the videotape surface, between 78 and 31μm. The temperatures of the trapped clouds varied between 1.3 and 12.6μK. The figure shows how the amplitude of the axial disorder potential felt by the atoms decreased as these moved away from the chip surface. Far from the surface, the high-frequency fluctuations of the potential disappeared and only the longer-wavelength fluctuations remained. Since the imaging resolution was determined by the camera's pixel size, equal to 6.8μm (see section 3.5.3), potential variations with wavelengths smaller than $\sim 10\mu$m could not be detected by our imaging system.

The rms depth of the disorder potential was $\sim 3\mu$K at a distance of $\sim 31\mu$m from the chip surface, and decreased to $\sim 0.3\mu$K at a distance of $\sim 78\mu$m. Clouds with thermal energies of the order of a few μK broke up in clear, separate axial fragments for small atom-surface separations below $\sim 40\mu$m whereas, at larger distances from the chip surface, $\sim 80\mu$m, only clouds with temperatures of the order of a few hundreds of nK appeared

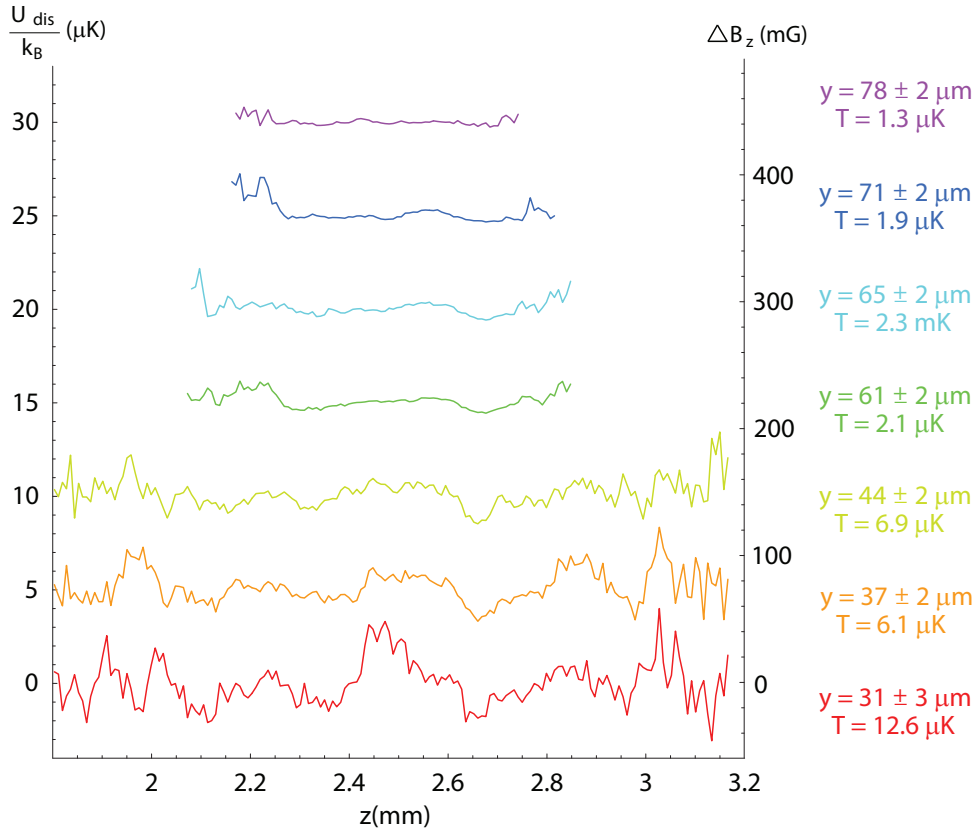

Figure 6.6: Axial disorder potential measured with ultra-cold atoms in videotape magnetic traps. The atom-surface separation decreases from top to bottom, as indicated by the labels. The potentials are separated vertically from each other by 5μK for clarity. Note that the larger noise present at the beginning and end of some of the traces is not real potential roughness as it corresponds to regions where hardly any atoms were present.

strongly fragmented.

The disorder potential could only be obtained in the regions occupied by the atoms. Colder clouds were used for the measurements far from the chip surface than for those close to the videotape surface. Therefore, far from the surface, it was possible to obtain the disorder potential only for a limited range of axial positions.

In the central region for which data was available for all atom-surface separations (2.27mm $\leq z \leq$ 2.73mm in figure 6.6), it was possible to calculate the rms amplitude of the disorder potential as a function of the distance between the trapped atoms and the chip surface. For each of these distances, between 4 and 6 different absorption images were recorded and used to obtain the disorder potential. The rms potential roughness was calculated for each of these images as the standard deviation of the fluctuations of the disorder potential around zero. The results obtained from all images were then averaged and the error of the average rms potential roughness for each different atom-surface separation was considered to be the standard deviation of the distribution of 4-6 results obtained from the available images.

Figure 6.7 shows a plot of all the disorder potentials used to calculate the average rms potential roughness in the limited range of axial positions 2.27mm $\leq z \leq$ 2.73mm, and for

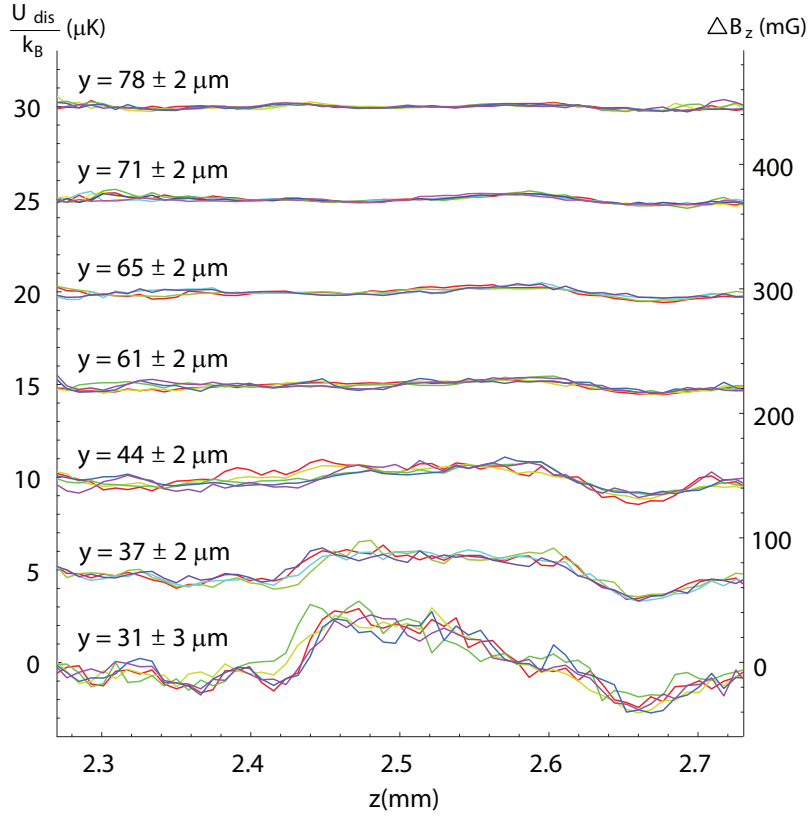

Figure 6.7: Plots of all the disorder potentials used to calculate the average rms potential roughness in the region 2.27mm $\leq z \leq$ 2.73mm. The atom-surface separation decreases from top to bottom as indicated by the labels. Each set of potentials was offseted vertically from the previous one by 5μK, for clarity.

the same atom-surface separations as figure 6.6. The number of images used for averaging, for each atom-surface separation, from top to bottom, was: 5, 6, 4, 5, 5, 4 and 5. Each measured absorption image corresponded to a different realisation of the experimental sequence. Figure 6.7 evidences the reproducibility of the shape of the disorder potential on the different experimental realisations. The shot-to-shot variations could be related to small movements of the camera during data taking.

Figure 6.8 shows the obtained average rms potential roughness as a function of the distance from the atoms to the chip surface. A fit of the data measured with cold atoms to a function of the form $A + Bd^{-C}$, where d was the atom-surface separation in μm, was carried out leading to the result: $A = (0.06 \pm 0.02)\mu$K, $B = (3 \pm 2) \times 10^4 \mu\text{K}\mu\text{m}^{2.9}$ and $C = 2.9 \pm 0.2$. The constant A corresponds to the residual experimental noise of our measurement, as explained below. From the results of the fit we can write:

$$\left\langle \sigma \left(\frac{U_{dis}}{k_B} \right) \right\rangle \simeq 3 \times 10^4 \, d^{-2.9} \, \mu\text{K} \,, \tag{6.4}$$

where $\left\langle \sigma \left(\frac{U_{dis}}{k_B} \right) \right\rangle$ is the average rms potential roughness in units of temperature, σ denotes the standard deviation and $\langle\rangle$ denotes an average over several measured absorption images.

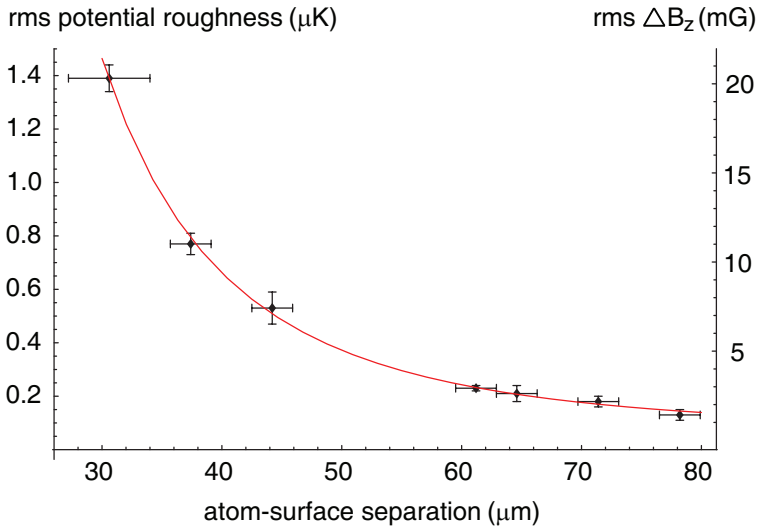

Figure 6.8: Average rms potential roughness as a function of the atom-surface separation. The data points were obtained from measurements with cold atoms confined in videotape traps. The solid line shows a fit of the data to the function $A + Bd^{-C}$, yielding $(0.06 + 3 \times 10^4 d^{-2.9})\mu$K, with d in μm.

The offset of the fit, $A = (60 \pm 20)$nK, equivalent to rms axial magnetic field fluctuations of 92nT (0.92mG), indicates the limiting experimental noise in the trapping potential at large distances from the chip surface, and gives an idea of the order of magnitude of the smallest magnetic field fluctuations detectable on this videotape atom chip. This high magnetic field sensitivity was of the same order as that reported by the experimental group from Melbourne [138, 141], but poorer than that reported by the group of J. Schmiedmayer [56–58]. Our spatial resolution was a factor of two lower than that reported by the same two experimental groups, determined by the camera's pixel size of 6.8μm and by the imaging set-up ("set-up I", see section 3.5.3).

In order to establish a comparison between the amplitudes of the magnetic potential roughness measured on different atom chip experiments up to date, it can be useful to calculate $\frac{\Delta B_z}{B}$, which is commonly used in the literature for this purpose. However we note here that comparison is not really fair when the elements that generate the confining magnetic fields are not of the same type, and that, hence, in our opinion, this parameter is not entirely relevant. ΔB_z is the rms amplitude of the axial magnetic field corrugations and B is the main transverse magnetic field created by the atom chip at the position of the trap. The main field B can be generated either by a current-carrying wire or by a permanent magnet on the chip. In our videotape atom chip experiment, B is the magnitude of the videotape magnetic field (which is equal to the bias field) and ΔB_z is the calculated rms potential roughness shown on figure 6.8. The values of $\frac{\Delta B_z}{B}$ measured on our videotape chip are of the order of 10^{-3}, as shown on figure 6.9. The magnitude of $\frac{\Delta B_z}{B}$ increases with the atom surface separation d since, as the rms potential roughness decays as $d^{-2.9}$, the videotape field decays faster as $\exp(-kd)$, with $k = \frac{2\pi}{\lambda}$, where λ is the spatial period of the videotape magnetisation.

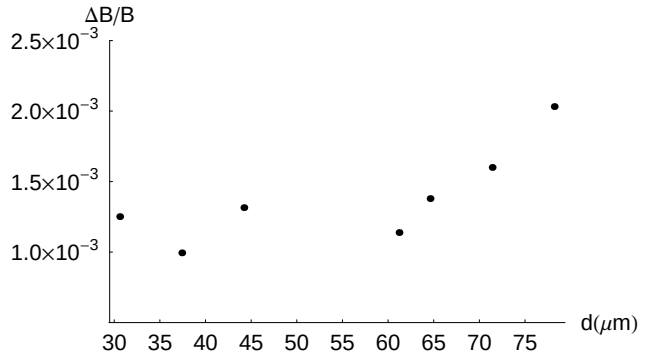

Figure 6.9: Plot of $\frac{\Delta B_z}{B}$ measured on our videotape atom chip as a function of the atom surface separation, d.

On atom chips based on a single current-carrying wire, the magnetic field created by the wires (B) decays linearly with the distance to the wire, while the decay of ΔB_z has been measured to be faster, as d^{-C}, with C between 2 and 2.5 (see section 6.2.1). Consequently, on these chips, the magnitude of $\frac{\Delta B_z}{B}$ was seen to decrease for increasing atom-surface separations.

Most atom chip experiments based on macroscopic wires or electroplated micro-wires have measured values of $\frac{\Delta B_z}{B}$ between 3×10^{-4} and 3×10^{-3}, for the same range of atom-surface separations as we used on our videotape chip (see reference [131] for a summary). The roughness measured on our videotape traps is of a similar order of magnitude to that detected on those chips. The permanent-magnet atom chip used in Melbourne showed unusually high roughness, with a reported value of $\frac{\Delta B_z}{B}$ of the order of 10^{-2} [137–141]. On the other hand, atom chips that use lithographically patterned and evaporated micro-wires to create magnetic traps have shown a much weaker potential roughness, with $\frac{\Delta B_z}{B}$ ranging between 5×10^{-6} and 5×10^{-5} for an atom-surface separation of $\sim 30\mu$m (see summary in reference [131]).

Spectral analysis of the videotape potential roughness

It is possible to calculate the Fourier spectrum of the measured disorder potentials in order to investigate the length scale of the observed fluctuations of the z-component of the magnetic field in the videotape traps. Using the same set of calculated disorder potentials as in figure 6.7 and looking at the same range of axial positions, 2.27mm $\leq z \leq$ 2.73mm, an averaged Fourier spectrum was derived for each of the atom-surface separations, as shown in figure 6.10.

The higher-amplitude spatial frequency components in the spectra correspond to fluctuations in the axial magnetic field with wavelengths of a few hundred micrometres. Higher-frequency components with wavelengths down to $\sim 20\mu$m can also be found in all the spectra. The amplitude of all frequency components decreases as the atom-surface separation increases. As the distance from the chip surface increases the spectrum of the potential roughness becomes somewhat narrower as the effect of long-ranged fluctuations becomes more relevant. At a given atom-surface separation, d, the largest contribution to disorder

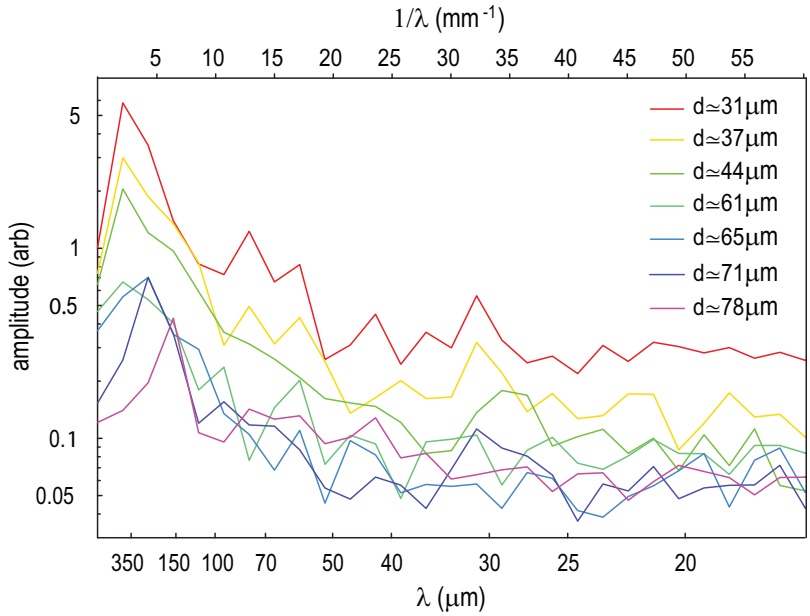

Figure 6.10: Fourier spectra of the disorder potentials measured in the videotape traps for different atom-surface separations.

in the axial magnetic field is that from fluctuations with wavelengths larger or comparable to d, while fluctuations with wavelengths much smaller than d average out and have a much weaker effect. This behaviour is very similar to that of the disorder potentials measured in the proximity of current-carrying wires and magnetic films in other experiments. A similar spectral dependence with atom-surface separation has been reported by several experimental groups, with higher frequencies appearing in the disorder potential as the atoms were moved closer to the chip surface [77, 120, 123, 124, 128, 129].

Our experimental set up did not allow the detection of potential-roughness features with wavelengths below $\sim 10\mu$m. The order of magnitude of this limit was set by the imaging resolution, i.e., by the camera's pixel size, equal to 6.8μm (see section 3.5.3). Consequently, measuring potential fluctuations at distances from the chip surface below a few tens of micrometres would be meaningless with such imaging resolution.

Given the experimental sequence used to load atoms in videotape magnetic micro-traps, it is most probable that two micro-traps were loaded, separated by a distance of $\sim 106\mu$m along the x direction (see section 4.5). Given that absorption images were acquired using "imaging set-up I" (see section 3.5.3), the two videotape traps would appear on the image plane close to being overlapped, with their centres separated along the horizontal direction of the image (which we use to measure z) by a small distance of ~ 8.5 pixels, equivalent to $\sim 70\mu$m along z, on the scale of the absorption images previously shown on this chapter. The centres of the two clouds would appear to be separated by a distance of ~ 3.5 pixels along the vertical direction of the image, equivalent to $\sim 24\mu$m. Given the fact that the coldest clouds we measured had approximate dimensions of $500\mu\text{m} \times 50\mu$m along the horizontal and vertical directions of the image, respectively, it would be nearly impossible to distinguish

two videotape traps using "imaging set-up I".

The fact that the measured images most probably correspond to two overlapped, fragmented density profiles introduces additional disorder in our measurements of potential roughness. If the two atomic clouds felt equal disorder potentials and were perfectly overlapped, even though the total absorption profile would be equal to twice the profile of a single cloud, the correct magnitude of the disorder potential would still be obtained, since the factor of 2 would be suppressed by the fitting during the analysis procedure. However, the fact that the two clouds are not perfectly overlapped, introduces some error in our calculations. Assuming similar potential roughness (with similar spectra) for two adjacent videotape traps formed at the same distance from the surface, the spectrum of the sum of the two spatially displaced but similar disorder potentials would have the same frequency components as any of the individual spectra. However, the spectral amplitude of the disorder would increase due to the overlap of the images of two clouds of atoms in two adjacent videotape traps.

Origin of fragmentation

We recall at this point the fact that only anomalous magnetic field components, ΔB_z, along the axial direction of the cloud can be responsible for the axial disorder potentials measured on our videotape atom traps. The observed axial potential roughness may originate from fluctuations in both the magnitude and direction of the recorded videotape magnetisation.

Equations 2.18 and 2.19 in section 2.3.5 show how to obtain the magnetic field generated by a given magnetisation pattern. The videotape magnetisation should be in-plane along the x direction, transverse to the axis of the elongated videotape traps and parallel to the chip surface.

Fluctuations along the axial direction of the cloud (z) in the amplitude of the videotape magnetisation would lead to anomalous videotape-field components directed along z. Such fluctuations would also cause small height variations along the length of the cloud, which would in turn lead to changes in the axial confinement felt by the atoms in the trap, since the distance to the end wires would be modified.

On the other hand, variation with z in the direction of the videotape magnetisation could also be a possible cause for the observed axial potential roughness. Alternating magnetisation components along the y or z directions would give rise to small anomalous magnetic fields along the z direction, leading to disorder in the axial trapping potential.

Several physical causes could be responsible for the variations in magnitude or direction of the magnetisation vector. Failure of the videotape to lie flat as it is glued onto the chip surface would result in small y-components of the magnetisation and noise in the magnitude of the main videotape magnetisation along the axial direction of the traps. Thickness variations would also cause fluctuations of the magnitude of the videotape magnetisation. Surface defects, height variations and inhomogeneities in the structure of the magnetic layer would lead to modulations in both the amplitude and direction of the videotape magnetisation.

The surface topography of the magnetic layer of a piece of videotape was inspected using an atomic force microscope (AFM). Height variations of up to $\sim$ 20nm with wavelengths

of the order of tens of microns were found on the AFM-scan pictures. These could result from the inability of the videotape to lie completely flat or from variations in its thickness. Together with these broad features the AFM scans revealed some deeper holes in the surface of the magnetised layer. These holes were typically around 100nm deep and a few μm wide, with a spacing of around 10μm. An example of these AFM-scan pictures can be found in references [65, 81]. As mentioned in section 2.2, the 3.5μm-thick magnetic layer of the videotape consisted of iron-composite needles 100nm in length and 10nm in radius, embedded in glue and aligned parallel to each other along the x direction. A hole such as the deep ones observed on the AFM scans would constitute a magnetisation defect with hundreds of magnetised needles missing. The magnetic field created by the videotape directly below one of these defects would change direction at the edges of the defect, in the plane of the videotape, giving rise to non-zero magnetic field components along the z direction.

It seems most probable that the combined effects of height and thickness variations, and defects present across the videotape surface were responsible for the measured fluctuations in the z-component of the total magnetic field.

It would be interesting to construct a model including the appropriate noise in both the modulus and direction of the videotape magnetisation vector in order to try to reproduce the observed axial potential roughness and its decay with atom-surface separation. The correct noise spectra would need to be chosen based on all the previously mentioned experimental observations. However, the realisation of such model is beyond the scope of this thesis.

Several types of magnetic videotape[2] were inspected through atomic force microscopy leading to the conclusion that the one used in our experiment was the one with the smoothest surface topography of all the ones examined.

Suppressing fragmentation in the videotape atom chip

The existence of fragmentation in the videotape atom traps prevented us from reaching the tight transverse confinement needed to enter the one-dimensional regime, since the small atom-surface separations required to achieve such high frequencies would have led to strong fragmentation of the confined clouds.

It is possible to overcome the effects of fragmentation in our videotape traps by reducing the strength of the corrugations in the axial potential seen by the atoms in these traps.

As mentioned in section 6.2, fragmentation in a current-carrying wire atom chip was successfully reduced by rapid modulation of the current through the trapping wire [133,134]. The method we propose here is similar to that suggested in reference [131], and also based on time-averaged potentials. It was not implemented experimentally due to the unfortunate accident that led to the destruction of the videotape atom chip. The method is described here and applied to the typical experimental parameters for our videotape traps.

[2]The following digital videotapes were inspected: Quantegy DBC-D12A, Quantegy D2V-126LC and Fuji D2001-D-2-S-12. Analog videotape is no longer sold these days.

It is based on replacing the offset axial field present in the videotape trap with an orbiting transverse field. The net offset axial field is created by the end wires that generate the axial confinement (see section 2.3.3) and can be cancelled by applying an appropriate uniform axial field, B_z. When this is the case, the value of the magnetic field strength at the bottom of the trap is zero, which would lead to spin-flip losses. However, in order to avoid this zero and produce an effective time-averaged potential, a rotating magnetic field, B_{rot}, can be superimposed onto the usual bias field in the plane transverse to the axis of the trap, causing the minimum of the magnetic field to describe a circle in that same transverse plane. If the frequency of the rotating transverse field, B_{rot}, is high enough compared to the trapping frequencies and low enough compared to the Larmor frequency, the atoms are unable to follow the movement of the field minimum in the transverse plane and feel a time-averaged potential. The resulting trap is the so-called TOP (time-averaged orbiting potential) trap, described in reference [156], in which the time average over one field rotation yields a parabolic transverse potential close to the trap centre, with the field at the bottom of the trap being equal to B_{rot}:

$$|\vec{B}|(r) \approx B_{rot} + \frac{\alpha^2}{4B_{rot}} r^2 \,, \tag{6.5}$$

where $\alpha = kB_b$ is the gradient of the instantaneous transverse quadrupole field in our videotape traps. The zero of the total magnetic field orbits around the trap centre in a trajectory of radius equal to $R_0 = B_{rot}/\alpha$. From equation 6.5 we can deduce that the frequency of the transverse oscillations in the time-averaged potential is $\omega_r = \alpha\sqrt{\frac{\mu_B g_F m_F}{2mB_{rot}}}$.

Along the trap axis we have that the field at the bottom of the time-averaged potential is B_{rot}, and the confinement from the end wires, assumed to be harmonic, is βz^2, so that we can write:

$$|\vec{B}|(z) = \sqrt{B_{rot}^2 + (\beta z^2)^2} \approx B_{rot} + \frac{\beta^2}{2B_{rot}} z^4 \,, \tag{6.6}$$

where no disorder potential has been included up to this point. Equation 6.6 shows that the axial confinement in the time-averaged trap is flattened, with a consequent reduction of the axial trapping frequency. The axial confinement is of the form z^4, flatter than a harmonic potential and closer to a box-like potential, offering interesting possibilities for studies of one-dimensional quantum gases [157].

Now, considering the effect of the disorder potential, at the effective position of the trap ($r = 0$), the time-averaged axial potential results from the contribution of the axial potential roughness, ΔB_z, the axial confinement from the end wires, βz^2, and the transverse rotating field, B_{rot}. These different components add up in quadrature so that the effective, time-averaged axial magnetic field strength is:

$$|\vec{B}|(r=0,z) = \sqrt{B_{rot}^2 + (\Delta B_z + \beta z^2)^2} \approx B_{rot} + \frac{\beta^2}{2B_{rot}} z^4 + \frac{\Delta B_z^2}{2B_{rot}} + \frac{\beta \Delta B_z}{B_{rot}} z^2 \,, \tag{6.7}$$

where the first two terms give the axial confinement and the last two terms are proportional to the magnetic field roughness. The approximation is valid in the region where $\left(\Delta B_z + \beta z^2\right)^2 \ll B_{rot}^2$. In this region, the potential roughness is attenuated by a factor of

$\left(\frac{\Delta B_z}{2B_{rot}} + \frac{\beta z^2}{B_{rot}}\right)$, with the greater reduction taking place at the bottom (z=0) of the axial potential.

Even though the time-averaged potential gives a non-zero magnetic field at the bottom of the trap, spin flips can still occur if atoms have high enough energy to reach the position of the instantaneous zero field, which orbits in a ring of radius $R_0 = B_{rot}/\alpha$ around the time-averaged trap centre [156]. The atoms reach the position of this ring when their total energy is $E \geq \mu_B B_{rot}/4$. In order to avoid the loss of atoms from the trap, the condition $B_{rot} \gg 4k_B T/\mu_B$ needs to be fulfilled, where T is the temperature of the atoms in the trap. For a cloud of atoms with a temperature of $\sim 1\mu$K, this condition means that $B_{rot} \gg 0.06$G, which is perfectly feasible. Additionally, larger values of B_{rot} lead to a more effective attenuation of the potential roughness, given by the factor $\left(\frac{\Delta B_z}{2B_{rot}} + \frac{\beta z^2}{B_{rot}}\right)$. However, this is at the expense of a larger loss of transverse confinement, since the transverse frequency in the time-averaged trap is proportional to $1/\sqrt{B_{rot}}$.

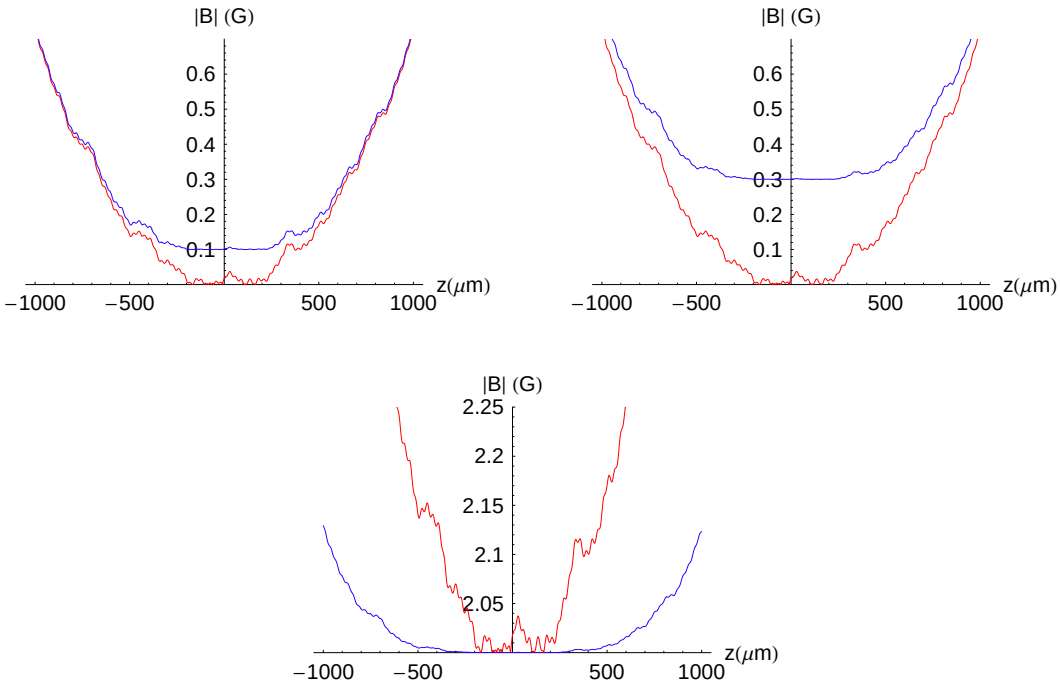

Figure 6.11: Predicted reduction of the axial potential roughness by removing the net axial offset field and superimposing a rotating transverse field of amplitude B_{rot}=0.1, 0.3 and 2G, from left to right and from top to bottom, to the bias field. Solid red lines show the static axial field strength with disorder, including the end-wire field, before the rotating field is added. Solid blue lines show the time-averaged field strength after adding the rotating field. In the last graph, an offset equal to $B_{rot} = 2$G was added to the static field (red line) to enable comparison.

Figure 6.11 shows a calculated example of the reduction of the axial potential roughness with this method in a videotape trap with an end-wire current of 15A and a bias field of 15G, at a distance of $\sim 34\mu$m from the chip surface. The value of B_z is 4.76G in order to cancel out the z-component of the field produced by the end wires at the bottom of the trap, leading to a zero net-axial magnetic field. The figure shows the effect of the addition

of a rotating transverse field, for three different values of B_{rot}: 0.1, 0.3 and 2G. The total magnetic field modulus is plotted as a function of the axial position in the trap, z. The red curves show the field strength before the rotating field is included. The blue curves show the resulting time-averaged field strength after the rotating field is included. On the last graph, an offset equal to $B_{rot} = 2$G was added to the red curve for easy comparison with the smoother time-averaged field strength (blue curve). It is clear how the axial field fluctuations are reduced in the central region of the trap, where $\left(\Delta B_z + \beta z^2\right) < B_{rot}$. The corresponding maximum reduction factors at $z = 0$ are $\sim 1/6$, $\sim 1/17$ and $\sim 1/114$, for $B_{rot} = 0.1$, 0.3 and 2G, respectively. The graphs also show how the field at the bottom of the trap is raised by an offset equal to B_{rot}, as given by equation 6.7.

The transverse trap frequencies of the atoms in the videotape traps in which we measured fragmentation were between 0.5 and 6kHz, the axial frequency was around 13Hz, and the Larmor frequencies ranged between 140kHz and a few MHz. Therefore, a transverse rotating field with a frequency of a few tens of kHz would be a good choice to create a time-average potential resulting in reduced potential roughness in our videotape traps.

Another way to overcome fragmentation would be to use a videotape with a longer period of recorded magnetisation. As shown in appendix D, a period of $\sim 360\mu$m would lead to transverse trapping frequencies around 8 times larger than those with the current magnetisation period of 100μm, for atom-surface separations around 100μm. This would allow us to achieve tight transverse confinement further from the chip surface, avoiding the effects of potential roughness.

6.3.2 Fragmentation in the wire magnetic trap

Fragmentation was also observed in the wire magnetic trap. The experimental procedure was the same as the one used to produce ultra-cold atoms in videotape traps, previously described in chapter 4, but the atoms were kept in the compressed wire trap for the final RF evaporation ramp and imaged after release from the wire trap without ever being loaded into videotape traps. The wire magnetic trap was formed by running 15A through the centre wire and 15A through the end wires, with a horizontal bias field of 44G and a uniform axial field $B_z = 2.8$G. Three consecutive exponential RF sweeps with different time constants were carried out in this wire trap in order to cool the atoms. The first sweep went from an initial RF of 30MHz to a final RF of 11MHz in a time of 4.5s, with a time constant of 4s; the second one went from 11MHz to 4MHz in 10.6s, with a time constant of 7s; the final sweep went from 4MHz to a final RF between 2.19MHz and 2.14MHz depending on the value of the sweep time (between 7s and 8s), with a time constant of 3s.

The atoms in the wire trap were confined at a distance of $\sim 200\mu$m from the chip surface, i.e., around 700μm away from the axis of the centre wire. The radial and axial oscillation frequencies in this trap were 460Hz and 16Hz respectively.

Figure 6.12 shows two clear fragments appearing in the absorption image of a cold cloud, recorded 7ms after release from the wire magnetic trap, as the temperature decreases. The

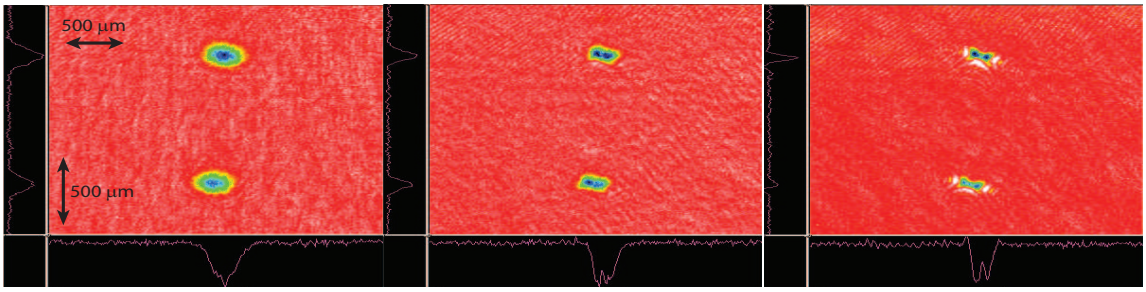

Figure 6.12: Fragmentation in the wire magnetic trap. The double absorption images were taken after 7ms of time of flight. The temperature of the cloud decreases from left to right. The scale is the same for all three images.

imaging set-up used was "set-up I", described in section 3.5.3. The final frequencies at the end of the RF evaporation were, from left to right, 2.157MHz, 2.147MHz and 2.145MHz, resulting in temperatures of $\sim$ 500nK, $\sim$ 250nK and $\sim$ 150nK respectively. At these low temperatures, a Bose-Einstein condensate probably formed in each of the fragments. However, no conclusive evidence of condensation was found in the measured data.

6.4 Conclusion

I have shown in this chapter how it is possible to use ultra-cold rubidium atom clouds confined in videotape magnetic traps as a tool to measure the irregularities of the magnetic field generated by a permanently-magnetised videotape, with high magnetic field sensitivity and high spatial resolution. By varying the distance between the confined cloud and the chip surface, the corrugations in the axial trapping potential were measured for several values of the atom-surface separation between 30 and 80μm. A power law of the form $d^{-2.9}$ was derived from the measurements with cold atoms, for the dependence of the rms potential roughness on the atom surface separation, d.

The decrease of potential roughness with height was due to the loss of the higher-frequency components at large atom-surface separations.

The relative strength of the observed potential roughness in the videotape traps was comparable to that observed on atom chips based on macroscopic or electroplated micro-wires, but between two and three orders of magnitude higher than for lithographically patterned micro-wires. As for the absolute potential roughness we can say that we observed strong fragmentation in atomic clouds with temperatures of a few microKelvin, confined at distances of $\sim$ 30μm from the surface of our videotape atom chip, while reference [131] reported a smooth axial density profile, i.e., no fragmentation, for thermal clouds with temperatures of the same order and down to distances of $\sim$ 2μm from the surface of their atom chip based on micro-structured wires fabricated using optical lithography and gold evaporation.

A method was proposed for reducing fragmentation in the videotape traps. It was shown that a small field of $\sim$0.1G rotating in the plane transverse to the trap axis at a frequency of a few tens of kHz, would be enough to reduce the axial corrugations of the potential by a factor of $\sim$1/6 in an axial region around 600μm-long.

As for the physical origin of the measured fragmentation, height and thickness variations of the videotape surface together with defects in the topography of the magnetic layer were established as the most plausible causes for the observed videotape potential roughness.

It was possible to transport the cloud along its transverse direction, parallel to the chip surface, in order to study the features of the disorder potential in different regions across the videotape chip surface. The next chapter in this thesis describes a novel technique for the transport of cold atoms in videotape traps by large distances across the surface of the chip, by means of a rotating bias field. Experimental measurements of fragmentation after transporting the cold clouds to different locations on the chip are shown in the next chapter.

Chapter 7

Transport of cold atoms in videotape magnetic traps

7.1 Introduction and motivation

As a way to expand the capabilities of our videotape-atom chip we implemented a simple and effective method to transport cold atoms with temperatures between a few micro-Kelvin and a few hundred micro-Kelvin. Cold atoms were conveyed over distances of several millimetres, parallel to the chip surface, while they remained confined in all three dimensions, in arrays of videotape magnetic traps.

Our simple transport mechanism was based on the rotation of the applied bias field that, together with the videotape magnetic field, created the elongated videotape magnetic traps (see section 2.3.6), in order to smoothly translate the trapping potential along its transverse direction. Full control of the atomic position along the transport direction was achieved.

Our conveyor belt for trapped atoms proved to be a useful tool for surveying the chip surface, enabling us to observe the disorder features of the magnetic trapping potential close to different regions of the magnetised videotape.

The achievement of full control in the manipulation of cold atoms is a crucial step in the field of experimental studies with ultra-cold gases, including research on quantum information processing with neutral atoms. The need to convey cold atoms from a reservoir to a zone of operations or to a detection region, for instance, makes the implementation of controlled atomic transport essential for this type of study.

Section 7.2 of this chapter begins by reviewing the progress in the field of cold-atom transport up to date, with special emphasis on the experiments carried out on atom chips. Section 7.3 continues by describing the transport experiments in the videotape atom chip, explaining the transport mechanism and presenting the experimental results.

7.2 Transport of cold atoms

It is possible to transport cold neutral atoms making use of either magnetic forces or optical dipole forces. The use of the former exploits the interaction of the atom's intrinsic magnetic dipole moment with an external magnetic field, while the use of the latter exploits the interaction of the induced, atomic, electric-dipole moment with the electric field from a laser beam of light.

Cold atoms can be transported in cylindrical guides, i.e., in pipes for atoms, in which they are only subjected to two-dimensional transverse confinement and are free to propagate along the axial direction of the guide. If the guide is tight enough for the energy quantum of transverse excitation to be below the thermal energy of the guided atoms, the transverse motion of the atoms freezes out and the guide becomes a waveguide in which single-mode, one-dimensional propagation of the atoms is possible.

Alternatively, a higher degree of control can be achieved by transporting the cold atoms while they stay confined in a trap in three-dimensions.

The development of atom chips has enabled the use of small-scale, compact devices for the magnetic transport of ultra-cold atoms or Bose-Einstein condensates in single traps or arrays of traps. The use of optical dipole traps and lattices, on the other hand, has enabled controlled transport and positioning of single neutral atoms, as well as of Bose-condensed clouds.

This section offers a brief review of the experimental work on cold atom transport to date.

7.2.1 Transport based on magnetic forces

The Stern-Gerlach force (see section 2.3.1) that paramagnetic atoms experience in the presence of an inhomogeneous magnetic field can be exploited to create a cylindrical magnetic guide (see section 2.3.2) along which atoms can be guided while remaining transversely confined. These guides are usually based on magnetic multipole configurations generated by either current-carrying wires or permanent magnets.

The first cylindrical guide for the transport and focusing of an atomic beam was realised experimentally by Friedburg and Paul in 1951 [158, 159]. They used six conductor rods symmetrically arranged parallel to the guide axis to create a hexapole magnetic field that provided a radially confining harmonic potential for the atoms. The same idea was followed by A. Lemonick et al. [160], who used permanent magnets to create a focusing atomic beam apparatus for the measurement of the spins and hyperfine splittings of four radioactive nuclides.

The development of laser cooling and trapping led to a reduction of the atomic temperatures by six orders of magnitude or more, compared to those of the atomic beams used in the first guiding experiments. In this way, the use of smaller magnetic fields became possible for guiding cold atoms loaded from a magneto-optical trap, usually to transfer them to a

spatially separated second chamber at lower pressure.

A hexapole magnetic guide generated by six wires placed cylindrically around a transfer tube was used by C. J. Myatt et al [161] for this purpose, transporting cold atoms from a MOT, along a distance of 40cm, to a second vacuum chamber. A curved magnetic quadrupole beam guide made from permanent magnets was used by A. Goepfert et al. to guide cesium atoms coming from a Zeeman slower through a 24.5° arc along an arc length of 12.8cm [162]. D. Müller et al. [163] also guided cold atoms around curves between two chambers, along a distance of 10cm, in the 100μm-gap between two 100×100μm wires electroplated on a glass surface. Four copper wires embedded in a silica fiber were used by M. Key et al. [164] to transport 25μK rubidium atoms from a MOT in a quadrupole guide along distances of several centimetres without appreciable loss. A four-wire quadrupole magnetic guide was also employed by B. K. Teo et al. [165] and P. Cren et al. [166], to guide cold ^{87}Rb atoms for distances of up to 17cm and 40cm respectively. A guiding configuration based on two interwound helical coils was used by J. A. Richmond et al. [167] to create a 3.8cm-long guide for laser-cooled cesium atoms.

A disadvantage of two-dimensional atom guides is the decrease in density due to the axial expansion of the atoms as they propagate in the guide. One way to solve this problem is to use pulsed magnetic lenses for the focusing of the atoms in the guide (see [168–172] and references therein). Another way to avoid the loss of density is to keep the atoms magnetically confined in all three dimensions during transport. Some examples of the transport of trapped cold atoms over large distances of the order of tens of centimetres are provided by references [173–176]. M. Greiner et al. [173] used a chain of overlapping quadrupole coils to transport cold ^{87}Rb atoms by displacing the quadrupole trapping potential over a distance of 33cm around a 90° corner, with a view to enabling effective delivery of cold atoms for continuous BEC production. K. Nakagawa et al. [174] and H. J. Lewandowski et al. [175] transported cold ^{87}Rb atoms in a quadrupole magnetic trap along 50cm and 45cm, respectively, by moving the two anti-Helmholtz trap coils along a track with a linear actuator. T. Lahaye et al. [176] were able to produce a chain of moving magnetic Ioffe-Pritchard traps to transport cold atoms from a MOT to a detection region as far as 170cm from the MOT. They combined the transverse confinement of a two-dimensional guide created by two wires parallel to the guide's axis, with the longitudinal trapping produced by an array of 50 rare-earth permanent magnets fixed on a conveyor belt that was set in motion along the guide's axis by an electric motor.

On-chip magnetic transport

The development of atom chips has allowed the integration of all the elements needed for magnetic trapping and transport in a compact planar geometry with a total size of a few centimetres. Atoms from a magneto-optical trap can be loaded into a magnetic guide or trap created by an atom chip and subsequently transported parallel to the surface of the chip.

The expansion of cold neutral lithium atoms in a tube-like, quadrupole, magnetic guide

created on the side of a current-carrying wire by superimposing the magnetic field from the wire with a homogeneous bias field orthogonal to the wire, was measured by the group of J. Schmiedmayer first using a free-standing wire [177] and later using micro-fabricated wires mounted on the surface of an atom chip [13]. Two different configurations based on two and four micro-fabricated wires with alternating currents on a chip were used by N. H. Dekker et al. [178] to create a two-dimensional vertical guide for laser-cooled cesium atoms.

Several different configurations for guides and waveguides for cold atoms, including those integrated on atom chips, were reviewed and proposed in the article by E. A. Hinds and I. G. Hughes [10]. This article, along with references [11, 70, 179], proposed a method for the controlled transport of cold atoms in arrays of videotape magnetic traps by rotating the direction of the applied bias field that gives rise to the traps (see section 2.3.6). Section 7.3 of this thesis is dedicated to detailing the results of the transport experiments based exactly on this idea.

An equivalent idea, applied to electrostatic potentials, has recently been used to trap and transport CO molecules from a supersonic beam in travelling potential wells along a length of 5cm [180]. A chip containing more than 1200 micro-structured electrodes was used to create an array of potential minima which could be translated smoothly by applying sinusoidally-varying potentials to the electrodes.

The group of T. W. Hänsch and J. Reichel [14, 181–183] realised a magnetic conveyor belt for the transport of cold neutral atoms on an atom chip. A moving chain of potential wells was created using time-dependent currents in lithographically patterned gold wires. The atoms remained trapped in all three dimensions during transport. A wire along the direction of transport and an orthogonal bias field were used to create a static two-dimensional quadrupole potential for transverse confinement. Two sets of meandering wires with time-varying currents were used together with another bias field to create a moving longitudinal confinement for transport. A thermal cloud of atoms was transported in this way over a distance of 3.4mm [181], and non-destructive transport of a BEC over a distance of 1.6mm was also achieved [14]. In order to reduce heating effects during transport, due to transverse deviations from a linear transport path and changes in the shape of the trapping potential, numerical optimisation of the currents in the wires and bias-field coils was used, as described in [182]. However, all position and trap-frequency deviations could not be eliminated at once, limiting the transport speed and distance. An improved, two-layer version of this conveyor belt, together with numerical optimisation allowed smoother and faster transport of a thermal cloud of atoms over larger distances, up to 24cm [183].

In a very similar dual-layer, chip set up, the group of C. Zimmermann and J. Fortágh [184] used a set of three parallel micro-fabricated wires along the transport direction, together with periodically repeated sets of eight transport wires orthogonal to them, to demonstrate adiabatic transport of a 6μK thermal cloud over 1.95mm. They proposed an optimised transport scheme with constant trap frequencies and transverse position, that would enable transport over a distance of 17.5mm in their chip.

The propagation of a Bose-Einstein condensate of sodium atoms in a magnetic waveguide

created by a single micro-fabricated wire, along a distance of 12mm, was studied experimentally by A. E. Leanhardt et al. [123]. Single-mode propagation in the lower transverse vibrational state was observed along homogeneous segments of the waveguide. Transverse excitations, leading to non-single mode propagation, were caused by perturbations in the waveguide potential. The reflection and transmission of the BEC through these perturbations was studied as a function of its incident velocity in the waveguide.

The group of R. J. C. Spreeuw [185] recently presented results with cold atoms in a two-dimensional array of hundreds of tight magnetic traps generated by a lithographically-patterned, magnetic FePt film, permanently magnetised in the direction perpendicular to the chip surface. An array of traps formed 10μm away from the chip surface was continuously displaced up to a round-trip distance of 360μm by rotating an external bias field. A 40% atom loss was observed, higher than the background loss rate, attributed to the slow time-response of the bias field coils that failed to reproduce the computed optimum magnetic fields for transport at constant height and field minima.

7.2.2 Transport based on optical forces

The optical-dipole force arises from the interaction of the induced, atomic, electric-dipole moment, $\vec{d}$, with the intensity gradient of a light field (electric field $\vec{E}$). At low intensity, the resulting optical-dipole potential, U, is directly proportional to the intensity of the light, $I(\vec{r})$, and inversely proportional to the detuning, $\triangle$, of the light with respect to the atomic resonance: $U = -\frac{1}{2}\langle\vec{d}\cdot\vec{E}\rangle \propto \frac{I(\vec{r})}{\triangle}$ (see reference [186]). When the laser is red-detuned with respect to the atomic transition ($\triangle < 0$), atoms are attracted towards the potential minima that correspond to the regions of high laser intensity. For blue-detuned laser light ($\triangle > 0$) atoms are attracted towards the regions of low-light intensity.

These concepts have been used in order to transport atoms both in optical two-dimensional guides and in optical traps while confined in three dimensions.

M. J. Renn et al. [187,188] used red-detuned light propagating inside the hollow core of an optical fibre by grazing incidence reflection to guide rubidium atoms along the axis of the fibre for a distance of 3.1cm. In similar experiments [189–191], blue-detuned laser light propagated through the glass region of a hollow-core optical fibre through total internal reflection, and the evanescent field inside the hollow core of the fibre was used to guide cold rubidium atoms along the fibre axis for distances of a few centimetres.

A blue-detuned hollow laser beam with a field mode with zero intensity along the beam axis has been employed as a guide for the transport of cold atoms along distances up to 20cm [192–195], and also as a waveguide for Bose-Einstein condensates [196].

Similarly, far-off-resonance, red-detuned, focused laser beams have been used to transport cold atoms in vertical guides [197–200] and horizontal guides [201] along distances between a few millimetres and 30cm.

Single-atom transport in a moving, standing-wave, dipole trap was realised by the group

of D. Meschede, who adiabatically transported single cesium atoms with sub-micrometre precision over distances of the order of 1cm [202, 203]. The potential wells created by the standing wave were translated along the optical axis by changing the frequency difference between two counter-propagating laser beams.

A Bose-Einstein condensate was transported in a one-dimensional moving optical lattice by A. Browaeys et al. [204], for the study of the properties of the lattice band structure.

T. L. Gustavson et al. [205] loaded a Bose-Einstein condensate of sodium atoms from a magnetic trap into an optical dipole trap and transported it over 44cm using optical tweezers for the first time. Transport was accomplished moving the focus of an infrared laser beam by displacing a lens on a linear translation stage.

W. Guerin et al [206] realised a guided quasi-continuous atom laser by outcoupling atoms from a Bose-Einstein condensate from a hybrid opto-magnetic trap into a horizontal atomic waveguide made by a far-off-resonance optical trap. They observed propagation of the atoms in the waveguide over distances of $\sim$ 1mm.

7.3 Transport experiments in the videotape atom chip

This section describes the transport mechanism employed to displace the potential that confined the atoms in the videotape magnetic traps. The evolution of the trap properties during transport is discussed in section 7.3.1 and the experimental procedure and results are presented in section 7.3.2.

7.3.1 Description of the transport mechanism

Cold rubidium atoms confined in arrays of elongated videotape magnetic traps were translated along the x direction, transverse to the traps axes and parallel to the chip surface, by rotating the direction of the uniform bias magnetic field in time.

The videotape magnetic traps are created at the positions in which the videotape field is cancelled out by the applied uniform bias field (see section 2.3.6). At a given distance from the chip surface, the field created by the magnetised videotape changes direction along x, while its modulus remains unchanged. A simple but effective way of translating the confining potential along this direction is to use a bias field with constant modulus and with its direction rotating in the x-y plane as time progresses. Figure 7.1 shows the videotape magnetic field lines in the x-y plane, together with a rotating bias field. We can see that the bias field rotation enables the continuous displacement of an array of videotape traps along the x direction.

One full rotation of the bias field corresponds to a translation of the traps along x by a distance equal to the spatial period of the videotape magnetisation, $\lambda \sim 110\mu$m. The rotating bias field can be expressed as:

$$\vec{B}_{bias} = B_b \left(\cos(\Omega t)\hat{\mathbf{x}} + \sin(\Omega t)\hat{\mathbf{y}}\right) , \tag{7.1}$$

where Ω is the bias-field rotation frequency. The displacement of the trap centre along x takes place with a velocity that depends on the bias-field rotation frequency, and that we can write as $v_x = \frac{\lambda\Omega}{2\pi}$.

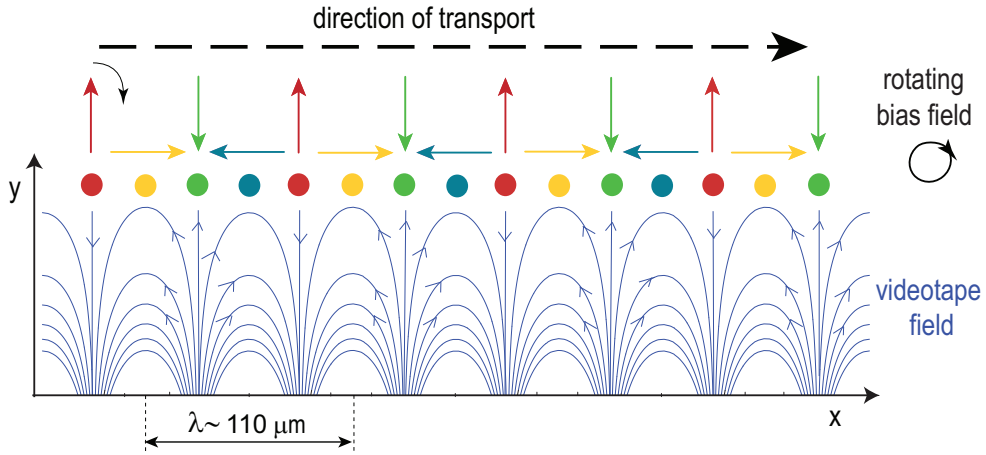

Figure 7.1: Videotape magnetic field lines and rotating bias field in the x-y plane, used to displace the trapping potential along x, as indicated by the dashed arrow. The traps form at the positions (different colour points) along x determined by the direction of the bias field, which is uniform across the chip. As the orientation of the bias field direction changes in time during one rotation, the traps translate along x by a distance equal to λ.

Tilt of the traps in three dimensions during transport

It is important to consider the contribution of the y-component of the magnetic field generated by the end wires to the confining potential felt by the atoms during a conveying cycle. As described in section 2.3.3, this y-component changes sign as we move along the z axis, from $z < 0$ to $z > 0$. Note that any field components added in the x-y plane will contribute towards cancelling the videotape field, shifting the position of the trap centre on that plane.

Figure 7.2 shows the calculated cross-sections of the potential in the videotape traps through the x-y, x-z and z-y planes, respectively, from left to right, through the position of the trap centre. The plots in this figure correspond to a videotape magnetisation period of $\lambda = 110\mu$m, a bias field $B_b = 2.2$G, a field from the z-coils equal to $B_z = 0$, and a current through the end wires of $I_{end} = 10$A. The height of the trap centre is $y_0 \simeq 68\mu$m. These parameters are used in all the calculated examples throughout this section, and correspond to some of the experimental conditions during data taking.

The contours of constant magnetic field strength are plotted for times equal to 0, $T/4$, $T/2$ and $3T/4$, from top to bottom, where $T = 2\pi/\Omega$ is the period corresponding to one transport cycle, i.e., to one full rotation of the bias field. These times correspond to bias fields, $\vec{B}_{bias}$, equal to $B_b\hat{\mathbf{x}}$, $B_b\hat{\mathbf{y}}$, $-B_b\hat{\mathbf{x}}$ and $-B_b\hat{\mathbf{y}}$, respectively.

For $t = 0$ and $t = T/2$ we observe a tilt of the potential on the x-z plane, so that the axis of the trap is at an angle of $\sim 0.7^\circ$ to the z direction, while for $t = T/4$ and $t = 3T/4$ the trap is tilted by a similar angle, but on the z-y plane. When the bias field used to create the videotape magnetic trap is $\vec{B}_{bias} = B_b\hat{\mathbf{x}}$ ($t = 0$, first row of plots in figure 7.2), the y-field component from the end wires adds up to the bias field causing a displacement of the trap towards positive x for $z > 0$, towards negative x for $z < 0$, and no displacement for $z = 0$ (see section 2.3.6). This produces a tilt of the trap when we look at its cross-section through the x-z plane. The tilt for $\vec{B}_{bias} = -B_b\hat{\mathbf{x}}$ is in the opposite direction ($t = T/2$, third row of plots in figure 7.2). On the other hand, when the bias field is purely along y, $\vec{B}_{bias} = \pm B_b\hat{\mathbf{y}}$, the y-component of the field from the end wires adds up to the total bias field increasing its magnitude on one side of $z = 0$ and decreasing it on the other side. This means the trap is tilted on the y-z plane, as seen on the second and fourth rows of plots in figure 7.2 ($t = T/4$ and $t = 3T/4$, respectively).

When the bias is purely along x, the y-component of the end wires also causes a decrease in trap height of the order of a few micrometres at the edges of the trap, where $|z| \sim 2$mm, due to the increase of the total modulus of the bias field, caused by the added y-component of the end-wire field (see section 2.3.6 and future figure 7.5).

Note that, since the potential felt by the atoms in the traps is proportional to the modulus of the total magnetic field, the contours of constant magnetic field strength are equivalent to the contours of constant potential. It is instructive to look at a contour of constant magnetic field strength in three-dimensional space to gain a better understanding of the effect of the previously mentioned tilts during transport. Figure 7.3 shows a 3D plot of the 3.4G-magnetic-field contour during a transport sequence corresponding to two full rotations of the bias field. The parameters used are the same as those in figure 7.2. As the elongated trap progresses from $x = -110\mu$m to $x = 110\mu$m, we observe a movement of the trap edges that resembles that of the pedals of a moving bicycle. The tilts on the x-z and z-y planes evolve during transport giving rise to this "bicycle-like" movement.

Due to the presence of the force of gravity, the oscillating vertical tilt of the videotape traps during transport results in an axial sloshing of the centre of mass of the trapped cloud, which can give rise to an important heating rate during the conveying process. This effect grows when the length of the cloud increases, possibly due to the increase in the amplitude of the "bicycle-like" movement at the edges of the trap. The circular movement of the trap edges can also lead to a centrifugal acceleration of the atoms at the ends of the trap, inducing heating.

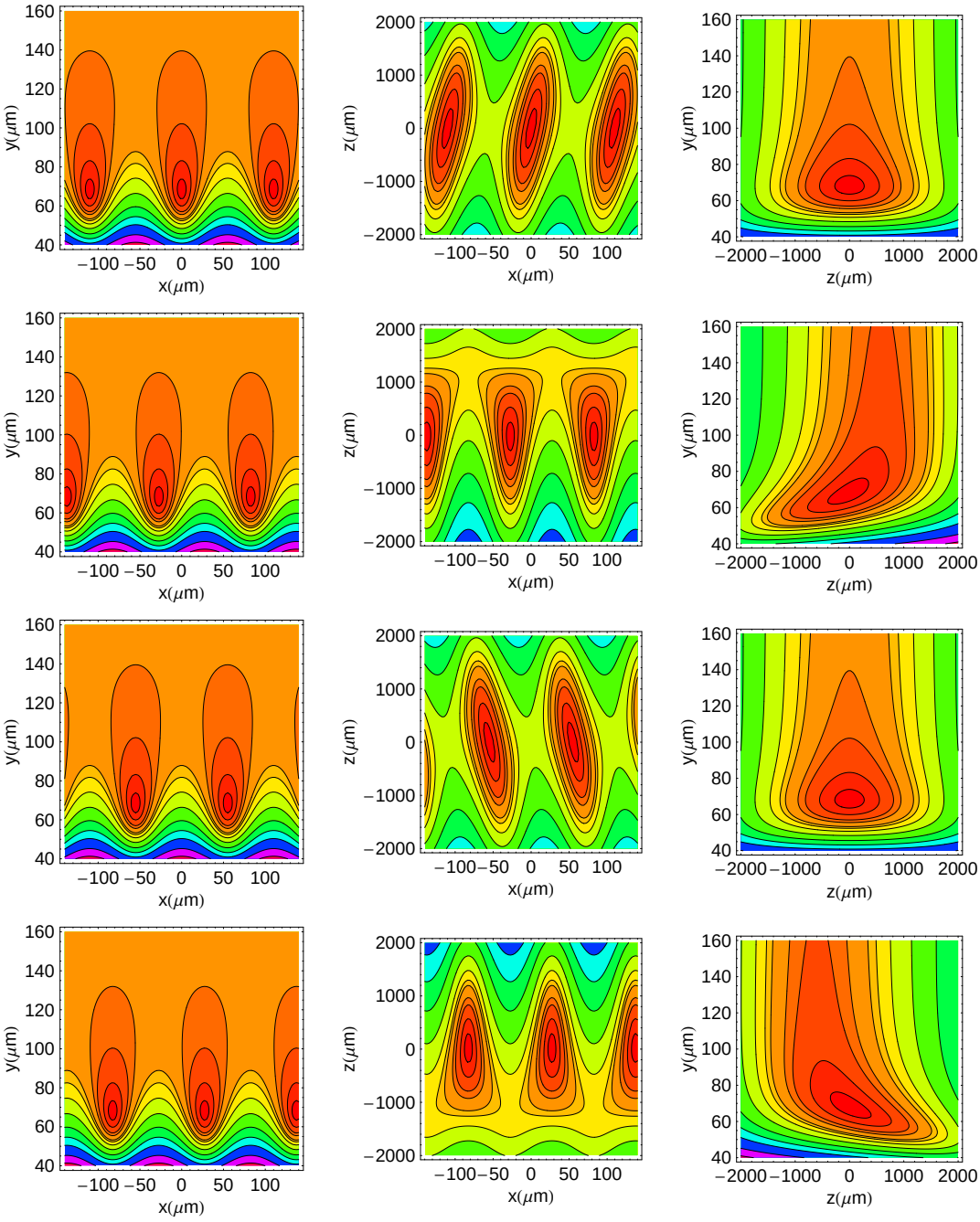

Figure 7.2: Contours of constant magnetic field strength corresponding to a full rotation of the bias field direction. Cross-sections through the x-y, x-z and z-y planes, passing through the centre of the trap are shown from left to right. From top to bottom, the times are $t = 0$, $t = T/4$, $t = T/2$ and $t = 3T/4$. The corresponding bias fields, $\vec{B}_{bias}$, are $B_b\hat{\mathbf{x}}$, $B_b\hat{\mathbf{y}}$, $-B_b\hat{\mathbf{x}}$ and $-B_b\hat{\mathbf{y}}$, respectively. Other parameters used are: $\lambda = 110\mu$m, $B_b = 2.2$G, $B_z = 0$ and $I_{end} = 10$A. The contours shown corresponds to magnetic field strengths between 3.3G and 14G.

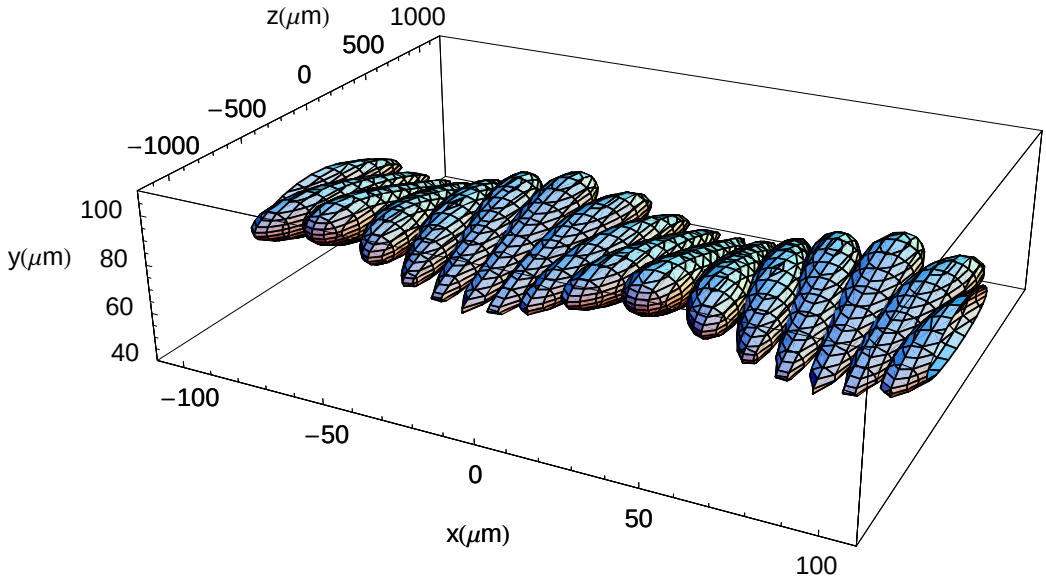

Figure 7.3: Plot of the 3.4 Gauss magnetic-field-strength contour during two full transport cycles, as the trap moves from $x = -110\mu$m to $x = 110\mu$m. The parameters used in the calculation were: $\lambda = 110\mu$m, $B_b = 2.2$G, $B_z = 0$ and $I_{end} = 10$A. Each contour corresponds to a different time during transport. No gravity was included in the calculation.

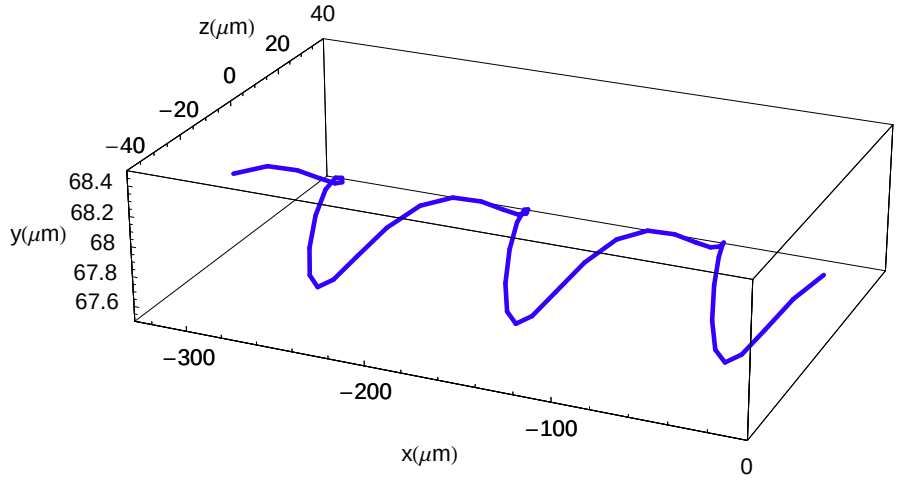

Figure 7.4: Plot of the calculated path of the trap centre (position of minimum field strength) during three full transport cycles, from $x = -330\mu$m to $x = 0$. The parameters used in the calculation were: $\lambda = 110\mu$m, $B_b = 2.2$G, $B_z = 0$ and $I_{end} = 10$A. No gravity was included in the calculation.

It is important to consider whether the trap frequencies or the position of the trap centre vary during transport, since changes in trap shape or position could lead to heating of the trapped atoms as they are transported.

Changes in trap-centre position during transport

In the example corresponding to the parameters used in most of our experiments, the position of the minimum magnetic field of a single videotape trap deviates slightly from the straight-line path along x that we would expect for the smoothest possible transport.

Figure 7.4 shows a plot of the calculated path described by the trap centre during three full transport cycles. We observe an oscillation of the y-coordinate of the trap centre with a very small amplitude of $\sim$ 150nm, and a frequency equal to 2Ω, where Ω is the bias-field-rotation frequency. The z-coordinate of the trap centre oscillates around 0 with an amplitude of $\sim 24\mu$m, at a frequency equal to Ω.

The temperatures of the atomic clouds during transport experiments were between $\sim 500\mu$K and $\sim 6\mu$K, corresponding to rms sizes of $\sigma_z \simeq 2720\mu$m, $\sigma_{x-y} \simeq 23\mu$m, and $\sigma_z \simeq 300\mu$m, $\sigma_{x-y} \simeq 2.5\mu$m, respectively. At a temperature of $\sim 500\mu$K, the oscillations of the trap centre position are at least two orders of magnitude smaller in amplitude than the atomic oscillations in the trap. At a temperature of $\sim 6\mu$K, the amplitudes of the trap centre oscillations are still a factor of $\sim$ 15 times lower than the corresponding rms-trap sizes at that temperature.

The minimum magnetic field strength at the bottom of the trap oscillates very slightly with a frequency of 2Ω and an amplitude of $\sim$ 0.13mG, equivalent to $\sim$ 8.7nK.

These periodic variations of the trap centre can induce oscillations of the atoms in the trap. Axial sloshing of the cloud in the trap would be the most noticeable of these oscillations. The trap-centre displacements will therefore contribute to heating the trapped atoms during transport. We expect these heating rates to be low if we avoid heating the atoms resonantly, i.e., if we use bias-field-rotation frequencies far enough from the values of the trap frequencies.

Variation of the trapping frequencies during transport

The shape of the transverse confinement at the centre of the trap (looking at a cross-section of the potential through the x-y plane, passing through the trap centre), hardly changes during transport, which means that the transverse trap frequencies stay practically constant at the trap centre. We can see in the plots on the first column of figure 7.2, that there are no obvious changes in the shape of the potential at the centre of one videotape trap, in the x-y plane, during transport. The potential is simply translated along x without changing much in shape.

However, there are obvious changes in transverse trap frequency as we move away from the centre of the trap, along its axis, and look at the x-z or y-z cross-sections, as explained in the next paragraphs.

In order to find out how the axial frequency varies during transport, we need to move along the effective axial line of minimum magnetic field strength (see end of section 2.3.6), that we denote as ξ, and which is tilted in three dimensions, as we can see in figure 7.5, where the evolution of the position of this line during transport is shown. The line ξ is calculated by finding the position of the minimum magnetic field strength in the x-y plane for a given z value, and then moving along z, for values between $z = -2$mm and $z = 2$mm.

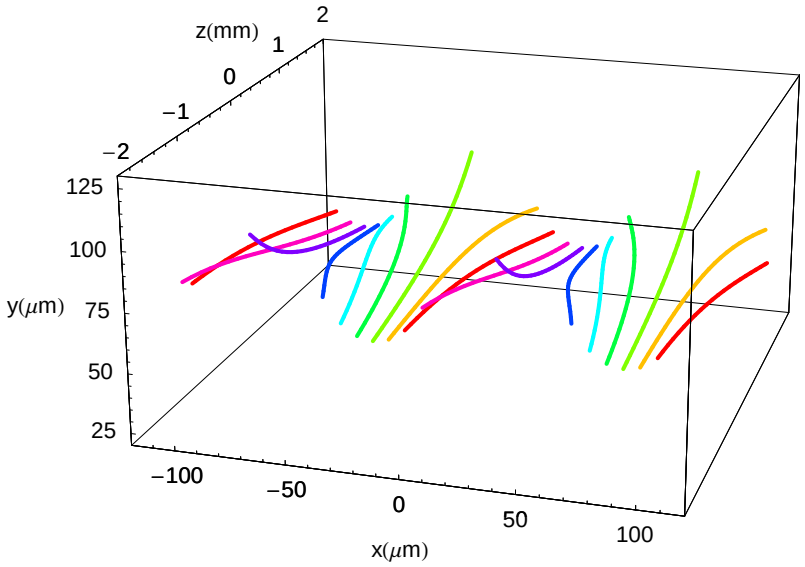

Figure 7.5: Axial line (ξ) of minimum magnetic field strength as seen in 3D during two cycles of bias-field rotation for the transport of atoms in videotape traps with $\lambda = 110\mu$m, $B_b = 2.2$G, $B_z = 0$ and $I_{end} = 10$A.

Plotting the magnetic field strength along the line ξ, we find that the axial confinement varies periodically during one transport cycle. Figure 7.6 shows such a plot, for the extreme changes of the axial confinement, which take place at the positions in which the trap is tilted in the $z - y$ plane, i.e., at $t = T/4$ and $t = 3T/4$ during one transport cycle of period T. The change in the shape of the axial potential can lead to axial sloshing and also to a variation of the axial trapping frequency during transport. A periodic variation of the trapping frequency can result in a parametric excitation (see section 5.3.3) of the atoms in the trap if the transport frequency, i.e., the frequency of bias-field rotation, Ω, is close enough to twice the value of the axial trap frequency. In our experiments, the transport frequency, $\Omega = 50$Hz, was close enough to the value, ~ 30Hz, of twice the axial trap frequency for heating due to parametric resonance during several transport cycles to be possible.

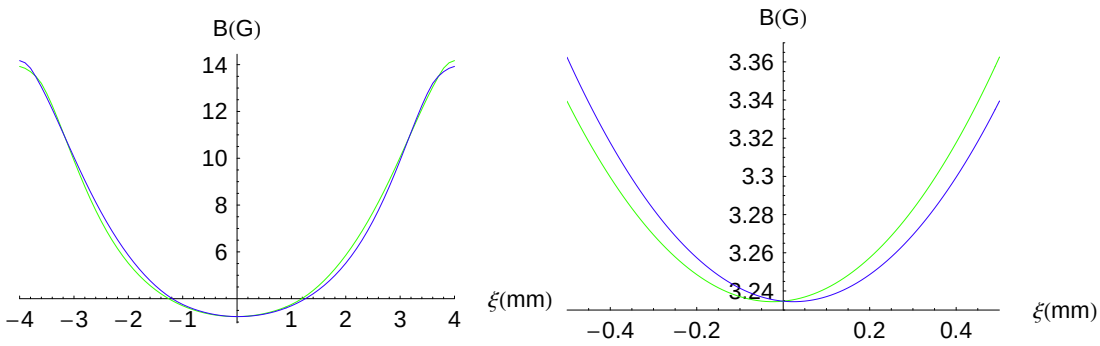

Figure 7.6: Axial magnetic field strength along the line ξ, for the extreme changes of the axial confinement, which correspond to $t = T/4$ (green) and $t = 3T/4$ (blue), during one transport cycle of period T. The videotape trap parameters are: $\lambda = 110\mu$m, $B_b = 2.2$G, $B_z = 0$ and $I_{end} = 10$A. The plot on the right hand side zooms into the central region of the axial confinement.

Knowing the coordinates (x, y, z) of the line ξ of minimum magnetic field strength in three-dimensional space (see figure 7.5), it is possible to plot the contours of constant magnetic field strength of the videotape traps on the $x - \xi$ and $\xi - y$ surfaces, respectively, as shown on figure 7.7. These plots were calculated moving along the line ξ by calculating the variation of the magnetic field strength as a function of either x (first column in the figure) or y (second column in the figure), for every point along the line ξ. From top to bottom, the plots correspond to the same times and bias fields, during one transport cycle, as those of figure 7.2. We can see that the tilts of the traps that we observed in figure 7.2 have now disappeared because we are moving along the coordinate ξ, which corresponds to the effective trap axis.

We notice large changes in the shape of the transverse confinement for different positions along ξ, for the second and fourth rows of plots in figure 7.7. In the second row of plots, the transverse confinement becomes tighter for negative values of ξ, which correspond to the edge of the trap which is closer to the magnetised videotape when the trap is vertically tilted (see second row of plots in figure 7.2). On the other hand, the trap edge at positive ξ is further away from the videotape surface and therefore the transverse confinement is relaxed at this end of the trap. For the fourth row of plots in figure 7.7 the effect is opposite since the vertical tilt is also opposite, and the transverse confinement becomes tighter for positive ξ. These changes in transverse trap frequency can result in a parametric resonant excitation (see section 5.3.3) of the transverse trapping potential during transport, when the frequency of bias field rotation, Ω, is close to twice the transverse trap frequencies. The excitation would have opposite phases at the opposite ends of the elongated trap. The frequencies of bias-field rotation we employed in our experiments were of the order of 50Hz, far from the transverse trap frequencies, which were of the order of a kHz, so that we expect the periodic compression and de-compression of the ends of the trap to be adiabatic compared to the much faster transverse motion of the atoms in the trap.

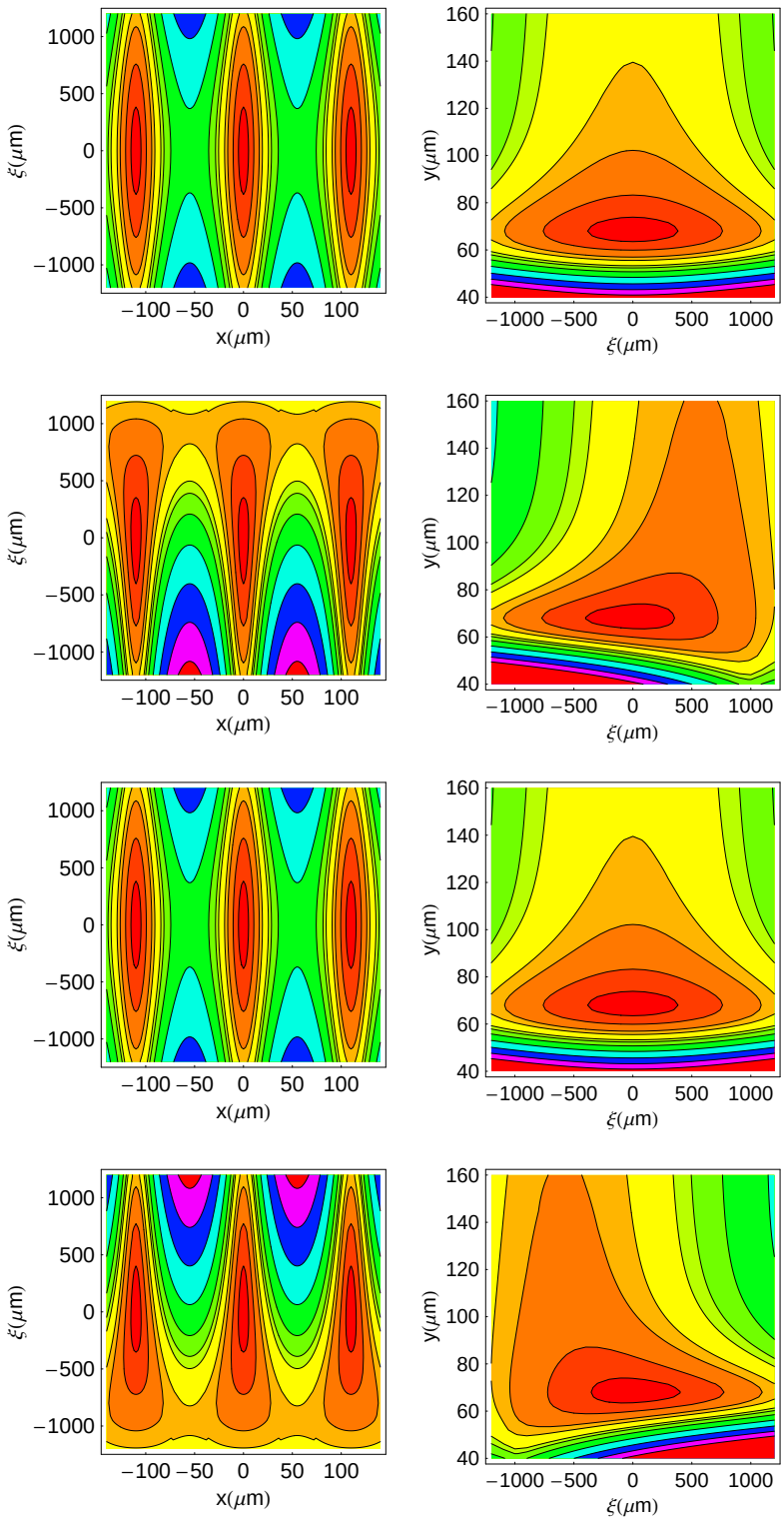

Figure 7.7: Contours of constant magnetic field modulus corresponding to a full rotation of the bias field. Cross-sections through the $x-\xi$ and $\xi-y$ surfaces are shown on the left- and right-hand sides respectively. From top to bottom, the times are $t=0$, $t=T/4$, $t=T/2$ and $t=3T/4$, corresponding to bias fields: $\vec{B}_b = B_b\hat{\mathbf{x}}$, $\vec{B}_b = B_b\hat{\mathbf{y}}$, $\vec{B}_b = -B_b\hat{\mathbf{x}}$ and $\vec{B}_b = -B_b\hat{\mathbf{y}}$, respectively. The parameters used in these plots are: $\lambda = 110\mu$m, $B_b = 2.2$G, $B_z = 0$ and $I_{end} = 10$A. The contours shown corresponds to magnetic field strengths between 3.3G and 14G.

However, the compression and de-compression of the trap ends induces a displacement of the atoms along the axial direction of the cloud towards the region of lower transverse confinement. This can lead to axial sloshing of the cloud in the trap. If we consider a line parallel to the line of minimum field strength of the trap, ξ, but displaced from it along x by a distance Δx, we find that the change in transverse magnetic field strength along that line combines with the axial confinement of the end wires shifting the centre of the total potential along that line towards the end of the trap with relaxed transverse confinement. This shift is larger for larger Δx, due to the more dramatic change of transverse confinement along that line. Hence, we would expect hotter clouds with larger transverse sizes (larger Δx) to be more affected by this effect during transport. We calculate that the centre of the potential along a line parallel to ξ but displaced from it by $\Delta x = 8.4\mu$m, oscillates with an amplitude of $\sim 250\mu$m along that line during transport. This value of Δx corresponds to the rms transverse size of a cloud with a temperature of 66μK, for the experimental conditions described in section 7.3.2. For a temperature of 6μK, the rms transverse size of the cloud is $\sim 2.5\mu$m and, at this distance from the effective trap axis, we obtain an oscillation amplitude of only a few micrometres for the centre of the confinement along the longitudinal direction of the cloud. The frequency of this oscillation is equal to the bias-field-rotation frequency during transport (50Hz), and is probably too far from the frequency of the axial motion of the atoms in the trap (13Hz) to lead to resonant heating. However, far enough from the effective trap axis (and therefore for large enough temperatures), the displacements of the centre of the potential can be large enough to result in axial sloshing of the cloud in the trap.

Sources of heating and atom loss

Therefore, we have seen that there are several processes that can contribute to heating the trapped atoms as the confining potential is translated in our videotape atomic conveyor. The deviations of the position of the trap centre from a straight-line path during transport, the changes in axial trap frequency and in transverse trap frequencies at the ends of the trap, and the transport-induced axial sloshing of the atoms and angular acceleration at the ends of the trap due to the "bicycle-like" movement of the confining potential as it is translated, can be responsible for any possible temperature increase or atom loss during the transport process. Transporting the potential at a velocity much slower than that of the movement of the atoms in the trap, and avoiding resonant effects, will minimise heating during transport.

The changes in the trapping potential will be adiabatic with respect to the magnetic sublevels if they are slow enough compared to the Larmor frequencies of the atomic spins in the trap, which are usually of the order of MHz. Since the transport frequencies we used were of the order of 50Hz, we expect no atom loss due to spin flips caused by non-adiabatic movement.

The fact that the confining potential is transported faster (at a transport frequency of 50Hz) than the axial movement of the atoms in the trap ($\sim$ 13Hz axial trap frequency) can induce some additional heating on the atoms during transport.

The slight tilt of the surface of the videotape atom chip by an angle of $\sim 2.6^\circ$ with respect

to the horizontal (see section 2.2) has the effect of inducing additional axial displacements of the atoms when the shape of the axial confining potential of the trap changes. It is therefore possible that the tilt of the chip is partly responsible for driving the axial sloshing of the cloud during transport. However, the variation of axial frequency at the centre of the trap is too small to see in figure 7.6(left) and therefore this is unlikely to be a main contribution to the effect.

Finally, the initial acceleration at the start of the transport process can also be an important source of heating for the transported atoms. When transport starts, the velocity of the cloud increases in a time of about 1ms, corresponding to the response time of the bias field coils, from 0 to a value of ~ 5.5mm/s along x, resulting in an initial acceleration of $\sim 5.5\text{m/s}^2$, that would cause an excitation and temperature increase of the trapped atoms.

7.3.2 Experimental procedure and results

Apparatus

Two pairs of coils with their axes along orthogonal directions ($(\hat{\mathbf{x}} + \hat{\mathbf{y}})$ and $(\hat{\mathbf{x}} - \hat{\mathbf{y}})$, as in figure 3.2) were used to generate a rotating bias field for the transport of cold atoms in videotape magnetic traps, as expressed in equation 7.1.

Two bipolar operational power supplies were purchased for this purpose from Kepco Inc., model BOP 36-12M, in order to be able to run both positive and negative currents through the bias-field coils. They were capable of supplying maximum output currents and voltages of $\pm$12A and $\pm$36V. They were operated as current supplies in current control mode, in such a way that they generated an output current of 1.2A per Volt of control voltage received as input. No separate FET circuits were needed for current control, since they were already included in the design of the bipolar power supplies.

Figure 7.8 shows a schematic view of the set up used to implement the transport. The value of the voltage sent to each coil pair was entered in the computer interface in Volts. The corresponding DC control voltage signal generated by the computer was added to a sinusoidal voltage signal generated by a DS345 Stanford function generator using a home-built summing operational-amplifier circuit. The Stanford function generators were operated in "burst" mode so that controlling the frequency, amplitude, offset, phase and number of cycles of the sine function was possible. The sinusoidal signal for bias field rotation could be triggered on and off through a TTL control connected to the computer interface. For added flexibility, the output of one of the Stanford function generators was passed through an inverter circuit, which could be triggered using the computer interface, before being sent to the corresponding summing circuit. The combined output voltage of the summing circuit was then used as control voltage input for the bipolar power supply. The output current generated by the bipolar power supply followed the variations of the combined control voltage that it took as input. This current output was finally fed into the corresponding bias field coil pair.

The graph on the left of figure 7.9 shows an example of the voltages used as input for the bipolar power supplies during one bias-field-rotation cycle, while the graph on the

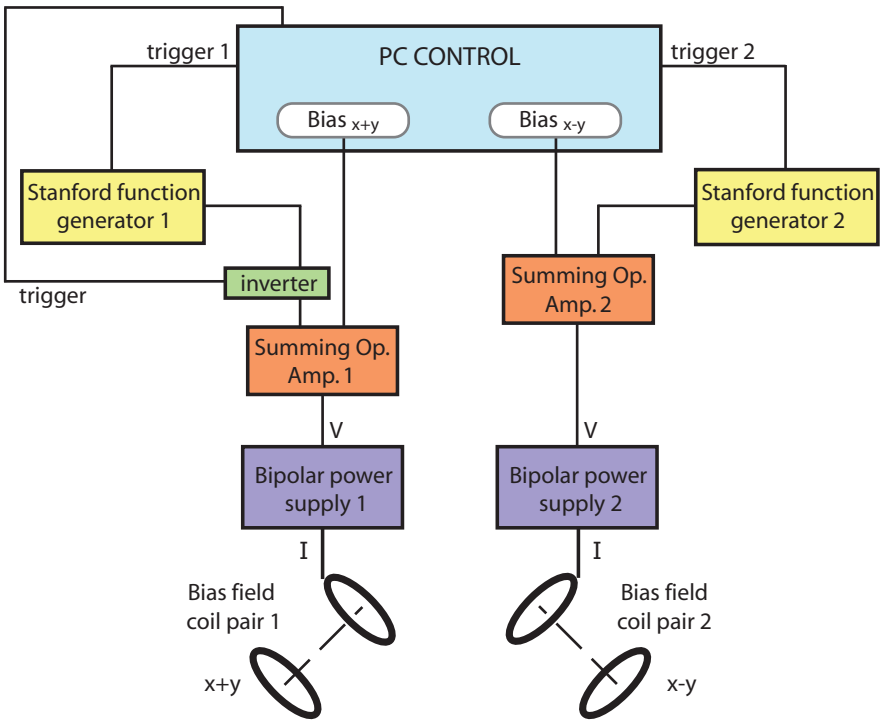

Figure 7.8: Schematic of the experimental set up used for the transport experiments.

right shows the measured currents that ran through the bias-field coils during three bias-field-rotation cycles for transport. The two graphs correspond to two different transport realisations. The current running through each bias-coil pair was measured from the voltage drop through a sense resistor connected in series with it. The magnetic field created by each bias-coil pair (Bias_{x+y} along $(\hat{\mathbf{x}}+\hat{\mathbf{y}})$, and Bias_{x-y} along $(\hat{\mathbf{x}}-\hat{\mathbf{y}})$) was proportional to the measured currents. In the example of the figure on the right hand side, the videotape traps were loaded with $\text{Bias}_{x+y} \simeq 26.4\text{G}$ and $\text{Bias}_{x-y} = 0$, then conveyed for 3 cycles by rotating the direction of the total bias field at a frequency of 50Hz, and then held for imaging.

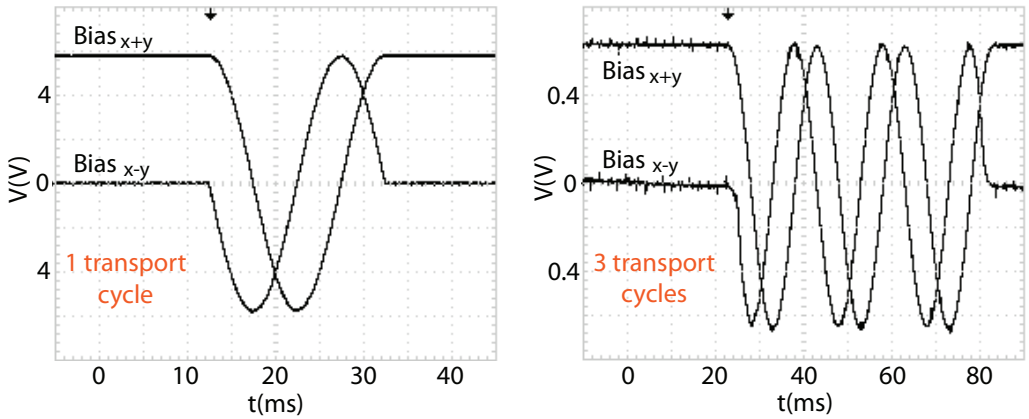

Figure 7.9: Oscilloscope traces of the control voltage sent to the bipolar power supplies (left), and of the voltage difference measured through a 0.1Ω-sense resistor connected in series with each of the bias-field-coil pairs (right).

The relatively high inductance of our bias-field coils (see section 3.2.2) set an experimental higher limit to the frequency of bias-field rotation used for transport. The slow response time of these coils, measured to be of the order of 1ms, limited the transport frequencies to a few hundred Hz. The frequency used for most transport experiments was 50Hz. It is possible to compare the sharp initial change of the control voltages used as input for the bipolar power supplies, shown in figure 7.9(left), with the slower response of the bias-coils current, shown in figure 7.9(right).

Preliminary results conveying hot atoms

Preliminary transport experiments were carried out without any radio-frequency evaporation stage in the wire magnetic trap (see section 4.4). Atoms were therefore transferred from a "hot" wire magnetic trap into videotape magnetic traps, in such a way that around 5 or 6 elongated videotape traps were loaded, with temperatures of the order of $\sim 500\mu$K. This loading procedure was far from being optimum: the transfer efficiency was low, and so were the atom numbers measured in the loaded videotape traps. However, it is interesting to compare the transport of these "hot" atoms with that of colder atoms with temperatures between 6 and 66μK, detailed in the next subsection.

The experimental sequence used to load cold atoms in videotape magnetic traps was similar to the one detailed in chapter 4. The initial wire magnetic trap was compressed during 150ms by ramping the bias field up to 26G and the atoms were transferred from the wire trap to the videotape traps in three stages, each with a duration of 800ms. During the first stage the centre-wire current was reduced to 7A, the bias field increased to 37G and B_z decreased to 1.8G. During the second stage the current in the centre wire was reduced from 7 to 3A and the bias field was ramped to a value of 31.7G. Up to this point the bias field remained along the x-direction, i.e., with equal currents through both bias-field-coil pairs so that Bias_{x+y} =Bias_{x-y}, each equal to 22.4G at the end of this stage. During the last stage the centre wire current was lowered to 0, the value of B_z was decreased to 0.7G, and the values of Bias_{x+y} and Bias_{x-y} were ramped to 18.7G and 0, respectively. The atoms were then transported over variable distances in these videotape traps by rotating the bias field direction with a frequency of 50Hz. An absorption image of the atoms was recorded at the end of the entire sequence, using an imaging set-up similar to "set up II", described in section 3.5.3.

Figure 7.10 shows absorption images of atoms confined in arrays of videotape traps at temperatures around 500μK, and transported along the transverse x-direction, over distances of up to $\sim$ 1mm, as the bias field goes through 0 to 9 rotation cycles.

The distance from these traps to the chip surface was of the order of $\sim 30\mu$m. The limiting trap depth was equal to $\sim$ 14G along the y-direction. At the temperatures of the atoms in these traps ($\sim 500\mu$K), the rms axial size of the clouds was of the order of 2.7mm. The corresponding ratio of thermal energy to potential depth was high, around 0.5, meaning that, after the atoms were loaded in the videotape traps, there was already an important loss rate that led to a short lifetime of the atoms in these non-optimised traps. This explains in part the obvious atom loss that we observe in figure 7.10, where we see that there are

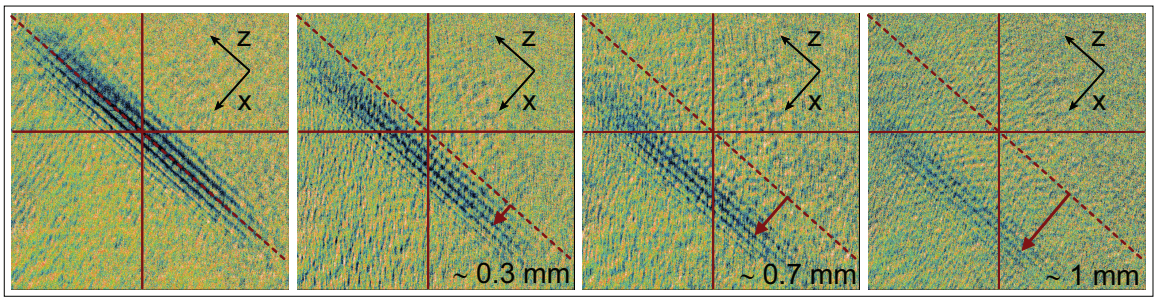

Figure 7.10: Absorption images of an array of 5-6 videotape magnetic traps transported parallel to the chip surface, along the x direction, indicated by the arrow. From left to right the transported distances were: 0, $\sim$ 0.33mm, $\sim$ 0.66mm and $\sim$ 1mm, corresponding to 0, 3, 6 and 9 cycles of bias field rotation at a frequency of 50Hz. The solid and dashed lines are fixed at the same positions on all images.

fewer atoms left after 9 transport cycles. The other contribution to the atom loss comes from the transport-induced, axial sloshing of the atoms in the videotape traps, due to the "bicycle-like" movement the traps describe as they are conveyed. This excitation heats the atoms and enhances the atom loss. We found that, at these temperatures, the amplitude of the induced, axial-dipole oscillations of the centre of mass of the cloud after one transport cycle was of the order of 300μm, around 4-5 times larger than the amplitude of the dipole oscillations before transport.

Results conveying cold atoms

This subsection describes experiments in which colder atoms with temperatures between 6 and 66μK were loaded into two videotape-magnetic traps and transported parallel to the chip surface, along x, over distances of several millimetres to both sides of the centre of the chip. The atoms were loaded into videotape traps from a wire magnetic trap in which they had been previously cooled through RF evaporation. The lower temperatures reached in this way meant that atoms from the wire trap were very efficiently loaded into two videotape traps. In this case, higher atom numbers per trap and longer lifetimes were measured, compared to the lower values measured after the inefficient loading of hotter atoms into 5 or 6 videotape traps, described in the previous subsection.

The experimental procedure used for loading cold atoms into videotape traps followed all the optimised steps described in chapter 4. The dispensing time was 30s. During the final stage of transfer of atoms from the compressed wire magnetic trap into videotape magnetic traps (see section 4.5), the bias-field direction was changed from being along $\hat{\mathbf{x}}$ to being along $(\hat{\mathbf{x}}+\hat{\mathbf{y}})$, so that the final values of Bias_{x+y} and Bias_{x-y} were 2.2G and 0, respectively. A final RF ramp was used to cool the atoms in the videotape traps to temperatures down to 6μK before conveying them. The atoms were transported in two videotape traps (see section 4.5), over distances of several millimetres to both sides of their original position, by rotating the bias field direction up to a maximum of 65 turns, at a frequency of 50Hz. The maximum transport distance was $\sim$ 7mm. At the end of the transport sequence an

absorption image of the atoms in-trap was recorded on the CCD camera, using imaging "set-up II", described in section 3.5.3.

The distance from the videotape traps to the chip surface was $\sim 68\mu$m, the radial and axial trap frequencies were ~ 1.5kHz and ~ 13Hz, respectively, and the limiting trap depth was $\sim 150\mu$K ($\sim$2G). At the experimental temperatures of the atoms in these videotape traps, the ratio of thermal energy to limiting potential depth was between 0.04 and 0.4. All these parameters correspond to those used in the calculations presented in section 7.3.1, where the transport mechanism was described.

It is worth mentioning here the fact that all transport studies were abruptly interrupted by the disastrous accidental destruction of the videotape-atom chip (see section 4.7). Even though some results were obtained, as presented in this chapter, it would have been interesting to carry out a more complete study, for instance varying the frequency of bias field rotation, which was kept at 50 Hz for almost every measurement.

Figure 7.11 shows a sequence of absorption images of atoms confined in two videotape traps and transported along x, over 2.67mm to the left, and over 4.44mm to the right of their initial position on the image plane, corresponding to 24 and 40 full rotations of the bias-field direction, respectively.

The frequency of bias-field rotation was 50Hz. The expected transport velocity along the x-direction was ~ 5.5mm/s, corresponding to a displacement of $\sim 110\mu$m every transport cycle.

For this particular example, the temperature of the atoms after the RF evaporation cooling stage in the videotape traps before transport was around 16μK.

The same region of interest is shown on all images and the camera was not moved during the process of data taking. The clouds were transported until they left the field of view on both sides of the image.

We observe noticeable changes in the shape of the trapped clouds, along their axial direction, as they are conveyed. These effects will be discussed in section 7.3.3.

Colder atom clouds with temperatures around 6μK were transported over even larger distances, up to $\sim$ 4mm (36 bias-field-rotation cycles) towards the left-hand side on the image plane, and up to $\sim$ 7mm (65 bias-field-rotation cycles) towards the right-hand side. The transported atoms were imaged along a mixed direction, using imaging "set-up I" (see section 3.5.3), so that transport was not as obvious as it is on the images of figure 7.11, but we could be certain that the atoms had survived transport over the previously mentioned, large distances. The total width of the magnetised videotape layer that formed the chip was equal to 22mm along the transport direction. These large transport distances corresponded to around one half of that total width.

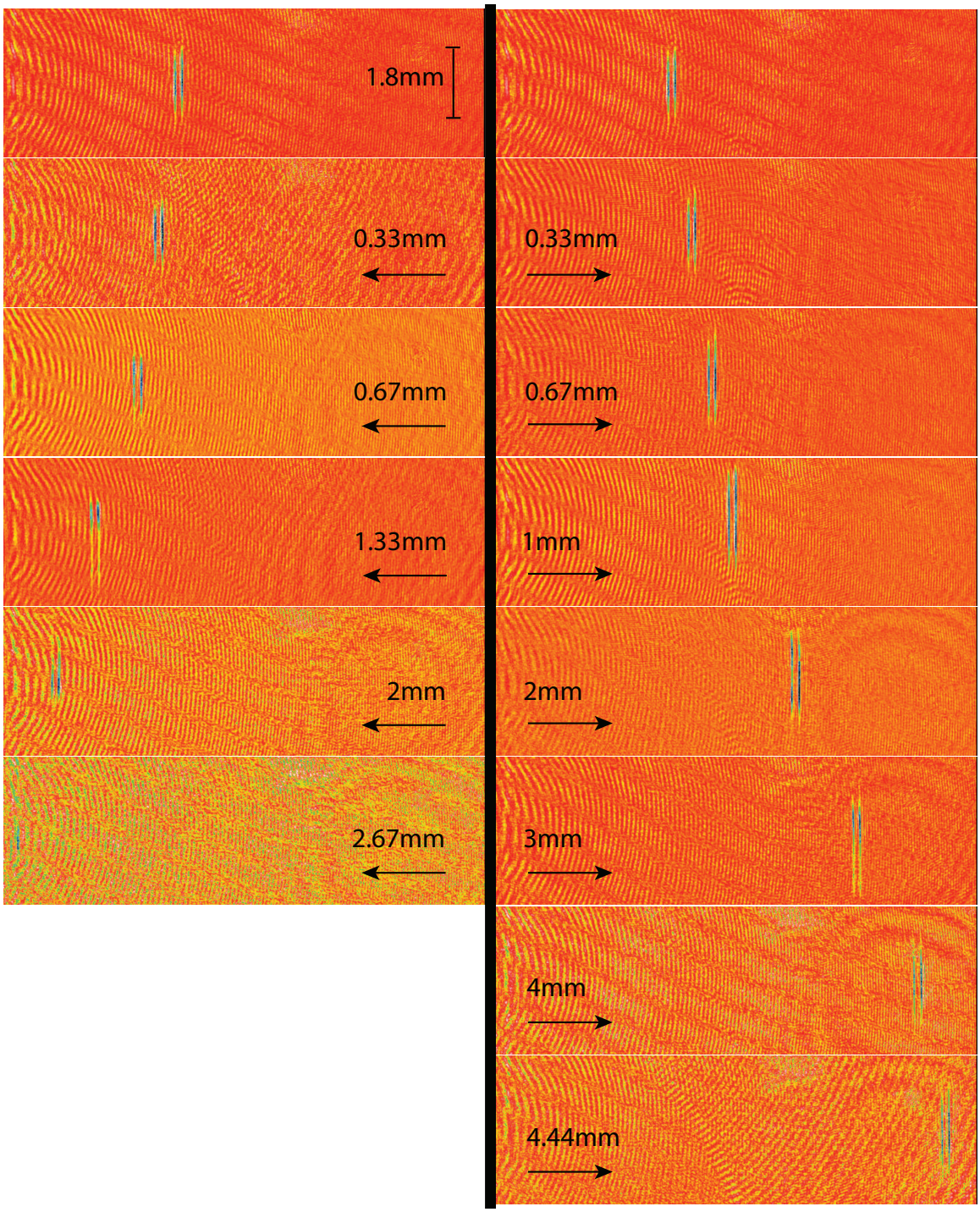

Figure 7.11: Sequences of absorption images of cold atoms (16μK), confined in two videotape traps, and transported along the transverse direction of the traps. **Left**: transport over distances of up to 2.67mm towards the left on the image. **Right**: transport over distances of up to 4.44mm towards the right. The frequency of bias field rotation was 50Hz, and the trap height was $\sim 68\mu$m. The images were acquired using "set-up II" (see section 3.5.3).

Atom loss during transport

The lifetime of the atoms in the videotape traps was obtained by measuring the atom number as a function of time as the atoms were held in the traps, both before they were transported and after one transport cycle. The same lifetime was obtained in both cases, equal to around 30s, for atoms with initial temperatures around 16μK.

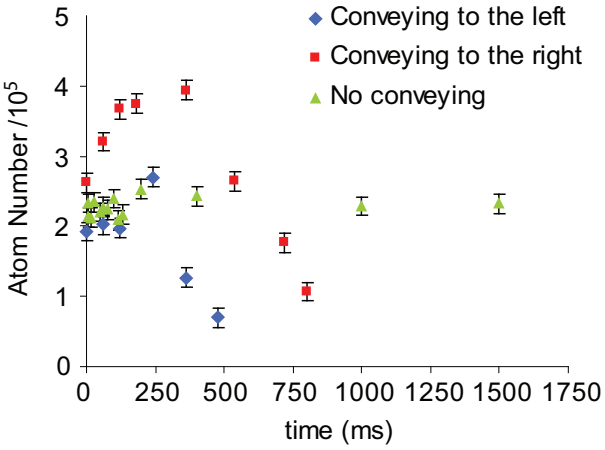

Figure 7.12: Atom number as a function of elapsed time during the transport of cold atoms in videotape traps along the x-direction, away from the chip centre. **Diamonds**: conveying towards the left. **Squares**: conveying towards the right. Each data point corresponds to the measured atom number for each of the images in figure 7.11. **Triangles**: holding the atoms without any transport.

Figure 7.12 shows a plot of the atom number as a function of time, measured from the images in figure 7.11. The evolution of the atom number during the conveying process is compared to the atom number measured by holding the two traps at their initial positions, without any transport. An initial increase in measured atom number is observed when the atoms are transported towards both sides on the image plane. We attribute this to possible changes in the intensity of the light that reached the atoms, which could be due to the intensity profile of the imaging beam ($\sim$22mm of total diameter) as well as to variations of the chip-surface reflectivity. We observe a significant atom loss after conveying the atoms over distances of a few millimetres towards either side. Large or sudden changes in the shape of the confining potential as the atoms are transported are a possible explanation for the observed atom loss. Section 7.3.3 will show how we actually measured large changes in the shape of the trapping potential during transport over several cycles. These changes would be caused by either videotape inhomogeneities or by stray fields, as we will discuss in the same future section.

Transport-induced axial sloshing of the clouds

The conveying process induced an excitation of the atoms in the trapped clouds that resulted in a measurable axial oscillation of the centre of mass of each cloud. The possible causes for this transport-induced axial sloshing were described in section 7.3.1, where we identified the deviations of the trap centre from a straight line along the z-direction, the "bicycle-like" movement of the trapping potential, the periodic transverse compression and de-compression

of the trap ends, the changes in axial confinement and the initial "kick" given to the atoms at the start of the transport process, as possible sources of axial excitations for the atoms during transport.

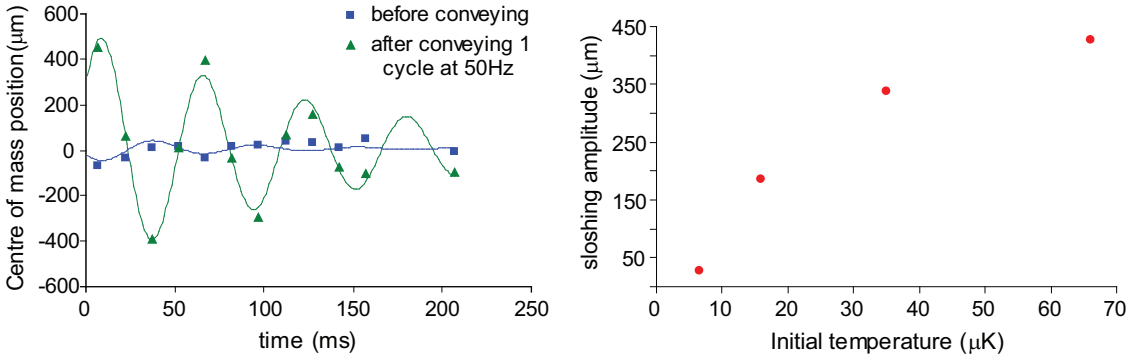

Figure 7.13: **Left**: axial oscillations of the position of the centre of mass of one of the clouds measured before and after one transport cycle. The solid lines are damped sinusoidal functions. The fitted frequency of the larger oscillations was (17.5 ± 0.2)Hz, for an end-wire current of 15A, corresponding to the data shown. The initial temperature of the atoms in the videotape traps before transport was $\sim 66\mu$K. **Right**: amplitude of the transport-induced, axial sloshing measured after one transport cycle, as a function of the initial temperature of the atoms in the videotape traps before transport. The end-wire current in the videotape traps was 10A for all points except for the one at 66μK, for which it was 15A.

The amplitude of the induced axial oscillations of the centre of mass of the clouds after one transport cycle was measured for several different initial temperatures of the atoms in the videotape traps. We can see an example of this in figure 7.13(left), where the amplitudes of the axial sloshing before and after one transport cycle are compared. In this particular example, no RF evaporation was carried out in the videotape traps after loading the atoms, and the initial temperature of the atoms before transport was $\sim 66\mu$K. The bias-field-rotation frequency was 50Hz and the end-wire current was 15A during transport. While there seemed to be a very small oscillation of the centre-of-mass position before transport, due possibly to the videotape-trap loading process, the amplitude of the oscillations increased by about a factor of 10 after one full rotation of the bias-field direction. On the right-hand side of figure 7.13 we see how the measured amplitudes of the axial sloshing induced in the clouds after one transport cycle decreased as we lowered the initial temperatures of the atoms in the traps via RF evaporation before they were transported. This tendency can be explained by the fact that, due to the compression and de-compression of the trap ends during transport (see the previous section about variation of the trapping frequencies during transport), higher-amplitude displacements of the centre of the potential occurred along the longitudinal direction of the trap when the transverse distance to the effective trap axis was larger and, therefore, when the temperature of the cloud was higher. Additionally, higher-amplitude excitations took place at the ends of the trap than at its centre, in such a way that the increased axial extent of a hotter atom cloud enhanced the effect of these excitations. The smaller axial sloshing amplitude measured after one transport cycle for an initial atomic temperature of $\sim 6\mu$K, was comparable to the sloshing amplitude before transport.

Measuring the axial sloshing of the cloud after three transport cycles under the same conditions as for the data shown in figure 7.13(left), we found that the sloshing amplitude was ~ 1.8 times lower than that after one transport cycle, i.e., the sloshing was damped during the transport process. This fact suggests that the initial acceleration given to the atoms at the start of the transport process was partly responsible for the axial sloshing of the cloud. This initial acceleration was probably larger at the edges of the trap, since they moved faster than the trap centre, explaining why larger sloshing amplitudes were measured for longer, hotter clouds.

Measured transport speed and heating rates

In order to measure the speed of the atoms and to study the heating rate during the transport process we recorded in-trap absorption images of the atoms after a number of transport cycles between 0 and 8. The atoms were held in the videotape traps for 2s at their final positions after transport, in order to wait for the axial oscillations of the centre of mass of each cloud to be completely damped before recording the absorption image.

The position of the centre of mass of one of the two clouds along the direction of transport (x) was measured on the recorded images and plotted as a function of time during the transport process, as seen in figure 7.14. The transport speed, obtained from the linear fit shown in the figure, was found to be of (6.20 ± 0.01)mm/s. This value is slightly higher than 5.5mm/s, which is the calculated value for a bias-field-rotation frequency of 50Hz and a videotape-magnetisation period of $\sim 110\mu$m. An imaging set up with a single lens in a "2f-2f" configuration (see section 3.5.3) was used to focus the imaging beam onto the CCD chip of the camera with unit magnification. It is entirely possible that the lens could have been placed slightly closer to the imaged atoms than twice the focal length of the lens. This would have given rise to an imaging magnification factor slightly larger than 1 in the image plane, explaining why the measured transport speed was a factor of ~ 1.1 larger than expected.

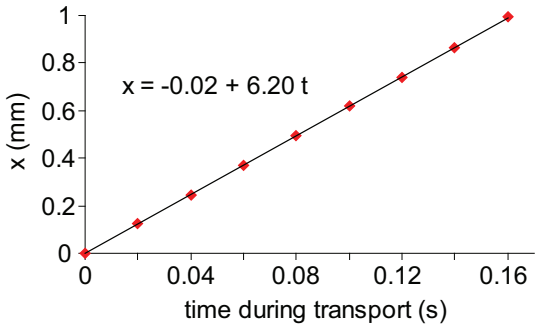

Figure 7.14: Distance travelled by the atomic clouds along the transport direction (x), measured using absorption images recorded after conveying the atoms and waiting for 2s. Each data point corresponds to a different number of transport cycles, from 0 to 8. The error bars are smaller than the marker size.

The heating rate during transport was obtained as follows. The axial rms size, σ_z, of one of the trapped clouds was measured using the same set of recorded images, by fitting a Gaussian to the integrated axial profile of the cloud. The temperature of the cloud during transport was calculated as $T = \frac{m}{k_B}\omega_z^2\sigma_z^2$ (see section 4.4.1), using the measured values of σ_z, and $\omega_z = 2\pi 12.8Hz$, which corresponded to the axial frequency that we had previously measured for the atoms in the initial videotape traps with an end-wire current of 10A. Figure 7.15 shows the heating rates measured during transport for three different initial temperatures of the atoms before transport: $\sim 6\mu$K, $\sim 19\mu$K and $\sim 35\mu$K. Each data point corresponds to transport over a number of bias-field-rotation cycles from 0 to 8. The measured heating rates during transport were between 70 and 117nK/ms or, equivalently, between 13 and 22nK/μm. These rates were obviously larger than the heating rate measured when holding the atoms in the initial videotape traps without any transport, which was equal to (4 ± 10)nK/ms, as shown in the same figure, and therefore consistent with zero.

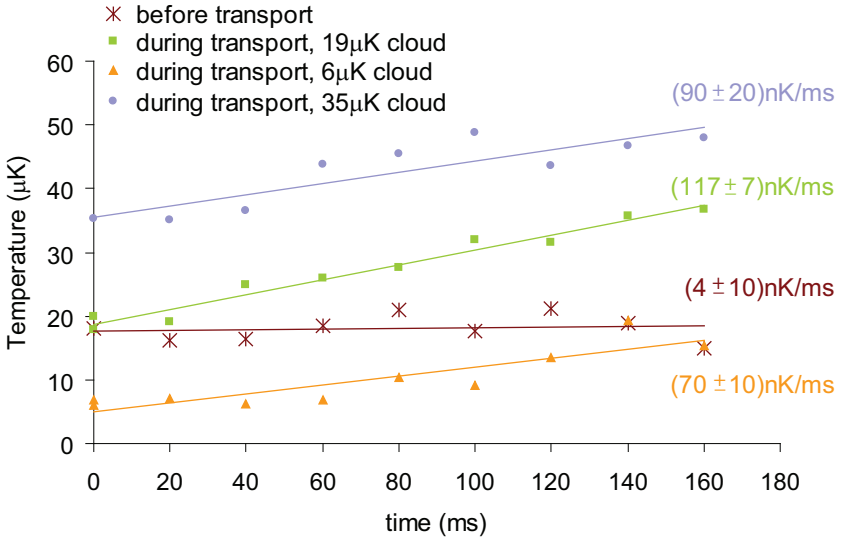

Figure 7.15: Variation of the temperature of the atoms in time, measured during transport for three different initial temperatures of the atoms in the videotape traps (filled circles, squares and triangles), or holding the atoms in the traps without transport (stars). Each data point in a set corresponds to a number of transport cycles between 0 and 8. The solid lines show linear fits to the data, with the slope giving the heating rate, as printed on the right hand side.

We can consider the energy increase per transport cycle caused by the axial oscillations of the centre of mass of the clouds in order to calculate the contribution of axial sloshing to the heating rate. Assuming that every cycle of transport induces an axial displacement of the centre of mass of the clouds equal to z_{slosh}, where z_{slosh} is the sloshing amplitude measured after one transport cycle as presented in figure 7.13, we can calculate the energy increase associated with the axial sloshing of the cloud as $\Delta U = \frac{1}{2}m\omega_z^2 z_{slosh}^2 = \frac{1}{2}k_B\Delta T$. The calculated values of ΔT are between 30nK and 4μK, and the heating rate can be obtained as $\Delta T/\Delta t$, where $\Delta t = 20$ms is the time duration of one transport cycle. The heating rates inferred from the measured amplitudes of axial sloshing are 1nK/ms, 58nK/ms and 192nK/ms, corresponding to initial temperatures before transport of $\sim 6\mu$K, $\sim 16\mu$K and $\sim 35\mu$K, respectively. If we compare these heating rates with the measured ones, shown

in figure 7.15, we find that they are of the same order of magnitude except for an initial temperature of $\sim 6\mu$K, for which the measured heating rate is more than an order of magnitude larger than the one expected from the measured axial sloshing.

The other possible sources of heating apart from the transport-induced axial sloshing of the cloud, were summarised at the end of section 7.3.1. We expect the changes in the shape of the trapping potential (see section 7.3.3), and the non-adiabatic initial push given to the atoms at the start of the transport process to contribute significantly to the heating rate during transport.

It was difficult to measure these small heating rates precisely, since the shot-to-shot variations in the data points were of a similar order to the temperature variations. The relative errors in the measurements of the heating rates range between 6% and 22%. The temperature increase was not measured over longer transport distances and times due to the strong changes observed in the shape of the axial potential when conveying the atoms over more than 8 transport cycles, as we will describe in section 7.3.3.

Therefore, the lowest heating rate for a bias-field-rotation frequency of 50Hz, was measured during the transport of cold thermal atoms with initial temperatures around 6μK, and was equal to $\sim 1.4\mu$K per transport cycle. This heating rate is not small if we consider transporting atom clouds with temperatures of a few μK, or even Bose-Einstein condensates with temperatures of a few hundred nK, over distances of the order of several hundred microns. In the case of a BEC, the measured heating rates would be enough to transform the condensate into a thermal cloud over a single transport cycle. Unfortunately, we were not able to collect data for transport frequencies different from 50Hz, since the videotape atom chip was accidentally destroyed while we were in the middle of carrying out these transport studies. However, it would have been interesting to find out whether it was possible to achieve lower heating rates using different bias-field-rotation frequencies, i.e., faster or slower transport velocities, transporting the atoms at larger distances from the chip surface, or making the beginning of the transport process smoother to avoid the initial "kick" given to the atoms.

7.3.3 Measured changes in the trapping potential in different regions of the chip: fragmentation features after transport

The shape of the atomic clouds during transport was studied as a function of the number of bias-field-rotation cycles. The distance over which the atoms were conveyed each cycle was $\sim 110\mu$m. The inhomogeneities of the axial trapping potential were seen to change, both in shape and magnitude, as the atoms were transported parallel to the videotape chip surface, to different locations away from the chip centre. The videotape atomic conveyor belt allowed us to study the features of the axial disorder potential, U_{dis} (see section 6.3.1 of chapter 6), felt by the atoms when confined in videotape magnetic traps close to different regions of the magnetised videotape.

Several absorption images were recorded, each taken after conveying the atoms for a

number of transport cycles between 0 and 21, following the same experimental procedure described for the images shown in figure 7.11. Two videotape traps were initially loaded and therefore two clouds were simultaneously transported in these experiments.

We observed strong and large-scale inhomogeneities in the axial trapping potential when conveying the atoms over distances larger than ~ 0.88mm from their initial loading position, along x. We measured how, over a total transport distance of ~ 1.5mm, each atom cloud divided axially into two clouds which then merged back into one cloud, as evidenced by the sequence of absorption images shown in figure 7.16. Each absorption image corresponds to a different experimental realisation in which atoms were conveyed over a number of transport cycles, from 7 to 21, from left to right, corresponding to distances of ~ 0.77mm to ~ 2.31mm from the initial position of the atoms at the centre of the chip before transport.

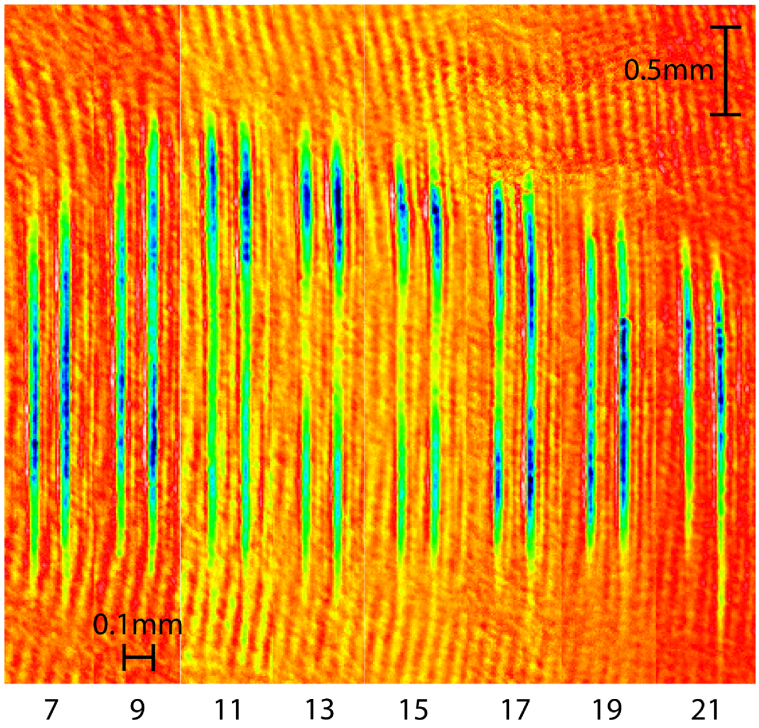

Figure 7.16: Absorption images of two clouds of atoms confined in videotape traps and transported to different positions along the horizontal direction on the image, following the same experimental sequence as for the images in figure 7.11. From left to right, the clouds were conveyed over 7 to 21 transport cycles, as indicated by the numbers below the images, corresponding to distances between ~ 0.77mm and ~ 2.31mm, respectively. The atom-surface separation was $\sim 68\mu$m.

The fluctuations in the axial trapping potential were analysed in more detail as follows. The integrated axial density profiles of the right-hand-side cloud, for four of these images, corresponding to 7, 11, 15 and 19 transport cycles, are plotted in figure 7.17(left). The temperature of the cloud after 7 transport cycles was of the order of 30μK. The cloud split along its axis into two clouds separated by a distance as large as ~ 1.75mm after 15 transport cycles, as seen on the profiles. The approximate axial disorder potentials were calculated following the same analysis that we used in chapter 6 to study fragmentation effects in the videotape traps without any transport. Note that the atoms were not at equilibrium at the

time of measurement, since no time was allowed for the transport-induced sloshing of the cloud to be damped before recording the absorption image of the atoms when acquiring this particular set of data. The disorder potentials that we obtained, shown in figure 7.17(right), have amplitudes of up to 50-60μK at the locations in which the cloud splitting was most obvious. These amplitudes are much larger than those observed at the initial position of the atoms (0 transport cycles), measured to be of the order of a few microKelvin in chapter 6.

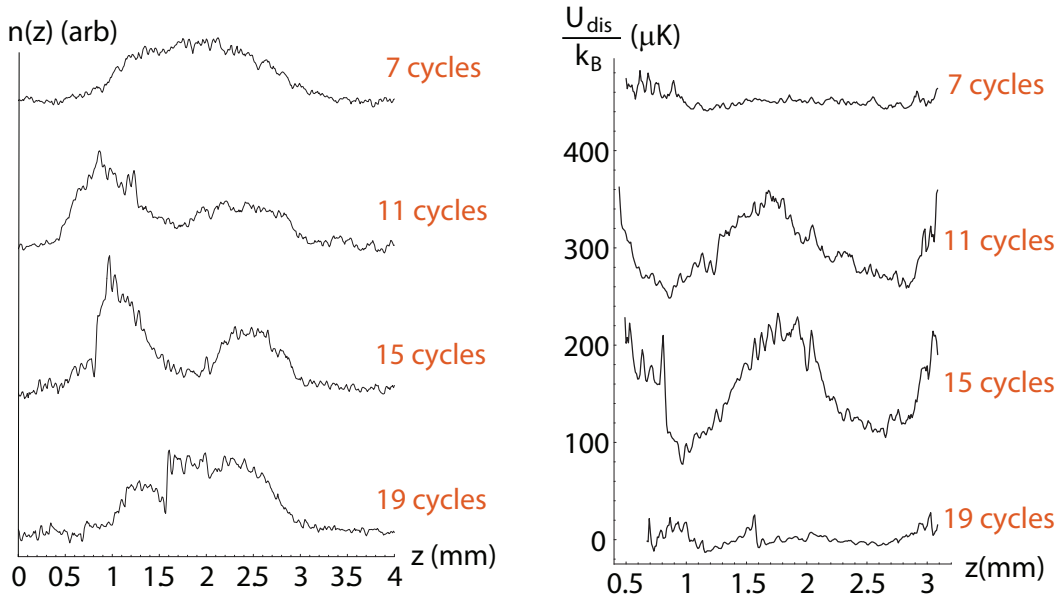

Figure 7.17: Integrated axial density profiles (left) and axial disorder potentials (right) of a cloud of atoms transported over 7, 11, 15 and 19 transport cycles, from top to bottom, corresponding to transport distances of $\sim$ 0.77mm, $\sim$ 1.21mm, $\sim$ 1.65mm and $\sim$ 2.09mm. Each fragmentation potential has been vertically offsetted by 150μK from the previous one, for clarity.

Figure 7.18 shows a sequence of four absorption images recorded after the atoms were first conveyed over 18 transport cycles, i.e., over a distance of $\sim$ 2mm, and then cooled in the videotape traps trough an RF evaporation sweep from $f_{start} = 1.36$MHz to $f_{\infty} = 0.96$MHz (see section 4.4.2), with a time constant of 0.5s and a duration equal to 0, 0.2s, 0.7s and 2s, respectively from left to right. Evaporating at the final position of the two clouds after transport made the fragments of the axial trapping potential more obvious, as shown on the figure. From left to right, the temperature of the atoms was reduced approximately by a factor of 10.

There are two possible causes for the observed axial splitting of the clouds as they pass through that particular region of the videotape. One of them would be the presence of a stray magnetic field (see section 4.6.2) along the axis of the trap. The total axial field, created by both the end wires and the B_z coils, at the bottom of the initial trap before transport, was measured to be of the order of 1.4G. A stray axial magnetic field opposite and larger in magnitude than the field at the bottom of the trap would cause the axial potential to split in two parts along its axis. Such a stray field could be created by the pieces of

wire that connected the two end wires in series inside the chamber, or even by the machined steel plate that formed the base where the videotape was mounted (see section 2.2). The other possible cause would be the presence of large inhomogeneities in the surface of the videotape atom chip, which would lead to strong, long-wavelength fluctuations of the axial trapping potential close to certain regions of the videotape. Such inhomogeneities could be geometric defects of the videotape piece or height variations, i.e., failure of the videotape to lie flat on the chip, possibly caused by air bubbles or thickness variations in the layer of glue located under the videotape.

Two atomic clouds were conveyed over the same distance ($\sim$ 2mm, 18 transport cycles) as in figure 7.18, and then the end wires and B_z field were switched off to release and let the clouds expand axially during times of flight of up to 14ms. The two large axial fragments were seen to move away from each other and expand when the temperature of the cloud was large enough, while, for low enough temperatures, the colder fragments stayed localised. This observations indicate that the observed axial splitting of the clouds could not be due to the combination of a stray axial field with the axial confining potential, and that it was therefore most probably due to videotape defects and inhomogeneities.

Even though further studies of the observed cloud splitting were not carried out, we can say that it would offer the interesting possibility of implementing the controlled splitting and recombination of two clouds of atoms for atom-interferometry studies. Such studies would require control over the inhomogeneities of the trapping potential, and there remains the question of whether the splitting and recombination using videotape potentials would be smooth enough for being used with Bose-Einstein condensates as matter waves.

Finally, other unusual features of the trapping potential were observed when first conveying atoms over 14 to 16 transport cycles and then moving them away from the chip surface in 50ms, from an atom-surface separation of $\sim 68\mu$m to $\sim 90\mu$m. Features resembling the shape of a so-called edge dislocation in solid-state physics were observed, as shown in figure 7.19. The nature of this localised change in the phase of the videotape trapping potential along the x direction was not investigated, but it could be due to stray fields present on that region of the videotape and at that distance from the chip surface. The effect of small, local stray fields directed along the x or y directions would become increasingly more important for decreasing bias fields, and therefore might only be noticed in videotape traps far enough from the chip surface.

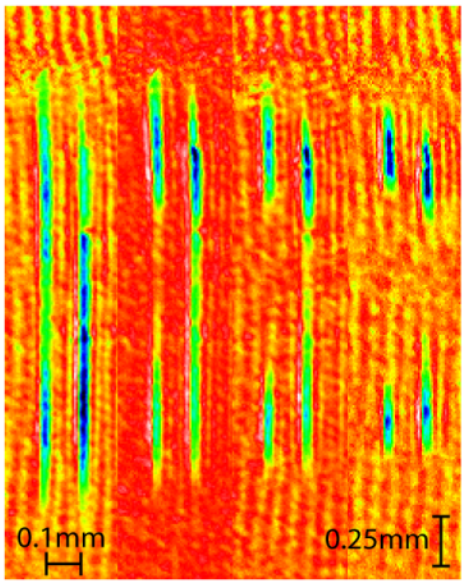

Figure 7.18: Sequence of four absorption images of two clouds of atoms confined in videotape traps, after they were transported over $\sim$ 2mm (18 cycles) and then evaporated to different final temperatures. The temperature was reduced by a factor of $\sim$ 10 from left to right.

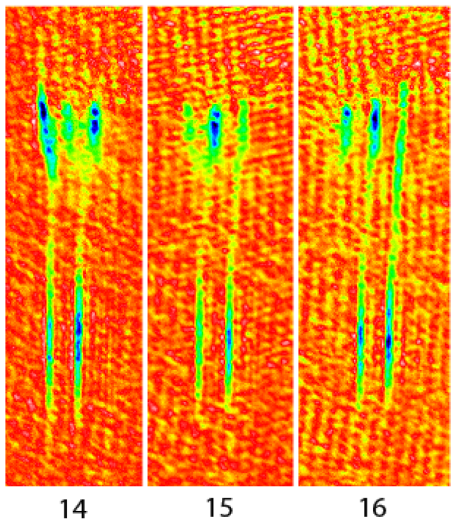

Figure 7.19: Unusual features of the videotape trapping potential as the atoms were conveyed over 14, 15 and 16 transport cycles, from left to right, and then moved from a distance of $\sim 68\mu$m from the chip surface to a distance of $\sim 90\mu$m, in 50ms.

7.4 Conclusions

We have demonstrated experimentally how it is possible to transport cold atoms with temperatures between a few micro-Kelvin and a few hundred micro-Kelvin in arrays of videotape-magnetic traps using a transport mechanism that was easily implemented on our atom chip.

Cold atoms were transported over distances as large as 7mm while they remained trapped in three dimensions, with the lowest heating rates measured to be $\sim$ 70nK/ms for a bias-field-rotation frequency of 50Hz. No appreciable atom loss was measured when conveying the atoms over distances of a few millimetres.

This transport mechanism enabled controlled positioning of ultra-cold atoms close to different regions of the magnetised videotape, opening the possibility of surveying the chip surface with the aim of studying fragmentation features in different areas of the chip.

Chapter 8

Outlook and conclusion

8.1 Conclusions

This thesis has presented the experimental research carried out with ultracold rubidium atoms confined in microscopic magnetic traps created by an atom chip based on periodically magnetised videotape.

The descriptions of the videotape atom chip and of the apparatus with which the experiments were realised, have been given in chapters 2 and 3, followed by a detailed explanation, in chapter 4, of all the steps in the experimental sequence that led to the confinement of ultracold atoms in videotape magnetic micro-traps.

Experimental and simulated results of the resonant excitation of the transverse motion of cold thermal atoms in videotape traps were presented and compared in chapter 5. We showed how certain characteristics of the videotape traps, such as their anharmonicity, shifted the temperature resonance towards frequencies below the calculated harmonic frequency of the trap (valid only for small oscillations close to the trap centre), as well as causing an increased frequency width of the measured resonances. These results led to the determination of the transverse oscillation frequencies of the atoms in the videotape traps, at a certain temperature. A complete model which includes anharmonicity effects and interatomic collisions, and which closely reproduces our experimental measurements was also presented.

Measurements of fragmentation effects in clouds of ultracold atoms with temperatures of a few microKelvin, confined in a videotape magnetic trap at different distances, between 30μm and 80μm, from the chip surface, were presented in chapter 6 and used to determine the irregularities of the magnetic field generated by the magnetised videotape. Height and thickness variations, and defects in the surface of the videotape magnetic layer were established as possible causes for the observed potential roughness.

The potential roughness felt by atomic clouds trapped in close proximity to the chip surface effectively set an upper limit to the transverse trap frequencies achievable in our experiment, preventing us from reaching tight enough transverse confinement to explore the

one-dimensional gas regime. An effective method for reducing fragmentation in our videotape traps, based on the idea of the TOP trap, was proposed at the end of chapter 6. It was not realised experimentally due to the accident that destroyed the videotape atom chip.

A novel mechanism for transporting cold atoms in arrays of videotape magnetic traps was experimentally demonstrated and used to transport rubidium atoms with temperatures of the order of 10^{-6}–10^{-4} Kelvin over distances as large as $\sim$ 1cm, parallel to the surface of the chip and along the transverse direction of the traps.

This transport mechanism enabled us to survey the chip surface and to study potential roughness effects at different locations of the chip.

Our effective transport mechanism constitutes an essential tool for the controlled positioning of ultracold atoms confined in magnetic traps, expanding the capabilities of our videotape atom chip. The confinement and controlled transport of atoms in arrays of microtraps on a chip is certainly a step forward towards the realisation of an atomic quantum register for quantum information processing.

8.2 Outlook

The videotape atom chip would be a suitable tool for the study of one-dimensional quantum gases in the near future, since very elongated, high-aspect-ratio traps can be generated by this chip to confine ultracold atoms. Implementing the technique proposed at the end of chapter 6 to reduce fragmentation in cold atom clouds trapped close to the chip surface, would allow us to reach tight-enough transverse trap frequencies to explore the one-dimensional (1D) gas regime. In this regime the energy of the system is much smaller than the energy quantum of transverse excitation, and the transverse motion of the atoms is frozen out. The following condition needs to be fulfilled in order to reach the 1D regime:

$$\mu, k_B T \ll \hbar\omega_r \tag{8.1}$$

where μ is the chemical potential, T is the temperature of the atoms in the trap, $\omega_r = 2\pi f_r$ is the transverse trap frequency, k_B is Boltzmann's constant and $\hbar = h/(2\pi)$, where h is Planck's constant.

Figure 8.1 shows the phase diagrams of a one-dimensional quantum gas of ^{87}Rb atoms confined in a trap. The atom number is plotted as a function of the temperature of the atoms for three different values of the transverse frequency of the atoms in the trap. These plots were produced following the ideas in references [27–29], in which D. S. Petrov et al. reported a full theoretical study of the different regimes of a 1D trapped Bose gas. Atom numbers or temperatures outside the range shown on each plot correspond to the three-dimensional regime ($\mu, k_B T > \hbar\omega_r$), while those shown in the plots correspond to $\mu, k_B T \leq \hbar\omega_r$. Three 1D quantum degenerate regimes can be found below the degeneracy temperature: a quasi-condensate, a pure condensate and the Tonks-Girardeau gas. We can see how increasing the transverse trap frequency makes these regimes more accessible experimentally.

It is possible to choose an optimum period of recorded videotape magnetisation in order to maximise the transverse trap frequencies in the videotape traps at a given distance from

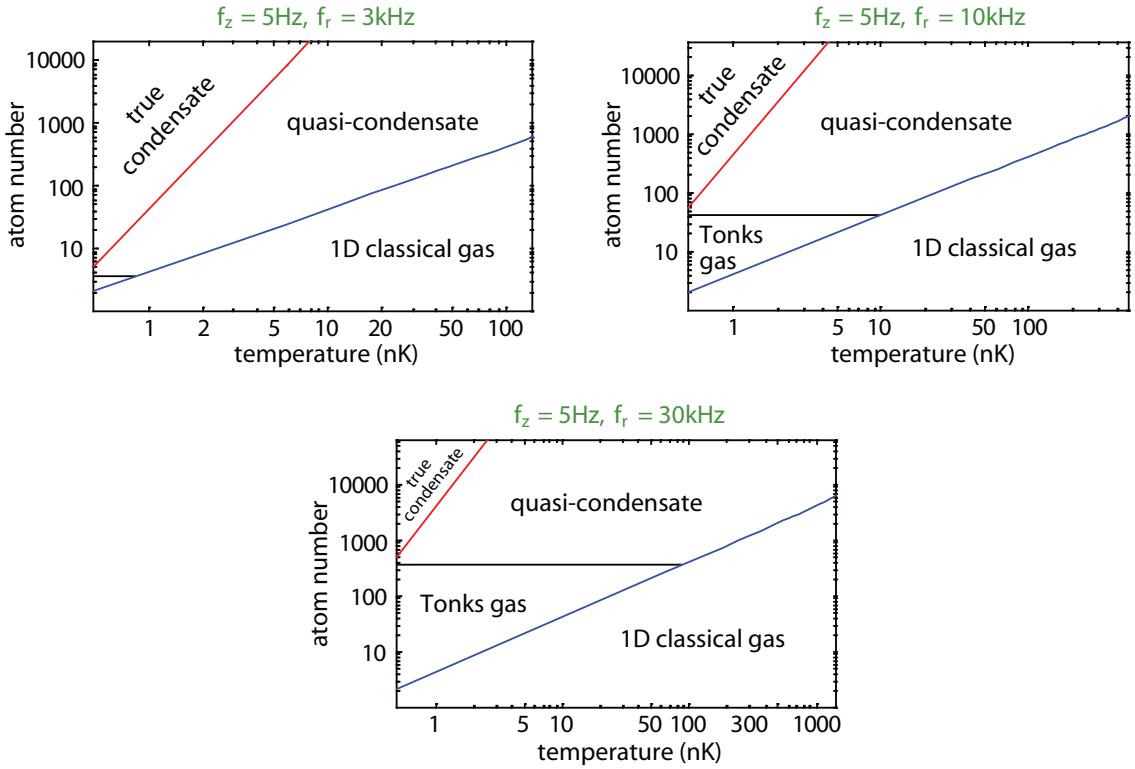

Figure 8.1: Phase diagrams of the different quantum regimes in a trapped, one-dimensional quantum gas of ^{87}Rb atoms. Number of trapped atoms versus temperature for different transverse trap frequencies, as indicated by the labels on top of each plot. These plots were produced following the ideas in references [27–29]. The gas behaves classically to the right of the degeneracy line (blue line). Three quantum regimes can be found below the degeneracy temperature: a quasi-condensate, a pure condensate and the Tonks-Girardeau gas.

the chip surface, as described in appendix D. This appendix shows how, for instance, it is possible to achieve transverse trap frequencies of the order of 30kHz in the videotape traps at a distance of 20μm from the chip surface, using a period of recorded magnetisation of $\sim$ 70μm. With this period of magnetisation and implementing the method based on the idea of the TOP trap to reduce fragmentation, the one-dimensional quasi-condensate regime could be studied with temperatures of a few hundred nanoKelvin and atom numbers of the order of 10^4, and possibly the Tonks-Girardeau gas regime for lower temperatures and lower atom numbers, as shown in the lower graph of figure 8.1.

These studies would require an imaging set up capable of detecting low atom numbers. In fact, a common goal of many current atom-chip experiments is the integration of on-chip microscopic optical components for the detection of low atom numbers. Several proposals have explored the possibility of single-atom or low-atom-number detection on atom chips [207–212], and a few experiments have shown results using optical fibres and macroscopic or micro-fabricated Fabry-Perot resonators mounted on an atom chip [212–219] for the detection of atoms confined in a MOT or in a magnetic trap. Efforts have also been made to integrate detectors based on photoionisation of the trapped neutral atoms followed by ion detection on atom chips [220–222].

A test atom chip with two tapered optical fibres glued on its surface was built to succeed the videotape atom chip that was destroyed. These tapered fibres were 250μm in diameter and were able to focus light to a mode-waist radius of 2μm at a distance of 15μm from their tips. Figure 8.2 shows a photograph of the chip with the fibres inside the vacuum chamber.

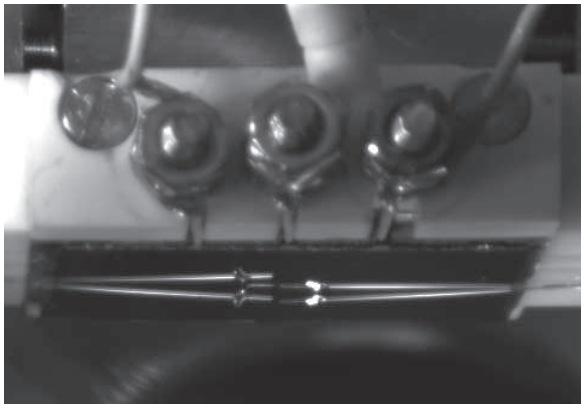

Figure 8.2: Photograph of a test atom chip with two tapered optical fibers on its surface. The reflection of the fibres on the gold-coated glass slide that forms the chip surface can be seen in the photograph.

Preliminary results were obtained with this chip by detecting the fluorescence of atoms in a magneto-optical trap located at a distance of $\sim 200\mu$m from the chip surface. A newly designed atom chip is currently being constructed and tested in our group. This new chip includes microscopic silica-glass waveguides on its surface for the on-chip detection and manipulation of magnetically-trapped atoms.

The combination of integrated, on-chip atom detection with an effective atomic transport mechanism and with the possibility of storing and manipulating a quantum atomic system in a well-defined quantum state, in an array of magnetic traps with a high degree of control, could lead one day to the experimental realisation of a reliable system for quantum information processing with neutral atoms.

Appendix A

Analysis of the videotape magnetisation using polarisation microscopy

It is possible to visualise the spatial pattern of magnetisation recorded onto a piece of videotape by using a garnet sensor and a polarisation microscope. Professor Horst Dötsch, from Osnabrück University in Germany, kindly provided us a garnet sensor that allowed us to make these measurements. The working principle of this magneto-optical sensor is the Faraday rotation of the polarisation of light travelling through the magnetic garnet film.

The sensor consisted of a transparent substrate of GGG (Gadolinium Gallium Garnet) with a thickness of 0.5mm and a diameter of 30mm. A thin magnetic garnet film of thickness 7.5μm and composition $(PrYBi)_3(FeGa)_5O_{12}$, had been grown by liquid phase epitaxy on both sides of the substrate. The garnet film on one side of the substrate had been removed mechanically or chemically. The film on the other side had been covered with a $\sim$1μm thick mirror by coating it with evaporated silver. This mirror was thin enough to allow the garnet film to be close enough to the videotape for our measurements. The garnet film plane was the easy plane of magnetisation, while the hard axis of magnetisation was perpendicular to the film plane. A magnetic field of 36mT was needed to saturate the film perpendicular to its plane. This meant that the magnetic field of the videotape could not saturate the sensor, since its maximum value was of $\sim$11mT at the surface of the videotape. The garnet sensor had a high spatial resolution in the range of a few micrometres.

The sensor was placed flat on top of the videotape with the silver mirror facing down, in contact with the videotape. Linearly polarised white light was sent perpendicular to the sensor plane with a polarisation microscope. The magnetic field of the videotape induced some circular magnetic birefringence and dichroism in the thin garnet film so that light reflected off the sensor came out elliptically polarised and at an angle to the incident linear polarisation. The reflected light was observed in the microscope after going through an analyser set at the right polarisation axis to produce the best possible contrast in order to reveal the spatial magnetisation pattern recorded in the videotape. The microscope focus was set to the lower surface of the sensor, close to the videotape surface. Both Faraday rotation and ellipticity effects depended on the local magnetic field generated by the videotape, and

therefore on the orientation of the videotape magnetisation, so that different magnetisation directions resulted in different grey scale fringes in the microscope image.

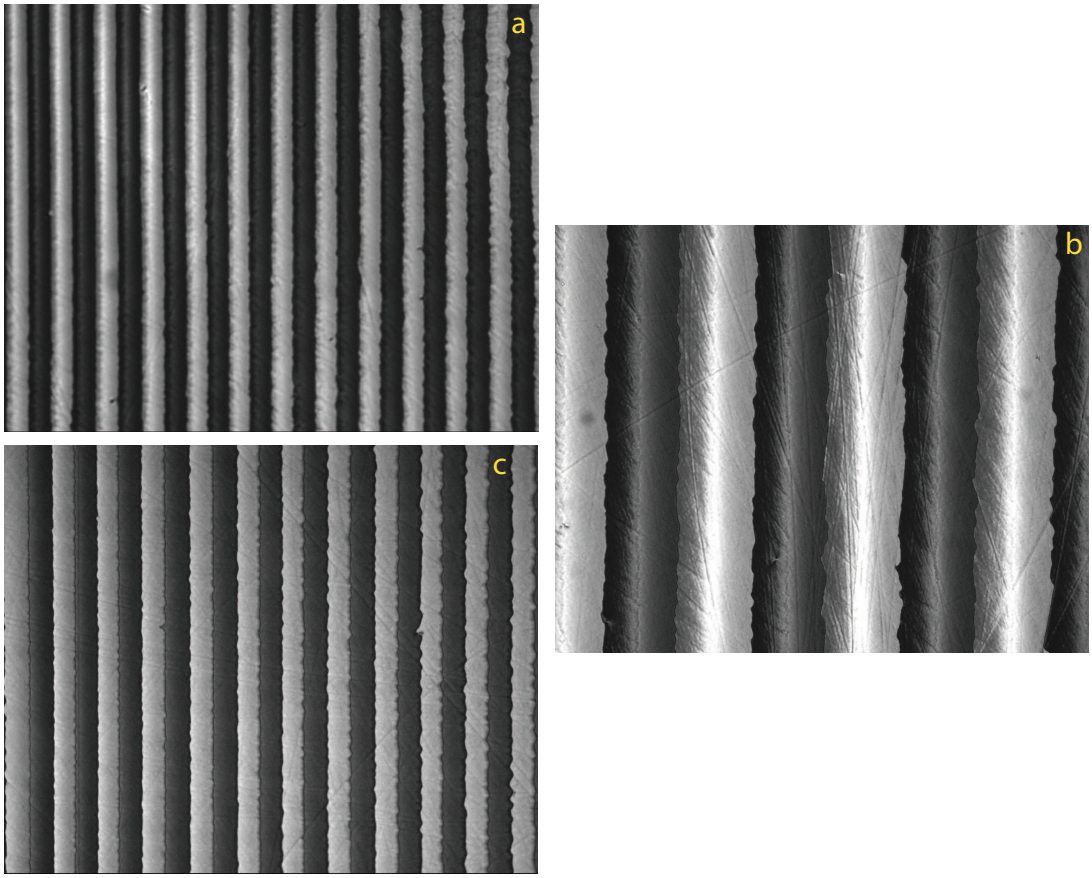

Figure A-1: Images of the videotape magnetisation pattern taken with a polarisation microscope and a magneto-optical garnet sensor. **a** and **b**: recorded samples with measured periods of magnetisation of $102.1 \pm 0.4\mu$m and $361 \pm 2\mu$m, respectively. **c**: piece from the actual videotape atom chip used in the experiments described in this thesis. The measured spatial period of magnetisation was $106.5 \pm 0.4\mu$m.

Figure A-1 shows images of the recorded magnetisation patterns of three different pieces of videotape. Images **a** and **b** correspond to pieces of videotape that we found stored in the laboratory and that had been recorded around the years 2000-2001. The spatial periods of magnetisation were $102.1 \pm 0.4\mu$m and $361 \pm 2\mu$m, respectively. Image **c** corresponds to a piece of the videotape atom chip that was inside the vacuum chamber and that was actually used to carry out the experiments described in this thesis. The spatial period of magnetisation of this piece was measured to be of $106.5 \pm 0.4\mu$m. The periods were determined by counting as many periods of magnetisation as possible in the images and using the microscope image of a 10μm-period square grid as a reference to provide a real length scale.

The image depended critically on the distance between the videotape and the sensor so that it was important to lay the videotape flat enough to obtain good images. Small variations of this distance were seen to cause changes in the contrast and saturation of the images. The noise on the edges of the lines possibly came from inhomogeneities in the garnet

sensor, since displacing the sensor along a fixed spot of the videotape changed the shape of this noise. The scratches observed in the image were seen to come from scratches in the garnet sensor surface itself.

The analysis of images corresponding to the piece of videotape that was once part of the actual videotape atom chip used in our experiments is presented in the following paragraphs. A measured light-intensity profile was obtained from the grey-scale image shown in figure A-1(**c**) by averaging over several rows of the image and normalising to the maximum value, and is presented in figure A-2(left, blue line).

It is possible to compare the measured light-intensity profile with the expected profile, which can be calculated by taking into account the effect of the field generated by the videotape on the garnet-film sensor and how this affects the polarisation of light during the acquisition of the images. These effects are given by equations (see reference [223]):

$$I_{out} = I_{in}\exp(-2\bar{\alpha}d)[\cosh^2(2\phi_{max}d\cos\vartheta)\cos^2(\beta - 2\Theta_{max}d\cos\vartheta) + \\ + \sinh^2(2\phi_{max}d\cos\vartheta)\sin^2(\beta - 2\Theta_{max}d\cos\vartheta)]\,, \tag{A.1}$$

$$\cos\vartheta = \frac{B_\perp}{B_A} - \frac{B_\parallel}{B_A}\cot\vartheta\,, \tag{A.2}$$

where I_{in} and I_{out} are the intensities of the input and output light beams, $\bar{\alpha}$ is the intrinsic absorption coefficient, d is the garnet film thickness, β is the angle between the polariser and analyser, ϕ_{max} and Θ_{max} are the maximum specific Faraday dichroism and maximum specific Faraday rotation, respectively, ϑ is the angle between the normal to the sensor surface and the garnet-film-sensor magnetisation, $B_\parallel$ and $B_\perp$ are the in-plane and out-of-plane components of the applied magnetic field, and B_A is the characteristic induction of uniaxial magnetic anisotropy of the garnet film, related to its saturation magnetisation and uniaxial anisotropy constant (see reference [223]).

The magnetic field applied to the garnet film was that created by the videotape which, assuming no videotape-to-sensor distance variations, was constant in modulus and changed direction when moving across the image fringes, as described in section 2.3.5. We can write $B_\parallel = B_1\cos(\frac{2\pi}{\lambda}x + \varphi)$ and $B_\perp = B_1\sin(\frac{2\pi}{\lambda}x + \varphi)$, where $B_1 \simeq 110\text{G} = 11\text{mT}$, $\lambda \simeq 110\mu\text{m}$ is the period of recorded magnetisation and φ is an adjustable phase. We can neglect the absorption of light by the sensor and assume that $\bar{\alpha} = 0$. We know that the garnet-film thickness was $d = 7.5\mu\text{m}$, the maximum Faraday rotation was $\Theta_{max} \simeq 11800\text{degrees/cm} = 20595\text{m}^{-1}$ (specific to our garnet film), and we can make the approximation that $\phi_{max} \simeq 0.6 \times \Theta_{max}$ (see reference [223]). Therefore we can treat B_1, λ, d, Θ_{max} and ϕ_{max} as known parameters and vary the rest of the parameters, B_A, φ, I_{in} and β, in order to obtain the calculated image profile, I_{out}, that best resembles the measured one.

Figure A-2 (left) shows the measured image profile together with the calculated one for parameters $B_1 = 11\text{mT}$, $\lambda = 110\mu\text{m}$, $d = 7.5 \times 10^{-6}\text{m}$, $\Theta_{max} = 20595\text{m}^{-1}$, $\phi_{max} = 12357\text{m}^{-1}$, $B_A = 22\text{mT}$, $\varphi = -0.4$, $I_{in} = 1.8$ (arbitrary units) and $\beta = \frac{2.86\pi}{4}$. The calculated profile reproduces well most of the features of the observed image profile. Figure A-2 (right) shows a comparison of the Fourier transforms of the measured and calculated image profiles. The positions and amplitudes of the first peaks are very similar in both profiles, with the

high-frequency components being lost from the measured image profile. Note that, despite choosing the videotape-magnetic-field components to be a pure sine and cosine, and since the imaging process is non-linear, the Fourier transform of the calculated image profile has not one single frequency component but several, and the same occurs for the measured image profile.

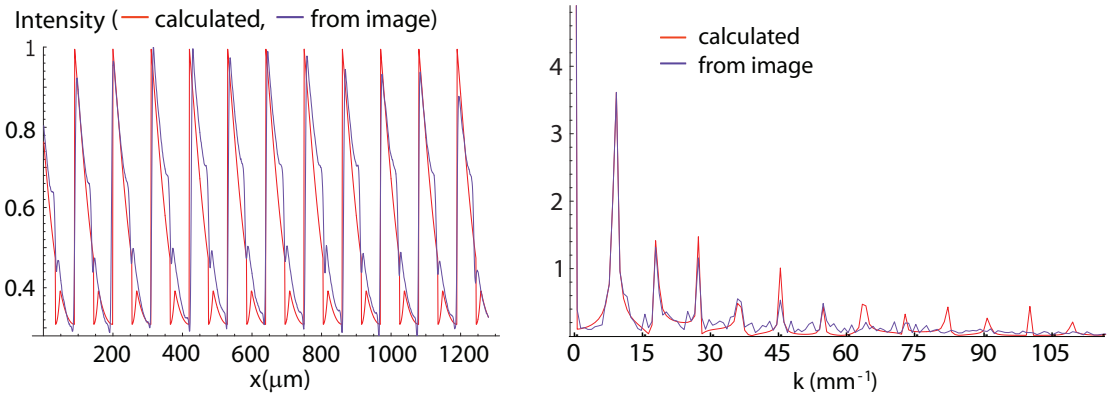

Figure A-2: **Left**: intensity profiles of a videotape magneto-optical image: measured from the actual microscope image (blue), and calculated (red) for a videotape field with pure sine and cosine components, and parameters $B_1 = 11\text{mT}$, $\lambda = 110\mu\text{m}$, $d = 7.5 \times 10^{-6}\text{m}$, $\Theta_{max} = 20595\text{m}^{-1}$, $\phi_{max} = 12357\text{m}^{-1}$, $B_A = 22\text{mT}$, $\varphi = -0.4$, $I_{in} = 1.8$ (arbitrary units) and $\beta = \frac{2.86\pi}{4}$. **Right**: modulus of the amplitude of the Fourier transforms of the measured (blue) and calculated (red) image profiles.

We can consider additional, higher-frequency components of the videotape magnetic field in the calculation, in order to try to reproduce the observed image profile with more accuracy. Figure A-3 shows an example of the calculated profile for two frequency components: $\lambda_1 = 110\mu\text{m}$ and $\lambda_3 = 110/3\mu\text{m}$, with phases $\varphi_1 = -0.4$ and $\varphi_3 = 1.6$, and relative amplitudes 1 and 0.29, respectively. The rest of the parameters are the same as before, except for $I_{in} = 1.9$ (arbitrary units). A third harmonic is chosen because possible saturation effects during the process used to record the videotape magnetisation could generate such harmonics. The image shows the measured profile together with the calculated one. Most features of the real profile are reproduced very closely by the calculated one.

We have shown how the measured image profile is reasonably similar to the expected one, which was obtained starting from the known videotape magnetic field components and calculating the intensity of the output light. The match between calculation and measurement is not exact. The facts that the absorption of light by the sensor has been neglected and that the value $\Theta_{max} = 20595\text{m}^{-1}$, used in the calculations, is valid for 610nm-wavelength light, rather than for white light, as used for our measurements, also contribute to the overall error.

Inverting the process, it is possible to obtain the videotape field components, $B_{\parallel}$ and $B_{\perp}$ from the measured image profile. Using the values: $I_{in} = 1.8$ (arbitrary units), $d = 7.5 \times 10^{-6}\text{m}$, $\beta = \frac{2.83\pi}{4}$, $\phi_{max} = 12357\text{m}^{-1}$ and $\Theta_{max} = 20595\text{m}^{-1}$ as parameters in equation A.1, with I_{out} given by the intensity profile of the measured microscope image, we can first

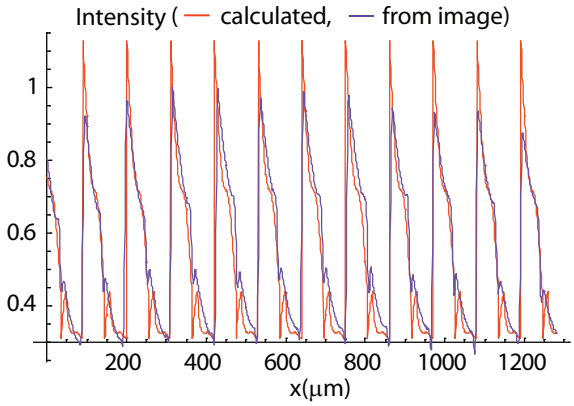

Figure A-3: Measured (blue) and calculated (red) intensity profiles of an image of videotape magnetisation. The calculated one assumes two frequency components for the videotape field, with periods $\lambda_1 = 110\mu$m and $\lambda_3 = 110/3\mu$m, phases $\varphi_1 = -0.4$ and $\varphi_3 = 1.6$, and relative amplitudes 1 and 0.29, respectively. Other parameters are $B_A = 22$mT, $I_{in} = 1.9$ (arbitrary units), $\beta = \frac{2.86\pi}{4}$, $\phi_{max} = 12357\text{m}^{-1}$, $\Theta_{max} = 20595\text{m}^{-1}$ and $d = 7.5 \times 10^{-6}$m.

solve for $\cos\vartheta$ in equation A.1. Then taking into account that:

$$B_\perp^2 + B_\parallel^2 = B_1^2\,, \tag{A.3}$$

where B_1 has the known value of 11mT, and using the previously obtained value of $B_A = 22$mT, we can solve equations A.2 and A.3 in order to obtain $B_\perp$ and $B_\parallel$. Initial guesses of $B_\perp/B_A$ and $B_\parallel/B_A$ were required in order to find a solution. The solution depended on these initial guesses, and on the chosen parameters.

A plot of the Fourier transforms of the obtained field components can be seen in figure A-4, where two solutions for different initial guesses have been plotted together for each field component. The position of the largest peak in these graphs provides the main frequency component of the field, and therefore, the period of recorded videotape magnetisation, which is measured to be $107 \pm 5\mu$m. The image resolution is what limits the precision of this measurement, which agrees with the more accurate measurement presented before, obtained by using the microscope image of a fine square grid to calibrate the length scale of the magnetisation-pattern image.

Higher-frequency components can also be observed in these plots. The amplitude of the second and third harmonics is at most 30% of that of the main frequency component. The frequencies of these harmonics are consistent with twice and three times that of the main peak, respectively. This implies that the videotape field components are not a pure sine and cosine but have some additional higher harmonics, although the amplitude of these would be considerably smaller than that of the main frequency component. The amplitude of the n^{th} order harmonic with wave-vector nk decays with the distance to the videotape surface, y, as $\exp(-nky)$ (see section 2.3.5), so that higher-order harmonics decay faster than the fundamental frequency component. For this reason, at the typical atom-surface separations of $30-100\mu$m, only the main frequency components of the videotape field are relevant. At a distance of $\sim 30\mu$m from the videotape surface the amplitude of the second harmonic would be around 5% that of the first harmonic, and at a distance of $\sim 100\mu$m, the amplitude of

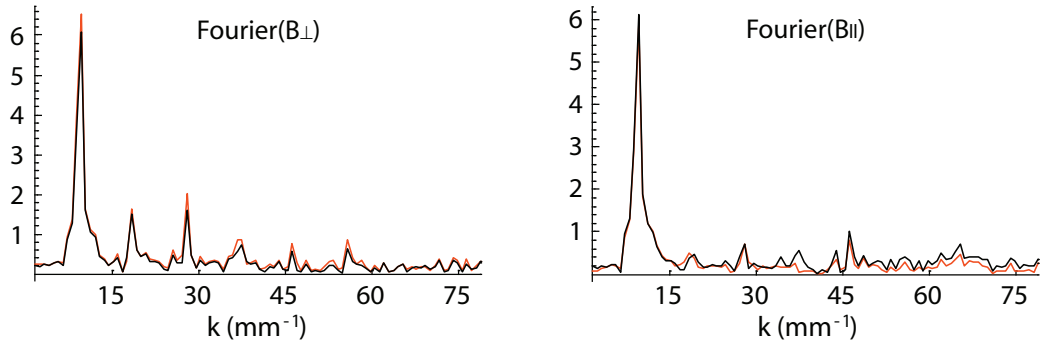

Figure A-4: Modulus of the amplitude of the Fourier transform of the videotape field components ($B_\perp$ on the left, and $B_\parallel$ on the right) obtained from the measured intensity profile of the videotape magnetisation image. Black and red lines correspond to solving for $B_\perp$ or $B_\parallel$ for different initial guesses.

the second harmonic would be approximately 0.1% that of the first harmonic.

It follows from the analysis in this section that, we can consider the videotape magnetic-field components to be close enough to pure sine and cosine functions, as is assumed throughout this thesis, where the effect of higher harmonics in the expression of the videotape magnetisation has always been neglected, and the videotape magnetic field has always been considered to be that of equation 2.25.

Appendix B

Working with Ultra High Vacuum

This appendix is a summary of the procedure followed to recover ultra-high vacuum (UHV) pressures below 3×10^{-11} Torr in our main vacuum chamber after opening it for a short time in order to substitute the old videotape-atom chip with the newly-fabricated fibre chip.

The process of recovering such low pressures after opening the main chamber for some minutes under argon pressure took of the order of 7-10 days. Most of this time was spent baking out the chamber, i.e., heating it as evenly as possible and maintaining it at a high temperature in order to increase the outgassing rates of the different parts and materials inside the chamber, to release the substances trapped within them so that they could be pumped out of the system.

The first time the vacuum system was opened after it had been closed for more than three years, the main chamber was left empty, with no atom chip inside, and baked at a high temperature of up to 230°C. Subsequent bake-outs were performed at lower temperatures of around 120°C, which was the maximum temperature that certain atom-chip components inside the chamber could stand.

Note that, since baking the LVIS chamber was not necessary, the all-metal valve placed between the LVIS chamber and the main chamber was closed to allow complete isolation of the LVIS chamber, which had its own ion pump attached to it.

All materials inside the main vacuum chamber needed to be vacuum compatible, i.e., they had to be not porous, have low outgassing rates and resist baking temperatures of up to around 120°C or more. Our vacuum chamber was made of stainless steel. The rest of materials inside the chamber included glass, ceramics (alumina, Macor, Shapal M), copper, gold, videotape, two-component epoxy glue (Bylapox 7285), low-outgassing UV glue, teflon, optical fibres with acrylate covers, etc.

To start, everything that was going to be placed inside the vacuum chamber needed to be extremely clean, and therefore, appropriate gloves had to be worn to handle all in-vacuum components. The usual cleaning procedure for most materials (glass, Macor, Shapal M, steel, teflon) was the following sequence of ultrasonic baths, mostly aimed to eliminate grease from the material: 30-minute bath in tap water with Decon 90 detergent, rinse with distilled water, 30-minute bath in distilled water, rinse with distilled water, 30-minute bath

in pure acetone, rinse with distilled water, 30-minute bath in distilled water and 30-minute bath in pure methanol, followed by letting the parts dry in the clean atmosphere of a laminar-air-flow box.

Large copper pieces usually need to be cleaned more carefully using acids, but thin, oxygen-free, bare copper wires from just-bought, sealed packets, were placed inside the chamber without previous cleaning.

Aluminium and alumina ceramic were corroded by Decon 90 detergent and hence were not cleaned in such bath. No cleaning was applied to ceramic-coated wires, since their ceramic coating was very fragile and some substances could easily remain trapped within the alumina ceramic.

Optical glass fibres wrapped in an acrylate cover could not be cleaned in acetone or methanol baths, since this process was found to detach the external acrylate cover from the fibre glass cladding. Wiping these fibres with methanol proved to be a sufficiently good cleaning procedure which did not damage the acrylate.

Before opening the chamber, all appropriate screws, washers, nuts, plate-nuts and gaskets for sealing flanges needed to be prepared along with the appropriate tools to handle them. The threads of all screws used to close the flanges were brushed with a mixture of methanol and molybdenum powder in order to prevent the bolts from seizing while baking the chamber. A torque wrench was needed to open and tighten the double valve that gave access to the main chamber.

For the purpose of baking out the main vacuum chamber, all coils and optics around it needed to be removed, and the chamber was wrapped in heater tape and in several layers of tightly packed foil. Optics tissue was placed on the windows beforehand to protect the glass from being scratched by the foil, and a good number of thermocouples were positioned in direct contact with several parts of the chamber, before wrapping it in foil, in order to monitor the temperature during bake-out. Electrical connections to the dispenser, chip wires and getter-pump feedthroughs were also made before wrapping the chamber in foil. A couple of over-all loose layers of foil with air in between them were placed surrounding everything on the outside to make the temperature uniform and to the prevent heat from escaping. The heater tapes were connected to various current supplies and temperature controllers.

A pumping station with a turbo pump and an oil-free, membrane backing pump, together with an RGA (residual gas analyser) and a Pfeiffer pressure gauge on a T-piece, were connected to the valve in the main chamber either directly or via $2\frac{3}{4}$inch flexible bellows. The bellows was baked out and pumped for $\sim$10 hours at a temperature of around 150℃, in order to make them as clean as possible before opening the connecting valve to our chamber.

The ionisation gauge and ion pump were turned off just before opening the chamber. The metal shield and large magnet were removed from the ion pump after it was switched off, and the pump was also wrapped in heater tape and foil.

Once everything was ready and in place, with the whole system at room temperature and the turbo pump completely off, the bellows first and then the chamber were vented with

argon in order to keep a high pressure inside the chamber while opening it. The purpose of this was to prevent air and dust particles from entering the vacuum chamber. The argon pressure was maintained during the whole time the chamber was open and until it was sealed again. Then, the argon flow was stopped and the backing and turbo pumps were started. It took around 30 minutes for the turbo pump to reach its full speed. If no large leaks had been detected, the RGA could be turned on approximately 45 minutes after switching the pumps on. The RGA analysed the gases evolved from the parts inside the chamber and produced a bar graph of partial pressures versus atomic mass number. For stainless steel systems, the usual gases evolved during bake-out are H_2, H_2O, N_2 and CO, and CO_2, with mass numbers of 2, 18, 28, and 44, respectively. At this point, a gauge (Pfeiffer) was turned on to monitor the pressure.

The next step was to turn on the heater tapes in order to start heating the main chamber. It took up to 6-7 hours to reach a constant temperature of ∼120℃. The heating rate needed to be slow enough and to not exceed ∼ 3 degrees per minute, which was the maximum rate for the glass windows in our chamber. During bake-out, the pressure increased as the temperature rose, and then started to decrease while the chamber was kept at constant temperature.

A current of 5-7A should be run through the chip wires during bake-out to outgas them and to prevent them from being the coldest part inside the chamber. Similarly, a small current (∼2A) should be run through the dispenser if the LVIS chamber is baked.

After 24 hours baking at constant temperature, the measured pressure was around 10^{-6}-10^{-7} Torr, and therefore it was safe to turn on the ionisation gauge attached to the main chamber, which had a maximum pressure limit of 10^{-4} Torr. The ionisation gauge was degassed by pressing the DEGAS button on its controller, a process which lasted around 15-20 minutes. The pressure increased quickly by around one order of magnitude in the first minute and then dropped slowly during the following 15-20 minutes.

The next step consisted of reactivating the non-evaporative getter pump. The getter pump was connected to one port of the main vacuum chamber and its function was mainly to remove hydrogen from the system by adsorbing it into its large effective surface. During the process of reactivation, gases were desorbed from the getter surface by running current through a heating element in the getter cartridge. The current was increased from 0 to 4A over 40 minutes, held at 4A for around 100 more minutes and then decreased from 4A to 0 in 40 minutes, as shown in figure B-1. A first layer of gases evolved from the getter pump as the current increased, resulting in a fast initial pressure rise, evidenced by the peak at around 30 minutes in figure B-1. As the current was held at 4A, mostly hydrogen was released from the getter and detected on the RGA. On lowering the current, the pressure started to fall until it was around one order of magnitude lower than the starting pressure, reaching values in the 10^{-8} Torr range, as shown in the same figure.

At this point, the magnet was placed back on the ion pump in order to switch it back on.

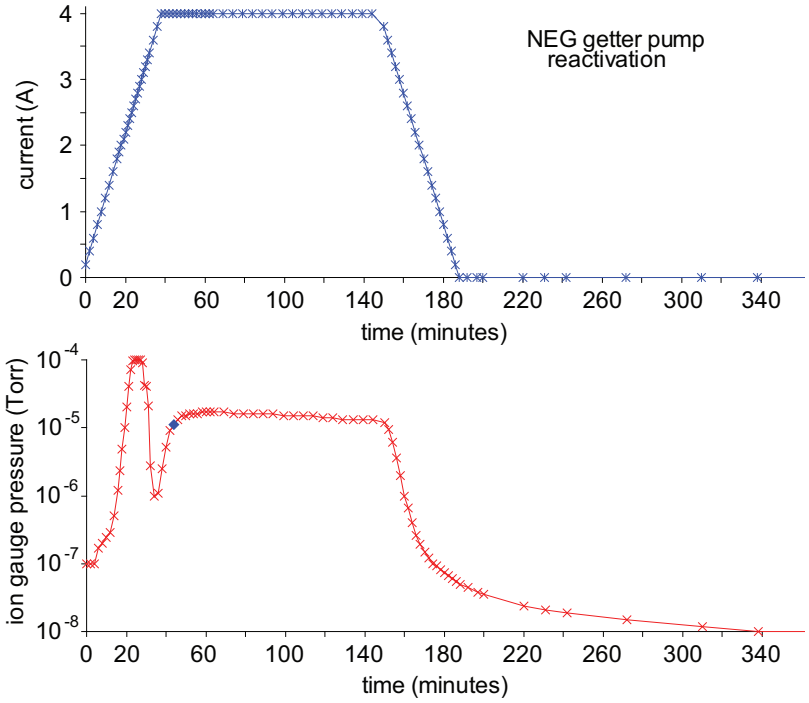

Figure B-1: SAES non-evaporative getter-pump reactivation process. Current run through the heating element in the getter cartridge (top) and pressure inside the chamber, measured by the ionisation gauge (bottom). The blue diamond in the pressure plot shows the point at which hydrogen started to dominate the RGA spectrum.

The current in the ion pump, which was proportional to pressure, was seen to come down immediately. We found that switching this pump on and off a few times helped improve its performance. The ion pump was again covered in foil and heated, while switched on.

The constant heat in the chamber was maintained with the main valve open and the heater tapes, turbo pump, ionisation gauge, RGA and ion pump on, until the pressure was seen to stop falling. By the time this point was reached, the chamber had been heated at constant temperature for up to ∼7 days from the start of the bake-out cycle. During this time, the temperature, pressure and gases evolved from the chamber were continuously monitored.

When the ion gauge read a pressure of around 8×10^{-9} Torr, the gate valve was closed finger-tight and the chamber was allowed to cool down slowly by reducing the current in the heater tapes. After around 8 hours, the chamber's temperature was close to room temperature and the pressure had dropped to a few 10^{-10} Torr. The chamber valves were then closed tightly with the torque wrench (at around 140 lbf×in). The pressure continued to decrease over the following hours, until the reading "E03" appeared on the ionisation gauge, which meant that a pressure below 3×10^{-11} Torr had been reached.

When optical fibres were placed inside the vacuum chamber, connected to the outside through swagelock-type feedthroughs with teflon ferrules, the pressure had not decreased below $\sim10^{-10}$ Torr after a couple of days, indicating the presence of a leak. We tightened the swagelock nuts to improve the vacuum seal and then the pressure fell to around 3×10^{-11}

Torr over a period of a few seconds.

Once a pressure below 3×10^{-11} Torr was achieved in the main vacuum chamber with the LVIS valve closed, we found that it was necessary to carefully open and close this valve a few times in order to remove possibly trapped particles and recover the same low pressures in the main chamber, with the LVIS gate valve open.

Helpful information about vacuum techniques and materials can be found in references [224–228].

Appendix C

FET circuits for current control

The currents running through the wires in the chip (centre wire and end wires), through the coils (LVIS quadrupole coils, MOT quadrupole coils, bias coils, B_z coils, and LVIS and MOT shim coils), and through the rubidium dispenser, were controlled and stabilised by means of FET-driver circuits as shown in figure C-1.

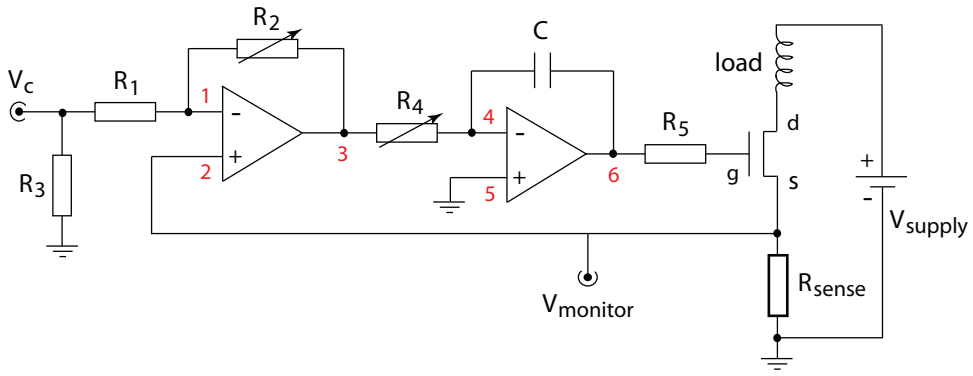

Figure C-1: FET circuit for the stabilisation and control of the current running through the chip wires, external coils and dispenser.

The voltage at the gate (g) of the FET determined the current that ran through the load and sense resistor. The voltage at the source (s) of the FET, proportional to the current through the load, was fed back to the first operational amplifier in the circuit, which was connected as a differential amplifier and regulated the gate voltage (and hence the output current) by comparing the sense voltage to a control voltage V_c. The control voltage was generated by a computer and could be set on a user interface. The second operational amplifier was connected as an integrator. The differential feedback corrected for fast deviations of the output current from the required value, while the integral feedback corrected for slower, long-term drifts.

The differential gain of the circuit was set by the values of R_1, R_2 and R_{sense}, and the integral gain depended on the values of R_4 and C. The total gain of the circuit could be modified with the potentiometer R_2, while the delay time of the current response of the circuit could be adjusted by regulating the variable resistor R_4.

The power supplies we used were switch-mode power supplies (ISOTECH IPS 1820D, 3610D, 606D, 303D and 1810H; TENMA 726153; Hewlett Packard E3610A; Agilent E3610A), and bipolar operational power supplies (KEPCO BOP 36-12M). The voltage in the supplies was set to a value just above the one needed to drive the corresponding loads, but not much higher, in order to avoid too much power being dissipated in the FETs, as this could destroy them. A small positive voltage (around 10mV) was always applied as control voltage even when the wires or coils were not used, in order to keep the FETs active and avoid delays in their initial response. These small voltages corresponded to currents of the order of 10mA and generated very small magnetic fields, of the order of a few tens of milliGauss, at the typical experimental values of the atom-surface separation in our traps.

The FETs used were MTW32N20E (power MOSFET, 32A, 200V), and the operational amplifiers were LF412CN and TL072CN. The typical values of the electronic components in the diagrams were $R_1 = 36k\Omega$, $R_2 = 10k\Omega$, R_3 was $5.6k\Omega$ or $10k\Omega$, $R_4 = 200k\Omega$, $R_5 = 75\Omega$ and $C = 3.3nF$. The sense resistors were 0.1Ω or 0.47Ω power resistors.

The FET circuits were mounted on heat sinking elements to remove the heat dissipated during their operation. Some of the circuits were additionally mounted on water-cooled copper plates for additional heat sinking.

Appendix D

Optimum period of videotape magnetisation

The frequency, f_r, of the transverse atomic oscillations in a videotape magnetic trap is given by the following expression (see section 2.3.6):

$$f_r = \frac{kB_b}{2\pi}\sqrt{\frac{\mu_B g_F m_F}{mB_{z-net}}}\,, \tag{D.1}$$

where B_b is the bias field applied usually along the x direction, $k = 2\pi/\lambda$ and λ is the period of the recorded videotape magnetisation, and the rest of the symbols were described in section 2.3.6.

At the height, y_0, at which the videotape trap is formed, the magnitude of the bias field is equal to that of the field generated by the videotape (see equation 2.25), so that we can write:

$$B_b = B_1 e^{-ky_0} = \frac{\mu_0 M_1}{2}(1 - e^{-kb})e^{-ky_0}\,, \tag{D.2}$$

where we have used equation 2.26 to substitute for the field, B_1, at the surface of the videotape, μ_0 is the free-space magnetic permeability, b is the thickness of the videotape magnetic layer, and M_1 is the amplitude of the fundamental frequency component of the videotape magnetisation.

Substituting B_b of equation D.2 into equation D.1, we find:

$$f_r = \frac{\mu_0 M_1}{2\lambda}\sqrt{\frac{\mu_B g_F m_F}{mB_{z-net}}}\left(e^{-ky_0} - e^{-k(y_0+b)}\right)\,. \tag{D.3}$$

It is possible to maximise this expression with respect to the period of recorded videotape magnetisation, λ, in order to find the optimum value of λ that generates the tightest possible transverse confinement for atoms trapped in videotape traps at a given distance, y_0, from the chip surface.

Figure D-1(left) shows a plot of the transverse frequency of the trap as a function of the period of recorded magnetisation for a height $y_0 = 100\mu$m and $B_{z-net} = 1$G. The transverse trap frequency for a period of 100μm is 165Hz, while that for a period of 320μm is maximum and equal to 1.4kHz, at the same distance of 100μm from the chip surface. Therefore, the larger period of magnetisation leads to an increase in transverse trap frequency by a factor

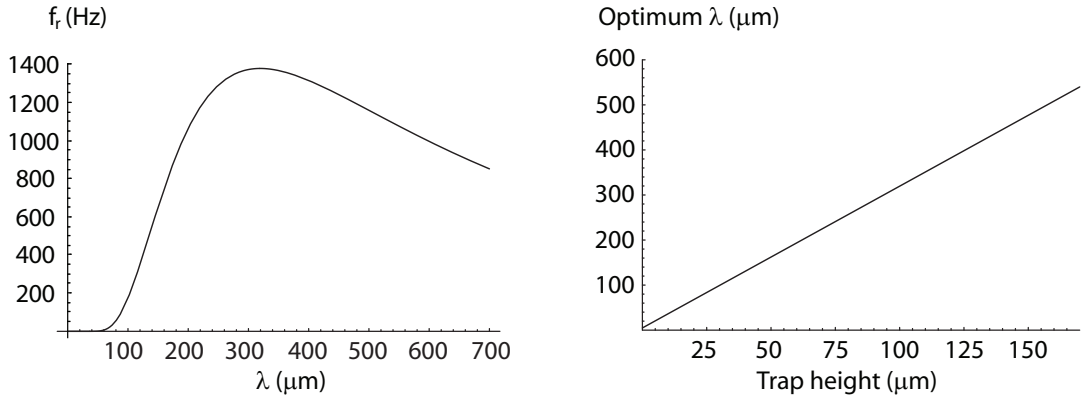

Figure D-1: **Left:** transverse videotape trap frequency, f_r, versus period, λ, of recorded videotape magnetisation, for $y_0 = 100\mu$m, $B_{z-net} = 1$G, $b = 3.5\mu$m and $M_1 = 88684$A/m. The value of M_1 was derived from equation 2.26 using the values $B_1 = 110$G, $\lambda = 106\mu$m and $b = 3.5\mu$m (see section 2.3.5). **Right:** optimum period, λ, of recorded magnetisation that maximises the transverse trap frequency as a function of the trap height, y_0.

of approximately 8 at this trap height. Figure D-1(right) plots the numerically-calculated optimum period of magnetisation, i.e., the one that maximises the radial trap frequency, as a function of the distance from the trap to the chip surface (y_0). This optimum period, λ_{opt}, can be expressed analytically as $\lambda_{opt} \approx \pi y_0$ if we assume that $\lambda \gg 2\pi b$. We are interested in trapping atoms at distances $\geq 100\mu$m from the chip surface in order to avoid fragmentation effects (see chapter 6 for fragmentation measurements in our videotape atom chip, for $\lambda \sim 110\mu$m). The optimum period of magnetisation for a height of 100μm is 320μm, while 100μm is the optimum period for a trap height of around 33μm.

Figure D-2 shows the numerically-calculated maximum value of the transverse trap frequency achieved when the optimum period of videotape magnetisation, shown in figure D-1(right), is used. Again an analytical expression is found if we assume that $\lambda \gg 2\pi b$, leading to the result $f_{r-max} \approx \frac{\mu_0 M_1 b}{\pi e^2 y_0^2} \sqrt{\frac{\mu_B g_F m_F}{m B_{z-net}}}$.

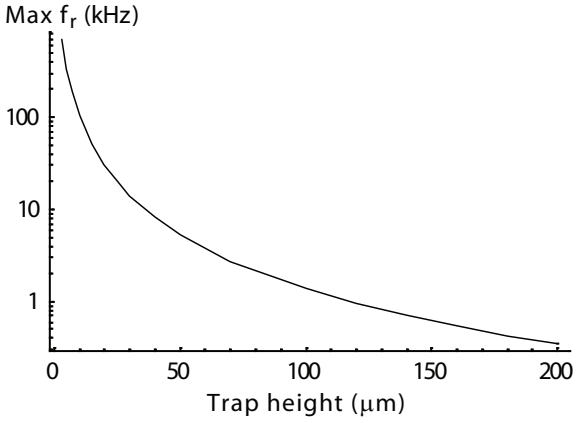

Figure D-2: Maximised transverse trap frequency in a videotape trap when the optimum period of recorded magnetisation (shown in figure D-1(right)) is used, as a function of the trap height. The value of B_{z-net} is 1G (equivalent to a 0.7MHz trap bottom).

Figure D-3 shows the transverse trap frequency as a function of trap height for different

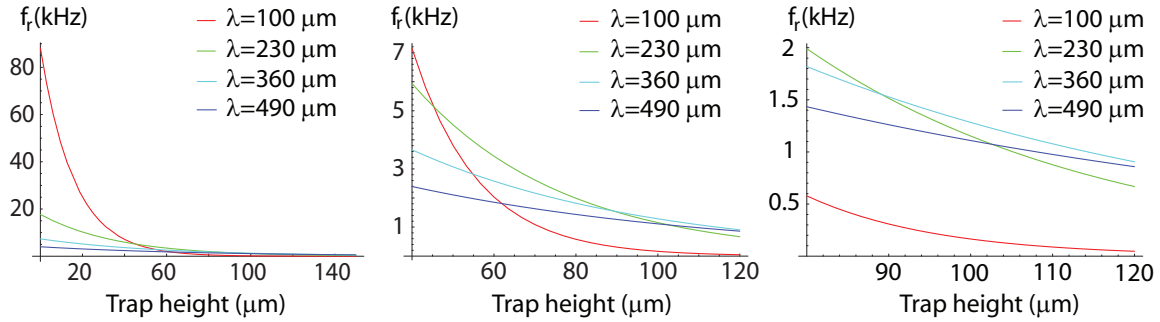

Figure D-3: Transverse videotape trap frequency versus trap height for different periods of recorded videotape magnetisation. The three graphs correspond to the same plot but show different ranges of trap height, for clarity.

periods of recorded videotape magnetisation, λ. The three graphs show three different ranges of the same plot, for clarity. We can see that a period of magnetisation of 100μm is a good choice if atoms are going to be confined at short distances from the chip, below 40μm. However, longer periods of magnetisation are more convenient for trapping atoms at distances $\geq$100μm from the chip, resulting in larger radial trap frequencies. For example, with a period of 360μm and a trap height of 217μm it is possible to achieve the same radial trap frequency as for a period of 100μm and a height of 100μm.

A piece of videotape recorded some years ago with a period of magnetisation of $\sim$360μm was found in the laboratory and studied with a microscope (see appendix A). It would be very interesting to build a new videotape atom chip with this larger recorded period of magnetisation. This could test how high a radial trap frequency can be achieved at large distances from the chip surface, and how small the fragmentation effects can be.

Bibliography

[1] S. Chu. *Nobel Lecture: The manipulation of neutral particles.* Rev. Mod. Phys., **70**, 685 (1998).

[2] C. N. Cohen-Tannoudji. *Nobel Lecture: Manipulating atoms with photons.* Rev. Mod. Phys., **70**, 707 (1998).

[3] W. D. Phillips. *Nobel Lecture: Laser cooling and trapping of neutral atoms.* Rev. Mod. Phys., **70**, 721 (1998).

[4] E. A. Cornell and C. E. Wieman. *Bose-Einstein Condensation in a Dilute Gas: The First 70 Years and some Recent Experiments (Nobel Lecture).* Chem. Phys. Chem., **3**, 476 (2002).

[5] W. Ketterle. *When Atoms Behave as Waves: Bose-Einstein Condensation and the Atom Laser (Nobel Lecture).* Chem. Phys. Chem., **3**, 736 (2002).

[6] J. D. Weinstein and K. G. Libbrecht. *Microscopic magnetic traps for neutral atoms.* Phys. Rev. A, **52**, 4004 (1995).

[7] M. Drndić, K. S. Johnson, J. H. Thywissen, M. Prentiss, and R. M. Westervelt. *Micro-electromagnets for atom manipulation.* Appl. Phys. Lett., **72**, 2906 (1998).

[8] J. H. Thywissen, M. Olshanii, G. Zabow, M. Drndić, K. S. Johnson, R. M. Westervelt, and M. Prentiss. *Microfabricated magnetic waveguides for neutral atoms.* Eur. Phys. J. D, **7**, 361 (1999).

[9] J. Denschlag, D. Cassettari, A. Chenet, S. Schneider, and J. Schmiedmayer. *A neutral atom and a wire: towards mesoscopic atom optics.* Appl. Phys. B, **69**, 291 (1999).

[10] E. A. Hinds and I. G. Hughes. *Magnetic atom optics: mirrors, guides, traps, and chips for atoms.* J. Phys. D: Appl. Phys., **32**, R119 (1999).

[11] E. A. Hinds. *Controlling cold atoms above a magnetic reflector.* Phil. Trans. R. Soc. Lond. A, **357**, 1409 (1999).

[12] J. Reichel, W. Hänsel, and T. W. Hänsch. *Atomic Micromanipulation with Magnetic Surface Traps.* Phys. Rev. Lett., **83**, 3398 (1999).

[13] R. Folman, P. Krüger, D. Cassettari, B. Hessmo, T. Maier, and J. Schmiedmayer. *Controlling Cold Atoms using Nanofabricated Surfaces: Atom Chips.* Phys. Rev. Lett., **84**, 4749 (2000).

[14] W. Hänsel, P. Hommelhoff, T. W. Hänsch, and J. Reichel. *Bose-Einstein condensation on a microelectronic chip.* Nature, **413**, 498 (2001).

[15] J. Reichel. *Microchip traps and Bose-Einstein condensation.* Appl. Phys. B, **75**, 469 (2002).

[16] H. Ott, J. Fortagh, G. Schlotterbeck, A. Grossmann, and C. Zimmermann. *Bose-Einstein Condensation in a Surface Microtrap.* Phys. Rev. Lett., **87**, 230401 (2001).

[17] J. Reichel, W. Hänsel, P. Hommelhoff, and T. W. Hänsch. *Applications of integrated magnetic microtraps.* Appl. Phys. B, **72**, 81 (2001).

[18] R. Folman, P. Krüger, J. Schmiedmayer, J. Denschlag, and C. Henkel. *Microscopic atom optics: from wires to an atom chip.* Adv. At. Mol. Opt. Phys., **48**, 263 (2002).

[19] J. Fortágh and C. Zimmermann. *Magnetic microtraps for ultracold atoms.* Rev. Mod. Phys., **79**, 235 (2007).

[20] T. Schumm, S. Hofferberth, L. M. Andersson, S. Wildermuth, S. Groth, I. Bar-Joseph, J. Schmiedmayer, and P. Krüger. *Matter-wave interferometry in a double well on an atom chip.* Nature Physics, **1**, 57 (2005).

[21] G.-B. Jo, Y. Shin, S. Will, T. A. Pasquini, M. Saba, W. Ketterle, D. E. Pritchard, M. Vengalattore, and M. Prentiss. *Long Phase Coherence Time and Number Squeezing of Two Bose-Einstein Condensates on an Atom Chip.* Phys. Rev. Lett., **98**, 030407 (2007).

[22] A. Günther, S. Kraft, C. Zimmermann, and J. Fortágh. *Atom Interferometer Based on Phase Coherent Splitting of Bose-Einstein Condensates with an Integrated Magnetic Grating.* Phys. Rev. Lett., **98**, 140403 (2007).

[23] G.-B. Jo, J.-H. Choi, C. A. Christensen, T. A. Pasquini, Y.-R. Lee, W. Ketterle, and D. E. Pritchard. *Phase-Sensitive Recombination of Two Bose-Einstein Condensates on an Atom Chip.* Phys. Rev. Lett., **98**, 180401 (2007).

[24] G.-B. Jo, J.-H. Choi, C. A. Christensen, Y.-R. Lee, T. A. Pasquini, W. Ketterle, and D. E. Pritchard. *Matter-Wave Interferometry with Phase Fluctuating Bose-Einstein Condensates.* Phys. Rev. Lett., **99**, 240406 (2007).

[25] S. Hofferberth, I. Lesanovsky, T. Schumm, A. Imambekov, V. Gritsev, E. Demler, and J. Schmiedmayer. *Probing quantum and thermal noise in an interacting many-body system.* Nature Physics, **4**, 489 (2008).

[26] A. D. Cronin, J. Schmiedmayer, and D. E. Pritchard. *Atom Interferometers.* arXiv:0712.3703v1, (2007-2008).

[27] D. S. Petrov, G. V. Shlyapnikov, and J. T. M. Walraven. *Regimes of Quantum Degeneracy in Trapped 1D Gases.* Phys. Rev. Lett., **85**, 3745 (2000).

[28] D. S. Petrov, D. M. Gangardt, and G. V. Shlyapnikov. *Low-dimensional trapped gases.* J. Phys. IV. Proceedings. France, **116**, 5 (2004).

[29] D. S. Petrov, *Bose-Einstein Condensation in Low-Dimensional Trapped Gases*, Ph.D. thesis, FOM Institute AMOLF. Amsterdam University. The Netherlands (2003).

[30] L. Tonks. *The Complete Equation of State of One, Two and Three-Dimensional Gases of Hard Elastic Spheres.* Phys. Rev., **50**, 955 (1936).

[31] M. Girardeau. *Relationship between Systems of Impenetrable Bosons and Fermions in One Dimension.* J. Math. Phys., **1**, 516 (1960).

[32] M. D. Girardeau, E. M. Wright, and J. M. Triscari. *Ground-state properties of a one-dimensional system of hard-core bosons in a harmonic trap.* Phys. Rev. A, **63**, 033601 (2001).

[33] V. Dunjko, V. Lorent, and M. Olshanii. *Bosons in Cigar-Shaped Traps: Thomas-Fermi Regime, Tonks-Girardeau Regime, and In Between.* Phys. Rev. Lett., **86**, 5413 (2001).

[34] D. Hellweg, S. Dettmer, P. Ryytty, J. J. Arlt, W. Ertmer, K. Sengstock, D. S. Petrov, G. V. Shlyapnikov, H. Kreutzmann, L. Santos, and M. Lewenstein. *Phase fluctuations in Bose-Einstein condensates.* Appl. Phys. B, **73**, 781 (2001).

[35] S. Dettmer, D. Hellweg, P. Ryytty, J. J. Arlt, W. Ertmer, K. Sengstock, D. S. Petrov, G. V. Shlyapnikov, H. Kreutzmann, L. Santos, and M. Lewenstein. *Observation of Phase Fluctuations in Elongated Bose-Einstein Condensates.* Phys. Rev. Lett., **87**, 160406 (2001).

[36] D. Hellweg, L. Cacciapuoti, M. Kottke, T. Schulte, K. Sengstock, W. Ertmer, and J. J. Arlt. *Measurement of the Spatial Correlation Function of Phase Fluctuating Bose-Einstein Condensates.* Phys. Rev. Lett., **91**, 010406 (2003).

[37] B. Paredes, A. Widera, V. Murg, O. Mandel, S. Fölling, I. Cirac, G. V. Shlyapnikov, T. W. Hänsch, and I. Bloch. *Tonks-Girardeau gas of ultracold atoms in an optical lattice.* Nature, **429**, 227 (2004).

[38] B. Laburthe-Tolra, K. M. O'Hara, J. H. Huckans, M. Anderlini, J. V. Porto, S. L. Rolston, and W. D. Phillips. *Study of a 1D interacting quantum Bose gas.* J. Phys. IV France, **116**, 227 (2004).

[39] B. Laburthe-Tolra, K. M. O'Hara, J. H. Huckans, W. D. Phillips, S. L. Rolston, and J. V. Porto. *Observation of Reduced Three-Body Recombination in a Correlated 1D Degenerate Bose Gas.* Phys. Rev. Lett., **92**, 190401 (2004).

[40] T. Kinoshita, T. Wenger, and D. S. Weiss. *Observation of a One-Dimensional Tonks-Girardeau Gas.* Science, **305**, 1125 (2004).

[41] T. Kinoshita, T. Wenger, and D. S. Weiss. *A quantum Newton's cradle.* Nature, **440**, 900 (2006).

[42] Z. Hadzibabic, P. Krüger, M. Cheneau, B. Battelier, and J. Dalibard. *Berezinskii-Kosterlitz-Thouless crossover in a trapped atomic gas.* Nature, **441**, 1118 (2006).

[43] J. Esteve, J.-B. Trebbia, T. Schumm, A. Aspect, C. I. Westbrook, and I. Bouchoule. *Observations of Density Fluctuations in an Elongated Bose Gas: Ideal Gas and Quasicondensate Regimes.* Phys. Rev. Lett., **96**, 130403 (2006).

[44] J.-B. Trebbia, J. Esteve, C. I. Westbrook, and I. Bouchoule. *Experimental evidence for the breakdown of a Hartree-Fock approach in a weakly interacting Bose gas.* Phys. Rev. Lett., **97**, 250403 (2006).

[45] S. Hofferberth, I. Lesanovsky, B. Fischer, T. Schumm, and J. Schmiedmayer. *Non-equilibrium coherence dynamics in one-dimensional Bose gases.* Nature, **449**, 324 (2007).

[46] A. H. van Amerongen, J. J. P. van Es, P. Wicke, K. V. Kheruntsyan, and N. J. van Druten. *Yang-Yang Thermodynamics on an Atom Chip.* Phys. Rev. Lett., **100**, 090402 (2008).

[47] Y. Lin, I. Teper, C. Chin, and V. Vuletić. *Impact of the Casimir-Polder Potential and Johnson Noise on Bose-Einstein Condensate Stability Near Surfaces.* Phys. Rev. Lett., **92**, 050404 (2004).

[48] D. M. Harber, J. M. Obrecht, J. M. McGuirk, and E. A. Cornell. *Measurement of the Casimir-Polder force through center-of-mass oscillations of a Bose-Einstein condensate.* Phys. Rev. A, **72**, 033610 (2005).

[49] J. M. Obrecht, R. J. Wild, M. Antezza, L. P. Pitaevskii, S. Stringari, and E. A. Cornell. *Measurement of the Temperature Dependence of the Casimir-Polder Force.* Phys. Rev. Lett., **98**, 063201 (2007).

[50] T. Könemann et al. (20 authors). *A freely falling magneto-optical trap drop tower experiment.* Appl. Phys. B, **89**, 431 (2007).

[51] D. Bouwmeester, A. Ekert, and A. Zeilinger, *The Physics of Quantum Information* (Springer, Berlin, 2000).

[52] P. Zoller et al. (39 authors). *Quantum information processing and communication. Strategic report on current status, visions and goals for research in Europe.* Eur. Phys. J. D, **36**, 203 (2005).

[53] P. Treutlein, T. Steinmetz, Y. Colombe, P. Hommelhoff, J. Reichel, M. Greiner, O. Mandel, A. Widera, T. Rom, I. Bloch, and T. W. Hänsch. *Quantum Information Processing in Optical Lattices and Magnetic Microtraps.* Fortschr. Phys., **54**, 702 (2006).

[54] M. Trupke, J. Metz, A. Beige, and E. A. Hinds. *Towards quantum computing with single atoms and optical cavities on atom chips.* Journal of Modern Optics, **54**, 1639 (2007).

[55] P. Krüger, A. Haase, L. M. Andersson, and J. Schmiedmayer. *Quantum information processing with neutral atoms on an atom chip.* Journal of Modern Optics, **49**, 1375 (2002).

[56] S. Wildermuth, S. Hofferberth, I. Lesanovsky, E. Haller, L. M. Andersson, S. Groth, I. Bar-Joseph, P. Krüger, and J. Schmiedmayer. *Microscopic magnetic-field imaging.* Nature, **435**, 440 (2005).

[57] P. Krüger, S. Wildermuth, S. Hofferberth, L. M. Andersson, S. Groth, I. Bar-Joseph, and J. Schmiedmayer. *Cold Atoms close to surfaces: Measuring magnetic field roughness and disorder potentials.* Journal of Physics: Conference Series, **19**, 56 (2005).

[58] S. Wildermuth, S. Hofferberth, I. Lesanovsky, S. Groth, P. Krüger, J. Schmiedmayer, and I. Bar-Joseph. *Sensing electric and magnetic fields with Bose-Einstein condensates.* Appl. Phys. Lett., **88**, 264103 (2006).

[59] S. Aigner, L. D. Pietra, Y. Japha, O. Entin-Wohlman, T. David, R. Salem, R. Folman, and J. Schmiedmayer. *Long-Range Order in Electronic Transport Through Disordered Metal Films.* Science, **319**, 226 (2008).

[60] P. D. D. Schwindt, S. Knappe, V. Shah, L. Hollberg, J. Kitching, L. Liew, and J. Moreland. *Chip-scale atomic magnetometer.* Appl. Phys. Lett., **85**, 6409 (2004).

[61] J. M. Obrecht, R. J. Wild, and E. A. Cornell. *Measuring electric fields from surface contaminants with neutral atoms.* Phys. Rev. A, **75**, 062903 (2007).

[62] S. Knappe, P. D. D. Schwindt, V. Shah, L. Hollberg, J. Kitching, L. Liew, and J. Moreland. *A chip-scale atomic clock based on ^{87}Rb with improved frequency stability.* Optics Express, **13**, 1249 (2005).

[63] P. Treutlein, P. Hommelhoff, T. Steinmetz, T. W. Hänsch, and J. Reichel. *Coherence in Microchip Traps.* Phys. Rev. Lett., **92**, 203005 (2004).

[64] F. Reinhard, J. Reichel, C. Lacroûte, and P. Rosenbusch. *TACC: Trapped Atom Clock on a Chip. Ongoing project.* Laboratoire Kastler Brossel, Paris, France, (2008).

[65] C. D. J. Sinclair, J. A. Retter, E. A. Curtis, B. V. Hall, I. Llorente-Garcia, S. Eriksson, B. E. Sauer, and E. A. Hinds. *Cold atoms in videotape micro-traps.* Eur. Phys. J. D, **35**, 105 (2005).

[66] C. D. J. Sinclair, E. A. Curtis, I. Llorente-Garcia, J. A. Retter, B. V. Hall, S. Eriksson, B. E. Sauer, and E. A. Hinds. *Bose-Einstein condensation on a permanent-magnet atom chip.* Phys. Rev. A, **72**, 031603(R) (2005).

[67] I. G. Hughes, P. A. Barton, T. M. Roach, M. G. Boshier, and E. A. Hinds. *Atom optics with magnetic surfaces: I. Storage of cold atoms in a curved "floppy disk".* J. Phys. B: At. Mol. Opt. Phys., **30**, 647 (1997).

[68] I. G. Hughes, P. A. Barton, T. M. Roach, and E. A. Hinds. *Atom optics with magnetic surfaces: II. Microscopic analysis of the "floppy disk" mirror.* J. Phys. B: At. Mol. Opt. Phys., **30**, 2119 (1997).

[69] C. V. Saba, P. A. Barton, M. G. Boshier, I. G. Hughes, P. Rosenbusch, B. E. Sauer, and E. A. Hinds. *Reconstruction of a Cold Atom Cloud by Magnetic Focusing.* Phys. Rev. Lett., **82**, 468 (1999).

[70] P. Rosenbusch, B. V. Hall, I. G. Hughes, C. V. Saba, and E. A. Hinds. *Manipulation of cold atoms by an adaptable magnetic reflector.* Appl. Phys. B, **70**, 709 (2000).

[71] B. V. Hall, S. Whitlock, F. Scharnberg, P. Hannaford, and A. Sidorov. *A permanent magnetic film atom chip for Bose-Einstein condensation.* J. Phys. B: At. Mol. Opt. Phys., **39**, 27 (2006).

[72] S. Ghanbari, T. D. Kieu, and P. Hannaford. *A class of permanent magnetic lattices for ultracold atoms.* J. Phys. B: At. Mol. Opt. Phys., **40**, 1283 (2007).

[73] M. Singh, M. Volk, A. Akulshin, A. Sidorov, R. McLean, and P. Hannaford. *One-dimensional lattice of permanent magnetic microtraps for ultracold atoms on an atom chip.* J. Phys. B: At. Mol. Opt. Phys., **41**, 065301 (2008).

[74] I. Barb, R. Gerritsma, Y. T. Xing, J. B. Goedkoop, and R. J. C. Spreeuw. *Creating Ioffe-Pritchard micro-traps from permanent magnetic film with in-plane magnetisation.* Eur. Phys. J. D, **35**, 75 (2005).

[75] R. Gerritsma, S. Whitlock, T. Fernholz, H. Schlatter, J. A. Luigjes, J.-U. Thiele, J. B. Goedkoop, and R. J. C. Spreeuw. *Lattice of microtraps for ultracold atoms based on patterned magnetic films.* Phys. Rev. A, **76**, 033408 (2007).

[76] T. Fernholz, R. Gerritsma, S. Whitlock, I. Barb, and R. J. C. Spreeuw. *Fully permanent magnet atom chip for Bose-Einstein condensation.* Phys. Rev. A, **77**, 033409 (2008).

[77] M. Boyd, E. W. Streed, P. Medley, G. K. Campbell, J. Mun, W. Ketterle, and D. E. Pritchard. *Atom trapping with a thin magnetic film.* Phys. Rev. A, **76**, 043624 (2007).

[78] A. Jaakkola, A. Shevchenko, K. Lindfors, M. Hautakorpi, E. Il'yashenkoa, T. H. Johansen, and M. Kaivola. *Reconfigurable atom chip on a transparent ferrite-garnet film.* Eur. Phys. J. D, **35**, 81 (2005).

[79] A. Shevchenko, M. Heiliö, T. Lindvall, A. Jaakkola, I. Tittonen, M. Kaivola, and T. Pfau. *Trapping atoms on a transparent permanent-magnet atom chip.* Phys. Rev. A, **73**, 051401(R) (2006).

[80] J. A. Retter, *Cold Atom Microtraps above a Videotape Surface*, Ph.D. thesis, University of Sussex (2002).

[81] C. D. J. Sinclair, *Bose-Einstein Condensation in Microtraps on Videotape*, Ph.D. thesis, Imperial College London (2005).

[82] S. A. Hopkins, E. A. Hinds, and M. G. Boshier. *UHV-compatible magnetic material for atom optics.* Appl. Phys. B, **73**, 51 (2001).

[83] D. A. Steck. *Rubidium 87 D Line Data.* Oregon Centre for Optics and Department of Physics, University of Oregon, (Updated May 2008).

[84] W. Ketterle, D. S. Durfee, and D. M. Stamper-Kurn. *Making, probing and understanding Bose-Einstein condensates.* Bose-Einstein condensation in atomic gases, Proceedings of the International School of Physics "Enrico Fermi", Course CXL, edited by M. Inguscio, S. Stringari and C.E. Wieman (IOS Press, Amsterdam), pp. 67–176 (1999).

[85] D. M. Brink and C. V. Sukumar. *Majorana spin-flip transitions in a magnetic trap.* Phys. Rev. A, **74**, 035401 (2006).

[86] I. G. Hughes, P. A. Barton, T. M. Roach, and E. A. Hinds. *Atom optics with magnetic surfaces: II. Microscopic analysis of the "floppy disk" mirror.* J. Phys. B: At. Mol. Opt. Phys., **30**, 2119 (1997).

[87] J. D. Jackson, *Classical electrodynamics. Third edition.* (John Wiley and Sons Inc., 1998).

[88] A. S. Arnold, J. S. Wilson, and M. G. Boshier. *A simple extended-cavity diode laser.* Rev. Sci. Instrum., **69**, 1236 (1998).

[89] M. L. Harris, C. S. Adams, S. L. Cornish, I. C. McLeod, E. Tarleton, and I. G. Hughes. *Polarization spectroscopy in rubidium and cesium.* Phys. Rev. A, **73**, 062509 (2006).

[90] H. J. Metcalf and P. V. der Straten, *Laser cooling and trapping* (Springer, 1999).

[91] C. S. Adams and E. Riis. *Laser Cooling and Trapping of Neutral Particles.* Prog. Quant. Electr., **21**, 1 (1997).

[92] J. Dalibard and C. Cohen-Tannoudji. *Laser cooling below the Doppler limit by polarization gradients: simple theoretical models.* J. Opt. Soc. Am. B, **6**, 2023 (1989).

[93] O. J. Luiten, M. W. Reynolds, and J. T. M. Walraven. *Kinetic theory of the evaporative cooling of a trapped gas.* Phys. Rev. A, **53**, 381 (1996).

[94] W. Ketterle and N. J. van Drutten. *Evaporative cooling of trapped atoms.* Adv. At. Mol. Opt. Phys., **37**, 181 (1996).

[95] K. B. Davis, M.-O. Mewes, and W. Ketterle. *An analytical model for evaporative cooling of atoms.* Appl. Phys. B, **60**, 155 (1995).

[96] J. E. Lye, C. S. Fletcher, U. Kallmann, H.-A. Bachor, and J. D. Close. *Images of evaporative cooling to Bose-Einstein condensation.* J. Opt. B: Quantum Semiclass. Opt., **4**, 57 (2002).

[97] J. P. Burke, J. L. Bohn, B. D. Esry, and C. H. Greene. *Prospects for Mixed-Isotope Bose-Einstein Condensates in Rubidium.* Phys. Rev. Lett., **80**, 2097 (1998).

[98] E. A. Guggenheim, J. E. Mayer, and F. C. Tompkins, *The International Encyclopedia of Physical Chemistry and Chemical Physics* (Pergamon Press. Oxford).

[99] L. D. Landau and E. M. Lifshitz, *Course of Theoretical Physics. Mechanics.*, vol. 1 (Pergamon Press, 1976).

[100] F. Reif, *Fundamentals of Statistical and Thermal Physics* (McGraw-Hill).

[101] J. H. V. Vleck and V. F. Weisskopf. *On the Shape of Collision-Broadened Lines.* Reviews of Modern Physics, **17**, 227 (1945).

[102] N. Poli, R. J. Brecha, G. Roati, and G. Modugno. *Cooling atoms in an optical trap by selective parametric excitation.* Phys. Rev. A, **65**, 021401(R) (2001).

[103] S. Zhou, Z. Xu, S. Zhou, L. Liu, and Y. Wang. *Parametric excitation of Rb^{87} atoms in a quadrupole-Ioffe-configuration trap.* Phys. Rev. A, **75**, 053414 (2007).

[104] M. Kumakura, Y. Shirahata, Y. Takasu, Y. Takahashi, and T. Yabuzaki. *Shaking-induced cooling of cold atoms in a magnetic trap.* Phys. Rev. A, **68**, 021401(R) (2003).

[105] P. Paasche, T. Valenzuela, D. Biswas, C. Angelescu, and G. Werth. *Individual and centre-of-mass resonances in the motional spectrum of an electron cloud in a Penning trap.* Eur. Phys. J. D, **18**, 295 (2002).

[106] G. Tommaseo, P. Paasche, C. Angelescu, and G. Werth. *Subharmonic excitation of the eigenmodes of charged particles in a Penning trap.* Eur. Phys. J. D, **28**, 39 (2004).

[107] K. Kim, H. R. Noh, H. J. Ha, and W. Jhe. *Direct observation of the sub-Doppler trap in a parametrically driven magneto-optical trap.* Phys. Rev. A, **69**, 033406 (2004).

[108] K. Kim, H. R. Noh, and W. Jhe. *Measurements of trap parameters of a magneto-optical trap by parametric resonance.* Phys. Rev. A, **71**, 033413 (2005).

[109] T. A. Savard, K. M. O'Hara, and J. E. Thomas. *Laser-noise-induced heating in far-off resonance optical traps.* Phys. Rev. A, **56**, R1095 (1997).

[110] M. E. Gehm, K. M. O'Hara, T. A. Savard, and J. E. Thomas. *Dynamics of noise-induced heating in atom traps.* Phys. Rev. A, **58**, 3914 (1998).

[111] C. W. Gardiner, J. Ye, H. C. Nagerl, and H. J. Kimble. *Evaluation of heating effects on atoms trapped in an optical trap.* Phys. Rev. A, **61**, 045801 (2000).

[112] R. Jáuregui, N. Poli, G. Roati, and G. Modugno. *Anharmonic parametric excitation in optical lattices.* Phys. Rev. A, **64**, 033403 (2001).

[113] R. Jáuregui. *Nonperturbative and perturbative treatments of parametric heating in atom traps.* Phys. Rev. A, **64**, 053408 (2001).

[114] S. Friebel, C. D'Andrea, J. Walz, M. Weitz, and T. W. Hänsch. *CO_2-laser optical lattice with cold rubidium atoms.* Phys. Rev. A, **57**, R20 (1998).

[115] G. Roati, W. Jastrzebski, A. Simoni, G. Modugno, and M. Inguscio. *Optical trapping of cold fermionic potassium for collisional studies.* Phys. Rev. A, **63**, 052709 (2001).

[116] M. D. Barrett, *A QUEST for BEC: an all-optical alternative*, Ph.D. thesis, Georgia Institute of Technology (2002).

[117] M. A. van Eijkelenborg, K. Dholakia, M. E. M. Storkey, D. M. Segal, and R. C. Thompson. *A driven, trapped, laser cooled ion cloud: a forced damped oscillator.* Optics Communications, **159**, 169 (1999).

[118] H. Imajo, S. Urabe, K. Hayasaka, and M. Watanabe. *Measurements of motional frequencies for laser-cooled ions in a Penning trap.* J. Mod. Optics, **39**, 317 (1992).

[119] H. Higaki, K. Ito, R. Takai, K. Nakayama, W. Saiki, K. Izawa, and H. Okamoto. *Axial resonances of Ar^+ ions observed in a linear Paul trap.* Hyperfine Interact, **174**, 77 (2007).

[120] J. Fortágh, H. Ott, S. Kraft, A. Günther, and C. Zimmermann. *Surface effects in magnetic microtraps.* Phys. Rev. A, **66**, 041604(R) (2002).

[121] S. Kraft, A. Günther, H. Ott, D. Wharam, C. Zimmermann, and J. Fortágh. *Anomalous longitudinal magnetic field near the surface of copper conductors.* J. Phys. B: At. Mol. Opt. Phys., **35**, L469 (2002).

[122] J. Fortágh, H. Ott, S. Kraft, A. Günther, and C. Zimmermann. *Bose-Einstein condensates in magnetic waveguides.* Appl. Phys. B, **76**, 157 (2003).

[123] A. E. Leanhardt, A. P. Chikkatur, D. Kielpinski, Y. Shin, T. L. Gustavson, W. Ketterle, and D. E. Pritchard. *Propagation of Bose-Einstein Condensates in a Magnetic Waveguide.* Phys. Rev. Lett., **89**, 040401 (2002).

[124] A. E. Leanhardt, Y. Shin, A. P. Chikkatur, D. Kielpinski, W. Ketterle, and D. E. Pritchard. *Bose-Einstein Condensates near a Microfabricated Surface.* Phys. Rev. Lett., **90**, 100404 (2003).

[125] M. P. A. Jones, C. J. Vale, D. Sahagun, B. V. Hall, and E. A. Hinds. *Spin Coupling between Cold Atoms and the Thermal Fluctuations of a Metal Surface.* Phys. Rev. Lett., **91**, 080401 (2003).

[126] M. P. A. Jones, C. J. Vale, D. Sahagun, B. V. Hall, C. C. Eberlein, B. E. Sauer, K. Furusawa, D. Richardson, and E. A. Hinds. *Cold atoms probe the magnetic field near a wire.* J. Phys. B: At. Mol. Opt. Phys., **37**, L15 (2004).

[127] C. J. Vale, B. Upcroft, M. J. Davis, N. R. Heckenberg, and H. Rubinsztein-Dunlop. *Foil-based atom chip for Bose-Einstein condensates.* J. Phys. B: At. Mol. Opt. Phys., **37**, 2959 (2004).

[128] J. Estève, C. Aussibal, T. Schumm, C. Figl, D. Mailly, I. Bouchoule, C. I. Westbrook, and A. Aspect. *Role of wire imperfections in micromagnetic traps for atoms.* Phys. Rev. A, **70**, 043629 (2004).

[129] T. Schumm, J. Estève, C. Figl, J.-B. Trebbia, C. Aussibal, H. Nguyen, D. Mailly, I. Bouchoule, C. I. Westbrook, and A. Aspect. *Atom chips in the real world: the effects of wire corrugation.* Eur. Phys. J. D, **32**, 171 (2005).

[130] D.-W. Wang, M. D. Lukin, and E. Demler. *Disordered Bose-Einstein Condensates in Quasi-One-Dimensional Magnetic Microtraps.* Phys. Rev. Lett., **92**, 076802 (2004).

[131] P. Krüger, L. M. Andersson, S. Wildermuth, S. Hofferberth, E. Haller, S. Aigner, S. Groth, I. Bar-Joseph, and J. Schmiedmayer. *Potential roughness near lithographically fabricated atom chips.* Phys. Rev. A, **76**, 063621 (2007).

[132] Z. Moktadir, B. Darquié, M. Kraft, and E. A. Hinds. *The effect of self-affine fractal roughness of wires on atom chips.* Journal of Modern Optics, **54**, 2149 (2007).

[133] J.-B. Trebbia, C. L. G. Alzar, R. Cornelussen, C. I. Westbrook, and I. Bouchoule. *Roughness Suppression via Rapid Current Modulation on an Atom Chip.* Phys. Rev. Lett., **98**, 263201 (2007).

[134] I. Bouchoule, J.-B. Trebbia, and C. L. G. Alzar. *Limitations of the modulation method to smooth wire-guide roughness.* Phys. Rev. A, **77**, 023624 (2008).

[135] J. Fortágh, S. Kraft, A. Günther, C. Trück, P. Wicke, and C. Zimmermann. *Perspectives of ultracold atoms trapped in magnetic micro potentials.* Optics Communications, **243**, 45 (2004).

[136] J. Fortágh and C. Zimmermann. *Magnetic microtraps for ultracold atoms.* Rev. Mod. Phys., **79**, 278 (2007).

[137] S. Whitlock, R. Anderson, B. Hall, P. Hannaford, and A. Sidorov. *Bose-Einstein condensates on a magnetic film atom chip.* Australian Optical Society News, **20**, 7 (2006).

[138] S. Whitlock, B. V. Hall, T. Roach, R. Anderson, M. Volk, P. Hannaford, and A. I. Sidorov. *Effect of magnetization inhomogeneity on magnetic microtraps for atoms.* Phys. Rev. A, **75**, 043602 (2007).

[139] B. V. Hall, S. Whitlock, F. Scharnberg, P. Hannaford, and A. Sidorov. *Bose-Einstein condensates on a permanent magnetic film atom chip.* Laser Spectroscopy XVII. Proceedings for the International Conference On Laser Spectroscopy (ICOLS) 2005, .

[140] B. V. Hall, S. Whitlock, R. Anderson, P. Hannaford, and A. I. Sidorov. *Condensate Splitting in an Asymmetric Double Well for Atom Chip Based Sensors.* Phys. Rev. Lett., **98**, 030402 (2007).

[141] M. Volk, S. Whitlock, C. H. Wolff, B. V. Hall, and A. I. Sidorov. *Scanning magnetoresistance microscopy of atom chips.* Rev. Sci. Instrum., **79**, 023702 (2008).

[142] M. Greiner, O. Mandel, T. Esslinger, T. W. Hänsch, and I. Bloch. *Quantum Phase Transition from a Superfluid to a Mott Insulator in a Gas of Ultracold Atoms.* Nature, **415**, 39 (2002).

[143] L. Fallani, J. E. Lye, V. Guarrera, C. Fort, and M. Inguscio. *Ultracold Atoms in a Disordered Crystal of Light: Towards a Bose Glass.* Phys. Rev. Lett., **98**, 130404 (2007).

[144] L. Sanchez-Palencia, D. Clément, P. Lugan, P. Bouyer, and A. Aspect. *Disorder-induced trapping versus Anderson localization in Bose-Einstein condensates expanding in disordered potentials.* New Journal of Physics, **10**, 045019 (2008).

[145] T. Schulte, S. Drenkelforth, J. Kruse, W. Ertmer, J. Arlt, K. Sacha, J. Zakrzewski, and M. Lewenstein. *Routes Towards Anderson-Like Localization of Bose-Einstein Condensates in Disordered Optical Lattices.* Phys. Rev. Lett., **95**, 170411 (2005).

[146] D. Clément, A. F. Varón, M. Hugbart, J. A. Retter, P. Bouyer, L. Sanchez-Palencia, D. M. Gangardt, G. V. Shlyapnikov, and A. Aspect. *Suppression of Transport of an Interacting Elongated Bose-Einstein Condensate in a Random Potential.* Phys. Rev. Lett., **95**, 170409 (2005).

[147] D. Clément, A. F. Varón, J. A. Retter, L. Sanchez-Palencia, A. Aspect, and P. Bouyer. *Experimental study of the transport of coherent interacting matter-waves in a 1D random potential induced by laser speckle.* New Journal of Physics, **8**, 165 (2006).

[148] C. Fort, L. Fallani, V. Guarrera, J. E. Lye, M. Modugno, and D. S. W. land M. Inguscio. *Effect of Optical Disorder and Single Defects on the Expansion of a Bose-Einstein Condensate in a One-Dimensional Waveguide.* Phys. Rev. Lett., **95**, 170410 (2005).

[149] J. E. Lye, L. Fallani, C. Fort, V. Guarrera, M. Modugno, and D. S. W. land M. Inguscio. *Effect of interactions on the localization of a Bose-Einstein condensate in a quasiperiodic lattice.* Phys. Rev. A, **75**, 061603(R) (2007).

[150] L. Sanchez-Palencia, D. Clément, P. Lugan, P. Bouyer, G. V. Shlyapnikov, and A. Aspect. *Anderson Localization of Expanding Bose-Einstein Condensates in Random Potentials.* Phys. Rev. Lett., **98**, 210401 (2007).

[151] P. Lugan, D. Clément, P. Bouyer, A. Aspect, M. Lewenstein, and L. Sanchez-Palencia. *Ultracold Bose Gases in 1D Disorder: From Lifshits Glass to Bose-Einstein Condensate.* Phys. Rev. Lett., **98**, 170403 (2007).

[152] D. Clément, P. Bouyer, A. Aspect, and L. Sanchez-Palencia. *Density modulations in an elongated Bose-Einstein condensate released from a disordered potential.* Phys. Rev. A, **77**, 033631 (2008).

[153] J. Chabé, G. Lemarié, B. Grémaud, D. Delande, P. Szriftgiser, and J. C. Garreau. *Experimental observation of the Anderson transition with atomic matter waves.* arXiv:0709.4320, (2007).

[154] J. Billy, V. Josse, Z. Zuo, A. Bernard, B. Hambrecht, P. Lugan, D. Clement, L. Sanchez-Palencia, P. Bouyer, and A. Aspect. *Direct observation of Anderson localization of matter waves in a controlled disorder.* Nature, **453**, 891 (2008).

[155] G. Roati, C. D'Errico, L. Fallani, M. Fattori, C. Fort, M. Zaccanti, G. Modugno, M. Modugno, and M. Inguscio. *Anderson localization of a non-interacting Bose-Einstein condensate.* Nature, **453**, 895 (2008).

[156] W. Petrich, M. H. Anderson, J. R. Ensher, and E. A. Cornell. *Stable, Tightly Confining Magnetic Trap for Evaporative Cooling of Neutral Atoms.* Phys. Rev. Lett., **74**, 3352 (1995).

[157] J. Reichel and J. H. Thywissen. *Using magnetic chip traps to study Tonks-Girardeau quantum gases.* J. Phys. IV France, **116**, 265 (2004).

[158] H. Friedburg. *Optical focusing of neutral atoms.* Zeitschrift für Physik, **130**, 493 (1951).

[159] H. Friedburg and W. Paul. *Optical focusing of neutral atoms.* Naturwissenschaften, **38**, 159 (1951).

[160] A. Lemonick, F. M. Pipkin, and D. R. Hamilton. *Focusing Atomic Beam Apparatus.* Rev. Sci. Instrum., **26**, 1112 (1955).

[161] C. J. Myatt, N. R. Newbury, R. W. Ghrist, S. Loutzenhiser, and C. E. Wieman. *Multiply loaded magneto-optical trap.* Optics Letters, **21**, 290 (1996).

[162] A. Goepfert, F. Lison, R. Schütze, R. Wynands, D. Haubrich, and D. Meschede. *Efficient magnetic guiding and deflection of atomic beams with moderate velocities.* Appl. Phys. B, **69**, 217 (1999).

[163] D. Müller, D. Z. Anderson, R. J. Grow, P. D. D. Schwindt, and E. A. Cornell. *Guiding Neutral Atoms Around Curves with Lithographically Patterned Current-Carrying Wires.* Phys. Rev. Lett., **83**, 5194 (1999).

[164] M. Key, I. G. Hughes, W. Rooijakkers, B. E. Sauer, E. A. Hinds, D. J. Richardson, and P. G. Kazansky. *Propagation of Cold Atoms along a Miniature Magnetic Guide.* Phys. Rev. Lett., **84**, 1371 (1999).

[165] B. K. Teo and G. Raithel. *Loading mechanism for atomic guides.* Phys. Rev. A, **63**, 031402(R) (2001).

[166] P. Cren, C. F. Roos, A. Aclan, J. Dalibard, and D. Guéry-Odelin. *Loading of a cold atomic beam into a magnetic guide.* Eur. Phys. J. D, **20**, 107 (2002).

[167] J. A. Richmond, B. P. Cantwell, S. N. Chormaic, D. C. Lau, A. M. Akulshin, and G. I. Opat. *Magnetic guide for neutral atoms.* Phys. Rev. A, **65**, 033422 (2002).

[168] E. A. Cornell, C. Monroe, and C. E. Wieman. *Multiply Loaded, ac Magnetic Trap for Neutral Atoms.* Phys. Rev. Lett., **67**, 2439 (1991).

[169] E. Maréchal, S. Guibal, J.-L. Bossennec, R. Barbé, J.-C. Keller, and O. Gorceix. *Longitudinal focusing of an atomic cloud using pulsed magnetic forces.* Phys. Rev. A, **59**, 4636 (1999).

[170] T. Miossec, R. Barbé, J.-C. Keller, and O. Gorceix. *Pulsed magnetic lenses for producing intense and bright cold atom beams.* Optics Communications, **209**, 349 (2002).

[171] M. J. Pritchard, A. S. Arnold, S. L. Cornish, D. W. Hallwood, C. V. S. Pleasant, and I. G. Hughes. *Transport of launched cold atoms with a laser guide and pulsed magnetic fields.* New Journal of Physics, **8**, 309 (2006).

[172] D. A. Smith, A. S. Arnold, M. J. Pritchard, and I. G. Hughes. *Experimental single-impulse magnetic focusing of launched cold atoms.* J. Phys. B: At. Mol. Opt. Phys., **41**, 125302 (2008).

[173] M. Greiner, I. Bloch, T. W. Hänsch, and T. Esslinger. *Magnetic transport of trapped cold atoms over a large distance.* Phys. Rev. A, **63**, 031401(R) (2001).

[174] K. Nakagawa, Y. Suzuki, M. Horikoshi, and J. B. Kim. *Simple and efficient magnetic transport of cold atoms using moving coils for the production of Bose-Einstein condensation.* Appl. Phys. B, **81**, 791 (2005).

[175] H. J. Lewandowski, D. M. Harber, D. L. Whitaker, and E. A. Cornell. *Simplified System for Creating a Bose-Einstein Condensate.* J. Low Temp. Phys., **132**, 309 (2003).

[176] T. Lahaye, G. Reinaudi, Z. Wang, A. Couvert, and D. Guéry-Odelin. *Transport of atom packets in a train of Ioffe-Pritchard traps.* Phys. Rev. A, **74**, 033622 (2006).

[177] J. Denschlag, D. Cassettari, and J. Schmiedmayer. *Guiding Neutral Atoms with a Wire.* Phys. Rev. Lett., **82**, 2014 (1999).

[178] N. H. Dekker, C. S. Lee, V. Lorent, J. H. Thywissen, S. P. Smith, M. Drndíc, R. M. Westervelt, and M. Prentiss. *Guiding Neutral Atoms on a Chip.* Phys. Rev. Lett., **84**, 1124 (2000).

[179] P. Rosenbusch, B. V. Hall, I. G. Hughes, C. V. Saba, and E. A. Hinds. *Manipulation of cold atoms using a corrugated magnetic reflector.* Phys. Rev. A, **61**, 031404(R) (2000).

[180] S. A. Meek, H. L. Bethlem, H. Conrad, and G. Meijer. *Trapping Molecules on a Chip in Traveling Potential Wells.* Phys. Rev. Lett., **100**, 153003 (2008).

[181] W. Hänsel, J. Reichel, P. Hommelhoff, and T. W. Hänsch. *Magnetic Conveyor Belt for Transporting and Merging Trapped Atom Clouds.* Phys. Rev. Lett., **86**, 608 (2001).

[182] P. Hommelhoff, W. Hänsel, T. Steinmetz, T. W. Hänsch, and J. Reichel. *Transporting, splitting and merging of atomic ensembles in a chip trap.* New Journal of Physics, **7**, 063621 (2005).

[183] R. Long, T. Rom, W. Hänsel, T. W. Hänsch, and J. Reichel. *Long distance magnetic conveyor for precise positioning of ultracold atoms.* Eur. Phys. J. D, **35**, 125 (2005).

[184] A. Günther, M. Kemmler, S. Kraft, C. J. Vale, C. Zimmermann, and J. Fortágh. *Combined chips for atom optics.* Phys. Rev. A, **71**, 063619 (2005).

[185] S. Whitlock, R. Gerritsma, T. Fernholz, and R. J. C. Spreeuw. *Two-dimensional array of microtraps with atomic shift register on a chip.* arXiv:0803.2151 (physics.atom-ph), (2008).

[186] R. Grimm, M. Weidemüller, and Y. B. Ovchinnikov. *Optical dipole traps for neutral atoms.* Adv. At. Mol. Opt. Phys., **42**, 95 (2000).

[187] M. J. Renn, D. Montgomery, O. Vdovin, D. Z. Anderson, C. E. Wieman, and E. A. Cornell. *Laser-Guided Atoms in Hollow-Core Optical Fibers.* Phys. Rev. Lett., **75**, 3253 (1995).

[188] M. J. Renn, A. A. Zozulya, E. A. Donley, E. A. Cornell, and D. Z. Anderson. *Optical-dipole-force fiber guiding and heating of atoms.* Phys. Rev. A, **55**, 3684 (1997).

[189] M. J. Renn, E. A. Donley, E. A. Cornell, C. E. Wieman, and D. Z. Anderson. *Evanescent-wave guiding of atoms in hollow optical fibers.* Phys. Rev. A, **53**, R648 (1996).

[190] H. Ito, T. Nakata, K. Salaki, M. Ohtsu, K. I. Lee, and W. Jhe. *Laser Spectroscopy of Atoms Guided by Evanescent Waves in Micron-Sized Hollow Optical Fibers.* Phys. Rev. Lett., **76**, 4500 (1996).

[191] H. Ito, K. Salaki, M. Ohtsu, and W. Jhe. *Evanescent-light guiding of atoms through hollow optical fiber for optically controlled atomic deposition.* Appl. Phys. Lett., **70**, 2496 (1997).

[192] Y. Song, D. Milam, and W. T. H. III. *Long, narrow all-light atom guide.* Opt. Lett., **24**, 1805 (1999).

[193] M. Yan, J. Yin, and Y. Zhu. *Dark-hollow-beam guiding and splitting of a low-velocity atomic beam.* J. Opt. Soc. Am. B, **17**, 1817 (2000).

[194] K. Kim, H.-R. Noh, Y.-H. Yeon, X. Xu, and W. Jhe. *Optical Guiding of Atomic Fountain by a Hollow Laser Beam.* J. Korean Phys. Soc., **39**, 877 (2001).

[195] X. Xu, K. Kim, W. Jhe, and N. Kwon. *Efficient optical guiding of trapped cold atoms by a hollow laser beam.* Phys. Rev. A, **63**, 063401 (2001).

[196] K. Bongs, S. Burger, S. Dettmer, D. Hellweg, J. Arlt, W. Ertmer, and K. Sengstock. *Waveguide for Bose-Einstein condensates.* Phys. Rev. A, **63**, 031602(R) (2001).

[197] L. Pruvost, D. Marescaux, O. Houde, and H. T. Duong. *Guiding and cooling of cold atoms in a dipole guide.* Opt. Commun., **166**, 199 (1999).

[198] K. Szymaniec, H. J. Davies, and C. S. Adams. *An atomic fountain guided by a far-off resonance laser beam.* Europhysics Letters, **45**, 450 (1999).

[199] H. J. Davies and C. S. Adams. *Transferring laser-cooled atoms to a spatially separated magnetic trap using a far-off resonance optical guide.* J. Phys. B: At. Mol. Opt. Phys., **33**, 4079 (2000).

[200] B. T. Wolschrijn, R. A. Cornelussen, R. J. C. Spreeuw, and H. B. van Linden van den Heuvell. *Guiding of cold atoms by a red-detuned laser beam of moderate power.* New Journal of Physics, **4**, 69 (2002).

[201] D. Schneble, M. Hasuo, T. Anker, T. Pfau, and J. Mlynek. *Integrated atom-optical circuit with continuous-wave operation.* J. Opt. Soc. Am. B, **20**, 648 (2003).

[202] S. Kuhr, W. Alt, D. Schrader, M. Müller, V. Gomer, and D. Meschede. *Deterministic Delivery of a Single Atom.* Science, **293**, 278 (2001).

[203] D. Schrader, S. Kuhr, W. Alt, M. Müller, W. Gomer, and D. Meschede. *An optical conveyor belt for single neutral atoms.* Appl. Phys. B, **73**, 819 (2001).

[204] A. Browaeys, H. Häffner, C. McKenzie, S. L. Rolston, K. Helmerson, and W. D. Phillips. *Transport of atoms in a quantum conveyor belt.* Phys. Rev. A, **72**, 053605 (2005).

[205] T. L. Gustavson, A. P. Chikkatur, A. E. Leanhardt, A. Görlitz, S. Gupta, D. E. Pritchard, and W. Ketterle. *Transport of Bose-Einstein Condensates with Optical Tweezers.* Phys. Rev. Lett., **88**, 020401 (2002).

[206] W. Guerin, J.-F. Riou, J. P. Gaebler, V. Josse, P. Bouyer, and A. Aspect. *Guided Quasicontinuous Atom Laser.* Phys. Rev. Lett., **97**, 200402 (2006).

[207] P. Horak, B. G. Klappauf, A. Haase, R. Folman, J. Schmiedmayer, P. Domokos, and E. A. Hinds. *Possibility of single-atom detection on a chip.* Phys. Rev. A, **67**, 043806 (2003).

[208] B. R. Long, T. Steinmetz, P. Hommelhoff, W. Hänsel, T. W. Hänsch, and J. Reichel. *Magnetic microchip traps and single-atom detection.* Phil. Trans. R. Soc. Lond. A, **361**, 1375 (2003).

[209] B. Lev, K. Srinivasan, P. Barclay, O. Painter, and H. Mabuchi. *Feasibility of detecting single atoms using photonic bandgap cavities.* Nanotechnology, **15**, S556 (2004).

[210] M. Rosenblit, P. Horak, S. Helsby, and R. Folman. *Single-atom detection using whispering-gallery modes of microdisk resonators.* Phys. Rev. A, **70**, 053808 (2004).

[211] S. Eriksson, M. Trupke, H. F. Powell, D. Sahagun, C. D. J. Sinclair, E. A. Curtis, B. E. Sauer, E. A. Hinds, Z. Moktadir, C. O. Gollasch, and M. Kraft. *Integrated optical components on atom chips.* Eur. Phys. J. D, **35**, 135 (2005).

[212] M. Wilzbach, A. Haase, M. Schwarz, D. Heine, K. Wicker, X. Liu, K.-H. Brenner, S. Groth, T. Fernholz, B. Hessmo, and J. Schmiedmayer. *Detecting neutral atoms on an atom chip.* Fortschr. Phys., **54**, 746 (2006).

[213] P. A. Quinto-Su, M. Tscherneck, M. Holmes, and N. P. Bigelow. *On-chip optical detection of laser cooled atoms.* Optics Express, **12**, 5098 (2004).

[214] A. Takamizawa, T. Steinmetz, R. Delhuille, T. W. Hänsch, and J. Reichel. *Miniature fluorescence detector for single atom observation on a microchip.* Optics Express, **14**, 10976 (2006).

[215] K. P. Nayak, P. N. Melentiev, M. Morinaga, F. L. Kien, V. I. Balykin, and K. Hakuta. *Optical nanofiber as an efficient tool for manipulating and probing atomic fluorescence.* Optics Express, **15**, 5431 (2007).

[216] G. Sagué, E. Vetsch, W. Alt, D. Meschede, and A. Rauschenbeutel. *Cold-Atom Physics Using Ultrathin Optical Fibers: Light-Induced Dipole Forces and Surface Interactions.* Phys. Rev. Lett., **99**, 163602 (2007).

[217] T. Steinmetz, Y. Colombe, D. Hunger, T. W. Hänsch, A. Balocchi, and R. J. W. adn J. Reichel. *Stable fiber-based Fabry-Pérot cavity.* Appl. Phys. Lett., **89**, 111110 (2006).

[218] I. Teper, Y.-J. Lin, and V. Vuletić. *Resonator-Aided Single-Atom Detection on a Microfabricated Chip.* Phys. Rev. Lett., **97**, 023002 (2006).

[219] M. Trupke, J. Goldwin, B. Darquié, G. Dutier, S. Eriksson, J. Ashmore, and E. A. Hinds. *Atom Detection and Photon Production in a Scalable, Open, Optical Microcavity.* Phys. Rev. Lett., **99**, 063601 (2007).

[220] T. Campey, C. J. Vale, M. J. Davis, N. R. Heckenberg, H. Rubinsztein-Dunlop, S. Kraft, C. Zimmermann, and J. Fortágh. *Atom counting in ultracold gases using photoionization and ion detection.* Phys. Rev. A, **74**, 043612 (2006).

[221] S. Kraft, A. Günther, J. Fortágh, and C. Zimmermann. *Spatially resolved photoionization of ultracold atoms on an atom chip.* Phys. Rev. A, **75**, 063605 (2007).

[222] A. Stibor, S. Kraft, T. Campey, D. Komma, A. Günther, J. Fortágh, C. Vale, H. Rubinsztein-Dunlop, and C. Zimmermann. *Calibration of a single atom detector for atomic micro chips.* Phys. Rev. A, **76**, 033614 (2007).

[223] M. Klank, O. Hagedorn, C. Holthaus, M. Shamonin, and H. Dötsch. *Characterization and optimization of magnetic garnet films for magneto-optical visualization of magnetic field distributions.* NDT & E International, **36**, 375 (2003).

[224] K. M. Birnbaum and The Quantum Optics Group, *Ultra-High Vacuum Chambers*, California Institute of Technology. Internal Publication. http://www.its.caltech.edu/∼qoptics/Vacuum/UHV_chambers.pdf (2005).

[225] K. M. Birnbaum, *Cavity QED with Multi-Level Atoms*, Ph.D. thesis, California Institute of Technology (2005).

[226] L. Westerberg et al. *CHICSi- A compact ultra-high vacuum compatible detector system for nuclear reaction experiments at storage rings. General structure, mechanics and*

UHV compatibility. Nuclear Instruments and Methods in Physics Reasearch A, **500**, 84 (2003).

[227] T. A. Delchar, *Vacuum Physics and Techniques* (Chapman and Hall. Springer, 1993).

[228] Goodfellow Cambridge Limited, *Comparative data tables of material properties*, http://www.goodfellow.com/csp/active/gfHome.csp.